Max-Planck-Institut für extraterrestrische Physik
Garching bei München

Supernova Diagnostics from Gamma-Ray Lines in the Young Remnant Phase

Christoph Weinberger

Vollständiger Abdruck der von der Fakultät für Physik der Technischen Universität München zur Erlangung des akademischen Grades eines

Doktors der Naturwissenschaften

genehmigten Dissertation.

Vorsitzender:		Prof. Dr. Alejandro Ibarra
Prüfer der Dissertation:	1.	apl. Prof. Dr. Roland Diehl
	2.	Prof. Dr. Lothar Oberauer

Die Dissertation wurde am 09.06.2021 bei der Technischen Universität München eingereicht und durch die Fakultät für Physik am 13.09.2021 angenommen.

Zusammenfassung

Die Signatur von Supernovae wurde mit hochaufgelösten Spektren der Gammaemission von Atomkernen mithilfe des Teleskops INTEGRAL/SPI untersucht. Durch Bestimmung der Nukleosynthesemasse von ^{44}Ti konnten einige Explosionsmodelvarianten von Supernovae als unwahrscheinlich erkannt werden. Die galaktische Supernovarate wurde durch eine ^{44}Ti Himmelsdurchmusterung und Vergleich mit Simulationen bestimmt. Die Beschleunigung kosmischer Strahlung im Cas A SNR wurde mit Kernanregungslinien bestimmt.

Abstract

The signature of supernovae was investigated with high-resolution spectra of gamma-radiation from nuclei utilizing the gamma-ray telescope INTEGRAL/SPI. Several explosion model variants were recognized as unlikely by determining the nucleosynthesized ^{44}Ti mass. The Galactic supernova rate was determined by comparison of my ^{44}Ti survey with simulations. Cosmic ray acceleration in the Cas A SNR was determined by nuclear excitation lines.

Contents

List of Figures

List of Tables

List of Acronyms

ACS Anti-Coincidence Shield

c speed of light

CRGT Calcium Rich Gap Transient

Cas A Cassiopeia A

ccSN Core Collapse Supernova

CO WD Carbon Oxygen White Dwarf (star)

CR Cosmic Ray

DSA Diffusive Shock Acceleration

d.o.f. degree of freedom

EC Embedded Cluster

ECMF Embedded Cluster Mass Function

ECSN Electron-Capture Supernova

EOS Equation of State

FWHM Full Width at Half Maximum

FoV Field of View

GMC Giant Molecular Clouds

IGE Iron Group Elements

IME Intermediate Mass Elements

IMF Initial Mass Function

ISDC INTEGRAL Science Data Center

LECR Low Energy Cosmic Ray

LMC Large Magellanic Cloud

M_* Mass of an individual star

Mxx Object xx in the Messier catalogue

NGC xx Object xx in the New General Catalogue

NS Neutron Star

NSE Nuclear Statistical Equilibrium

NTB Non Thermal Bremsstrahlung

PMT Photo-Multiplier Tube

PNS Proto-Neutron Star

QSE Quasi Statistical Equilibrium

SASI Standing Accretion Shock Instability

SED Spectral Energy Distribution

SFR Star Formation Rate

SMC Small Magellanic Cloud

SN Supernova

SNR Supernova Remnant

SPI Spectrometer on INTEGRAL

WD White Dwarf (star)

ZAMS Zero-Age-Main-Sequence

Danksagung

Als Erstes möchte ich mich bei meinem Doktorvater Prof. Dr. Roland Diehl bedanken, dass er mir die Möglichkeit gegeben hat, bei ihm zu promovieren. Von ihm durfte ich eine wissenschaftliche Arbeits- und Argumentationsweise lernen. Gerade letzteres konnte ich durch die mir ermöglichte Teilnahme an internationalen Konferenzen fördern. Diese Erfahrungen haben mich sehr bereichert.
Ich bedanke mich auch bei meinen Kollegen am Institut Jochen Greiner, Björn Biltzinger, Micheal Burgess und Xiao-Ling Zhang für die Weitergabe ihres fachlichen Wissens und für ihre guten Ratschläge. Insbesondere durfte ich mich der ausdauernden Unterstützung meiner Freunde und Kollegen am Institut Thomas Siegert und Moritz Pleintinger erfreuen. Durch euch habe ich die Freude an der Arbeit nie verloren. Lieber Thomas, lieber Moritz, danke für die unzähligen Diskussionen und vor allem für die unvergessliche Freundschaft.
Besonders erwähnen möchte ich meine Freunde Sebastian Bauer und Matthias Ammerstorfer. Ich kann mich immerzu auf euch verlassen und konnte dank euch außerhalb des akademischen Umfeldes Kraft und Freude schöpfen.
An dieser Stelle möchte ich gerne meine großartige Familie hervorheben, auf deren Rückhalt ich stets zählen konnte, und die mich in all meinen Vorhaben immerzu bestärkt hat. Danke, dass ihr mir dies alles ermöglicht habt!
Der größte Dank gebührt aber dem wichtigsten Menschen in meinem Leben, Patricia Düsing. Liebste Patricia, wenngleich ich dich auch manchmal in den Wahnsinn getrieben habe, so konnte ich mich dennoch stets auf deinen treuen Beistand und deine liebevolle Unterstützung verlassen. Du hast mir den nötigen Halt und die Motivation gegeben, vor allem die letzten paar Monate so durchzustehen. Ich danke dir, dass du immer für mich da bist, und nie aufgehört hast, an mich zu glauben!

Chapter 1

Introduction

Supernovae; what a magnificent sight they must have been to behold for those lucky few generations that were able to observe their appearance in the sky with the naked eye. Challenging the idea of an unchanging night sky, that has been used for centuries to predict the course of seasons and years alike, it comes as no surprise that these astrophysical objects were long considered to be an omen of god, a harbinger to herald a new era. The transient appearance of the *guest stars*, rising in luminosity within several days and declining again afterwards within several months, has fascinated observers since ancient times. The earliest written record, dating back to 185, was found in the "Book of the later Han", with such precise information that the emission nebula RCW 86 could recently be identified as the remnant of this ancient supernova (Stephenson & Green 2002; Vink et al. 2006). Unfortunately though, since the beginning of modern astronomy some 500 yr ago, only two transients could be observed in the Milky Way, one in 1572 by Tycho Brahe and one by Johannes Kepler in 1604. The first extragalactic supernova (S Andromaedae), observed in 1885 in the Andromeda nebula, was initially misidentified to be a nova-like object. It took 35 yr and a refined distance estimate to the Andromeda nebula (Opik 1922) to realize, that the Andromeda nebula was actually an object outside the Milky Way, and that the luminosity of SN 1885A was underestimated by three orders of magnitude. With an increasing number of observed objects, Baade & Zwicky (1934b) introduced the term *super-nova* (SN) to distinguish these extremely bright objects from the much fainter novae. Within the last 100 yr, our understanding of SNe and their feedback on the Galactic evolution has progressed a long way, but even now, it still seems that more questions have been raised than answered.

Nucleosynthesis and Stellar Explosions

It has widely been understood that the abundance of chemical elements in the present universe was formed in later stages due to fusion processes in stellar environments, as primordial nucleosynthesis was only able to form very light elements such as hydrogen, helium and a minor fraction of isotopes with mass numbers higher than four. While stars can produce elements up to the iron group during their lifetime, SNe are considered as one of the main contributors to the enrichment of the universe in heavy elements through production of isotopes like gold and silver and a variety of radioactive nuclei.
Highly energetic decay radiation of these isotopes cannot readily escape from the SN due to the high density in the supernova remnant (SNR) at early stages and is instead thermalized, adding to the internal energy of the SNR, enhancing its physical evolution and also making it

shine bright at optical wavelengths. This facilitates their use as standard candles for distance estimates up to the Gpc-scale, which is utilized to measure the increasing expansion rate of the universe (Perlmutter et al. 1998). However, an increasing amount of observational data showed that a large variety of SN explosion characteristics cannot be explained by assuming a single explosion scenario. Even though the varying light curves can be calibrated (Phillips et al. 1999), a sophisticated understanding of SN explosions is required to precisely gain cosmological understanding from the *standard candles*.
Despite their frequent occurrence and a wealth of observational knowledge, the mechanisms that lead to the explosion are still not entirely understood. The main distinction is made between thermonuclear SNe (Type Ia), and core collapse SNe (ccSN) occurring at the end of the lifespan of massive stars with more than 8 solar masses.
Models for type Ia SNe commonly suggest the ignition of carbon burning in the central regions of its progenitor white dwarf (WD) star (Seitenzahl et al. 2013). While this process is widely accepted by the astrophysical community, different progenitor scenarios that lead to the ignition of the fusion processes have been suggested over the years to account for the large diversity in observational constraints. It is most likely not one particular model that can account for all explosions. More likely, multiple progenitor scenarios contribute to the overall population of type Ia SNe.
Providing a unified picture of ccSNe is an even larger problem, as so far, self-consistent models that explain the entire explosion process are not established. *Piston driven* models (Woosley & Weaver 1995) that inject the necessary energy into the central region of a star to launch an explosion are utilized to predict the long term evolution and nucleosynthesis of collapsed stellar cores. The driving force for providing this sufficient energy is, however, still not adequately explained (Janka 2012). While the consensus is that the interaction of neutrinos with stellar material plays a crucial role, recent multidimensional simulations show that additional mechanisms are required to consistently unbind the ejecta from the gravitational pull of the central compact remnant, either a neutron star or a stellar mass black hole.
One of the most promising ways of providing new insights into the driving physical mechanisms is by observing the nucleosynthesis products of SNe that are highly susceptible to the conditions during the early explosion. Their behavior can be determined indirectly from the temporal change of the light curve and emission of atomic shell transitions. Both methods, however, require additional knowledge of thermo- and hydrodynamic properties of the remnant. These dependencies can be avoided by searching for the decay radiation of freshly synthesized, radioactive isotopes present in the SN's ejecta. The properties of this radiation can be utilized to infer information on the physics during the explosion. The most prominent emission originates from the decay chain of the isotopes ^{56}Ni and ^{44}Ti. The significant difference in the half-life of these isotopes from 6 days up to 60 years allows the study of SNRs in various phases of its early evolution.

Identifying the Origin of Cosmic Rays

Since the discovery of *Höhenstrahlung* by Victor Hess in 1912 (Hess 1912), these energetic particles, afterwards named *Cosmic Rays* (CR), have been thoroughly investigated. The highest measured energies for CRs are in the range of 10^{20} eV. CRs arriving at Earth are mainly comprised of protons, with a smaller number of electrons, positrons and some heavy elements. CRs constitute up to one third of the energy content in the interstellar medium and

their propagation seems to contribute to the generation of magnetic fields (Bell 2013). As they are also considered to contribute a major fraction of energy in explosive environments, such as SNe, a detailed understanding of the nature of particle acceleration to ultrarelativistic energies, the transport of CRs in the Galactic environment and the emission of electromagnetic radiation from CR interactions with the ambient medium is highly required.
For a long time, SNRs have been considered as one of the prime acceleration sites for Galactic CRs up to an energy of 10^{15} eV. The extreme amount of energy released by such explosions could provide a place of origin for Galactic CRs (Baade & Zwicky 1934a). The expansion of a SN shock front into the surrounding interstellar medium hosts ideal conditions for the process of *diffusive shock acceleration*. While the acceleration of electrons in SNR shocks seems well established due to their emission of synchrotron radiation, the link between acceleration of protons and ions in SNRs has not yet been unambiguously determined. Electromagnetic radiation in the GeV–TeV range is observed in several SNRs, but the ambiguity of their origin, either of leptonic (electrons) or hadronic (protons and ions) interactions, cannot yet be fully settled. However, the interaction of CR protons and ions with the ambient medium is expected to excite level transitions in the surrounding nuclei. The predominant electromagnetic radiation of these processes would be emitted from excited ^{12}C and ^{16}O at 4.4 MeV and 6.1, 6.9 and 7.1 MeV, respectively. In addition, a large variety of secondary level transitions are expected in the energy range between 300 keV and 8 MeV.

For this thesis I utilized 18 years of exposure of the Spectrometer on INTEGRAL (Winkler et al. 2003; Vedrenne et al. 2003) to study the emission of the nuclear transitions at hard X-ray to soft γ-ray energies. A revised background model in the energy region, important to study the emission lines in the decay chain of ^{44}Ti, is adopted. Revisiting the Cassiopeia A remnant with increased exposure provides new insights into the underlying explosion physics. The improved understanding of SN explosion physics gained from this analysis motivates an extended analysis of other, previously known, young SNRs. As their number is limited, this revised analysis approach is utilized to search for previously unknown SNRs in the Galaxy that emit radiation in the ^{44}Ti decay chain. The observed scarcity of ^{44}Ti emitting remnants is either in disagreement with current theoretical understanding of ccSN physics or predetermined recurrence rates of SN explosions. This discrepancy is further investigated by modeling a synthetic distribution of ^{44}Ti bright remnants in the Galaxy, utilizing a simulation technique that is independent of predetermined recurrence rates, but rather follows the evolution of massive stars in the Galaxy.
An increased flux in one of the decay lines of ^{44}Ti is assessed to originate from the excitation of ^{44}Ca by CRs in the remnant. The presence of such a component would lead to a detectable emission in the high energy range of SPI above 2 MeV. As line emission in this energy range has not be investigated before, a high precision background model is developed for the high energy range of SPI and thoroughly calibrated. Observations of Cassiopeia A in the high energy range reveal a previously undiscovered emission between 1 and 8 MeV, which is attributed to the emission of CR-induced nuclear de-excitation radiation.

This thesis is structured as follows: In chapter 2, I give an overview of the current understanding of SN explosions and their impact on the Galaxy. This includes the various progenitor models leading to the explosion, the physical conditions occurring during the explosion and nucleosynthesis calculations. The chapter includes an overview of the signals detectable

at X- and γ-ray energies, including CR de-excitation lines. In chapter 3, I explain the principles of energy deposition in detector material, leading to strong instrumental background radiation in a spaceborne γ-ray telescope such as SPI. In chapter 4, a detailed description of SPI data analysis is given, including the modeling of a self-consistent background model for a γ-ray telescope in a space environment above 2 MeV. I analyze the emission of ^{44}Ti in historical SNRs in chapter 5. The discrepancies between our observations and predictions from sophisticated simulations (see e.g. Janka (2012); Hillebrandt et al. (2013)) are discussed. Due to the unexpected scarcity of ^{44}Ti emitting sources, I search for previously undetected ^{44}Ti sources in the Milky Way. The results from this survey are discussed and compared to a simulated distribution of core collapse SNRs in the Galaxy. I include a description of this modeling approach and a detailed analysis of the celestial distribution of remnants. Chapter 6 focuses on the analysis of the hadronic excitation of nuclear transitions in SNRs. I analyze the spectrum of a candidate source and discuss the implications on the nature of CRs. The compatibility of our results is compared with the spectral analysis at radio wavelengths and GeV energies. In chapter 7, I summarize the emission of nuclear transition lines and the implications for the puzzle of their astrophysical origins in the context of SN explosions.

Chapter 2

Supernova Explosions

2.1 What Are Supernova Explosions?

2.1.1 Classification of Supernovae

From the observational point of view, SNe are classically identified by the presence or absence of lines from atomic shell transitions. The main distinction between SNe is made by the presence of hydrogen lines in the early SN spectra in type II SNe, while type I SNe lack these lines. Instead, however, type Ia SNe show strong emission lines from silicon isotopes. However, a lack of silicon and hydrogen lines in the presence of helium lines classifies the SN as type Ib, while the lack of lines of all aforementioned elements classifies the SN as type Ic.

This classification is also represented in the temporal evolution of the SN's luminosity. In Figure 2.1 the schematic light curves of various SN sub-types are shown. In general, the bolometric light curve of SNe and their remnants is powered by the absorption of decay photons and energy depositions from positrons ejected in the decay of radioactive material. As shown in Figure 2.1, SNe show a fast early and a more gradual decay in the later SN evolution. The decline for both phases matches the decay rate in the decay chain of the isotope ^{56}Ni, that decays to ^{56}Co with a half-life of 6.1 days (Audi et al. 2017). The subsequent decay of ^{56}Co to ^{56}Fe with a half-life of 77.1 days (Audi et al. 2017) powers the late time light curve. Deviation from the expected decay law is observed in the later phases of the ^{56}Co powered phase, when the recycling efficiency for γ-rays in the SN envelope decreases due to the dilution of the expanding material.

The brightest transients are observed for SNe of type Ia, and these SNe also show the fastest decline rate of the blue band luminosity. This behavior can be explained by the ejection of roughly 1.5 $M_\odot$ of matter with high velocities of the order of 10000 km s^{-1} (Wilk et al. 2017). The ejecta are rich in ^{56}Ni that heat the matter accordingly, however, due to the high ejecta velocity, the remnant becomes optically thin early and the SN luminosity declines fast. SNe of this type are ascribed to the explosion of white dwarf stars that produce between 0.1 – 1.0 $M_\odot$ ^{56}Ni (Stritzinger et al. 2006) during explosive carbon oxygen burning.

All other sub-types of SNe are attributed to the explosion ensuing the core collapse of an evolved, massive ($M \gtrsim 8\,M_\odot$) star. The peak brightness and the width, with which the peak brightness decays, are considered to be directly dependent on the amount of matter in the

progenitor star's surface layers. Type II-P SNe are expected to arise from massive stars with a thick surface hydrogen layer (e.g. Kasen & Woosley 2009). When passing through the hydrogen layer, the explosion shock wave can ionize the hydrogen, increasing the optical depth of the surface layer and prohibiting photons from effectively escaping the ejecta. Only when the SN remnant cools adiabatically by expanding, the hydrogen atoms recombine, optically thinning the ejecta, which leads to a prolonged phase of high luminosity visible as a second plateau-like peak in the light-curve. In contrast, type Ib and Ic SNe have lost the majority of their hydrogen (Ib) and also helium (Ic) layer due to interaction with companion stars or solar winds, leading to a brighter and narrower peak luminosity (Filippenko 1997). This also explains the absence of hydrogen and helium lines in the respective spectra.

While the connection between the various SN types and their progenitor systems seems to be well established, modern SN astrophysics faces two major problems. For core collapse SNe (ccSN), the link between the massive progenitor and the SN explosion is observationally well shown (e.g. Dyk 2017), with more than 30 identified progenitors stars of ccSN explosions. However, on the theoretical side, simulations that can self-consistently explode a star after the collapse of its central core are still sparse. Whether newer physical models that utilize supercomputers for a 3D evolution of the collapsed star can explain the explosion, or some physical ingredients are still missing is not yet fully understood (see section 2.3). In contrast to that, simulations for type Ia SNe are well established and lead to the successful disruption of a white dwarf star while producing the required ejected amounts of radioactive material. However, the progenitor scenario, that leads to the onset of an explosion in a stable white dwarf star in the first place, is not yet determined, as observations of type Ia explosion progenitors are still missing (see section 2.4).

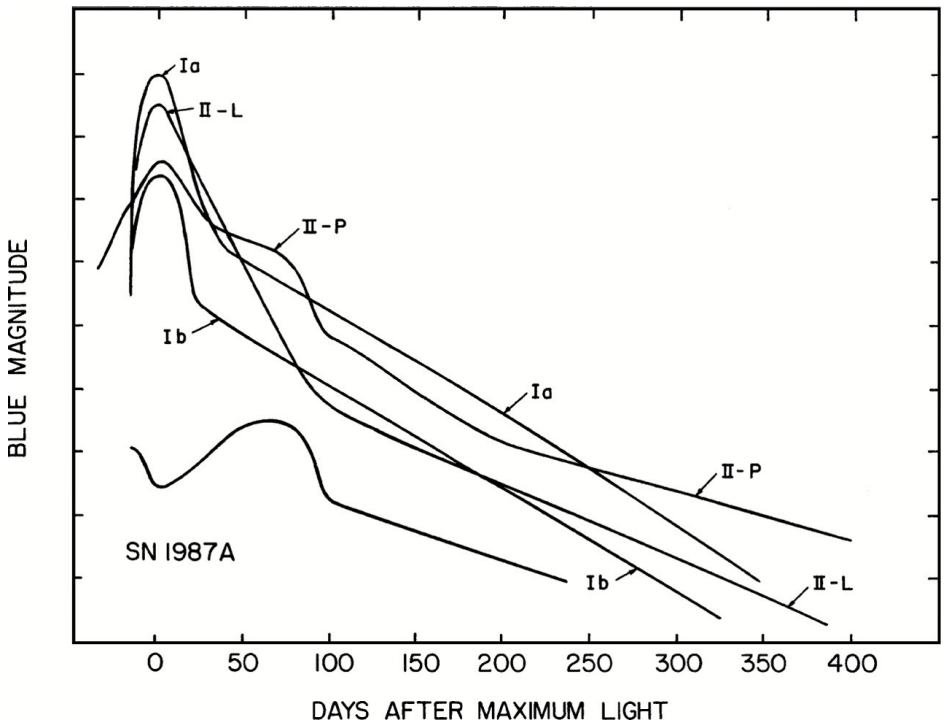

Figure 2.1: Schematic light curves of the different types of SNe. The luminosity is given in absolute blue band magnitude, i.e. in logarithmic scaling. Adopted from Filippenko (1997).

2.2 Stellar Evolution

In this section, the evolution of stars from their formation out of gas clouds to their eventual demise and final state are described. Specifically the evolution of massive stars with $M_{ZAMS} \gtrsim 8\,M_\odot$, when the star reaches its main sequence phase (ZAMS), is followed in detail, as these stars are the progenitors of ccSNe (cf. section 2.3). In section 5.3, a synthetic distribution of ccSNe is simulated, following the evolution of massive stars in the Galaxy. For that purpose, the physical processes and empirical laws that describe the distribution of Galactic gas into star groups and their individual stars is summarized in the following.

2.2.1 Star Formation

The formation of stars is a gravitationally driven process that transforms gas from the interstellar medium (ISM) into stars. The ISM, in general, is composed of gas, accelerated charged particles (cosmic rays), and dust. The gas of the ISM contains three distinct components: a hot phase, with temperatures of $\approx 10^6$ K, a warm phase with temperatures of 10^3–10^4 K and a cold phase with temperatures below ≈ 100 K. While the majority of the volume in the interstellar medium is filled with ionized gas, due to its low density below ≈ 1 particle per cm^3, only about 25% of the total mass are situated in that phase. Conversely, more than 50% of the gas mass is contained in the cold phase (McKee 1999) with a high density ranging between 10–100 particles per cm^3, that occupies only 1–2% of the interstellar volume (Klessen & Glover 2016). Within the cold medium, molecules can form when the extinction of UV radiation is sufficient. This requires a column density of H atoms between the surface of a gas cloud and the molecular interior of $N_H \gtrsim 2 \times 10^{21}\,g\,cm^{-2}$ for the formation of molecular H_2 and column densities $N_H \gtrsim 10^{22}\,g\,cm^{-2}$ for the formation of other molecules such as CO (Bohlin et al. 1978). These molecular clouds are of specific interest, as they are the site in which star formation occurs in the Galaxy. Within the diffuse molecular phase, giant molecular clouds (GMCs) can form due to colliding Galactic flows (Heitsch et al. 2005) or the presence of large scale gravitational instabilities (Ballesteros-Paredes et al. 2007). In both cases, sufficient cold gas mass is accumulated in a limited spatial volume and the gas becomes gravitationally bound against its outward thermal pressure. Assuming a uniform sphere in hydrostatic equilibrium, the stability condition for the sphere is given by the virial theorem, which states that $-2E_{kin} = E_{pot}$. This can be expressed as (Unsöld & Baschek 2002)

$$\frac{3k_b\,T\,M}{\mu\,m_u} = \frac{3\,G\,M^2}{5R}, \tag{2.1}$$

where k_b is the Boltzmann-constant, T is the gas temperature, G is the gravitational constant, μ is the molecular weight of the gas and m_u is the atomic mass unit. The sphere is defined by its radius R and its mass $M = 4/3R^3\pi\rho$, where ρ is the uniform density of the sphere.
For a gas cloud to collapse under its own gravity and allow star formation, the radius of the cloud needs to fall below the characteristic length scale, the Jeans radius (Jeans 1902), defined as

$$R_J = \sqrt{\left(\frac{15\,k_B\,T}{4\pi\,G\rho\mu\,m_u}\right)}. \tag{2.2}$$

At this radius, the gas sphere is in hydrostatic equilibrium. The mass contained in the sphere, the Jeans mass, is then given as

$$M_J = 5.46\left(\frac{k_b\,T}{\mu\,m_u\,G}\right)^{\frac{3}{2}}\rho^{-\frac{1}{2}} = 3.82\times10^{-9}\left(\frac{T}{\mu}\right)\rho^{-\frac{1}{2}}\times M_\odot, \tag{2.3}$$

where the temperature and the density are given in units of K and $kg\,m^{-3}$, respectively. Considering now a sphere of cold ISM gas with a characteristic density ranging between 10^{-21} to $10^{-18}\,kg\,m^{-3}$ and temperatures ranging between 10 and 100 K, the mass of a GMC can be estimated to be in the range of 10^2–$10^5\,M_\odot$. GMCs are formed with masses of entire star forming regions. While the interior of the GMCs are screened from UV radiation, cosmic rays (CRs) can penetrate deep into the GMCs, ionizing the molecular clouds such that the temperature of the clouds cannot fall significantly below 10 K. As the Jeans mass is proportional to $\rho^{-1/2}$, additional compression of the gas is required to incite individual star formation.

The gas in GMCs is not homogeneously distributed. Passages through high density regions such as Galactic spiral arms and the Galactic center exert an external compression on the GMCs. More importantly though, cloud internal supersonic turbulent motion leads to a fragmentation of the GMC's gas content (Dobbs et al. 2014; Padoan et al. 2014). The supersonic turbulence produces a filamentary structure inside the GMCs. Thereby, the GMCs are fragmented into high density clumps with hydrogen particle densities of $\approx 10^4\,cm^{-3}$. Within these clumps, the stability criterion is exceeded and the clumps become Jeans unstable. The clumps themselves, however, again show a substructuring into highest density regions, which are convergence points of interacting filaments. Within these cores, the density can be high enough that gravitational collapse occurs, making them the birth places of stars. The collapse of a single, substructured clump leads to a clustered star formation (Lada & Lada 2003).

Once the collapse of a core sets in, it collapses on the free-fall time scale as the thermal energy, liberated from gravitational collapse, is efficiently radiated away. The contraction of the central region stalls when the dense central core becomes optically thick for its infrared emission and the compressional heat cannot be radiated away anymore. In the center a protostar which is an object in quasi hydrostatic equilibrium without internal fusion processes forms. The mass of the central protostar further increases as additional mass settles on the surface of the central region from gravitationally bound, infalling gas. The infalling gas is stopped at the surface of the protostar, where a shock forms and the gas' kinetic energy is transformed into heat. The timescale for the collapse is given by the Kelvin-Helmholtz time, which is the time required to radiate away the gravitational energy $\tau_K = GM_*^2/RL$ with the luminosity L. As the luminosity is proportional to the mass with $L \propto M_*^{3.5}$, the Helmholtz time consequently is $\tau_K \propto M_*^{-3.5}$. Therefore, massive stars form faster in the same GMC than their lower mass companions (Kippenhahn et al. 2012). When the star has accreted more $0.075\,M_\odot$, the central region's temperature increases sufficiently that fusion processes of hydrogen start. The protostar's radiative energy losses are compensated by nuclear fusion processes. At a given point, the accretion of gas on the protostar stops, either because the entire mass has been accreted or because radiative feedback from the protostar has dispersed the parental core. In either case, the protostar finds a hydrostatic equilibirum condition and

becomes a main sequence star.

The formation of stars is an inherently inefficient process, in which only about 5–10% of a GMC's gas mass is transformed into stars (Clark et al. 2005; McKee & Ostriker 2007). An overall collapse of the cloud is counteracted by feedback mechanisms from the first stars in the cloud. Photo-ionization of hydrogen gas by UV radiation from newly formed, massive stars increases the internal energy and momentum of the gas. Additional kinetic energy is contributed to the gas by feedback from stars in the form of stellar winds and SN explosions. While the latter two can incite additional star formation as they are the driving forces of supersonic turbulence, the cumulative energy contribution to the gas leads to an overall mass loss of the GMC that is eventually disrupted within 20–30 Myr after formation (Krumholz et al. 2006).

2.2.1.1 Initial Mass Function

One of the fundamental quantities of star formation is the initial mass function, as the initial star's mass determines its further evolution (cf. section 2.2.2). The mathematical description for the mass spectrum of newly formed stars in *one star forming event* is given by the initial mass function (IMF). One star forming event here defines the gravitationally driven collective process of ISM gas conversion to stars within a finite volume of about 1 pc and a finite time of about 1 Myr (Kroupa et al. 2013). The outcome of such an event is classified as an embedded star cluster, as the cluster still resides in its host GMC (Lada & Lada 2003). The first empirical description of the IMF was introduced by Salpeter (1955) with a power-law function

$$\mathrm{dN} = \theta(\mathrm{M})\mathrm{dM} \propto \mathrm{M}^{-\alpha} \tag{2.4}$$

where dN is the number of stars in the mass interval M, M + dM with a single slope of $\alpha = 2.35$ in the mass range $0.4 \leq \mathrm{M}/\mathrm{M}_{\odot} \leq 10$. The IMF has three distinct properties that are robust in various environmental conditions. Above $\approx 1\mathrm{M}_{\odot}$ and below the maximum mass of stars around $150\,\mathrm{M}_{\odot}$ (Oey & Clarke 2005), the distribution is described by the originally determined power-law distribution. Below $1\,\mathrm{M}_{\odot}$, the distribution flattens towards a broad plateau with $\alpha = 1$ and an almost flat distribution in the lowest mass, brown dwarf regime (e.g. Kroupa et al. 2013). The functional form of the IMF can be parameterized in several ways. The two widely accepted forms are based on a continuous combination of multiple power-law segments (Kroupa 2001) and the combination of a log-normal distribution with a power law (Chabrier 2003). Both parameterizations return the power-law behavior with

Table 2.1: IMF for the Salpeter (1955); Kroupa (2001); Chabrier (2003) description. The parameters of the Chabrier (2003) IMF are the amplitude a = 0.158, the mean $\mu = 0.079$ and the width $\sigma = 0.69$.

IMF	Mass Range [$\mathrm{M}_{\odot}$]	θ(M)
Salpeter (1955)	$\mathrm{M}_{*} \geq 0.013$	c $\mathrm{M}^{-2.35}$
Kroupa (2001)	$\mathrm{M}_{*} \leq 0.08$	c $\mathrm{M}^{-0.3}$
	$0.08 \geq \mathrm{M}_{*} \geq 0.5$	c $\mathrm{M}^{-1.3}$
	$0.5 \geq \mathrm{M}_{*}$	c $\mathrm{M}^{-2.3}$
Chabrier (2003)	$\mathrm{M}_{*} \leq 1.0$	$\frac{\mathrm{a}}{\mathrm{Mlog}(10)} \exp\left\{-\frac{[\log(\mathrm{M})-\log(\mu)]^2}{2\sigma^2}\right\}$
	$1.0 \geq \mathrm{M}_{*}$	c $\mathrm{M}^{-2.3}$

$\alpha = 2.35$ for large star masses. The various IMFs are listed in table 2.1.

It needs to be stressed here that the IMF is observationally biased at both the high and the low end of the mass distribution. In general, the IMF is inferred from the star counts in clusters under the assumption of temporal invariance of the IMF (e.g Offner et al. 2014; Dib 2014). In the high mass end of the distribution, this can lead to a bias as the star count in a cluster only represents the current day population of stars, while massive stars with a livetime shorter than the host cluster's age have already vanished from the distribution. As a consequence, neither the observational nor the theoretical upper mass limit of a star are precisely known (Massey 2003; Vink et al. 2015). Whether an upper physical limit actually exists or is introduced by observational bias, as the number of stars at the high mass end is limited, is still debated. The theoretical upper limit for the formation of a star is reached when the radiation pressure exerted from the thermal radiation overcomes the gravitational pressure of the core (Kippenhahn et al. 2012). The irradiation would consequently disperse the gas cloud. The theoretical upper limit for star formation at the current age and metallicity of the Galaxy would be $\approx 200\,M_\odot$. However, observational evidence for the existence of such a star is missing and empirical evidence suggests an individual star upper mass limit of $M_{obs} \approx 150\,M_\odot$ (Weidner & Kroupa 2004; Oey & Clarke 2005; Figer 2005). In addition, evidence suggests that the IMF at the high mass end is dependent on the properties of the host cluster, where the individual star upper mass limit scales with the host cluster's mass (Weidner et al. 2010; Kroupa et al. 2013). The majority of massive stars do not form as individual stars but in a binary system with a low mass companion (Zinnecker & Yorke 2007). This introduces an additional bias, as these companion stars cannot be resolved from the high mass companion (Kroupa 2001). Specifically at the low mass end, this introduces a significant bias, as brown dwarf stars are faint objects that are difficult to study (Burrows et al. 2001). However, these systematic effects seem to be reasonably accounted for, as the inferred IMF from observations of stellar groups with various ages are in agreement (Luhman & Potter 2006).

While the IMF appears to be empirically well described, the description of the theoretical processes leading to its functional form are a topic of current research (Bonnell et al. 2007; Krumholz 2014). Stellar feedback from the first born stars affects the subsequent and ongoing star formation in the cluster, influencing the IMF. While these effects are difficult to model theoretically, the general description of the IMF branches of into three distinct regions, resembled by three fundamental processes of star formation. Low mass stars with $M_{ZAMS} \lesssim 0.5\,M_\odot$ form due to the turbulence induced, gravitational *fragmentation* of their host clump (Padoan et al. 2007). The ensuing collapse is governed by an explicit balance between gravitational forces and radiation effects. As the core, out of which these stars are born, is typically more massive than the required Jeans mass for collapse, accretion of matter subsequent to the formation of the protostar is expected to increase the initial mass of the star. However, the presence of a large number of lowest mass, i.e. brown dwarf, stars indicates, that very low mass stars need to be accelerated away from their birth place. This leads to an *ejection* of the star from the dense birth region. This stops accretion of additional matter and the star remains at low mass. On the other end of the IMF, the formation of massive stars is explained by a continuous accretion of gas (Zinnecker 1982). Due to a deeper gravitational potential in the host cluster's central region, higher gas accretion rates on the center's stellar content are facilitated (Bate 2009). This is in line with observations,

indicating that massive stars are primarily located at the center of star clusters (Bonnell et al. 2007).

2.2.1.2 Embedded Cluster Mass Function

The above introduced IMF describes the distribution of stellar masses in an individual star forming event in one cluster. For an entire galaxy, the present day stellar content represents the sum of all individual star formation processes in all clusters in a consistent formation epoch. The distribution function of stellar masses in an entire galaxy is given by the integrated Galactic initial mass function (IGIMF), which is related to the IMF with (Kroupa et al. 2013)

$$\theta_{\mathrm{IGIMF}}(\mathrm{M}) = \int_{\mathrm{M_{EC,min}}}^{\mathrm{M_{EC,max}}} \theta(\mathrm{M} \leq \mathrm{M_{max}}(\mathrm{M_{EC}}))\theta_{\mathrm{EC}}(\mathrm{M_{EC}})\,\mathrm{dM_{EC}} \tag{2.5}$$

where θ is the IMF (see above) for an individual star with mass M and θ_{EC} is the distribution function for initial embedded cluster masses $\mathrm{M_{EC}}$ (ECMF). For a purely stochastic star formation process, the galaxy wide stellar content should be probabilistic and the IGIMF would be identical to the IMF. As described in section 5.3.2, the formation of new stars in a cluster leads to feedback on the remaining cluster, suggesting that star formation is a self-regulatory process. Consequently, the IMF is determined from the boundary conditions of the individual clusters. This in turn allows for a deviation of the IGIMF from the IMF.
The influence of this self regulation of the star formation process can be observationally shown. Indeed it was found that the IGIMF has a different slope than the IMF, varying with the total star forming activity of a galaxy and its metal abundance. In the high mass regime, the IGIMF shows a steeper slope than the IMF with $\alpha_{\mathrm{IGIMF}} = 2.77$ (Weidner & Kroupa 2005). This implies that radiative feedback from a high mass star, if formed, disperses the birth clump and therefore suppresses the formation of higher mass stars. This is in line with observations that strongly indicate a universal upper mass limit of individual stars in the range of $\approx 150\,\mathrm{M_\odot}$ (Weidner & Kroupa 2004; Oey & Clarke 2005; Figer 2005). In general, the upper mass limit of individual stars formed in an individual cluster appears to vary with the total cluster mass $\mathrm{M_{EC}}$, which can be approximated by (Pflamm-Altenburg et al. 2007)

$$\log(\mathrm{M_{ZAMS,max}}) = 2.56\log(\mathrm{M_{EC}}) \left\{3.821^{9.17} + [\log(\mathrm{M_{EC}})]^{9.17}\right\}^{-\frac{1}{9.17}} - 0.38 \quad . \tag{2.6}$$

This gives an independent anchor point for the mass distribution in a specific cluster (cf. section 5.3.2).
The observational determination of the cluster masses is biased, as the clusters are embedded in their parental GMC and therefore highly obscurred by the surrounding gas. Therefore, the ECMF is generally inferred from the IGIMF according to equation 2.5. The derived Milky Way ECMF approximately follows a power-law function

$$\theta_{\mathrm{EC}}(\mathrm{M_{EC}}) = \frac{\mathrm{dN_{EC}}}{\mathrm{dM_{EC}}} \propto \mathrm{M_{EC}^{-\alpha_{EC}}} \tag{2.7}$$

with $\alpha_{\mathrm{EC}} = 2$ (Lada & Lada 2003; Krumholz et al. 2019). The integration limits in equation 2.5 range from the smallest star groups, containing only a minor star forming mass of $\approx 5\mathrm{M_\odot}$ (Pflamm-Altenburg et al. 2007), to the largest possible coherent clumps with a mass of up to $\approx 10^7\,\mathrm{M_\odot}$ (Pflamm-Altenburg et al. 2013; Schulz et al. 2015). The convolution of the large number of lower mass embedded star clusters with the mass dependence of the highest

star mass given in equation 2.6 leads to an overall underproduction of massive stars in the Galaxy with respect to a fully stochastic sampling along the IMF, resulting in the observed steeper IGIMF slope at high stellar masses.

2.2.2 Stars in Hydrostatic Equilibrium

In general, stars are hot spheres of gas that are visible due to the emission of light in form of black-body radiation. The surface temperature of stars commonly produces a black-body spectrum with a peak emission in the visible wavelength bands. To counteract the loss of energy by radiation, the star sustains its internal energy by tapping into two potential energy sources. On the one hand, the stellar matter sinks deeper into the gravitational well of the star, thereby releasing potential energy. According to the virial theorem, half of this energy is converted into internal energy of the star. Secondly, energy is released by fusion processes in the central regions of the star. The prime source of energy is the fusion of hydrogen to helium, which covers the majority of a star's lifetime. However, over the prolonged lifetime and depending on the star's initial mass, additional fusion processes can be ignited, leading to the production of heavier nuclei.

Fundamental Equations of Hydrostatic Stars

During the majority of its stellar evolutionary path, the star is in hydrostatic equilibrium, which means that the gravitational pull of the star's mass is countered by the internal pressure. The hydrostatic equilibrium condition can be expressed as (Unsöld & Baschek 2002, e.g.)

$$\frac{\mathrm{dP}}{\mathrm{dr}} = -\frac{\mathrm{GM(r)}\rho(\mathrm{r})}{\mathrm{r}^2} \tag{2.8}$$

where the mass M(r) is expressed as

$$\frac{\mathrm{dM(r)}}{\mathrm{dr}} = 4\pi \mathrm{r}^2 \rho(\mathrm{r}). \tag{2.9}$$

Here G is the gravitational constant, M is the mass of the star and ρ is the density of the star at the radial position $r \leq R$. The star's radius is given by R. The pressure at position r is given by P. During the majority of the star's lifetime, the pressure is dominantly given by a combination of gas pressure of the ionized atoms and electrons, and the radiation pressure of the photon gas. The gas pressure is $\mathrm{P_{Gas}} \propto \rho \mathrm{T}$, the radiation pressure is $\mathrm{P}_\gamma \propto \mathrm{T}^4$. The highly temperature dependent radiation pressure is subdominant in a regular star, and the star can be approximated with an ideal gas that is dominated by thermal pressure. The three fundamental quantities density, pressure and temperature are linked by the equation of state, which for an ideal gas is given by

$$\mathrm{P_{Gas}} = \frac{\rho\, \mathrm{k_b\, T}}{\mu\, \mathrm{m_u}}. \tag{2.10}$$

In order for the star to maintain hydrostatic equilibrium, its internal energy generation, either from gravitational collapse or nuclear fusion processes, needs to be balanced by an outwardly directed transport of energy. For an energy generation rate ϵ(r) per unit mass and unit time, the energy produced in a spherical shell with radius r and thickness dr per unit

time is given as $W = \rho\,\epsilon 4\pi\,r^2$. The energy flux through the spherical shell L(r) is then given by

$$\frac{dL(r)}{dr} = 4\pi\,r^2\,\rho(r)\,\epsilon(r). \tag{2.11}$$

The energy transport in the star is facilitated by convection and radiation. Spherical integration over the internal radiation field with energy density $u = 4\sigma_{SB}\,T^4/c$ yields the isotropic energy flux density

$$F(r) = -\frac{c}{3\kappa\rho}\frac{d}{dr}\left(4\sigma_{SB}\,T^4/c\right), \tag{2.12}$$

where σ_{SB} is the Stefan-Boltzmann-constant. The total energy radiated through the shell at radius r is given by $L(r) = 4\pi\,r^2\,F(r)$. The temperature gradient inside the star from radiative energy transport follows as

$$\frac{dT(r)}{dr} = -\frac{3\kappa\rho}{16\sigma_{SB}T^3}\frac{L(r)}{4\pi\,r^2}, \tag{2.13}$$

where κ is the opacity of the star that is dependent on the chemical composition of the gas. On the surface of the star, the total radiated energy is identical to the observable luminosity L of the star.
In addition, convection transports energy by large scale fluid motion between stellar regions. A convective region inside a star is defined as a region, where the energy transport by convection dominates the energy transport by radiation. The relationship between the temperature and the pressure are defined by the adiabatic equation which states that $T \propto P^{1-1/\gamma}$, where $\gamma = c_p/c_v$ is the adiabatic coefficient, which is the ratio of specific heats. By logarithmic differentiation of the adiabatic equation, the temperature gradient in a convection zone can be derived as

$$\frac{dT}{dr} = \left(1 - \frac{1}{\gamma}\right)\frac{T}{P}\frac{dP}{dr}. \tag{2.14}$$

The presence of convective zones inside a star can produce a complex structure of the temperature gradient in a star, while the temperature gradient from radiation alone leads to a temperature stratification in the star.

By replacing the derivatives and quantities in equations 2.8 and 2.9 with quotients and average values, respectively, a simple form for the central temperature T_c and surface luminosity L of a star can be derived (e.g. Janka 2012):

$$T_c \propto \frac{M}{R} \quad , \qquad L \propto M^{3.5} \tag{2.15}$$

Stars possess a finite lifetime that is mainly determined by the period of time they spend on the main sequence during central hydrogen burning. As the luminosity of the star, which is equal to the radiated energy, needs to be balanced by the production of energy in the star, the evolution timescale of the star can roughly be approximated by the time it requires to exhaust the fuel supply with $t_e \propto M/L$. With the mass-luminosity-relation of equation 2.15, the evolution timescale reduces to $t_e \propto M^{-2.5}$. Therefore, the more massive the star is the faster it burns its fuel supply, which significantly reduces the lifetime of massive stars with respect to their lower mass counterparts.

Central Nuclear Fusion

The energy production rate in a star is governed by the energy release per fusion reaction and the specific reaction rates. The energy release per fusion reaction ΔE is derived from the fundamental energy-mass-equivalency $\Delta E = \Delta mc^2$, where Δm is the difference between the initial mass of nucleons involved in the reaction and their final product. For the primary fusion reaction in the star, the conversion of 4 hydrogen atoms into one helium-4 atom, the Q-value is given by

$$Q = \Delta E = (m_{^4He} - 4m_{^1H})c^2 = 26.73\,\mathrm{MeV}, \tag{2.16}$$

where $m_{^4He}$ and $m_{^1H}$ are the atomic masses of helium-4 and hydrogen-1 respectively (Iliadis 2015). The release of energy is due to the fact that nucleons in helium are more tightly bound than in hydrogen. The released binding energy is divided into γ-rays and kinetic energy of the product nucleus and neutrinos. As the neutrinos can readily escape the star due to their small interaction cross section with the stellar material, on average only 26.23 MeV remain in the star to sustain its internal energy.

The reaction rate per unit volume is dependent on the particle densities n_a and n_b of the reactants, the relative velocity v of the reactants and the energy dependent specific cross section $\sigma(E)$ with (Unsöld & Baschek 2002)

$$\mathcal{P} = n_a\, n_b\, \langle \sigma\, v \rangle. \tag{2.17}$$

The probability distribution for finding a particle at velocity v in in a hot plasma with temperature T is described in energy space by the Maxwell-Boltzmann distribution. The connection between the kinetic energy and the velocity is given as $E_{kin} = m_{red}v^2/2$, where m_{red} is the reduced mass of the interacting particles. The velocity averaged reaction rate $\langle \sigma v \rangle$ is obtained by integrating the product of the cross section and the velocity over energy

$$\langle \sigma\, v \rangle = \sqrt{\frac{8}{\pi\, m_{red}\, (k_b T)^3}} \int_0^\infty E\sigma(E) \exp\left(-E/(k_b T)\right) dE \tag{2.18}$$

As the strong nuclear force is dominant on short ranges of 10^{-15}m, high velocities are required for the interacting particles to overcome the repulsive potential of positively charged nuclei. The E^{-1} dependence of the interaction cross section is removed by approximating the product $E\sigma(E)$ with the astrophysical, energy dependent S-factor (e.g. Iliadis 2015)

$$E\sigma(E) = \exp(-2\pi\eta) S(E), \tag{2.19}$$

where $\exp(-2\pi\eta)$ is the Gamov factor, which gives the probability of tunneling through the Coulomb barrier. It is approximated by

$$P(E) = \exp(-2\pi\eta) = \exp\left(-2\pi \sqrt{\frac{m_{red}}{2\hbar E}} Z_a Z_b e^2\right) \tag{2.20}$$

where $Z_{a,b}$ are the charge numbers of the reactants and e is the charge of an electron. In contrast to the cross section, the S-factor is only weakly dependent on the energy and can further be approximated with $S(E) = S_0$ (Angulo et al. 1999). With this defintion, equation 2.18 simplifies to

$$\langle \sigma\, v \rangle = \sqrt{\frac{8}{\pi\, m_{red}\, (k_b T)^{3/2}}} \int_0^\infty \exp\left(-2\pi \sqrt{\frac{m_{red}}{2\hbar E}} Z_a Z_b e^2\right) \exp\left(-E/(k_b T)\right) dE, \tag{2.21}$$

which is called the Gamov window. The Gamov peak E_p, which is the maximum of the probability function in the integral of equation 2.21, is determined from the derivative of the integrand with respect to energy to be

$$E_p = \left(\frac{\pi Z_a Z_b e^2 k_B T}{\hbar}\right)^{2/3} \left(\frac{m_{red}}{2}\right)^{1/3} . \tag{2.22}$$

Subsequent nuclear burning phases, after the initial hydrogen burning, involve nuclei with charge numbers higher than unity. For these, the Gamov peak shifts towards higher energy and the amplitude of the Gamov window decreases. Note here, that E_p is considerably higher than the average particle kinetic energy in the Boltzmann distribution. Therefore, the majority of fusion reactions occur with particles from the high energy tail of the Boltzmann distribution. For a constant temperature, the integral in equation 2.21 reduces with increasing charge number. This is the reason, why in low mass stars with a specific central temperature hydrogen fusion efficiently produces energy, while all subsequent burning stages are highly improbable. In general, this allows the definition of an *ignition temperature*, above which energy generation by the subsequent burning stages becomes efficient. These are listed in table A.1. The final hydrostatic burning state is silicon burning, during which subsequent captures of α particles on seed silicon nuclei produces ^{56}Ni. As iron group elements have the highest possible binding energy per nucleon, subsequent fusion processes do not release but consume energy. Hydrostatic nuclear burning is consequently finished after silicon burning.

As shown above, subsequent nuclear burning stages are highly temperature dependent. This leads to a stratification of the chemical composition inside the star. Due to the temperature gradient in the star (cf. equations 2.13 and 2.14), the efficiency of subsequent burning stages increases inversely with the radial coordinate. The stratification is fostered by sedimentation, i.e. heavier nuclei sink deeper into the gravitational potential and accumulate in the center. For a massive star, the stellar structure before collapse is resembled by an onion shell like structure (cf. Figure 2.2), with layers of nuclear fuel stacked ontop of the burning ashes. From the outside to the inside, the star consists of layers of ^{1}H, ^{4}He (containing ^{12}C, ^{16}O, and ^{22}Ne), ^{16}O layers (containing ^{12}C, ^{20}Ne, ^{24}Mg, ^{28}Si, and ^{32}S), a Si-S-Ar layer and a central iron core, containing iron group elements (IGE), such as ^{56}Ni. To first order, the onion shell structure represents a good description of the evolved massive star. However, Woosley et al. (2002) point out, that rotation of the star and convective motion of the burning products will lead to mixing of the ashes into the surface layers.

2.2.3 Late Time Evolution of Stars

The final fate of a star is governed by the mass of the He-core after H-burning. Neglecting mass loss due to winds and other subdominant processes, the mass of the He-core is directly linked to the zero-age main sequence (ZAMS) mass of the star. The ignition of the successive burning stages can only start, when a certain central temperature is reached. Due to the contraction of the stellar core, the density in the central region increases. In addition to the gas and photon pressure, the Fermi pressure, exhibited by degenerate fermions, increases with increasing central density. According to the Pauli exclusion principle, only one fermion can occupy the same quantum mechanical state in a confined space at the same time. Thus only one fermion occupies the same phase space element at a time. With increasing density,

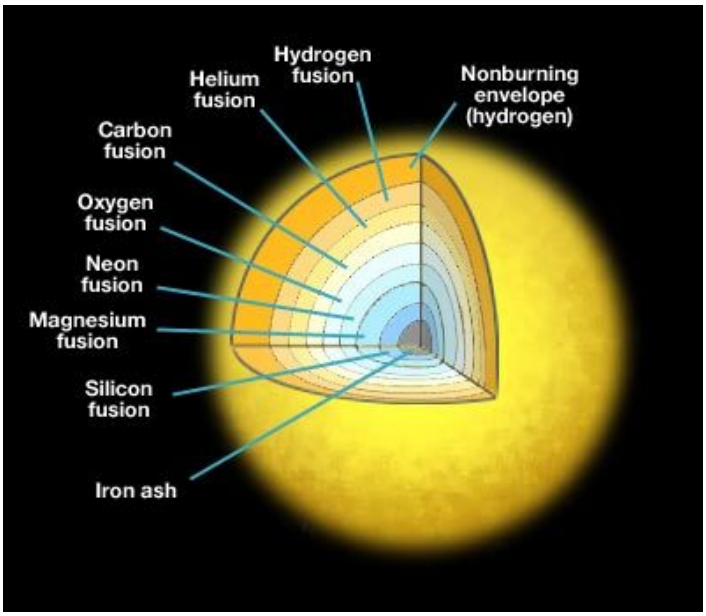

Figure 2.2: Artistic illustration of the onion shell structure of an evolved, massive star with $M_{ZAMS} = 25M_{\odot}$ prior to the collapse of the iron core. Heavier nuclei are concentrated closer to the center of the star. While no more fusion occurs in the central iron core, fusion processes in the stratified shells above continue, increasing the mass of the iron core up to its stability limit. Layers are not to scale and the simplified scheme neglects mixing of the layers due to convective motion.

fermions become trapped in a decreasing volume. Therefore, the states that are occupied by the fermions in phase space need to have an increasing momentum. As the Fermi momentum is inversely linked to the rest mass of the fermion gas particles, the first fermions to reach a degenerate state are electrons. In a degenerate gas, the pressure exerted by the electrons with highest momenta is dominant over the gas and radiation pressure. However, the degeneracy pressure is independent of the central temperature and is only proportional to the density $\rho^{5/3}$. Therefore, when degeneracy pressure becomes dominant, the contraction of the star is stopped without further increase in central temperature.

As long as nondegenerate particles are the dominate source of pressure in a star, hydrostatic equilibrium conditions demand that the central density ρ_c and central temperature T_c approximately follow the proportionality (Janka 2012)

$$\frac{{T_c}^3}{\rho_c} \propto M^2. \tag{2.23}$$

It is evident, that for a specific central density, a more massive star will always have a higher temperature. The upper part of the Figure 2.3 depicts the track in the ρ-T space for a 15 and a $25\,M_{\odot}$ star. Both stars can reach the required temperature for the ignition of all central burning phases. The track in the ρ-T plane follows the general trend of equation 2.23, where the central temperature is dependent on the density with a power-law index of $1/3$. A sudden increase in temperature occurs when each subsequent burning stage is ignited.

The lower part of the Figure 2.3 shows the exemplified stellar tracks in the ρ-T plane for stars with different masses:

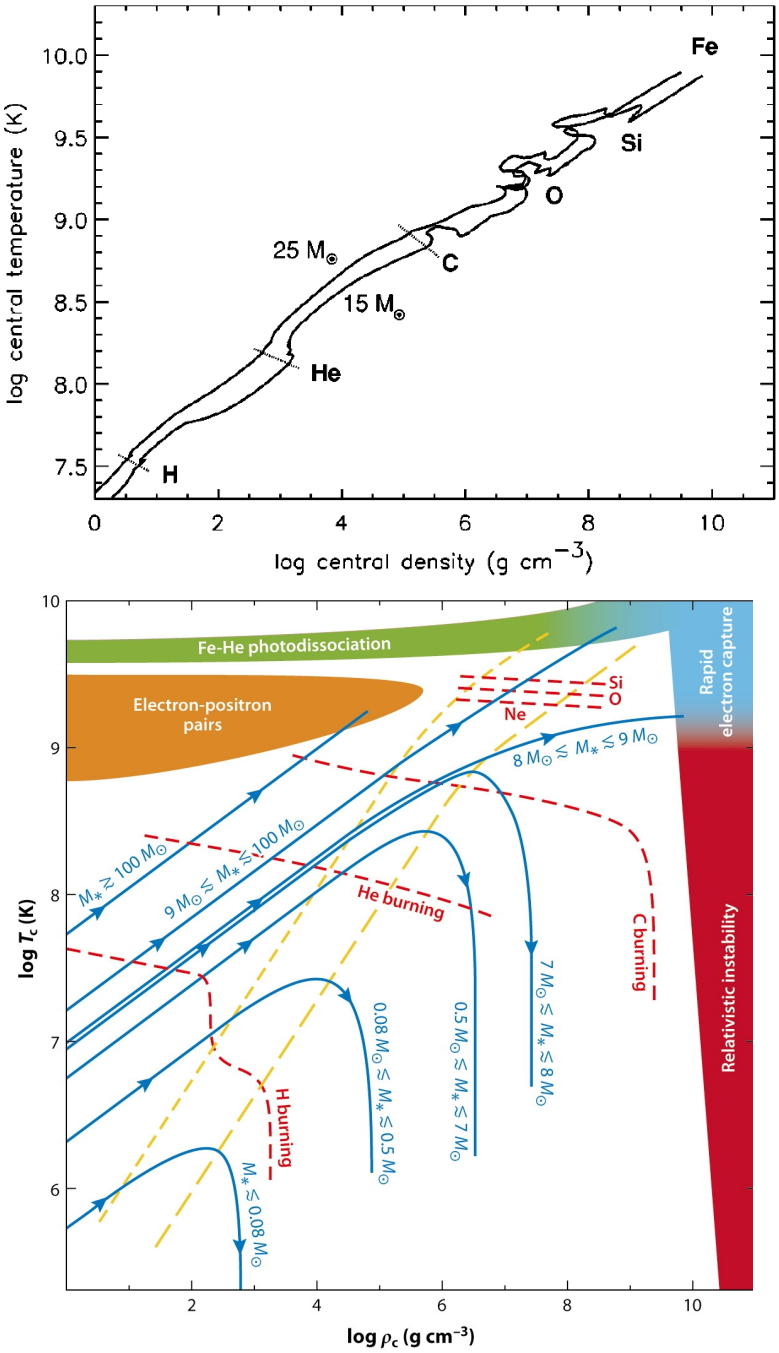

Figure 2.3: Evolutionary track in the ρ-T plane for the central regions of stars with varying masses. Upper panel: Evolutionary track of a 15 and a 25 $M_\odot$ star from Woosley et al. (2002). The evolution follows the proportionality law of $T \propto \rho^{1/3}$. Deviations from this law are found when the central temperature reaches the level for the ignition of burning stages, marked by the respective, burning isotopes. Lower panel: Exemplified evolutionary track for stars with different birth masses. As the central temperatures and densities of low mass stars are insufficient to start specific nuclear fusion processes, their stellar evolutionary tracks turn when the central nuclear fuel is exhausted. Massive stars with $M_{ZAMS} \gtrsim 8\,M_\odot$ undergo the majority of burning stages and end up on the upper part of the ρ-T plane. There, the stars reach electron degeneracy at temperatures that are sufficient to lead to a core-collapse SN explosion. The yellow dashed line mark the onset of degeneracy (left) and the state of fully electron degenerate matter (right).

Stars with an initial mass of less than $0.08\,M_\odot$ reach electron degeneracy before they reach central temperatures required for H-burning. However, a subdominant process occurs that fuses protons with primordial deuterium, that is present in the star from primordial nucleosynthesis and earlier generations of stars, to ^{3}He. This process is available starting from a mass of $\approx 0.013\,M_\odot$, equal to $\approx$13 Jupiter masses (Spiegel et al. 2011). These stellar bodies are very dim and classified as brown dwarf stars.
Stars with a mass of more than $0.08\,M_\odot$ and less than $7 - 8\,M_\odot$ reach temperatures for central hydrogen burning (Iben & Renzini 1983). However, central temperatures are sufficiently high to start helium burning only above $\approx 0.5\ M_\odot$. Temperatures for subsequent C und O burning cannot be reached. The compact cores eject their shells into a planetary nebular. What remains is a white dwarf star (see section 2.2.4), that is either composite of C+O or He, depending on the stars initial mass. White dwarfs are usually created with $\approx 0.6\,M_\odot$ (Kepler et al. 2007), however masses up to $1.25\,M_\odot$ are possible. When no binary star is present in the system from which mass transfer is possible (see section 2.4) the white dwarf star cools by the emission of light.
In the mass range between 7 and $9\,M_\odot$, central temperature is sufficient to also ignite carbon burning, however not high enough to fully go through all burning stages (Icko Iben et al. 1997; Ritossa et al. 1999; Miyaji & Nomoto 1987). In stars with $7 - 8\,M_\odot$, the remaining object is stabilized against gravity by electron degeneracy pressure to form an ONeMg white dwarf star. Between $8 - 9\,M_\odot$, the Fermi energy of the degenerate electrons is high enough that interactions with nuclei become possible. The resulting loss in pressure leads to a collapse of the core, marked as the blue zone in the upper right corner of Figure 2.3.

Stars in the mass range of $\approx 9 - 100\,M_\odot$ achieve all burning stages (Woosley et al. 2002; Smartt 2009). When no more fuel is present in the central region, the massive iron core still increases its mass from silicon burning in a shell around the core. Photons in the high temperature center have sufficient energy to disintegrate the iron group nuclei. The loss of photon energy leads to a reduction in gas pressure in the core, as the star is not yet fully degenerate at this point. Consequently the core cannot be stabilized against gravity anymore and collapses.

For the rare case of stars that are born with an initial mass of more than $100\,M_\odot$, electron degeneracy is never reached before the stellar death. At high central temperature, photons can be effectively converted into electron-positron pairs after carbon burning. Thereby, the star loses photon gas pressure and collapses. The result is either the formation of a black hole, or a potential pair-instability SN (Kasen et al. 2011), as the collapse leads to explosive oxygen burning.

2.2.4 Stellar Remnants

White Dwarf Stars

White dwarf stars (WD) are the remnants of less massive stars with a ZAMS mass of less than $8\,M_\odot$, that have lost their less dense envelopes. WDs are characterized by their high surface temperature, that produces black body radiation through which the star appears white. However, due to their small surface area, WDs are only dim celestial objects.
In a WD the pressure upholding the star against collapse is given by a degenerate Fermi

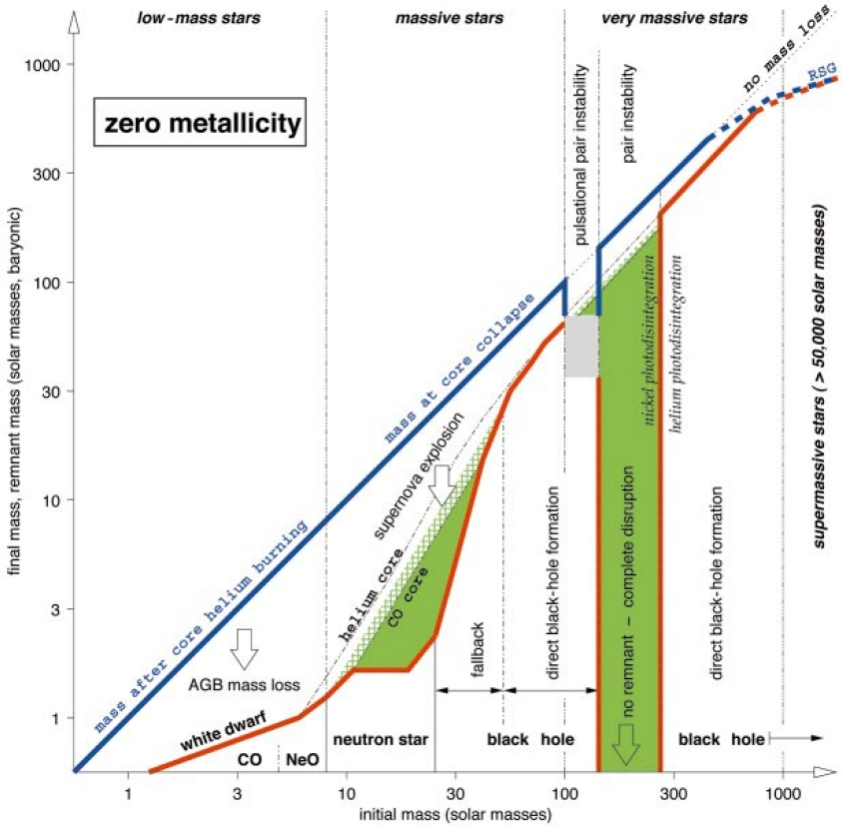

Figure 2.4: Remnants of stars with varying initial masses. The x-coordinate shows the initial mass of the star, the y-axis is in solar masses and shows the remnant mass and the mass of the star at the onset of the final evolutionary stages. The red line marks the mass of the compact remnant object, the blue line is the mass of the star at the end of its evolution. Green shaded areas show the mass regions of stars in which heavy elements are produced. From Woosley et al. (2002).

gas, with a polytropic relation $P = k\rho^{\lambda}$ between pressure (P) and density (ρ). The relation between degeneracy pressure and density changes from $\lambda = 5/3$ for non relativistic electrons to $\lambda = 4/3$ for relativistic electrons. Inserting the polytropic equation of state in the hydrostatic equilibrium condition (cf. equation 2.8), a uniform mass limit for an object stabilized by degenerate electron pressure can be derived. This Chandrasekhar mass limit (Chandrasekhar 1935) describes the maximum mass of a non-rotating stellar object, given by

$$M_{Ch} = 5.83 M_{\odot} Y_e^2, \tag{2.24}$$

where Y_e is the electron fraction of the degenerate material. In a carbon oxygen white dwarf (CO WD) or a helium white dwarf (He WD), mainly consisting of ^{16}O, ^{12}C, and ^{4}He, respectively, the electron fraction is $Y_e \approx 0.5$, which suggests a Chandrasekhar mass limit of $1.457\,M_{\odot}$. This limited mass range sets the boundary condition for type Ia SNe. The energy scale of the explosion ($\approx 10^{51}$ erg) is associated with the released amount of nuclear binding energy from the conversion of $\approx 1\,M_{\odot}$ of carbon and oxygen to elements between silicon and iron, minus the gravitational binding energy of the WD (few times $\approx 10^{50}$ erg), leading to rather uniform explosions (cf. section 2.4.3).

Similar to a WD, the core of an evolved star can be described with the same equation, where

$Y_e = 26/56 = 0.46$ for an evolved iron core, mainly consisting of ^{56}Fe.

Neutron Stars

For stars with a ZAMS mass of more than $8\,M_\odot$ the remnant object can either be a neutron star or a black hole. In the mass range between 8 and $\approx 25\,M_\odot$, the central region of the progenitor star collapses to a neutron star and an ensuing outward propagating shock wave can disrupt the outer stellar envelope (see Figure 2.4). For higher masses, the central region collapses to a black hole, and the SN explosion fails as the shock wave is not energetic enough (Hix et al. 2014). Neutron stars are stabilized against gravity by degeneracy pressure. During the collapse, inverse β-decays lead to the neutronization of the object. The neutron star consists of $\approx 90\%$ neutrons, and the degeneracy pressure is exerted from the neutrons in contrast to electrons in a WD. As the Fermi momentum is inversely proportional to the rest mass of the interacting particle, the density required to achieve degeneracy for neutrons is higher. In a neutron star, the remaining $1 - 2\,M_\odot$ of matter are compressed into a sphere with ≈ 10 km radius. Solving the hydrostatic equilibirum equation requires a fully relativistic treatment of the interacting particles and precise knowledge of the poorly constrained equation of state (EoS) of hadronic matter at extreme densities. Theoretical limits for the neutron star mass are in the range of $1.5 - 3.2\,M_\odot$ (Bombaci 1996). The observed upper mass limit for a neutron star is $2.3\,M_\odot$ from gravitational waves analysis (Shibata et al. 2019) and $2.14^{+0.10}_{-0.09}$ from a binary system (Cromartie et al. 2019) observation. Due to the limited accessibility of the supranuclear density regime in Earth bound experiments, the existing EoS descriptions are limited to cold high density matter (Lattimer & Swesty 1991; Shen et al. 1998), which are not necessarily an appropriate description of the ccSN environment. However, differences in the adopted EoS are reflected in differences as to how the proto-NS reacts to prolonged mass accretion after initial core bounce (cf. section 2.3.1). The stiffness of the adopted NS EoS results in a varying radius for equal masses, which sensitively influences the neutrino heating mechanism (cf. section 2.3.2) and thus the success of ccSN simulations (Janka et al. 2005; Hempel et al. 2012).

2.3 Core Collapse Supernovae

2.3.1 Core Collapse and the Stalled Shock Front

Massive stars with initial masses of more than $8\,M_\odot$ end their lives with the gravitational collapse of their stellar cores. When the nuclear fuel in the center is exhausted, the release of nuclear binding energy by nuclear fusion can no longer stabilize the core against its own gravitational pull. At this point, the stellar cores are either stabilized against gravity by radiation pressure, or the degeneracy pressure of a degenerate electron gas. Progressing upwards in the ρ-T plane (Figure 2.4, upper right and left corner) a phase transition occurs, that leads to a loss of stabilizing pressure. The compressability of the star escalates and the central core collapses within its free-fall time, forming a central object with a radius of a few hundred km.

In the most massive stars above $100\,M_\odot$, central temperatures above several 10^9 K are reached already after the carbon burning stage. At these temperatures, the photons in thermal equilibrium reach energies above twice the rest mass energy of an electron, which allows the

creation of electron positron pairs by

$$\gamma + \gamma \rightarrow e^- + e^+, \tag{2.25}$$

decreasing the stabilizing radiation pressure. This potentially leads to a pair-instability SN (Heger & Woosley 2002; Kasen et al. 2011). Explosive burning at high temperatures and densities of the still available nuclear fuel leads to a full disruption of the star with explosion energies of $\approx 10^{53}$ erg, producing more than $50\,M_\odot$ of ^{56}Ni.

In the mass range of 8 – $10\,M_\odot$ (Miyaji & Nomoto 1987), the massive ONeMg cores of the stars are stabilized against collapse by the degeneracy pressure of electrons. As off-center fusion processes increase the mass of the core, the star contracts and the central density increases. The Fermi momentum and thereby Fermi energy of electrons increases and inverse β-decays

$$(A, Z) + e^- \rightarrow (A, Z-1) + \nu_e \tag{2.26}$$

on ambient nuclei become possible. The dominant reactions are ^{24}Mg(e$^-$, ν_e)^{24}Na(e$^-$, ν_e)^{24}Ne starting at densities above $2.1{\times}10^9$ g cm^{-3} and ^{20}Ne(e$^-$, ν_e)^{20}F(e$^-$, ν_e)^{20}O above $8.9{\times}10^9$ g cm^{-3} (Miyaji & Nomoto 1987). The neutrino can readily escape the central region, reducing its internal energy. Due to the neutronization by the inverse β-decays, the electron fraction Y_e of the core decreases. Therefore, the maximum allowed mass of the core, which depends on Y_e^2 (cf. equation 2.24), decreases to $0.8\,M_\odot$. The core collapses, leading to an electron-capture SN (ECSN).

In stars above 10 and below $100\,M_\odot$ the electrons do not reach full degeneracy and the star is partially stabilized by radiation pressure. Above 5×10^9 K, thermal γ-rays have sufficient energy to photo-dissociate the iron group nuclei. The dominant reactions are

$$\gamma + {}^{56}\mathrm{Fe} \rightarrow 13\,{}^4\mathrm{He} + 4\mathrm{n} \qquad \text{followed by} \tag{2.27}$$

$$\gamma + {}^4\mathrm{He} \rightarrow 2\mathrm{p} + 2\mathrm{n} \tag{2.28}$$

causing a reduction of radiation pressure. The subsequent inverse β-decay on the protons further reduces Y_e and the pressure as the neutrino carries energy from the core. The star loses stabilizing pressure and collapses.

Whether the core of the star is composed of a massive ONeMg WD or an iron core, the collapse of the material in the center occurs adiabatically and homogeneously. When the density in the central region exceeds $\rho > 10^{12}$ g cm^{-3}, neutrinos become trapped in the central region as their free-fall time becomes smaller than their diffusion time in the dense material. The collapse of the core continues until a density of 2.7×10^{14} g cm^{-3} is reached, above which the strong nuclear interaction becomes repulsive. The sudden decrease of the core's compressibility halts the collapse, and the core *bounes* back, sending an outward propagating shock wave into the supersonically infalling surrounding medium. For the inner core, which has shrunk to a mass of $0.5\,M_\odot$ and an electron fraction of $Y_e = 0.25 - 0.27$ (Janka et al. 2012), a new stable configuration due to the repulsive force of the strong interaction is allowed in the form of a proto neutron star (PNS).

While it was believed, that this shock wave could promptly eject the surrounding layers, simulations suggest that the prompt mechanism fails to explode the star (van Riper 1978;

Mazurek 1982; Burrows & Lattimer 1985). The outward moving shock wave increases the heat and entropy in the shock region, where the shock starts to lose energy mainly by photo dissociation of heavy nuclei to nucleons, consuming $\approx 8.8\,\mathrm{MeV}$ per nucleon. Electron captures on the protons lead to the production of neutrinos, which escape the central region when the shock radius increases past the neutrino sphere[1]. A large amount of energy is promptly released in a highly energetic neutrino burst. Due to the energy losses, the shock front stalls 100 – 200 km above the newly formed PNS and transforms into a standing accretion shock (Janka 2017).

2.3.2 Reviving the Stalled Shock

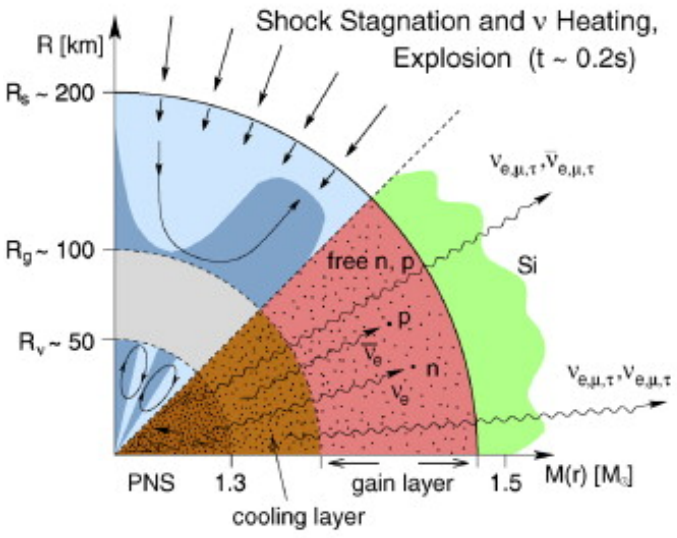

Figure 2.5: Neutrino heating of the stalled shock layer as schematic drawing. The stalled shock has already advanced to a radius of ≈200 km. Neutrinos emitted in the cooling layer (light brown) above the PNS can escape the central region and transport energy to the above layers. As the density in the gain layer is still high enough, that neutrino interactions are likely, energy from the neutrinos is deposited by scattering interaction and mainly by absorption of $\nu_e, \bar{\nu}_e$ on free protons and neutrons. Dark brown represents nuclear matter, where the density is commonly above nuclei density. Adopted from Janka et al. (2007)

In order to revive the stalled shock, sufficient energy needs to be deposited into the region between the PNS and the stalled shock front. Bethe & Wilson (1985) proposed the idea, that interactions of neutrinos with the high density matter transfers enough energy to create an explosion, by tapping into the large energy reservoir of the PNS. The collapse of the stellar core from a radius of $\approx 1000\,\mathrm{km}$ to several 10 km releases $\approx 10^{53}$ erg of gravitational binding energy, roughly 100 times the explosion energy of a ccSN, that is transformed into internal energy of the PNS. The PNS cools by the emission of neutrinos, that diffuse into the stalled

[1]The neutrino sphere, likewise to the photo sphere, of a star is the radius, from which 50% of all emitted neutrinos or photons, respectively, escape the star, while the rest interact due to some scattering process

shock. There, they deposit energy by charged current interactions

$$p + \bar{\nu_e} \rightarrow n + e^+ \tag{2.29}$$

$$n + \nu_e \rightarrow e^- + p, \tag{2.30}$$

accounting for 90% of the energy transfer (Janka 2017). The net energy change at radius r above the PNS is given by the sum of the neutrino heating gains and the energy losses of the neutrino re-emission. As the neutrino emission and the neutrino absorption are dependent on the radius with r^{-6} and r^{-2} (Janka 2012; Burrows 2013), respectively, a *gain radius* (Bethe & Wilson 1985) can be defined at which both terms cancel each other out. Above the gain radius material is efficiently heated by neutrino interactions, where the escaping neutrinos deposit their energy with an efficiency of 5 – 10 % into the stellar medium. Whether the stalled shock can be revived and transformed into an outward moving explosion sensitively depends on whether sufficient matter can be heated behind the shock, while matter that is still infalling from the outer layers is accreted through the shock front.

Despite extensive work and a state of the art treatment of neutrino physics, explosions in one dimensional simulations induced from the neutrino heating mechanism were only found for low mass progenitors with an ONeMg core. These resulted in explosions with a low kinetic energy and only a minor production of radioactive ^{56}Ni (Kitaura et al. 2006; Wanajo et al. 2010). For more massive progenitor stars with a central iron core, non-radial motion induced by various hydrodynamic effects that cannot be followed in one dimensional simulations apparently play a crucial role for a successful explosion. Indeed simulations have indicated that the heating of matter in the gain region produces a negative entropy gradient, where high entropy material is deeper in the PNS gravitational potential than the overlying, dense matter. This highly unstable configuration, as a consequence, leads to convective motion. Due to Rayleigh-Taylor instabilities, buoyant plumes rise up in radial coordinate, while cold, dense matter is funneled down to the PNS in the interjacent streams. This downward stream increases the fraction of matter that is heated close to the PNS, and thereby reinforces the explosion. On the other end, the heated matter rises in radial coordinate, where energy losses from neutrino emission are lower and the matter retains more energy. This in total increases the amount of energy stored in the post shock layer, which leads to an increase in temperature and pressure pushing the shock radius further out. Several studies indicate, that this violent motion can lead to the explosion of stars with ONeMg cores and very low mass iron cores near the low mass end of the ccSN scenario in stars with a ZAMS of 8-10 $M_\odot$ (Wanajo et al. 2010; Melson et al. 2015). However, properly treating all complex physics, including neutrino interactions, nuclear physics, general relativity and multidimensional hydrodynamics to also explode more massive stars still provides the theoretical ccSN simulation community with difficulties. While the consensus is that the neutrino heating mechanism leads in the right direction to explain ccSNe over a wide range of initial stellar masses, additional mechanisms to provide energy to the infalling matter appear necessary for successful explosions. Over the years, several phenomena have been observed in simulations that could enhance the shock radius. For example, small perturbations in the standing accretion shock lead to an instability of the shock front (SASI, e.g. Blondin et al. 2003; Ohnishi et al. 2008; Fernández 2010; Summa et al. 2016), where initial minor perturbations can grow significantly in size in an oscillatory way. In the SASI, the modes with the lowest-order spherical harmonics (i.e. dipolar motion) experience the highest growth rates. This leads to a sloshing motion of the shock radius between the hemispheres above the PNS

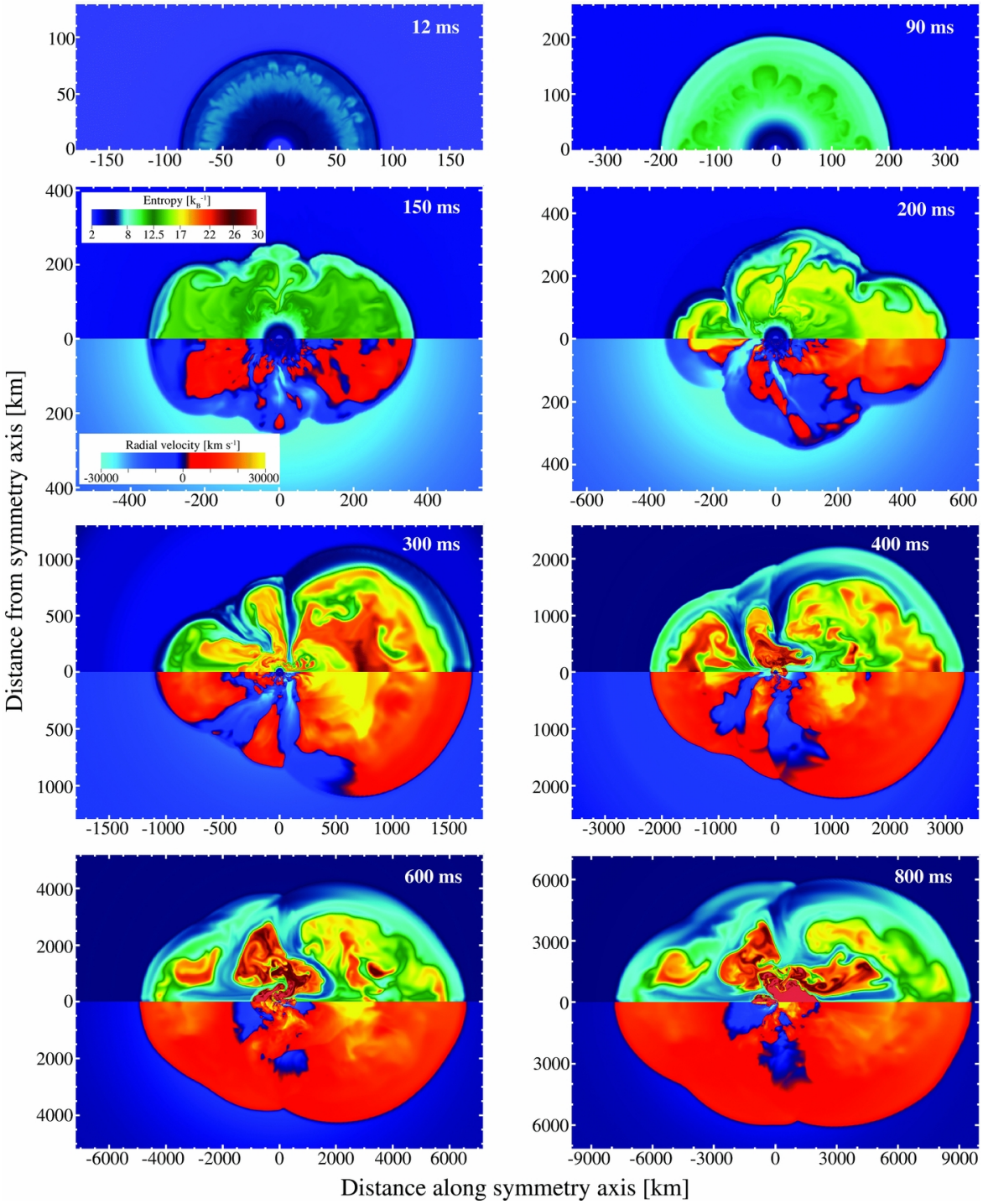

Figure 2.6: Evolution of the shock front in a 2D simulation of a 12 $M_\odot$ star adopted from Bruenn et al. (2013). The figure shows the dynamic evolution as snapshots at t = 12, 90, 150, 200, 300, 400, 600, 800 ms after core bounce. Upper part of each snapshot shows the entropy of the material, lower part the radial velocity. Color coding is identical for all snapshots, while the radial grid is increased to capture the entire shock surface. The rise of buoyancy driven convective bubbles begins at 90 ms, pushing the shock front outwards. The onset of the SASI causes distortions in the shock radius, best seen in the enlargement of the shock radius in the polar plane at 150 ms, while the equatorial regions contract, leading to an increase in the advection to heating timescale in the polar region and a decrease in the equatorial region, where low entropy matter is funneled downwards.

(cf. Figure 2.6). While in the one hemisphere the shock's surface is at a narrow radius, the shock radius is potentially lifted sufficiently in the other hemisphere, leading to highly asymmetric explosions. Although there is a large spread in treatment of the relevant physics in various simulation groups, lifting the constraints of spherical symmetry and allowing for violent motion in the gain region that lead to asymmetric explosions appears to be a required ingredient in successfully producing explosions, and to bring simulations in line with observations such as natal NS kicks and asymmetries in the ejecta distribibution (for recent works cf. e.g. Bruenn et al. 2013; Melson et al. 2015; Summa et al. 2016; Skinner et al. 2016; Roberts et al. 2016; Burrows et al. 2019).

While the viability of the neutrino driven mechanism appears to be well established due to the detection of a neutrino outburst in the Large Magellanic Cloud, preceding the explosion of SN 1987A (Hirata et al. 1987; Burrows & Lattimer 1987), recent microphysical adjustments to the simulations lead to explosion in a limited number of simulations. However, the viability of these input physics and their interplay needs to be tested. Observations, that can specifically target the processes occurring deep in the interior of the SNe, are required to disentangle this large parameter space. Specifically, the observation of nucleosynthesis products that originate from nuclear burning in the central region of the SN are of great importance, as the nuclear reaction rates are highly sensitive to the thermodynamic conditions.

2.3.3 Explosive Nucleosynthesis in Core Collapse Supernovae

Nucleosynthesis in ccSNe occurs under explosive conditions in a high density, high temperature regime, where large particle fluxes are available for reactions on short timescales (Woosley et al. 1973). The expanding shock of the early SN explosion encounters the infalling stellar layers, shock heating them in the process. Especially the silicon and oxygen layers of the star are consumed during explosive burning.

In such extreme conditions with peak temperatures above 5×10^9 K photons have sufficient energy to photodisintegrate nuclei into their nucleons and α-particles. However, competing reactions in form of fusion processes reassemble the constituents into heavier nuclei. In such environments an equilibrium between the forward strong assembly reactions and the electromagnetic backward disintegration reactions is reached, that preserves the number of protons and neutrons. The mass fraction of isotopes in the ejecta is dominated by the reactions of (p,γ), (α,γ) and (α, p). The mass fractions of isotopes directly follows from the Saha equation which means that the elemental composition of matter is dependent only on the temperature, density and the electron fraction (T, ρ, Y_e) (Clifford & Tayler 1965; Hartmann et al. 1985) and the reaction rates of the specific nuclear statistical equilibrium (NSE) trajectories (Hermansen et al. 2020).

The most important quantity for the prediction of the nucleosynthesis outcome is temperature, given a specific set of density and electron fraction. In the radiation dominated phase behind the shock (Weaver & Woosley 1980) the outcome of nucleosynthesis can be predicted by knowing the peak temperature T_{peak} of a specific mass element alone. The trajectories of the particles in ρ-T-space can be followed for an expansion and cooling of the material that follows a constant T^3/ρ evolution, until the temperatures have decreased sufficiently that

nuclear reactions cease (freeze-out; Magkotsios et al. 2010).

For mass elements, that start their nucleosynthesis in the high density regime $\rho \geq 10^8\,\mathrm{g\,cm^{-3}}$ with temperatures above 5×10^9 K, the forward α reactions are strong during the entire nucleosynthesis and the isotopic distribution is strongly forward peaked to mainly produce iron group elements (IGE), containing a significant amount of ^{56}Ni. As this leads to a small number of available α particles, they cannot readily combine to ^{12}C nuclei, as the reverse reaction of photo-disintegration is dominant. Therefore, isotopes with lower mass number between A = 12 and A = 44 along the track of α-captures become depleted in this regime with respect to the IGE elements. The isotopic composition after reactions start to freeze out is given by the composition during NSE. These conditions are typically not realized in ccSNe but more relevant for central fusion processes in type Ia explosions. After sufficient cooling mass elements in this regime encounter a normal freeze-out (Woosley et al. 1973; Meyer 1994).

The majority of nucleosynthesis in ccSNe occurs characteristically under *α-rich freeze out* (Woosley et al. 1973) conditions. At high temperature and lower densities ranging between $\approx 10^4\,\mathrm{g\,cm^{-3}} \leq \rho \lesssim 10^7\,\mathrm{g\,cm^{-3}}$, the captures of α particles are less efficient. Initially the triple-α process is disconnected from equilibrium as the inverse destruction by γ-rays dominates, which leads to a large abundance of α-particles. Due to this large excess of α's the triple-α process starts to dominant its inverse at cooler temperature. Local equilibrium is broken due to the increased amount of ^{12}C and its subsequent α neighbor ^{16}O. This equilibrium breaking further moves upward in mass number including an increase in the mass fraction of intermediate mass elements (IME) from silicon to titanium with respect to normal freeze-out conditions (Magkotsios et al. 2010; Thielemann et al. 2018).

Some additional nucleosynthesis occurs at less extreme values of density and temperature, when the expanding explosion front shock heats the subsequent layers of the stars. As the timescales for expansion of the matter and nuclear burning are comparable in this regime, local NSE cannot be achieved and nuclear burning progresses in QSE clusters with a limited number of isotopes per cluster. While the final composition of isotopes can be dependent on the initial composition, the fraction of ^{28}Si increases with decreasing density (Thielemann et al. 2018).
The shock front traverses the silicon and carbon-oxygen layer in ≈ 4 s, (Limongi & Chieffi 2003), after which the temperature drops below 10^9 K and nucleosynthesis is largely finished. As nucleosynthesis occurs in various density and temperature regimes, in addition to IGEs, also IMEs can be found in the composition of the ejected matter. In spherically symmetric models (Woosley & Weaver 1995; Thielemann et al. 1996; Limongi & Chieffi 2003), nucleosynthesis mainly occurs in the α-rich freeze out regime, containing a major fraction of ^{56}Ni and unburnt α-particles and IME. Mass fractions, after the nucleosynthesis is largely finished, are shown in Figure 2.7. Above the central region, a layer of material enriched with α-chain elements, such as ^{44}Ti, ^{40}Ca, ^{36}Ar, ^{32}S, ^{28}S is found, resulting from the incomplete burning of the silicon layer. The outer most layer in which nucleosynthesis occurs contains a large fraction of unburnt ^{16}O enriched with other, light α-nuclei such as ^{24}Mg, ^{20}Ne, ^{12}Ca. The detailed composition of each layer, however, is dependent also on the electron fraction during which the nucleosynthesis occurs, which can be altered depending on the strength of the neutrino interactions in the innermost region of the ejecta (Hartmann

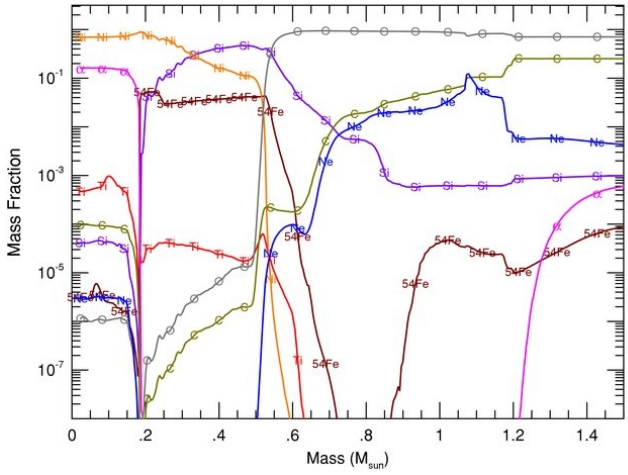

Figure 2.7: Mass fraction of produced isotopes in dependence on the interior mass for a 16 $M_\odot$ explosion model. Only material that is ejected, i.e. gravitationally unbound from the central NS, is considered in the interior mass. Fallback and the neutron star are excluded. Adopted from Magkotsios et al. (2010)

.

et al. 1985; Magkotsios et al. 2010; Nomoto et al. 2013).
Most of the current theoretical understanding of nucleosynthesis in ccSN explosions comes from parameterized models, that do not explicitly follow the engine driving the explosion, but replace it by some simplified scheme of energy insertion. Due to the lack of sufficient, self-consistent models that successfully lead to an explosion of the collapsed core, simulations of the SN engine and the nucleosynthesis have commonly been decoupled. While on the one hand asymmetry is required for the success of ccSN simulations, spherically symmetric models also fail to explain the observed isotopic abundances and ejecta distributions observed in recent SN explosions. The presence of high velocity ^{56}Ni in SN 2002ap (Mazzali et al. 2007) and asymmetric iron lines in SN 1987A (Spyromilio et al. 1990) indicating ejection of ^{56}Ni in single knots, provides a peculiar picture of a potential convective overturn, where the ejecta structure is turned inside-out with iron group elements at highest velocities. This behavior can only be explained by including multidimensional effects into SN nucleosynthesis calculations. As the explosion in the center emerges from convective motion and instabilities, the phase space in the ρ-T plane, that is sampled by the ejecta during nucleosynthesis can be much more complex than in a spherically symmetric explosion. For such conditions, studies (Magkotsios et al. 2010; Hermansen et al. 2020) indicate, that the mass fraction of ejected ^{44}Ti can vary by several orders of magnitude. Early, one dimensional calculations suggested an ejection of several times 10^{-5} $M_\odot$ ^{44}Ti (Timmes et al. 1996), that can vary by a factor of ≈ 3 with the progenitor stars initial mass. However, more recent studies that include the evolution of also multi-D models and a large range of progenitor ZAMS masses would predict a spread of ^{44}Ti ejecta masses of two orders of magnitude, ranging from 10^{-6} – 10^{-4} $M_\odot$ per supernova explosion (Magkotsios et al. 2010; Wongwathanarat et al. 2017; Limongi & Chieffi 2018; Wanajo et al. 2018).

In addition to the explosive nucleosynthesis in the shock heated ejecta layers, a peculiar flavor of isotopes is mixed into the ejecta by nucleosynthesis in the neutrino heated ejecta. These neutrino processed ejecta consist of two distinct components. The first component

is the material from inside the shock radius. Initially at high density and temperature, the chemical composition at freeze out is determined by the Y_e during the expansion of the ejecta. Close to the neutron star, neutrino interactions on the ejecta are dominant over the competing $\beta^{\pm}$ decays. Some of the material can maintain a low $Y_e \leq 0.5$ during the expansion, i.e. a relative neutron richness, resulting in a chemical composition of the ejecta away from the production of nuclei with N=Z towards nuclei with neutron excess (weak r-process). However, recent simulations suggest that neutrino irradiation leads to proton rich conditions in the post shock region that enhance the abundances of scandium, titanium, and cobalt (Arcones & Thielemann 2013; Thielemann et al. 2018) or a νp process that produces elements up Z = 42 (Fröhlich et al. 2006). The second component is a baryonic outflow from the PNS, that is driven by the neutrino irradiation of the ejecta above the PNS's surface. This neutrino wind is launched after the initial explosion of the SN has been launched, and is essentially spherically symmetric from the PNS. For a sufficient neutron excess, the accumulation of neutrons on heavy seed nuclei is faster than the competing β-decays in the isotopes. As a consequence, very neutron rich nuclei up to the neutron drip line are formed. Only when this limit is reached, the isotopes decay towards the line of stability. Within this *r-process*, isotopes with a nucleon number up to $A \approx 140$ are produced (e.g. Panov & Janka 2008; Janka 2012).

Besides the variations in the ejecta mass and composition, the simulated, arising hydrodynamic instabilities lead to observable asymmetries in the remnant of a supernova explosion, as the sloshing and convective motion are frozen into the shock morphology. The idea of an idealized, radial coordinate that separates the ejecta from fallback (cf. Figure 2.7; Hoffman et al. 1995) is thereby violated, and dependencies of the ejecta structure on the initial, 3D structure of the shock arise. Depending on the progenitor star's composition, the fractured structure of the ejecta from rising Rayleigh-Taylor fingers can become more pronounced due to hydrodynamical instabilities along the shock's traversal through the progenitor star. Because of the high density of material in these fingers, they are less decelerated than the surrounding ejecta and carry synthesized, radioactive isotopes (among a large pool of stable nuclei) from close to the PNS into the outer layers of the star at high velocities. Likewise, the large scale asymmetries in the two hemispheres from SASI motion, imprinted at the onset of the explosion, are expected to remain present until shock breakout from the progenitor star's surface (cf. Figure 2.8; Wongwathanarat et al. 2013; Stockinger et al. 2020). Therefore, the asymmetric ejection of matter at the onset of the explosion that is expected to lead to the large variation of ^{44}Ti ejecta masses (Messer et al. 2010; Hix et al. 2014; Ellinger et al. 2012) should also be imprinted in the distribution and kinematics of the ejected radioactive material after shock breakout.

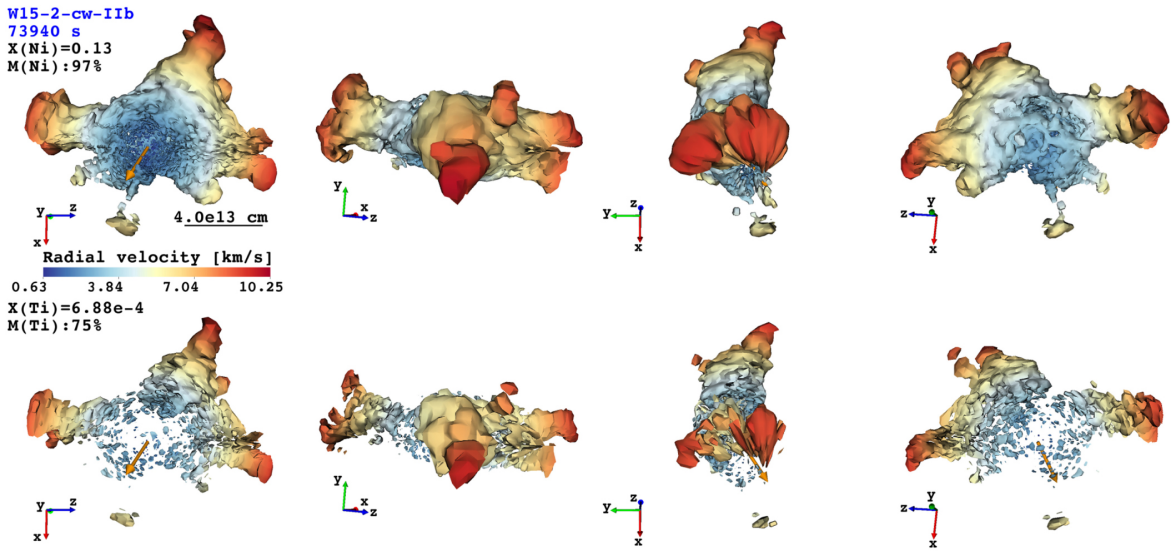

Figure 2.8: Isosurfaces containing constant mass fraction of ^{56}Ni (upper) and ^{44}Ti (lower). Surfaces are shown for the level containing 97% and 75% of the ejected mass of ^{56}Ni and ^{44}Ti, respectively for 4 different viewing angles. Color coding represents the radial velocity of the ejected material according to the color bar between the rows in 10^3 km s^{-1}. The orange arrow indicates the direction of the neutron star kick velocity. Large scale structures in the ejection of the nucleosynthesis products are visible in the "front" and "back" view of image 1 and 4. Adopted from (Wongwathanarat et al. 2017).

2.4 Type Ia/Thermonuclear Supernovae

2.4.1 Type Ia Explosions: The Standard Model

Type Ia supernovae are one of the brightest transient sources in the universe that are classified by a rather uniform peak luminosity, reaching an absolute magnitude of -19.3 mag in the visual band (Riess et al. 1999). In general, the type Ia SN light curve can be classified by a prompt rise in luminosity, that reaches a maximum approximately 20 days after the initial rise. After maximum light, the SN luminosity declines rapidly within the first month and exhibits a more gradual decline for the subsequent hundreds of days. Due to their extreme peak brightness, type Ia SN play a crucial role also in modern day cosmology, where they are used as *standard candles* to determine the expansion of the universe. With the help of the Phillips relation (Phillips 1993), linking the decline rate of the SN luminosity 15 days after peak luminosity to the intrinsic, B-band peak luminosity, *standard candles* values for type Ia brightness can be obtained within an uncertainty of 0.1 mag.

Type Ia SNe are commonly classified by the chemical composition of their ejecta, inferred from the lack of emission lines and the presence of absorption lines in the optical spectra near maximum light and during the early evolution of the young SNR. The description of the spectral evolution is based on Filippenko (1997); Hillebrandt et al. (2013). Near peak brightness, the SN shows no emission from hydrogen lines, and commonly also lacks strong helium lines. This indicates, that the progenitor system consists of an evolved, old star, that contains a hydrogen envelope of less than 0.01 $M_\odot$ (Leonard 2007). In addition, during the early phase, the spectra show strong absorption lines from IME, predominantly from silicon,

but also from sulfur, calcium, magnesium and oxygen at high velocities. As the abundance of these elements is elevated with respect to the Galactic and solar values, it is expected that these elements are produced during nucleosynthesis in the explosion. The expansion of the SN remnants (SNR) leads to a dilution of the ejecta. In the early phase, the time for photons to diffuse out from the central region is high, so that the spectra can only probe the surface layers of the explosion. When the remnant enters the nebular phase, also the interior regions of the young SNR are optically thin, an photons can escape this region. Spectra observed during the late time of the explosion contain of absorption lines from iron group elements (such as iron, cobalt, and nickel), at lower velocities in the interior of the remnant, further providing evidence for explosive nucleosynthesis.

The temporal evolution of the SN light curve cannot be reproduced from the thermal energy of the initial ejecta alone. The initial, internal energy of the explosion of $\approx 10^{51}$ erg is quickly transformed into kinetic energy by adiabatic expansion of the SNR. The internal energy has decreased to roughly 10^{44} erg at the time of peak luminosity, and can therefore not power the remaining SN lightcurve, which contains $\approx 10^{49}$ erg. The presence of an additional source, contributing energy to the ejecta, is required. The peak bolometric luminosity matches the production of roughly $0.1 - 1.0\,M_\odot$ of synthesized ^{56}Ni (Stritzinger et al. 2006).

The average expansion velocity of the ejected material lies between 5000 and 20000 km s^{-1}, with an average value of 10000 km s^{-1}. No major deviations from SN ejecta masses ranging between $1 - 2\,M_\odot$ are found (Scalzo et al. 2014), and only a minor fraction exceeds $2\,M_\odot$. The energy required to disrupt a WD and gravitationally unbind the ejected matter is $E_g = \frac{5}{3}\frac{GM}{R2} \approx 1.5 \times 10^{51}$ erg. The energy produced by nuclear burning of $\approx 1\,M_\odot$ of degenerate carbon-oxygen matter to intermediate and iron group elements matches the kinetic energy of the ejecta minus E_g.

Due to the apparent homogeneity in their appearance, it is widely accepted that type Ia supernovae are produced by the explosion of a WD (Hoyle & Fowler 1960). In the standard model of type Ia supernovae, a carbon-oxygen WD (CO WD) accretes matter from a binary companion. Thereby the WD's central density is gradually increasing until the nuclear burning of carbon and oxygen in the WD is ignited. The energy release in the central region leads to a convective core. As the star is stabilized fully by degeneracy pressure of the degenerate electron gas, the energy deposition from nuclear burning heats up the central core while only marginally decreasing the density in the central region. The increased temperature further speeds up the nuclear fusion processes until a thermonuclear runaway is reached. The energy released in this thermonuclear runaway is sufficient to fully disrupt the progenitor WD. During the burning of carbon and oxygen, nucleosynthesis occurs which mainly produces iron group elements in the dense central region. In the less dense outer regions, IME are also produced, while also some of the nuclear fuel remains largely unburnt as oxygen. Due to the thermonuclear origin of the explosion, type Ia SN are also distinguished as thermonuclear SNe. However, the energy released in this explosion is not what can be observed as the supernova. The radiation, emitted in the decay of the freshly synthesized radioactive material, is absorbed by the SN ejecta and recycled into photons in the infrared to ultraviolet wavelength bands. Only when the SN ejecta become optically thin in the late phases can the decay radiation escape the supernova.

2.4.2 The Thermonuclear Supernova Diversity

Using type Ia SNe as probes for cosmology relies on the fact that a homogeneous population of type Ia explosions exists (Branch & Tammann 1992). However, the detection of two extraordinary explosions, SN1991bg and SN1991T (Branch et al. 1993), made it evident that even in this homogeneous group of explosions peculiar sub-types do exist. Over the years, numerous explosions that can be classified as peculiar have been found. Nevertheless, the majority (70%; Li et al. 2011) of observed SNe in a volume limited survey belong to the standard type Ia SNe with a uniform peak luminosity. Outliers can be characterized into several sub-types (Taubenberger 2017), commonly referred to by their prototype explosions.

SN 1991bg is the prototype explosion for a subluminous SN event with a peak luminosity 2.5 mag, i.e. ten times, lower than a standard type Ia observed in the same galaxy (Filippenko et al. 1992a; Leibundgut et al. 1993; Turatto et al. 1996). The light curves for this sub-type usually decline fast in the visual, red, and infra-red band. In addition, a large abundance of intermediate mass elements including a large amount of ionized titanium is found in the early SN spectra, however, at slower velocities than commonly observed. Additionally, only a small amount of iron is found in the ejecta's spectra (Filippenko et al. 1992a). The low luminosity and the light curve decay suggest that SN of this sub-type commonly produce less than $0.1\,M_\odot$ of ^{56}Ni (Mazzali et al. 1997; Sullivan et al. 2011)

SN 1991T is noted as the prototype for bright explosions. These energetic events exhibit broad light curves (Ruiz-Lapuente et al. 1992; Phillips et al. 1992; Filippenko et al. 1992b), that show only few absorption lines from intermediate mass elements in the early spectra. Instead, lines from ionized iron are found at high velocities (Filippenko et al. 1992b). Calculations suggest, that these SNe could produce ^{56}Ni ejecta masses of between 0.7 and $\geq 1.4\,M_\odot$ (Taubenberger 2017), possibly exceeding the Chandrasekhar mass limit for WDs (equation 2.24).

Ca-rich transients are a rather new sub-type of type Ia explosions. Several of these explosions were characterized by Perets et al. (2010). The light curves of these objects are very dim, in accordance with a respectively low ^{56}Ni ejecta mass of only $10^{-2}\,M_\odot$. An alternative suggestion for their atypical light curve could be the total lack of ^{56}Ni in the ejecta. Instead the light curve is powered by the decay of radioactive IME isotopes, which would be related to the presence of strong Ca lines in the late time spectra. However, such an explanation would require the presence of up to $1\,M_\odot$ ^{44}Ti in the ejecta (Waldman et al. 2011).

In addition to the detection of varying luminosity and therefore ^{56}Ni production in thermonuclear SNe, correlations between the host galaxy mass, star formation rate, metallicity and the SN luminosity have been found (Howell 2001; Sullivan et al. 2006; Howell et al. 2009). Bright SNe, with a broad light curve as well as sub-luminous ones are dominantly found in evolved galaxies with old star populations. From these differences, progenitor systems leading to the production of thermonuclear SNe face two problems. First, a mechanism is needed, that can robustly produce the observed, rather uniform ^{56}Ni masses and similar properties in all explosions. On the other hand, the same mechanism and progenitor system may not be to rigid to be able to account for the varying properties and observed type Ia sub types. Also the correlation between host galaxy properties, especially host galaxy age and

SN luminosity need to be accounted for.

Whether the full spectrum of thermonuclear SNe can be reproduced by only one progenitor type or multiple ways of inducing an explosion in a WD are needed, remains an unsolved mystery to date. In the current understanding of thermonuclear SNe, three distinct models are considered as viable candidates to produce an explosion in a WD: 1) The explosion starts in the center of the WD, when its mass approaches the Chandrasekhar mass limit due to accretion from a binary star. 2) The detonation of an accreted He layer on the surface of the WD triggers a secondary explosion in the WD. 3) The explosion is the result of the merging of two WDs. Despite extensive theoretical and observational studies the solution to the unidentified progenitor system and the explosion mechanism for thermonuclear SNe is still not found. Indirect evidence, that either support the one or the other explosions model, have been found in extensive searches in different wavelength bands. However, a direct hint, pointing towards one scenario is still missing so far. Here, an approach, that has largely been neglected in previous studies, is utilized to infer the progenitor system. The nucleosynthesis in a WD explosion is mainly dependent on the density at which it occurs. While a large range of models can successfully reproduce the ejected ^{56}Ni mass necessary to power the explosions, and show the required stratification of the elements in the ejecta, the yields of IME elements, including ^{44}Ti, can be highly dependent on the assumed progenitor type. The three main candidates trajectories, that lead to the explosion of a WD as well as their nucleosynthesis imprints, as observable in the soft γ-ray regime are, in short, described in the following sections.

2.4.3 Chandrasekhar Mass Model

The Chandrasekhar mass model (Whelan & Icko 1973) requires the presence of a WD in a binary system with a main sequence or a giant star, that serves as hydrogen donor to the WD. The mass accretion rate on the WD needs to be fine tuned in this model to allow for a stable increase in mass. Stable burning of hydrogen on the surface of the WD is possible only for mass accretion rates in the order of $10^{-7}\,M_\odot\,yr^{-1}$. Below this mass accretion rate, hydrogen burning will occur explosively in recurring nova outbursts (Kato et al. 2014; Nomoto & Leung 2017). However, mass accretion on the WD will be hampered by the outburst as more mass will by ejected by the nova than accreted onto the WD. On the opposite site, when the mass accretion rate is too high, the WD is expected to form a red giant-like envelope, that would give rise to hydrogen lines in the SN's spectra. When the mass of the WD approaches the Chandrasekhar mass, the density and temperature in the center are sufficiently high ($\rho \geq 2\times10^9\,g\,cm^{-3}$, $T \geq 3\times10^8$ K; Caughlan & Fowler 1988) that carbon burning sets in, heating up the core in a *simmering phase* (Nomoto et al. 1984; Woosley et al. 1986). This can last several centuries. Eventually, when the central temperature exceeds $T \geq 7\times10^8$ K, a thermonuclear runaway in the core of the WD is triggered, which fully disrupts the WD. One of the advantages of this scenario is that it can naturally explain the homogeneity in the majority of type Ia explosions due to the similar masses of the exploding WDs.

The explosions of the WD in this scenario is sensitive to the propagation of the flame front, which can either be a deflagration, a detonation or of a composite nature, where a deflagration turns into a delayed detonation. However, a supersonic propagation of the nuclear flame front (detonation) in the WD would lead to conditions where nucleosynthesis in the entire

WD occurs in NSE conditions at high densities above $10^7\,\mathrm{g\,cm^{-3}}$ (Arnett et al. 1971), fully converting the WD to IGEs. The presence of silicon lines in type Ia spectra rules out this scenario. On the other side, simulations of pure deflagrations only show weak explosions. The energy release of nuclear burning transfers energy to the fuel ahead of the burning front. As the flame front only propagates with a velocity of $\approx$ 1% the speed of sound (Ma et al. 2013) in the medium, the fuel ahead of the flame has sufficient time to react and expand, decreasing the density outside the WD's core. Nuclear burning at NSE occurs only in the core of the WD, leading to a smaller amount of IGE, while the reduced density in the outer layers leads to the production of IMEs. This is compatible with early spectra. The general trend for the production of radioactive isotopes, relevant for powering the SN light curve and late time observability in γ-rays, suggest, that only a small amounts of ^{56}Ni, ranging between $3\times10^{-2} - 3\times10^{-1}\mathrm{M}_\odot$, and very little ^{44}Ti, ranging between $2\times10^{-7} - 3\times10^{-6}\mathrm{M}_\odot$ are produced (e.g. Fink et al. 2014). This would make pure deflagration models sub-luminous SNe with a weak ^{44}Ti signal. As parts of the nuclear fuel in the center remains unburnt as C and O, the model suffers from the problem of elemental stratification seen in type Ia spectra. While this scenario would be a viable explanation for some sub types of explosions, they cannot be responsible for the bulk of observed *normal* type Ia explosions.
To circumvent the shortcomings of the pure deflagration/detonation scenarios a delayed detonation is considered (Khokhlov 1991; Röpke 2007), where an initial deflagration flame transitions into a detonation. In this scenario, a subsonic deflagration flame produces IGE in the dense, central region. However, the energy input from the early fusion processes allows the star to pre-expand, before the induced delayed detonation sweeps through the WD. This scenario allows for the production of ^{56}Ni in the expected range necessary for the observed peak luminosities and also for the presence of IME in the surface layers of the exploded WD. The expected ^{44}Ti ejecta masses are in the range of $3\times10^{-6} - 10^{-5}\mathrm{M}_\odot$ is expected (e.g. Seitenzahl et al. 2013).

However, even state-of-the art simulations have difficulties in following the ignition of a deflagration flame through a convective carbon simmering phase for several hundred years prior to the explosion and modeling the spontaneous transition from a deflagration to a detonation flame. In numerical simulations, this problem is circumvented by artificially introducing a varying number of ignition sparks in the central region, where a low number of sparks or off-center ignition can lead to strong asphericities in the explosion (Seitenzahl et al. 2013; Fink et al. 2014).

2.4.4 Sub Chandrasekhar Mass Explosion by Double Detonation

An alternative for realizing nuclear burning in less dense fuel is the sub-Chandrasekhar mass explosion model. As the central density of the WD is related to its mass, a variety of densities profiles can be tested, when an explosion of a sub-Chandrasekhar mass WD with varying mass is triggered. For sub-Chandrasekhar mass WDs, spontaneous ignition of nuclear burning cannot be triggered by the gravity of the WD on its own, as masses close to the Chandrasekhar limit ($\mathrm{M_{WD}} \geq 1.38\,\mathrm{M}_\odot$) are necessary for a sufficient central density and temperature. An external method of triggering the compression is achieved by a primary detonation on the WD's surface. In this scenario, the primary CO WD accretes matter and forms a helium rich shell. Mass transfer can be from a helium WD (Guillochon et al. 2010; Pakmor et al. 2013) or an evolved, stripped helium core of a main sequence star (Nomoto

1982; Woosley et al. 1986). Alternatively, a main sequence star can transfer hydrogen, that quiescently burns to helium.

For mass accretion rates lower than $\approx 1 - 4 \times 10^{-8}\,M_\odot\,yr^{-1}$ of helium onto the CO WD, helium is not steadily fused to carbon and oxygen on the surface. Instead, massive helium layers up to $0.2\,M_\odot$ can be built up (e.g. Woosley et al. 1986; Fink et al. 2007; Woosley & Kasen 2011). At the base of the helium layer, the matter becomes degenerate, increases in temperature and density and finally ignites. The surface helium detonation loops around the WD and on the opposite site of the initial ignition point, a shock wave is focused towards the center. The compression of the core triggers carbon-oxygen burning in the center, resulting in a second detonation that disrupts the WD.

With a large range of potential progenitor masses, the central density of the carbon-oxygen core can vary by almost an order of magnitude, allowing for a wide range of centrally synthesized elemental abundance distributions. The central burning of nuclear fuel is similar to the prompt detonation of a Chandrasekhar mass WD, with the exceptions of the variable central density. Sim et al. (2010) find, that the central fusion of carbon and oxygen to IGE in WDs with inital masses ranging between 0.81 and $1.15\,M_\odot$ can produce a large range of ^{56}Ni spanning from 10^{-2} to $8 \times 10^{-1}\,M_\odot$. The production of IGE and IME elements is inversely proportional: For high masses of ^{56}Ni small masses of ^{44}Ti are produced and vice versa. However, low mass progenitor models do not reproduce the observed ^{56}Ni masses in type Ia SNe (Stritzinger et al. 2006). The variability in ejecta masses is one of the major strengths of the sub-Chandrasekhar mass model, as it can in principle be responsible for a major part of the observed type Ia SN diversity.
In addition to the centrally synthesized elements, nuclear fusion on the surface of the WD during helium detonation can produce a considerable amount of IGE and IME. Massive helium shells with masses of 0.1–$0.2\,M_\odot$ produce a large amount of ^{56}Ni on the surface of the WD in simulations. This, however, is in conflict with the observed spectra and light curves of SN explosions, as commonly no absorption lines of IGE are found in the early spectra at high velocities (Woosley & Weaver 1994; Hoeflich & Khokhlov 1996; Nugent et al. 1997). This influence can be minimized by the presence of less helium in the shell. Models from Bildsten et al. (2007); Fink et al. (2010); Pakmor et al. (2013) suggest, that also minimum helium shells with masses of less than $5 \times 10^{-2}\,M_\odot$ can lead to a successful central detonation. Due to the decrease in the helium shell mass, lower quantities of ^{56}Ni are produced on the surface in the range of $10^{-2}\,M_\odot$, more compatible with observations.
More important however, is the presence and production of significant amounts of IME in the helium shell detonation. Due to the overall lower density during nuclear burning on the stellar surface, the burning of minimum helium shell masses additionally produces a large variety of IME on the surface. Where the central fusion processes only produce a negligible amount of IMEs, the surface production can yield increased quantities by two orders of magnitude. For helium shell masses of $\approx 0.05\,M_\odot$, the production of the ^{44}Ti isotope is expected to be in the range of $2\times10^{-4} - 4\times10^{-3}\,M_\odot$ (Moll & Woosley 2013; Leung & Nomoto 2020).

2.4.5 Double Degenerate Merger Scenario

Attention for the double degenerate model, which involves the merging of two CO WDs, has only been regained again during the last decade. Early studies of this progenitor models showed, that it would not produce successful explosions. Instead, the less massive of the two WDs would leave a hot envelope on the more massive one, which would subsequently transform into a neon-oxygen WD (Saio & Nomoto 1998). The remaining object would finally collapse into a neutron star, once it reaches the Chandrasekhar mass limit (Nomoto & Kondo 1991).

Figure 2.9 shows the evolution of the final stages in the binary system with different masses. The description of the scenario is given for a $1.1\,M_\odot$ and a $0.9\,M_\odot$ CO WD binary system following Pakmor et al. (2012) (see also Pakmor et al. (2011); Sato et al. (2015, 2016). A similar situation follows from a setup of equal mass binaries. The more massive WD is referred to as the "primary" and the less massive one as the "secondary".
Following an inspiral of the WD binary system due to the emission of gravitational waves, that can last for several hundred million years, the final evolution of the merger lasts only for several minutes. During the final orbits stable mass transfer from the secondary to the primary occurs. In the final orbits, the secondary is disrupted by tidal forces exerted from the primary WD and becomes dynamically unstable. The secondary is accreted onto the surface of the primary WD, leading to compression of matter on the primary. Compressional heating leads to the creation of hot spots on the primaries surface, that can exceed temperatures of 2×10^9 K at densities of $\geq 10^6\,\mathrm{g\,cm^3}$, which are the necessary conditions for the initiation of carbon burning on the primaries surface.
The density distribution of the merged binary system produces a peculiar nucleosynthesis structure in the ensuing nuclear burning. The burning in the primary WD can be considered a detonation similar to the detonation of a single degenerate WD. As the velocity of the burning front is dependent on the density, the burning advances faster in the primary, undisrupted WD. Nucleosynthesis ashes, mainly consisting of radioactive ^{56}Ni are ejected with a directional dependence. As the expansion in the direction of the unburnt secondary is hindered, the radioactive nickel dominantly escapes in the opposite direction. Ejected ^{56}Ni masses are compatible with the standard type Ia ejecta yields. As the burning of nuclear fuel is slower in the disrupted secondary, the radioactive ^{56}Ni, produced in the primary, has already expanded before the secondary finishes burning. Nucleosynthesis in the disrupted secondary, in general, occurs at lower densities. Therefore, nucleosysnthesis in the secondary does produce no IGE, while large amounts of IME are produced. As a consequence, this scenario lacks iron group elements in the central region. For an equal mass merger of two $0.9\,M_\odot$ WD, Pakmor et al. (2010) find an ejected ^{44}Ti mass in the order of $10^{-5}\,M_\odot$.

In order to fully describe the entire range of the observed type Ia sub-types, probably more than one of the scenarios is required. While the ejected mass of radioactive ^{56}Ni of the order of $10^{-1}\,M_\odot$ is rather uniform in the majority of the simulated scenarios, the progenitor system for specific SNe can probably be identified by the detection of their ^{44}Ti decay signature, as the ejected mass can vary by several magnitudes between the different scenarios. In contrast to the sub-Chandrasekhar models, the double detonation models produce a major amount of ^{44}Ti. The recently discovered calcium rich gap-transients are considered to originate from special double detonation events. These are predicted to produce $\approx$ 50% of their ejecta in

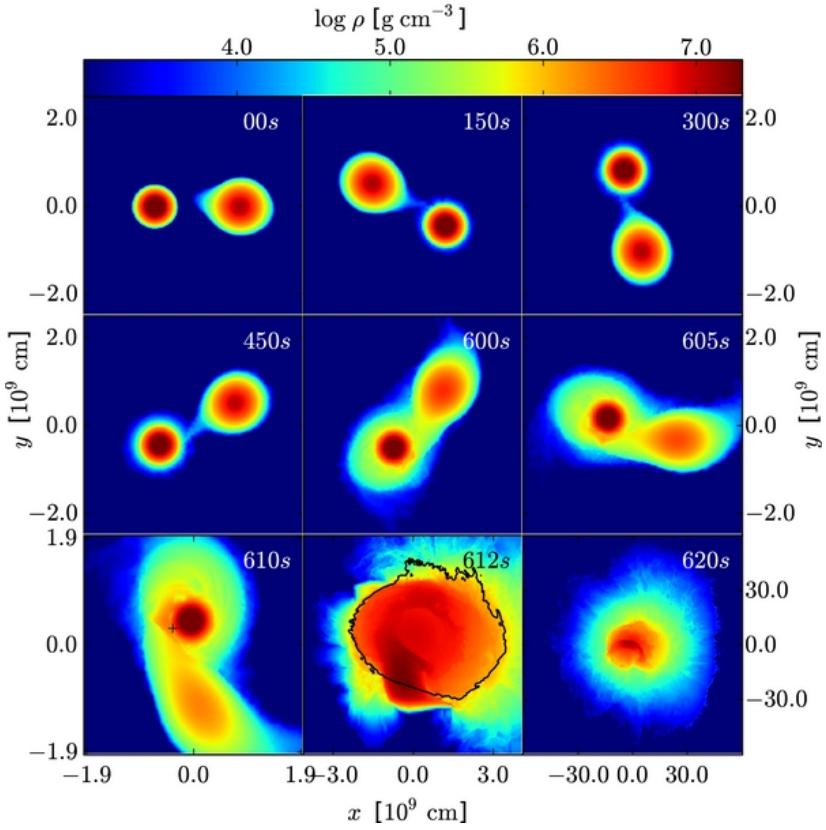

Figure 2.9: Simulation of a violent merger of a 1.1 $M_\odot$ and a 0.9 $M_\odot$ CO WD system during its final evolutionary stage. Color coding represents the density distribution in the binary system. During the final ≈35 orbits lasting ≈15 s stable mass transfer from the secondary to the primary WD occurs. In the final orbit, the secondary is tidally disrupted by the heavier primary. Matter on the interface between accretion and primary WD is compressionally heated. When the critical density and temperature are reached, nuclear burning is initiated and a detonation encompasses the merged remnant. The black cross (bottom left panel) marks the location of the initial burning. Figure adopted from Pakmor et al. (2012).

^{44}Ti (Filippenko et al. 2003; Perets et al. 2010; Kasliwal et al. 2012; Valenti et al. 2013), when the detonation of the surface helium layer fails to ignite a second central explosion in the WD.

2.4.6 The Window to the Core of the Explosion: Observing Nuclear De-Excitation Lines in γ-Rays

For the understanding and future modeling of SN explosions, observations of the innermost physics, driving the explosion, are of greatest importance. Unfortunately, this innermost explosion cannot be directly observed. During the early phase of the explosion, the density in the ejecta is still high, such that the optical depth is significantly higher than one. Therefore, radiation from the central region cannot readily escape the remnant without being absorbed or scattered several times. The explosion itself only becomes visible when the outward propagating shock front has reached the surface of the surrounding stellar envelope at timescales, when the important physical ingredients have long subsided. However, con-

Table 2.2: Radioactive isotopes and their respective decay signatures in SN explosions. The tabulated line energies are for the most prominent decay lines with probability of emission above 50% per decay. Additional lines are omitted. Due to the nature of ccSN and type Ia nucleosynthesis, some isotopes are dominantly produced in only one type. Elements, listed in the same row are from a singular decay chain, where the daughter isotope is not necessarily produced in large amounts during nucleosynthesis. All values are taken from NNDC (2020).

Isotope	Line Energy [keV]	Half-Life	Prominence
^{56}Ni	750.0, 811.9	6.1 d	Ia, ccSN
^{56}Co	846.8, 1238.3	77.2 d	Ia, ccSN
^{44}Ti; ^{44}Sc	67.9, 78.3; 1157.0	59.1 yr; 4.0 h	Ia, ccSN
^{26}Al	1808.7	717.0 kyr	ccSN
^{60}Fe ; ^{60}Co	–;1173.2, 1332.5	2.6 Myr	ccSN
^{48}Cr; ^{48}V	112.3, 308.2; 983.5; 1312.1	21.6 h; 16.0 d	Ia
^{52}Fe; ^{52}Mn	621.7, 869.9, 929.5, 2037.6; 1434.1	8.3 h; 5.6 d	Ia
^{55}Co; ^{55}Fe	931.1; –	17.5 h; 2.7 yr	Ia, ccSN
^{57}Ni; ^{57}Co	1377.6; 122.1	35.6 h; 271.7 d	Ia, ccSN

clusions on the driving force can be drawn from the observations of radioactive isotopes, which are produced during explosive nucleosynthesis in the high density environment. In ccSN explosions both the yields of the ejected, freshly synthesized material and its kinematic distribution are subject to the physical conditions during the explosion (see 2.3.3). In thermonuclear explosions a large parameters space is covered by the amount of ejected material, which directly depends on the progenitor type (see 2.4). It is possible to find indirect evidence of the radioactive material, which heat the ejecta by their decay and power the SN light curve over hundreds of years (e.g. Jerkstrand et al. 2011; Seitenzahl et al. 2013). However, deducing physical constraints from indirect evidence is model dependent.

The early light curve of a SN is powered by the decay of radioactive ^{56}Ni. After several years the principal energy supply is contributed by the decay of ^{44}Ti and its daughter nucleus (Seitenzahl et al. 2014). After approximately one year, the SNR is diluted and optically thin for γ-rays. The majority of decay photons can readily escape the SNR and can be detected with γ-ray telescopes such as INTEGRAL/SPI.

I utilize a model independent approach to infer the ejecta masses, by directly observing the decay radiation of the radioactive material. A large variety of radioactive isotopes are synthesized during SN explosions. The most prominent isotopes and their decay lines are listed in Table 2.2. Due to the very different half-life times of the isotopes, the SN explosions can be probed on different timescales. However, most of the isotopes are either produced with an abundance to small to be observed within the sensitivity of current γ-ray telescopes or decay before the SNRs become optically thin for γ-rays.
This thesis focuses on the observation of young SNRs (cf. section 2.6.1). In the context of observing decay radiation in SNe in the young remnant phase, the most promising isotope, produced in explosive nucleosynthesis, is ^{44}Ti. In Figure 2.10 the decay chain of ^{44}Ti is shown in detail. In a first step, ^{44}Ti decays to an excited state of ^{44}Sc via electron capture

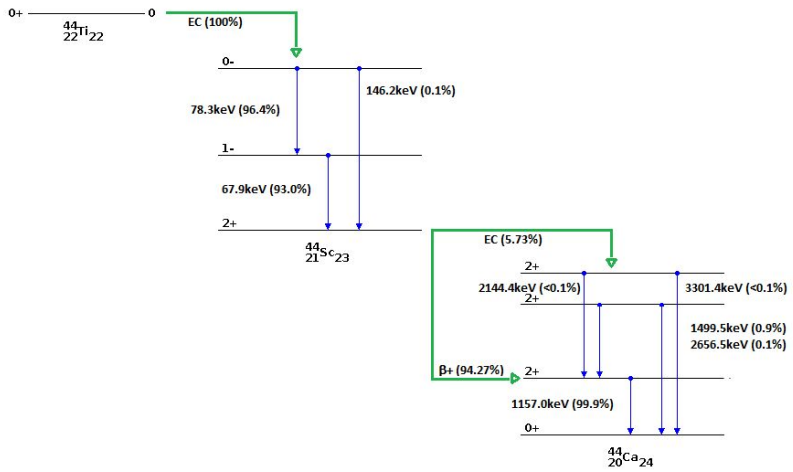

Figure 2.10: Decay scheme of ^{44}Ti and subsequent decay of the daughter nucleus ^{44}Sc to ^{44}Ca. In the initial step ^{44}Ti decays by electron capture (100 % probability) with a half-life time of 59.1 yr (Audi et al. 2017) to an excited state of ^{44}Sc at 146.4 keV. This excited state decays via subsequent emission of a 78.3 keV and a 67.9 keV hard X-Ray photon. The probabilities of photon emission are 96.4 % and 93.0 % per decay, respectively. The daughter nucleus ^{44}Sc further decays with a half-life time of 4.04 h (Audi et al. 2017) to an excited state of ^{44}Ca via electron capture (5.73 % probability) at 3301.4 keV or β^+ decay (94.27 % probability) at 1157.0 keV, respectively. The exited states of ^{44}Ca are subsequently decaying, with a dominant emission of a 1157.0 keV γ-ray (99.9 % probability per decay)

with a half-life time of 59.1 yr (Audi et al. 2017). This excited state promptly decays to the ground state of ^{44}Sc. It is possible that the excited state at 146.2 keV directly decays to the ground state under the emission of a 146.2 keV γ-ray, however, this channel is highly suppressed with a probability of less than 0.1% per decay. In the more likely event the excited state decays in a cascade, emitting two hard X-ray photons at 78.3 keV and 67.9 keV with a probability of 96.4% and 93.0% per decay, respectively. Subsequently, the daughter nucleus ^{44}Sc decays with a considerably shorter half-life time of 4.04 h (Audi et al. 2017) to an excited stated of ^{44}Ca. ^{44}Sc decays with a probability of 5.73% via electron capture and with 94.27% probability via β^+ decay, populating different excited states of ^{44}Ca in the process. In both cases, the subsequent de-excitation cascade populates the 1157 keV state, from which a γ-ray is emitted with a respective probability of 99.9% per decay. In addition to the prominent decay lines, Figure 2.10 also includes the excitation level and subsequent de-excitation photons, that are emitted with a probability on the sub percentage level. As the sensitivity of current instruments is not sufficient to detect the signatures of the weak lines, I focus on the detection of the prominent lines at 68, 78 and 1157 keV.
Due to the substantial difference in half-life times, where the first decay in the chain has a longer half-life time, the activity of both isotopes equalizes within days, when an equilibrium reservoir of ^{44}Sc has been built up. For SNRs with ages of several years, the flux from both decays can be safely considered equal, as the difference is solely governed by the difference in half-life times, that is significantly smaller than the uncertainties of the expected fluxes (see section 5.1.2).

2.5 γ-Ray Spectra from Radioactive Decay

In this thesis, I focus on analyzing the spectral shape of the measured radioactivity, i.e. the photon number per unit time and unit energy. Radiation emitted from nuclear transitions is not observed with a mono-energetic energy, but altered by several processes that lead to a finite line width. The fundamental line width is given from the uncertainty principle concerning the energy and the lifetime of the respective excited nuclear state such that

$$\Delta E = \frac{\hbar}{\tau}, \tag{2.31}$$

where τ is the lifetime of the excited state and ΔE is the intrinsic width of the line. For the three relevant excited states in the ^{44}Ti decay chain the lifetimes are 51 μs, 126 ns, and 3 ps, respectively (Firestone & Shirley 1998). This leads to an intrinsic line width of less than 2 meV, several orders of magnitude lower than the intrinsic energy resolution of γ-ray detectors (cf. section 3.1.2). The intrinsic line width can be neglected in astrophysical observations.

2.5.1 Considering Kinematic Behavior of Ejecta Spatial Distribution

The relative motion of an object with respect to the observer leads to a distortion of the emitted wavelength, such that a shift in energy is apparent in the observer's rest frame with respect to the emitted energy. This distortion is given by the Doppler formula

$$\frac{\lambda_0}{\lambda_{obs}} = \frac{\nu_{obs}}{\nu_0} = \frac{E_{obs}}{E_0} = \frac{\sqrt{1-\beta}}{\sqrt{1+\beta}} \tag{2.32}$$

where λ are the wavelengths, ν the frequencies and E the energies of the emitted photons in the rest frame of the emitter (denoted with the index 0) and as measured in the rest frame of the observer (denoted with the index obs). Here, the observer is moving relative to the emission rest frame with a velocity $\beta = \frac{v}{c}$. According to equation 2.32, the wavelength is *stretched*, i.e. *red-shifted*, when the emitter is moving away from the observer and *squeezed*, i.e. *blue-shifted*, when moving towards the observer. Likewise, the energy is shifted to lower or higher values, respectively.

For $\beta \ll 1$, the Doppler shift $\Delta E = E_0 - E_{obs}$ reduces to $\Delta E = \beta E_0$. For typical expansion velocities of SN ejecta of $v_{ej} \lesssim 10000\,\mathrm{km\,s^{-1}}$ (Filippenko 1997) this formula is correct up to 5%.

The ejection of matter by SN explosions can be highly asymmetric and in a fractured morphology, i.e. in separate ejecta clumps with varying kinematics. By observing a SNR without spatially resolving such a morphology, the measured photon flux is the superposition of separate emission regions, integrated over the volume of the remnant. Therefore, the spectral shape consists of the superposition of individual Doppler shifted and Doppler broadened emission lines. A study, detailing the spectral shape of a surface integrated emission is presented in section 5.1.2.

Similar considerations can be made for other ejecta morphologies. For example, Kretschmer (2011) showed that the emission of mono-energetic photons with energy E_0 from a spherically symmetric, infinitesimally thin ejecta shell with radius R at a distance $d \gg R$ produces a rectangular spectral shape. The analytic form of this spectral shape is given by

$$\frac{dF(E)}{dE} \propto \Theta\left(v_{ej} - \left|c\left(\frac{E}{E_0} - 1\right)\right|\right) \quad , \tag{2.33}$$

where the shell expands with the velocity v_{ej} and Θ is the heaviside function.

2.6 Footprints of Supernova Explosions

The description of nucleosynthesis in sections 2.3 and 2.4 has mainly focused on the production of radioactive ^{44}Ti, as it provides the best opportunity of observing nucleosynthesis in young SNRs. However, SNe of all types are the main drivers of chemical enrichment of the universe. After primordial nucleosynthesis, the ISM was mainly composed of H and He, and only minor fractions of less than 10^{-9} of heavier elements. 13.8 billion years later, the composition of the ISM has changed significantly, and the current mass fractions are 70% hydrogen, 28% He, while the fraction of metals, i.e. heavy elements, has increased to 2% (Klessen & Glover 2016). Therefore it is apparent, that some form of feedback mechanism has occurred over the history of the universe, that transfers back nucleosynthesis products from stellar environments into the surrounding medium.

2.6.1 Remnant Evolution

Feedback from SN explosions into the ISM is not instantaneous after the explosions. The evolution of the SN's remnant after the shock breakout from the progenitor's stellar surface is usually classified in four distinct phases (Chevalier 1977; Jones et al. 1998; Reynolds 2008; Vink 2011) until the ejecta are mixed back into the ISM. This general description is simplified and not all SNRs can be characterized by this scheme.

In the first phase, the mass of the ejecta is significantly higher than the mass of the swept up, circumsteller medium (CSM) or interstellar medium (ISM). As the velocity of the ejecta v_{ej}, ranging between 5000 and 10000 km s^{-1} for ccSN and Ia explosions, respectively, is significantly higher than the sound speed in the CSM, which is of the order of 1 km s^{-1}, a blast wave is formed. This phase is dominated by the dynamics of the ejecta. Even though it is called the free expansion phase, accumulation of CSM slows down the ejecta and the velocity of the blast wave (forward shock) is always lower than a full free expansion would suggest, i.e. $r_{FS} > v_s t_{SN}$, where r_{FS}, v_s and t_{SN} are the forward shock radius and velocity and the remnants age, respectively. The ejecta behind the blast wave cool adiabetically to low temperatures. When the successive material in the interior ejecta encounters the increasingly decelerated material ahead, it has to slow down instantaneously, producing a second shock (reverse shock) that traverses back into the ejecta in mass coordinate, reheating them. Note here, that at early times, both shock surfaces move outwards in radius. While in spherical symmetry, the shock heated ejecta and the CSM are separated by a contact discontinuity, in a more realistic setup, Rayleigh-Taylor instabilities will lead to turbulent mixing of CSM and ejecta across the shock. While energy losses from the emission of electromagnetic radiation

are negligible in this phase, the observation of photons from both the forward and reverse shock is of high interest, as in addition to a thermal component, electromagnetic emission from shock accelerated particles is expected here (cf. section 2.7).

The two shock structure can last for several hundred to thousands of years until the shock wave has swept up sufficient CSM, that the swept up mass M_{sw} is comparable to the ejecta mass. One dimensional simulations suggest, that the reverse shock reaches the center of the remnant, when M_{sw} is several times the mass of the ejecta. At this point, all interior ejecta are shocked and the evolution of the remnant can be described by a one shock solution for an adiabetic explosion (Sedov 1959). The phase transition typically occurs, when the expansion parameter $m = v_s t_{SN}/r_{FS}$ becomes 0.4 (Reynolds 2008). Remnants in the first two phases are typically considered as young SNRs.

Once the velocity of the shock is sufficiently slowed down, radiative energy losses are not negligable anymore and significantly affect the dynamical evolution of the remnant. The adiabetic solution is not appropriate anymore. The shell collapses into a thin and dense layer, while the interior of the ejecta still remain at high temperature and pressure. The expansion of the shell is driven by pressure, where the shell collects further material like a snowplow. When the interior starts to cool in this snowplow phase, the interior pressure reduces and the shell expansion becomes momentum conserving. Depending on the structure of the surrounding medium, parts of the remnant can be in different stages of the evolution. In regions, where the shock encounters dense material, the remnant may already be in the radiative phase, while other parts can still be in the adiabetic phase (Vink 2011).

When the temperature and velocity of the post shock material have decreased to values comparable with the surrounding medium, the remnant eventually merges with the ISM. At this point, these old remnants are extended structures and the ejecta finally mix into the ISM.

2.6.2 Chemical Evolution of the Milky Way

The Galactic chemical evolution is a feedback driven process, that is mainly governed by the efficiency of returning and mixing SN synthesized matter into the ISM and the effective timescales between formation of stars and their eventual demise as SNe. Especially ccSNe have strong environmental impact on the chemical evolution, as their r-process nucleosynthesis is required to explain the present day abundances of elements with nucleon number up to 140, while type Ia explosions are considered as the main producers of the highly abundant IGE. The production ratios of elements per respective SN trajectory can strongly differ from their average observed value in the galaxy. However, the superposition of a large number of SN explosions, previous to the formation of the solar system and ongoing nowadays in principle yields, once their ejecta have merged into the ISM, an abundance ratio of elements, that reproduces the observed, current chemical abundance ratios. The chemical feedback mechanism is therefore a fine tuned process, that is dependent on the recurrence time of the various SN scenarios. A precise knowledge of these quantities is necessary for all chemical evolution models of the Galaxy. Assuming that each type of SN explosion is expected to produce a specific abundance ratio, their rate of occurrence must be fined tuned to reproduce the solar abundances. Specifically, the solar abundance ratio of $[^{44}Ca/^{56}Fe]_\odot = 1.2 \times 10^{-3}$ (Anders & Grevesse 1989) is of great interest in this thesis, as these are the elements at the

end of the radioactive decay chains of ^{44}Ti and ^{56}Ni, respectively. While the recurrence rates of specific sub types of SNe, that over- or undershoot the solar value significantly, can be constrained from the abundance ratio, the ongoing, overall production rate of the specific isotope ^{44}Ti also needs to be fulfilled. From Galactic chemical evolution models, that are constrained to produce the ^{44}Ca abundance at the formation of the solar system 4.55 Gyr ago, a production rate of ^{44}Ca of $5.5 \times 10^{-6}\,M_\odot\,yr^{-1}$ at the present time is inferred (Leising & Share 1994; The et al. 2006). Adopting model dependent ccSN rates (Diehl et al. 2006a) a study by The et al. (2006) suggests, that the presence of short lived radioactive isotopes such as ^{44}Ti in the Galaxy is an indicator, that nucleosynthesis feedback is an ongoing process in the Galaxy. Thus, tracing its Galaxy wide emission provides insight in the current Galactic chemical evolution.

Models, predicting the chemical evolution of a galaxy, are based on three fundamental quantities. As indicated in section 2.2, the formation of individual stars from the ISM is a highly complex process, that involves gravitational collapse of matter on varying scales and can be hindered by the feedback mechanisms in the same GMC. However, it is possible to infer the global, i.e. Galaxy wide, production rate of new stars from the fundamental quantities of a Galaxy with the help of the star formation rate (SFR). The SFR describes the correlation between the gas surface density and the formation rate of new stars in a Galaxy. This is closely related to the spatial distribution of star forming region in the Galaxy, the second essential in chemical evolution models. After the initial formation process of new stars, the third fundamental quantity is the birth mass of the stars, which determines the evolutionary path and the eventual fate of the star (cf. section 2.2.3). The mass distribution is governed by the IMF discussed in section 2.2.

Star Formation Rate

One of the fundamental principles in tracing the Galactic chemical evolution is the global SFR. In combination with the IMF, this quantity determines the formation rate of massive stars with $M_{ZAMS} \geq 8\,M_\odot$, that eventually explode as ccSNe. The connection between the SFR and the gas density of a Galaxy was first introduced by Schmidt (1959) in the form of a power-law correlation. Many recent studies were able to refine this correlation. Inferring the global SFR from Milky Way observations is necessarily biased due to the observers position inside the Galactic disk. In particular, a correction factor needs to be introduced to account for missed, low mass stars that are to dim to be detected. An approach of determining the Milky Way SFR is by counting stellar objects in the Galactic plane and weighting it with the average lifetime of a stellar object of that mass (Kennicutt & Evans 2012). Robitaille & Whitney (2010) infer a Milky Way SFR of $(1.07 \pm 0.39)\,M_\odot\,yr^{-1}$ from a count of young stellar objects in the Galactic plane. However, a meta analysis of previously released data revealed, that such an approach typically leads to an SFR several times lower than other diagnostic methods (Chomiuk & Povich 2011). A unified picture of SFR is typically inferred from a combination of Galactic and extragalactic observations. As neither individual stars nor their star clusters can be spatially resolved in extragalactic measurements, the SFRs in these galaxies are inferred indirectly from the overall emission of the galaxy in multiple wavelength bands. Broadband observations allow for a distinction between the fraction of young and old stellar populations, allowing to infer the SFR on timescales of several

hundred million years (Kennicutt 1998). However, these determinations can be subject to environmental influences and are therefore imprecise. Refined diagnostic methods allow a translation of the ultraviolet-continuum, far infrared emission, the forbidden Hα transition and recombination lines of ionized gas into a SFR, as these are induced by the presence of young stars. A sample of SFR determinations for the Milky Way, utilizing the above methods, is given in table 2.3. The SFR determined in the meta analysis (Chomiuk & Povich 2011) yields an average value of $(1.9 \pm 0.4)\,M_\odot\,yr^{-1}$. Nevertheless, the large uncertainties in the determined SFRs are introduced as all these methods are subject to uncertainties in the IMF and the theoretical stellar evolution tracks, that require an independent systematic analysis.

Supernova Rate

For ccSNe, a conceptual link exists between the recurrence rate of the explosions and the formation of massive stars with $M_{ZAMS} \geq 8M_\odot$. Therefore, the ccSN recurrence rate is also a global parameter, that can be utilized to constrain the SFR and consequently also the Galactic chemical evolution. However, this argument is again biased by the adopted IMF, as it determines the fraction of stars that are formed with $M_{ZAMS} \geq 8M_\odot$ of the total ISM mass, converted into stars within a given unit of time. In fact, the ccSN rate further allows to narrow down the region, in which massive stars explode as a SN. The allowed mass range (cf. section 2.2.4) is currently not well constrained, and ranges between $8M_\odot \leq M_{ZAMS} \lesssim 25M_\odot$. The model predicted ccSN rate would always fall short of the observed rate, if indeed a wider M_{ZAMS} mass range, especially towards the high mass end, explodes.
Despite their expected frequent occurrence rate, the last ccSN in the Milky Way was Cassiopeia A (Cas A), which occurred around 1680. However, no written record of the transient exists and it was only later rediscovered at radio wavelengths (Ryle & Smith 1948). During the last millennium, only two written records of ccSN in the Galaxy exist. As the sparsity of observed SN in the last millennium provides a significant bias on a count based determination of the ccSN rate, van den Bergh & Tammann (1991) use the number of detected radio bright remnants in the Milky Way to infer a ccSN rate of 3.4 ± 2.0 explosions per century. In addition, the ccSN rate is often inferred from measurements of other Galaxies, with similar properties as the Milky Way. Even though these are biased by the varying morphology and mass content of the extragalactic Galaxies, the ccSN rate in spiral arm Galaxies typically agrees with the Milky Way values. A list of inferred ccSN rates is given in table 2.3. These suggest that the overall rate is in the range of a few events per century.

A unique way of inferring both the ccSN rate and the SFR is given by observing the decay radiation of ccSN-produced radioactive nuclei. Measurements of the Galaxy wide decay emission of radioactive ^{26}Al at 1.8 MeV can be translated into the currently present total mass of the respective isotope in the Milky Way. Assuming an exponential disk distribution to represent the morphology of ^{26}Al in the Galaxy, Diehl et al. (2006a) find a total ^{26}Al mass in the Galaxy of $(2.8 \pm 0.8)\,M_\odot$. This assumed steady-state mass is the results of a subtle balance between radioactive decay and ongoing resupply from massive stars. This resupply rate is subject to the convolution of the model predicted ^{26}Al yields from stars with the IMF. The SFR is then determined as the time normalization constant to meet the required resupply rate. Following the same argument, the same study determined a ccSN rate of (1.9 ± 1.1) ccSN explosions per century. This estimate can, however, be biased by

Table 2.3: Estimates of the Galactic star formation rate (upper panel) and core-collapse supernova rates (lower panel) for the Milky Way. Methods indicate the applied approach of determining the rates, including extragalactic observations that are extrapolated to the Milky Way spiral arm galaxy.

SFR [$M_\odot\,yr^{-1}$]	Source	Method
≈5	Smith et al. (1978)	Lyman Continuum
≈13	Güsten & Mezger (1982)	Free-free emission
≈4	McKee & Williams (1997)	Free-free emission
≈1	Kennicutt (1998)	Lyman Continuum
≈4	Diehl et al. (2006a)	^{26}Al Decay Radiation
(1.07 ± 0.39)	Robitaille & Whitney (2010)	Galactic Star Count
(1.9 ± 0.4)	Chomiuk & Povich (2011)	Meta-Analysis
8.25	Kennicutt & Evans (2012)	HI Mass
$3.6^{+8.3}_{-3.0}$	Adams et al. (2013)	Modeling Historical SN Distribution

ccSN Rate [$(100yr)^{-1}$]	Source	Method
≈ 2.5	Smith et al. (1978)	Lyman Continuum
3.4 ± 2.0	van den Bergh & Tammann (1991)	Galactic Remnant Count
1.7 ± 0.9	Cappellaro et al. (1993)	Blue Band Luminosity Relation
$2.5^{+0.8}_{-0.5}$	Tammann et al. (1994)	Historical Galactic SN
≈ 2	McKee & Williams (1997)	Free-free emission
1.5 ± 0.5	Reed (2005)	Massive Star Census
1.9 ± 1.1	Diehl et al. (2006a)	^{26}Al Decay Radiation
2.30 ± 0.48	Li et al. (2011)	Extragalactic ccSN Rate
$3.2^{+7.3}_{-2.6}$	Adams et al. (2013)	Modeling Historical SN Distribution

the assumed morphology of the emission. For example, Pleintinger et al. (2019) find, that neglecting potential foreground emission, either from close by star groups or recent SN activity in the sun's vicinity, leads to a significant overestimate of the ^{26}Al content.

With a half lime of 717 kyr (NNDC 2020), ^{26}Al traces the history of nucleosynthesis over the last several millions of years. As this thesis is dedicated to young SNRs, the Galactic emission of ^{44}Ti is utilized as a tracer for the recent Galactic SN activity. Due to the short half-life of this isotope, observation of the ejected ^{44}Ti is only possible with current instruments on timescales, when is has not yet mixed back into the ISM. Therefore, the decay radiation of this isotope should only be detectable in individual point sources on the sky. An analysis of the Galactic plane emission, separated into individual spot like emission regions is conducted in section 5.2. This snapshot of the current Galactic ^{44}Ti decay emission reflects the SN activity in the Galaxy over the last few hundred years. Nevertheless, this present day snapshot traces the formation of stars and their eventual demise in SN explosions over the last several millions years, as the delay time for a ccSN explosion after star formation is at least 10 Myr for an explodability cut off at $M_{ZAMS} = 25\,M_\odot$ (e.g. Limongi & Chieffi 2018) .

2.6.3 Constraining the Galactic Supernova Rate

One way to constrain the Galactic SN rate is to compare the observed current day snapshot of ^{44}Ti emission with theoretical predictions of how ^{44}Ti bright SNRs are distributed in the

Galaxy. Studying the theoretical distribution morphology of these remnants in dependence on their Galactic latitude and longitude allows to draw a wide range of conclusions about their detectability with current γ-ray instruments and whether ^{44}Ti producing explosions are a rarely occurring phenomenon or can be expected on a regular basis. In this thesis, the Galactic population synthesis code (PSYCO; Pleintinger 2020) is utilized to simulate the distribution of SNRs in the Milky Way. This code is developed to trace the evolution of stars from their formation in star clusters to the eventual demise of the clusters star content in ccSN explosions. PSYCO is particularly developed to trace the distribution of the stars radioactive ejecta (^{26}Al, ^{44}Ti, ^{60}Fe) in the Galaxy. The fundamental ingredients in the codes framework are the IMF, distributing star forming mass into individual stars, the ECMF, governing the mass distribution of star clusters, and the global, Galactic SFR. As such a code is intended to produce a 3D distribution of SNR, the observer is tasked with the problem of how such a distribution is translated into a 2D distribution of ^{44}Ti bright spots in a survey of the Galactic plane, that carries no inherent information on the distance to the target. Utilizing the code in a Monte Carlo fashion, a large parameter space of input parameters can be tested for their compatibility with the observed sky. A detailed description of the PSYCO simulation framework is given in section 5.3.

PSYCO traces the evolution of stars in clusters, and therefore the distribution of SNRs in 3D space eventually follows the distribution of star forming regions in the Galaxy. As the Sun is positioned roughly 8.5 kpc from the Galactic center (Kerr & Lynden-Bell 1986), but located in the Galactic plane, the Milky Way cannot be observed face on and determining the distribution of star forming regions in not readily possible. The all sky emission of the Milky Way, i.e. the 2D projection of the 3D distribution of stars, as seen from the point of view of the solar system is shown in Figure 2.11. From this projection, the structure of the Milky Way can be described as consisting of a central, bright bulge region containing young stars, upon which an extended fainter emission region is present that contains mainly population II, i.e. old, stars (Gaia Collaboration et al. 2018). A thin disk containing young

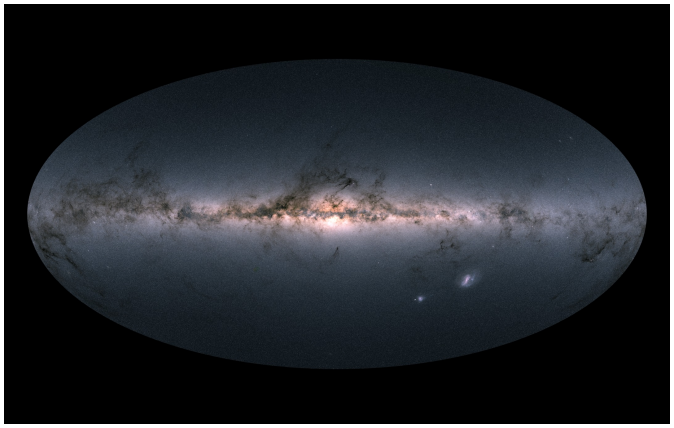

Figure 2.11: Gaia all sky map of the Milky Way obtained from measurements of 1.7 billion individual stars. The map shows the total flux measured in three bands. In the lower right quarter, the two neighboring galaxies LMC and SMC can be identified as bright spots. The Milky Way can be characterized by a bright central bulge region, and a thin, bright disk extending from the central bulge in both directions. The thin disk is surrounded by a fainter, thick disc component. Interstellar dust and gas coulds absorb the light of emission regions that are located behind the clouds, i.e. further away, leading to the dark patches in the image. Adopted from Gaia Collaboration et al. (2018).

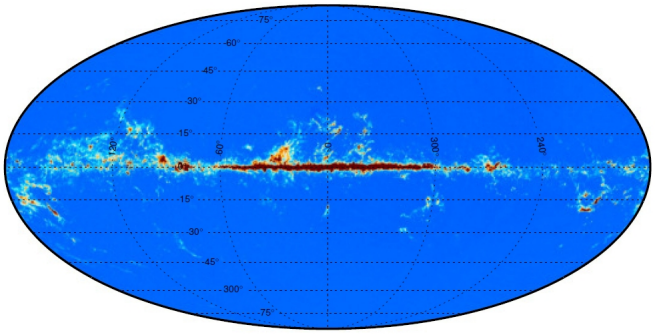

Figure 2.12: All-sky map of CO emission in the J = 1 → 0 transition. Adopted from Planck Collaboration et al. (2014).

stars extends from the central bright region, with a fainter thick disk, again containing old stars. The bright bulge region is associated with the Galactic Center region, while the thin disk component originates from the spiral arm structure that extends approximately 25 kpc from the Galactic center.
However, such a map projection does not contain any distance information, that is required to fully map star forming regions in the Milky Way in three dimensions. Such distance measurements are obtained from the parallax motion of individual objects (e.g. Reid et al. 2016, 2019), the Doppler shift velocities of molecular CO clouds (e.g. Dame et al. 2001), and by tracing the molecular H and CO distributions (e.g. Benjamin et al. 2005; Kennicutt & Evans 2012). The results of these measurements are summarized in the following. The Doppler shift of the CO line along the Galactic plane in combination with Galactic rotational models suggests, that the disk region is composed of four major spiral arms, named Perseus, Norma, Sagittarius-Carina, and Scutum-Centaurus. In addition, several spiral arm segments, or spurs, are present. In fact, the solar system is located in one of these spurs, named the Orion spur or local spur, in between the Sagittarius-Carina and Perseus main spiral arm. Despite this substructering, the density of star forming regions in the local spur is similar to the density of star forming regions in the neighboring main spiral arm Perseus. This Dopplershift determined structure of the Galactic disk is supported by the parallax determined distances to star forming H regions along the tangents of the spiral arms. Considering that star formation in the Milky Way occurs in molecular clouds, the density distribution of CO and H regions in the Galaxy also determines the surface density of star formation in the Galaxy. From the density distribution of CO emission regions in the outskirts of the spiral arms, Kennicutt & Evans (2012) determine an active star forming region that extends out to a radius of $r_{SF} = 13.5$ kpc from the Galactic center. In the Galactic center region, the density distribution of molecular H_2 regions can be modeled with an exponential disk with scale radius $r_s = (3.6 \pm 0.9)$ kpc (Benjamin et al. 2005). In addition, an overabundance of stars in one hemisphere in the central region was identified. This can be explained by an elongated, linear central bar structure with a radius of $r_{bar} = (4.4 \pm 0.5)$ kpc. The overabundance in one hemisphere originates from the inclination of the bar by an angle of $\theta_b = 44° \pm 10°$ with respect to the viewing direction from the solar system to the Galactic Center. A recent study (Wegg et al. 2015) suggests a slightly longer bar with $r_s = (4.6 \pm 0.3)$ kpc, that is however less inclined with an angle between $28° \leq \theta_b \leq 33°$.
And independent way of determining the distribution of star forming regions in the Galaxy is by tracing the distance to radio pulsars. As these result from the explosion of massive stars,

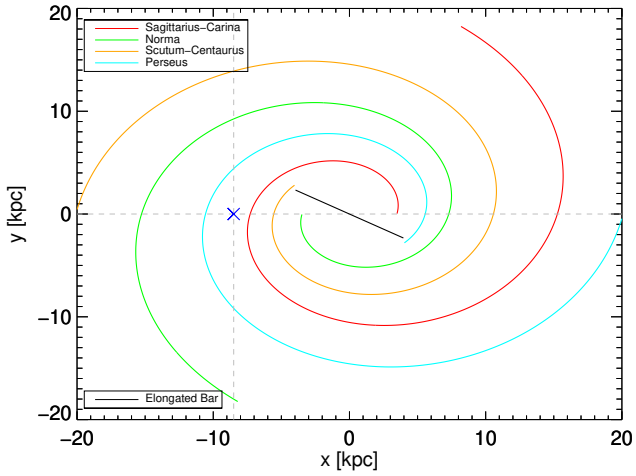

Figure 2.13: Schematic face-on structure of the Milky Way Galaxy. The spiral arm structure follows the description of the four major spiral arms in the Galaxy by Faucher-Giguere & Kaspi (2006). The central bar structure is indicated as a one dimensional structure with an inclination of 30.5° with respect to the connecting line (grey dashed line) of the observer at Earth (blue cross symbol) with the Galactic Center (Wegg et al. 2015). The sun is located at 8.5 kpc from the Galactic center in the local spur between the Sagittarius-Carina and Perseus main spiral arm.

their distribution in the Galaxy serves as a tracer of recent star formation. The distance to the radio pulsars is determined from the variation of their pulse frequency, as this is modulated by the propagation of the radio signal in the ISM (Rickett 1990; Taylor & Cordes 1993). Faucher-Giguere & Kaspi (2006) utilize this relation to construct a model of the spiral arm structure of the Galaxy.
A schematic plot, indicating the major features of the above described Galactic structure, is shown in Figure 2.13.

2.7 Nuclear De-Exitation Lines from Cosmic Ray Interaction

2.7.1 Diffusive Shock Acceleration

After decades of extensive observational and theoretical studies, the origin of CRs is still a central problem in high energy astrophysics. The differential energy spectrum of CR's above ≈ 10 GeV can be approximated by a power law with an index of -2.8 (cf. Figure 2.14 and Helder et al. 2012), which reaches up to the highest detected CR energies of $\approx 10^{21}$ eV. However, the overall spectral shape can be substructured into several distinct regions, containing a *knee* and *ankle*. In the energy range between GeV and several PeV, the spectrum is best described with a power law with index -2.7, above which it steepens to a power-law index of -3.1. This characteristic break is typically referred to as the *knee* of the CR spectrum. This part of the spectrum extends up to roughly 10^{18} eV. Above this energy the spectrum flattens again. Above $\approx 10^{20}$ eV, the spectrum turns over and terminates. The second break

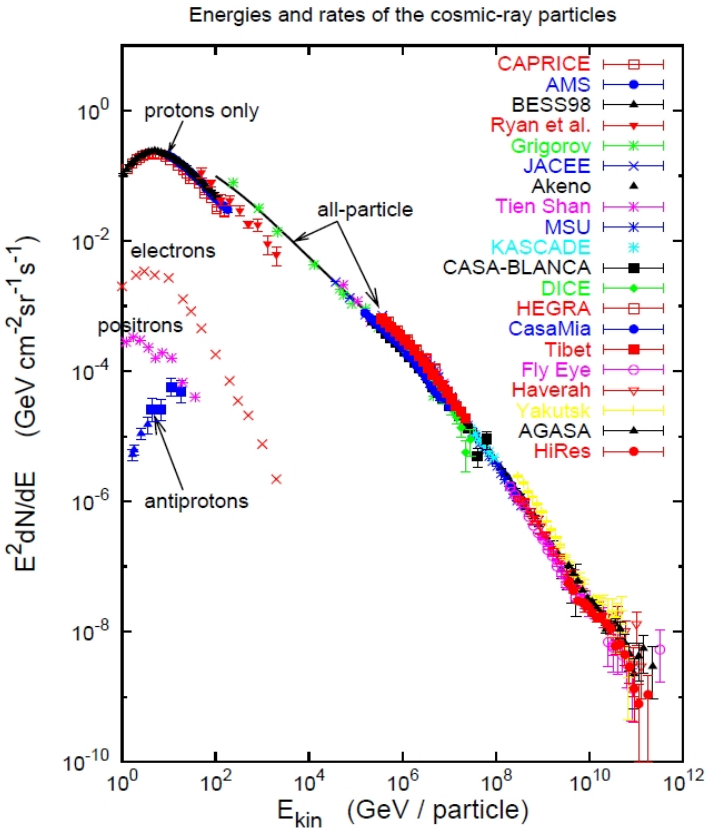

Figure 2.14: Compilation of CR measurements with various instruments. The CR spectrum can be best described by multiple power laws. CRs, commonly associated with SNRs are dominant up to the knee at $\approx 10^{15}$ eV, up to which the spectrum ray spectrum shows a power-law index of -2.7. Figure from Hillas (2006).

and flattening is typically called the *ankle* of the spectrum (Nagano & Watson 2000; Hillas 2006; Helder et al. 2012). Below GeV energies, the spectrum is not well known as it is strongly modified by solar modulation.
The CRs in the two distinct regions above and below the *knee* are considered to be of different origin. The gyro radius of protons is dependent on its energy. For protons with energies above the knee, the gyro radius is larger than the size of the Galaxy and they are consequently considered to originate from outside the Milky Way. In contrast, protons with energies below the knee have a gyro radius smaller than the extent of the Galaxy and must therefore originate in the Milky Way. Heavier nuclei can be accelerated towards higher energies even in the Milky Way, as the gyro radius is smaller for heavier nuclei with higher charge number with respect to protons of the same energy. However, the interstellar magnetic fields that lead to the residence of CRs in the Milky Way also deflect their flight path, so that CRs detected at Earth contain no information about the direction of their origin. For that reason, the determination of the Galactic CR sources relies on the detection of electromagnetic radiation, associated with the interaction of accelerated particles at the location of their acceleration (cf section 2.7.2).

SN explosions are considered as the dominant source of Galactic CRs with energies up to the *knee*. The argument for SNe is mainly based on the power required to maintain a constant

CR energy density in the Galaxy of $\approx 1\,\mathrm{eV\,cm^{-3}}$ (Castellina & Donato 2013). The average residence time of CRs in the Galaxy, i.e. the average time to diffuse out of the Milky Way, is approximately 15 Myr (Yanasak et al. 2001). This results in a required power of $\approx 10^{41}\,\mathrm{erg\,s^{-1}}$. With an average kinetic energy of 10^{51} erg and an average recurrence rate of 2–3 explosions per century (cf. table 2.3), the average total power of SNe can be estimated to be $\approx 10^{42}\,\mathrm{erg\,s^{-1}}$. For an average efficiency of transferring 10% of the explosions' kinetic energy into acceleration of particles, SNe can fully account for the energy balance of Galactic CRs (Helder et al. 2012). As the CR spectrum follows a steep power law, the majority of the energy density is contributed by low energy CRs (LECR). Due to solar modulation, this part of the CR spectrum is not well known, which reflects in an uncertainty of the total CR energy content.

The detailed acceleration mechanisms in SNRs are a matter of debate, however it is believed that the efficiency for particle acceleration is highest in the early remnant phases (Vink 2011). Besides SNRs, several studies suggest, that the Galactic CR content is produced by the collective acceleration of particles in several sites containing SNRs, the shocks of stellar winds in star forming regions and acceleration in flares of red dwarf stars (Parizot et al. 2004; Sinitsyna et al. 2019).

The general mechanism considered for acceleration of particles in shocks is the *diffusive shock acceleration* (DSA). Charged particles that are injected into the shock region can scatter of magnetic field irregularities, producing a random walk of the particles' trajectories that lead to multiple crossings and recrossings of the shock front. The energy gain of the particles per shock crossing is dependent on the shock velocity via the relation $\Delta E/E \propto v_s/c$, where v_s is the shock velocity. The DSA theory is favored, as it naturally produces a differential energy distribution of accelerated particles that follows a power law. The spectral shape can be derived by solving the Boltzmann equation of CRs in the vicinity of the shock front (macroscopic approach; Blandford & Ostriker 1978; Bell 2013), or following the random walk trajectory of a single CR particle (microscopic approach; Drury 1983).

The spectrum of the accelerated particles in the microscopic approach can be derived as described in the following. The derivation of the spectral shape was first introduced by Bell (1978), and requires several key assumptions. The accelerated test particles (electrons, protons, ions) exert no pressure on the medium and do not influence the hydrodynamics of the plasma. The magnetic field lines are parallel to the shock normal and the shock is planar. The velocity of the test particles is assumed to be significantly higher than the velocity of the shock. Small angle scatterings of particles on magnetic field irregularities lead to an isotropic particle distribution in the rest frames of the shock, of the upstream and of the downstream regions. The velocity of the shock is non-relativistic.
The velocity of flows in the up- and downstream region is described in the shocks rest frame with u_1 and u_2, respectively, as indicated in Figure 2.15. The number of particles that are advected with the medium in the downstream region and do not return to the upstream region is nu_2, where n is the number density of particles with velocity v in the local restframe. In an isotopric medium, the number of particles approaching and traversing the shock front per unit time is half the number of particles n. The average projected velocity in the local fluid frame is $v/2$, such that the flux over the shock is $nv/4$. The probabilities for not returning to

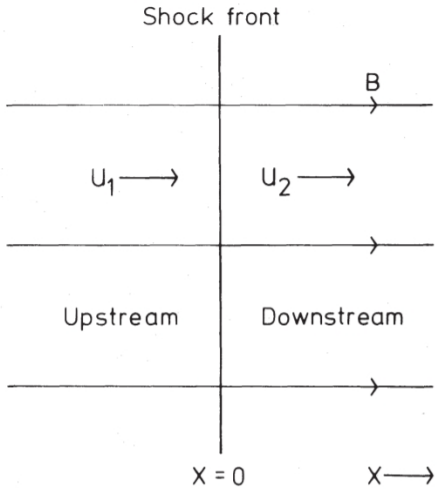

Figure 2.15: Schematic drawing of a planar shock depicted in the rest frame of the shock adopted from Bell (1978).

the upstream region and for an additional crossing are then given by

$$P_{return} = \frac{nu_2}{\frac{nv}{4}} = \frac{4u_2}{v} \tag{2.34}$$

$$P_{cross} = 1 - \frac{4u_2}{v}. \tag{2.35}$$

With the assumption that $u_2 \ll v$, the probability is high that particles cross the shock several times. After k cycles of crossing and recrossing the shock, the number of particles is

$$N = N_0 \left(1 - \frac{4u_2}{v}\right)^k, \tag{2.36}$$

where N_0 is the initial number of particles. The particles change in momentum with respect to the local fluid frame is (Schure et al. 2012)

$$\Delta p = p\frac{2(u_1 - u_2)}{3v}. \tag{2.37}$$

For a full cycle the total change in momentum is twice as described in the equation. The full momentum gain after k cycles is

$$\Delta p_{tot} = p_0 \left[1 + \frac{4}{3v}(u_1 - u_2)\right]^k, \tag{2.38}$$

where p_0 is the initial particle momentum at injection into the cycle. Utilizing the assumption that $v \gg u_1, u_2$ gives

$$\frac{\ln\left(\frac{N}{N_0}\right)}{\ln\left(\frac{p}{p_0}\right)} = \frac{k\ln\left(1 - \frac{4u_2}{v}\right)}{k\ln\left(1 + \frac{4}{3v}(u_1 - u_2)\right)} \approx \frac{-\frac{4u_2}{v}}{\frac{4}{3v}(u_1 - u_2)} = \frac{-3}{r - 1}, \tag{2.39}$$

where $r = u_1/u_2$ is the compression ratio of the shock. The particle number in terms of momentum follows with

$$\frac{N}{N_0} \propto \left(\frac{p}{p_0}\right)^{\frac{-3}{r-1}}. \tag{2.40}$$

The differential particle spectrum in momentum is

$$\frac{dN}{dp} \propto p^{-\frac{r+2}{r-1}}. \tag{2.41}$$

With a compression ratio of $r = 4$ for shocks with a high Mach number, the spectrum follows a power law with index -2. For highly relativistic energies, this translates into a differential proton spectrum in energy that also follows a power law with index -2. The fact, that DSA naturally produces an energy spectrum for CRs that follows a power law is the reason, why the theory is widely applicable to various scenarios where strong shocks are present in astrophysical situations. The compliance between observations and the predicted spectrum is notable. Even though a deviation between the Galactic CR spectrum with a power-law index of -2.7 and the theoretical prediction of -2 exists, this deviation might be explained by the propagation of CRs in the Galaxy. The situation, however, complicates, when feedback from the accelerated particles on the shock is taken into account, which is referred to as non linear CR acceleration. In the situation, where particle acceleration is highly efficient, the pressure exerted on the shock can alter the compression ratio at the shock, which can lead to a flattening of the high energy and a steeping of the low energy CR spectrum. Non linear DSA is further discussed in Ellison et al. (2000); Reynolds et al. (2008); Vink (2011); Caprioli et al. (2011).

2.7.2 Electromagnetic Radiation from Cosmic Ray Interactions

In addition to the direct detection of the Galactic CR particles, their interaction with the surrounding medium at their accelerations sites produces a characteristic electromagnetic emission that can be associated with their respective place of origin.

While a direct link for the acceleration of electrons in SN shocks seems well established due to observed synchrotron emission from a non thermal population of electrons (Medd & Ramana 1965; Allen & Barrett 1967; Parker & Shakeshaft 1968; Bell et al. 1975; Hales et al. 1995; Zirakashvili et al. 2014), a direct link between the acceleration of protons and ions in SN shocks is not confirmed. The signature for the hadronic CR components can be found in γ-ray observations with energies up to 100 TeV. In the GeV to TeV energy region, it is expected that either the majority or at least a part of the total emission of γ-rays is contributed by the decay of neutral pions. These pions are produced in the interactions of accelerated protons with the ambient, cold gas. The production of γ-rays thereby follows the production chain of

$$p + p \rightarrow p + n + \pi^+ \tag{2.42}$$

$$p + p \rightarrow p + p + \pi^- + \pi^+ \tag{2.43}$$

$$p + p \rightarrow p + p + \pi^0 \tag{2.44}$$

$$\pi^0 \rightarrow \gamma + \gamma. \tag{2.45}$$

The threshold for neutral pion production is a kinetic proton energy $E_{kin} \geq 280\,\mathrm{MeV}$, which is roughly twice the rest mass energy of a neutral pion. In general, the production of neutral pions in a proton-proton collision is only weakly dependent on the protons kinetic energy above several GeV (Norbury 2009) with

$$\sigma_{pp\rightarrow\pi^0}(E_p) = \left(0.007 + 0.1\frac{\ln E_{kin}}{E_{kin}} + \frac{0.3}{E_{kin}^2}\right)^{-1}\,\mathrm{mb}. \tag{2.46}$$

As the average pion kinetic energy can be approximated by $E_{kin,\pi} = \kappa_\pi E_{kin}$ (Dicke & Marshall 1943), it follows that the pion spectrum has a similar shape as the parent proton spectrum. The π^0 decay is a one body decay, which requires that in the rest frame of the π^0 the two γs are produced back to back, which leads to bump like feature in the γ-ray spectrum at $E_\gamma = m_{\pi^0}c^2/2 = 67.5\,\mathrm{MeV}$. The high energy spectrum above the bump feature follows the initial particle distribution and is consequently related to the incident proton spectrum.

However, two leptonic γ-ray emission processes are potentially competing with the π^0 decay emission in SNRs at GeV and TeV energies. Bremsstrahlung from the non thermal distribution of accelerated electrons is emitted by the interaction of electrons with ambient electrons, protons and helium ions. This emission can be characterized for the most abundant ambient material with

$$\frac{dn_\gamma(E_e, E_\gamma)}{dt} = v_e\left[(n_p + 4n_{He})\sigma_{e,p}(E_e, E_\gamma) + n_e\sigma_{e,e}(E_e, E_\gamma)\right], \tag{2.47}$$

where v_e is the relative collision velocity, n_e, n_p, n_{He} are the densities of ambient electrons, protons, and helium ions and $\sigma_{e,p}, \sigma_{e,e}$ are the cross sections for electron-ion and electron-electron interactions differential in photon energy. The first is dependent on the charge number of the ion with Z^2, leading to the factor $n_p + 4n_{He}$.
In addition, inverse Compton scattering (cf. 3.1.1) of electrons on ambient infrared photons and cosmic microwave background photons can contribute to the γ-ray emission above several GeV.

2.7.3 Electromagnetic Broadband Emission in Cassiopeia A From CRs

The correlation between a SNR and the emission of photons due to CR interaction was first established in Cassiopeia A (Cas A). Observations in the radio wavelength band showed a bright emission region $\approx$ 1.7 pc offset from the remnants center and a second plateau like emission at $\approx$ 2.5 pc radius (Medd & Ramana 1965; Allen & Barrett 1967; Parker & Shakeshaft 1968; Bell et al. 1975; Hales et al. 1995; Zirakashvili et al. 2014), which is complemented by the emission from several bright knots (Anderson et al. 1991). It is assumed that the outer emission ring is from the forward shock while the bright inner emission is related to the reverse shock region. The emission in the radio wavelength regime is attributed to synchrotron emission from a non-thermal distribution of electrons, which should extend up to several hundred keV (c.f. Figure 2.16). Indeed, a hard X-ray continuum was observed, ranging up to $\approx$ 300 keV (Vink et al. 2001; Renaud et al. 2006; Maeda et al. 2009), substantiating the synchrotron nature. However, due to the limited angular resolution of these observations, the location of the emission could not be attributed to either the forward or reverse shock. Observations in the lower keV region with the Chandra satellite (Patnaude

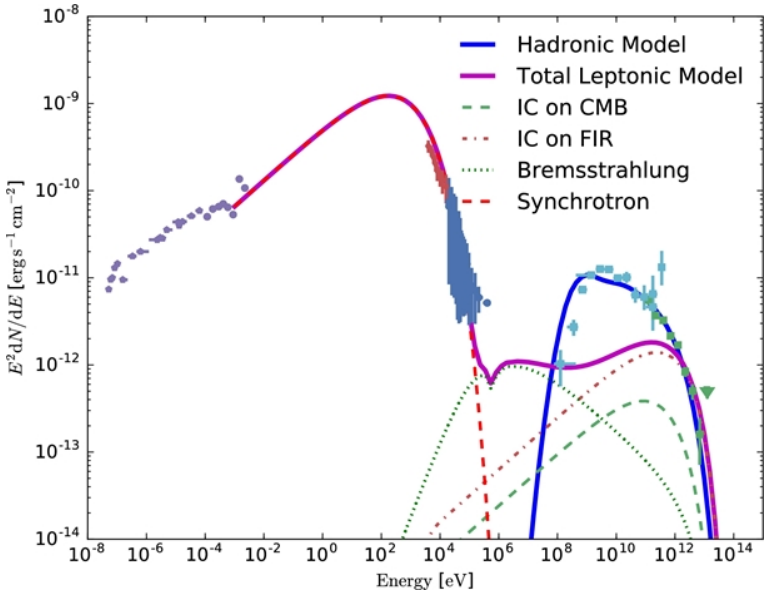

Figure 2.16: Broadband photon spectrum of Cas A from CR interactions. The different lines show the results for fitted models of a leptonic or hadronic photon emission in the GeV and TeV regime. Figure adopted from Ahnen et al. (2017).

& Fesen 2009) and more recently with NuSTAR (Grefenstette et al. 2015) identified synchrotron emission regions both in the forward as well as the reverse shock region, which was not considered an effective accelerator for electrons before. However, the magnetic field at the reverse shock, otherwise considered too weak for effective acceleration, can be significantly amplified (Ellison et al. 2005).

The excess flux in the GeV to TeV regime, as seen in Figure 2.16, from Cas A is commonly attributed to the emission from accelerated protons that produce neutral pions in interactions with the ambient medium (Abdo et al. 2010; Araya & Cui 2010; Yuan et al. 2013; Zirakashvili et al. 2014; Ahnen et al. 2017). The high energy γ-ray emission in the energy region above 60 MeV can be reproduced assuming a single power-law distribution of accelerated protons with a best fit index of 2.2 (Ahnen et al. 2017) for an ambient particle density of 10 cm^{-3} (Laming & Hwang 2003). However, the γ-ray emission also suggests an exponential high energy cut-off of the proton spectrum above 12 TeV, which shows that Cas A is very inefficient at accelerating particles to very high energies, and cannot explain particle acceleration up to the knee in the CR spectrum. This implies that the integral energy content of protons above 100 MeV amount to $\approx 5\%$ of the SNR kinetic energy of 2×10^{51} erg.

2.7.4 Production of Nuclear De-Excitation Lines by CR Interactions

Unlike in the highest γ-ray regime where the emission mechanism cannot be distinguished, nuclear transition lines in the hard X-ray to soft γ-ray regime can be distinctively linked to a hadronic component in CRs at their acceleration site. Interactions from energetic protons and ions in CRs with the ambient medium is expected to produce nuclear de-excitation lines in the energy range between tens of keV and $\approx$ 20 MeV in several ways. The emission of these nuclear de-excitation lines has been observed during solar flares, producing a wealth

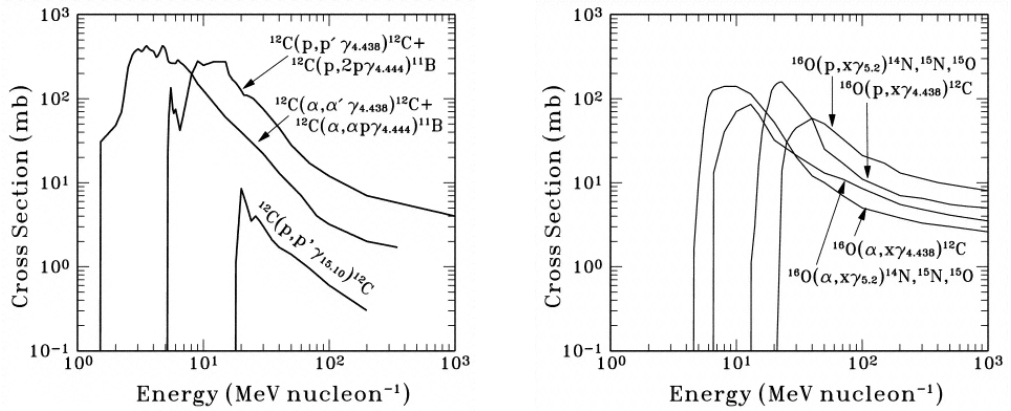

Figure 2.17: Measured cross sections for the production of the 4.438 MeV $^{12}C^*$ de-excitation line. Left: Inelastic scattering and spallation cross section of proton and α-particle interaction ^{12}C. Cross section measurements cannot distinguish between 4.438 MeV $^{12}C^*$ and 4.445 MeV $^{11}B^*$ line. Right: Cross section of spallation from bombardment of ^{16}O with protons and α-particles. Figures adopted from Kozlovsky et al. (2002).

of information on the composition of CRs and solar abundances (Murphy et al. 1996; Vestrand et al. 1999). Particle collisions can directly excite nuclear levels in the target nuclei or produce excited states in a secondary particle. Secondary particles can also include radioactive nuclei, that decay into an excited state of the daughter nucleus. Such isotopes can also be β^+ unstable, leading to the emission of a positron in the decay that later annihilates in the interstellar medium.

The essential reactions for the production of nuclear lines can be described by

$$^{n}A(p,\gamma)^{n+1}D \tag{2.48}$$

$$^{n}A(x,x')^{n}A^* \rightarrow {}^{n}A + \gamma \tag{2.49}$$

$$^{n}A(x,x'y)^{m}D^* \rightarrow {}^{m}D + \gamma \tag{2.50}$$

where the first equation is the thermonuclear capture of protons on a target nucleus, while the remaining two equations are the direct excitation of a nuclear level in the target nucleus A and the spallation of the target into a secondary nucleus D. The latter can be radioactive and decay further emitting a photon in the process. In the equation, n and m, are the mass number of the respective nucleus, x commonly are either protons or fully ionized helium, and y are the spallation products ejected from A. As the thermonuclear capture of protons on nuclei and the subsequent emission of photons is mainly governed by the electro-weak force, the cross sections for these respective reactions are typically orders of magnitude lower than the direct excitation of nuclear states by inelastic scattering. The latter reaction is governed by the strong nuclear force and is by far dominant in the energy regime of the accelerated, non thermal distribution of proton and helium kinetic energies (Tatischeff 2003).

In SNRs, some of the strongest lines from CR excitation are expected be produced from the interaction with the most abundant, ambient isotopes with Z > 2, which are ^{16}O and ^{12}C. A multitude of γ-ray lines are produced from the interaction of CRs with both isotopes. Here, the de-excitation line of ^{12}C at 4.438 MeV is considered, which is the first nuclear excitation

level of the respective nucleus. In general, nuclear transitions in inelastic scatterings as well as spallation reaction are mainly excited from low energy CRs (LECRs) in the energy range below 100 MeV/nucleon. Above that energy, the cross sections decrease by more than two orders of magnitude with respect to CR energies of ≈10 MeV/nucleon. In Figure 2.17, the cross sections for the excitation of the 4.438 MeV line of ^{12}C by proton and α-particle interactions are shown. The same figure also includes the spallation reaction of ^{12}C(p,2pγ)^{11}B, emitting a γ-ray at 4.445 MeV. These reactions cannot be seperated in cross section measurements, due to the kinematic broadening of the recoiling nucleus. In addition, a strong contribution to the ^{12}C line at 4.438 MeV is made by the spallation reactions on ^{16}O(x, x$'\alpha$)^{12}C*. The cross section for this reaction is also shown in 2.17, which again shows a strong peak at LECR energies and a strong decrease in cross section for higher energies. While some of the nuclear reactions have large cross section extending up to incident particle energies of several GeV, the majority of reactions contain a peak in cross section below 100 MeV, strongly declining by several orders of magnitude with increasing energy (Ramaty et al. 1979; Kozlovsky et al. 2002, and references therein). As the ^{12}C line at 4.438 MeV can be excited both from direct interaction with ^{12}C as well as spallation on ^{16}O, it is expected to be the strongest emission line related to CR excitation in SNRs. A detailed list of line transitions from CR interactions in SNRs can be found in Appendix A.

2.7.5 Spectral Shape of Nuclear De-Excitation Lines

In general, the decay of an excited nuclear state would produce a very narrow decay line, that can be described by a Lorentz profile. The width is thereby only given by the uncertainty principle, governed by the mean lifes of the excited state given in Table A.2, which amounts to $\lesssim$ 1 eV for the prompt de-excitation lines. However, due to the propagation of the recoiling target nucleus kinematic effects can broaden the decay line. The basic calculations for determining the γ-ray spectral shape take into account the following considerations (Ramaty et al. 1979). The probability of photon emission from a prompt de-excitation line into the solid angle dcos(θ_0)dϕ_0 following the interaction of a particle p with energy E_p on a target nucleus A* recoiling into the solid angle d cos(θ^*_{rec})dϕ_{rec} is given by

$$dP_\gamma = n_c \, v \frac{d\sigma}{d\Omega^*}(E_{rec}, \theta^*_{rec}) d\cos(\theta^*_{rec}) d\phi_{rec} \times g(E_p, \theta^*_{rec}, \theta_0, \phi_{rec} - \phi_0) d\cos(\theta_0) d\phi_0 \qquad (2.51)$$

in the reaction's center of mass frame. Here, n_A is the particle density of the target nuclei A, v(E_p) is the velocity of the incident CR particle, $d\sigma/d\Omega^*$ is the differential cross section of the interaction in the center of mass frame. The angular distribution of photons is given by g, which depends on all variables in equation 2.51. The particles incident direction is taken to be the z-direction, i.e. the angle θ_0 and θ^*_{rec} are taken with respect to the z-axis and ϕ_0 and ϕ_{rec} are given in the x-y-plane with respect to the x-axis. Then the photon energy in the laboratory frame is given by

$$E_\gamma = \frac{E_0}{\gamma_{rec} - (\gamma^2_{rec} - 1)^{0.5} \cos(\theta_\gamma)} \qquad (2.52)$$

given from the variables $E_p, \theta^*_{rec}, \theta_0, \phi_{rec} - \phi_0$ through the set of equations:

$$\gamma_{rec} = \gamma_c \gamma^*_{rec} + (\gamma_c^2 - 1)^{0.5}(\gamma^{*2}_{rec} - 1)^{0.5} \cos(\theta^*_{rec}) \tag{2.53}$$

$$E_{rec} = m_p c^2(\gamma_{rec} - 1) \tag{2.54}$$

$$\cos(\theta_\gamma) = \cos(\theta_{rec})\cos(\theta_0) + \sin(\theta_{rec})\sin(\theta_0)\cos(\phi_{rec} - \phi_0) \tag{2.55}$$

$$\cos(\theta_{rec}) = \frac{\gamma^*_{rec}(\gamma_c^2 - 1)^{0.5} + \gamma_c(\gamma^{*2}_{rec} - 1)^{0.5}\cos(\theta^*_{rec})}{(\gamma^2_{rec} - 1)^{0.5}} \tag{2.56}$$

$$\gamma_c = \frac{E^2_{cm} + (m_A c^2)^2 - (m_p c^2)^2}{2 m_A c^2 E_{cm}} \tag{2.57}$$

$$\gamma^*_{rec} = \frac{E^2_{cm} + (m_\Delta c^2)^2 - (m_p c^2)^2}{2 m_\Delta c^2 E_{cm}} \tag{2.58}$$

$$E_{cm} = \left[(m_p + m_A)^2 c^4 + 2 m_A c^2 E_p\right], \tag{2.59}$$

where γ_c, γ^*_{rec}, and γ_{rec} are the velocity dependent Lorentz factors of the particle-target center of mass, and the Lorentz factor of the recoil target in the center of mass and the laboratory frame, respectively. The two angles θ_{rec}, and θ_γ are the angle between the incident and recoil direction of the incident particle in laboratory frame coordinates and the angle between the recoil target A and the emitted de-excitation photon in the laboratory frame, respectively. The masses m_p and m_A are the incident and target particle masses, $M_\Delta = m_A + \Delta E_{line}/c^2$ is the rest mass of the excited target nucleus including the level energy ΔE_{line}. The photon energy in the exited target frame is given by $E_0 = \Delta E_{line} \times [1 - \Delta E_{line}/(2 m_\Delta c^2)]$, due to the additional recoil of the target nucleus during photon emission.
The total γ-ray spectrum can then be obtained by integrating equation 2.51 over θ^*_{rec}, θ_0, ϕ_{rec} and energy E for example by using a Monte Carlo simulation. For that purpose, the four equations

$$R_1 = \frac{1}{\sigma(E)} \int_{-1}^{\cos(\theta^*_{rec})} \frac{d\sigma}{d\Omega^*} d\Omega, \tag{2.60}$$

$$R_2 = \frac{\phi_{rec}}{2\pi}, \tag{2.61}$$

$$R_3 = C \int_0^E v N_p(E')\sigma(E')dE', \tag{2.62}$$

$$R_4 = \frac{1}{2}(1 + \cos(\theta_0)) \tag{2.63}$$

need to be solved for θ^*_{rec}, θ_0, ϕ_{rec} and E by choosing independent random numbers R_{1-4} uniformly distributed between 0 and 1. In equation 2.62, C is a normalization constant and $N_p(E)$ are the number of incident protons per unit energy. The probability for observing a photon in the energy range $E_\gamma + \Delta E_\gamma$ is then given by the sum over all distributions g for which $E_{\gamma,obs}$ is in the interval. In this thesis, the Monte Carlo technique by Ramaty et al. (1979)[2] and Kozlovsky et al. (2002) is used.

[2]http://lheawww.gsfc.nasa.gov/users/ramaty/code.htm

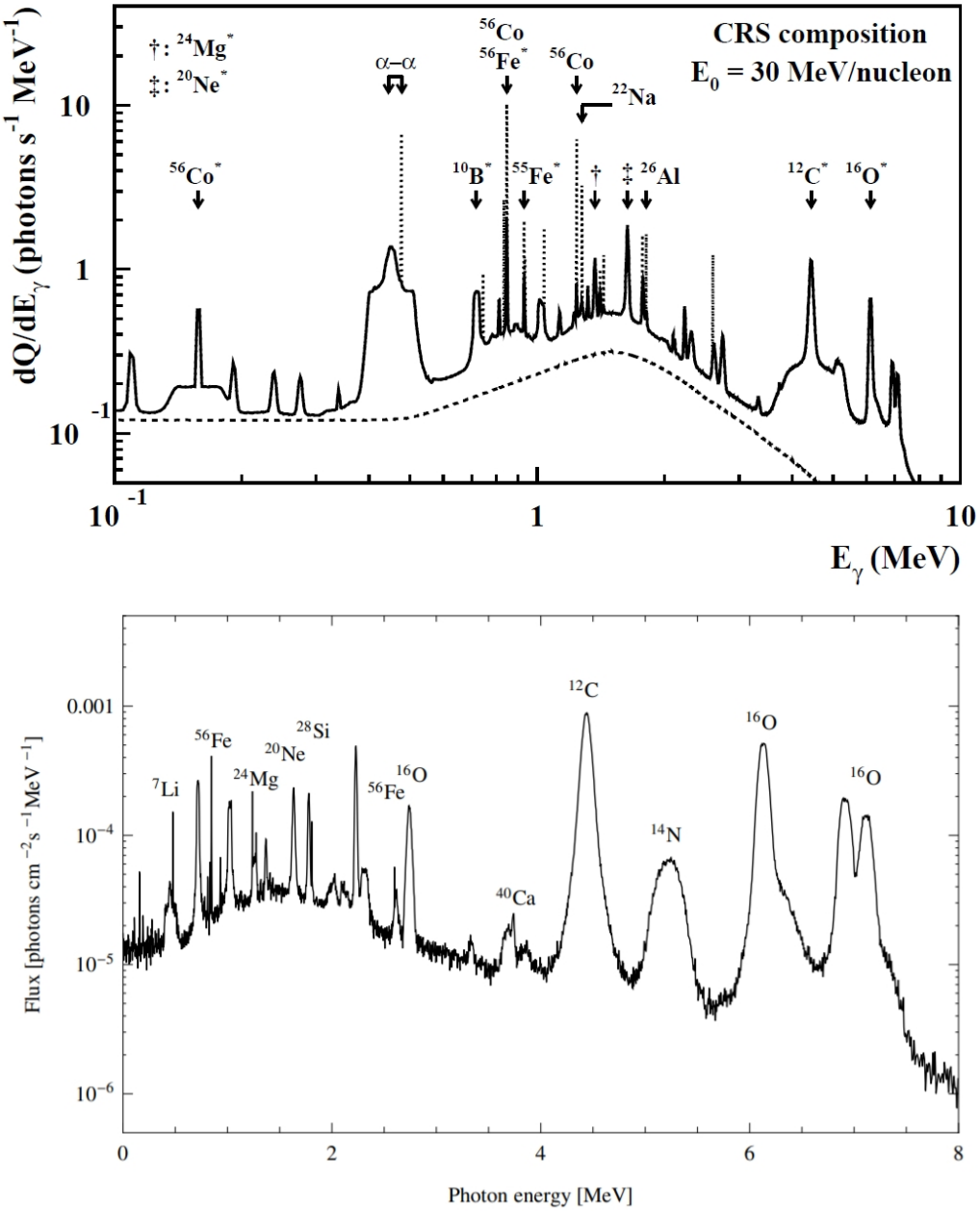

Figure 2.18: Simulated CR de-excitation spectrum at low γ-ray energies. Top: The γ-ray spectrum was produced assuming a ion source spectrum which follows $F_i \propto E_i^{-1.5} \exp(-E_i/E_{cut})$, where E_i is the kinetic energy of the ions and exponential cut-off E_0, assuming standard CR composition (Ramaty et al. 1996) and solar ambient abundances. Adopted from Tatischeff (2003). Bottom: Nuclear de-excitation spectrum for the specific case of the Cas A SNR ambient medium composition. The proton and ion source spectrum follows $F_p \propto E_p^{-2.2}$. Adopted from Summa et al. (2011).
The production of the different prompt de-excitation line features (broad, narrow) and the radioactive decay lines (narrow dotted) are discussed in the text. The dashed line represents the underlying superposition of unresolved broad lines from heavy nuclei.

In contrast to the total cross section, which is only dependent on the energy of the incident CR particle, the differential cross section in equation 2.51 can have a strong directional dependence, caused by the structure of the interacting nucleus. The differential cross section are commonly measured in collider experiments, where the target nuclei are irradiated with a monoenergtic, unidirectional beam. In a SNR however, irradiation of the target nuclei is isotropic as the CR particles have a randomized velocity distribution. Ramaty et al. (1979) have shown, that the de-excitation line profile from a large number of randomized incident particle directions and energies leads to a strong kinematic broadening of prompt de-excitation lines. In Figure 2.18, two simulated spectra of CR-induced de-excitation lines are shown, one for the typical CR composition with ambient medium of solar composition (Tatischeff 2003) and the second specific to the SNR Cas A (Summa et al. 2011). The spectrum contains a combination of both broad, narrow, and very narrow lines, that is superimposed on an underlying, continuum-like emission. The broad lines are produced from the de-excitation of nuclear states in accelerated (heavy) ions, that scatter of ambient protons and α-particles (cf. equation 2.48). As in this case, the kinetic energy of the ion is higher than from the inelastic proton scattering of the resting ion A, the resulting line is broader. However, the decay radiation from the majority of excited low energy levels in heavier ions cannot be resolved. The superposition of these decay lines leads to the underlying, continuum-like emission. The broad component is present for the majority of lines, such as the broad component of the $^{12}C^{*}$ de-excitation at 4.438 MeV ($\approx$ 1.5 MeV FWHM). The strongest narrow lines are produced from the low lying levels of the most abundant isotopes in the medium, which primarily are $^{56}Fe^{*}$,$^{24}Mg^{*}$,$^{20}Ne^{*}$,$^{12}C^{*}$ and $^{16}O^{*}$ at 847 keV, 1.37 MeV, 1.63 MeV, 4.44 MeV, and 6.13 MeV ordered by their γ-ray energy, respectively. Additionally, narrow lines are emitted from the spallation products of the abundant isotopes, e.g. from $^{55}Fe^{*}$ ($^{56}Fe(p, pn)^{55}Fe^{*}$) at 931 keV, or $^{15}N^{*}$ ($^{16}O(p, 2p)^{15}N^{*}$) at 5.27 MeV. The very narrow lines can originate from the decay emission of radioactive isotopes, produced in spallation reactions. As the half-lifes of some produced, radioactive isotopes are longer than the stopping time for the respective isotopes with average recoil energy $E_{rec,a}$ in the ambient medium, these isotopes can be slowed down before decaying. Hence, the nuclei are at rest with respect to the observer frame, producing a narrow decay line.

Chapter 3

γ-ray Measurements with the Spectrometer On INTEGRAL (SPI)

3.1 γ-ray Measurements

3.1.1 Dominant Interactions of Light with Matter at γ-Ray Energies

The detection of high energy photons in the range of several keV up to several MeV, e.g. produced by nuclear de-excitations, is facilitated by measuring their energy deposition in a detector material. This process is governed by three dominant interactions of light with matter: photo(-electric) effect (Einstein 1905), Compton scattering (Compton 1923) and pair production (Oppenheimer & Plesset 1933).

In the photo-effect a photon is transferring its entire energy to the bound electron of an absorber material. The interaction takes place with the entire atom and the photon is absorbed in the reaction. A photo-electron is emitted from the absorbing atom. The kinetic energy of the photo-electron is identical to that of the incident photon energy, corrected for the binding energy of the electron in its bound state. The cross section for the photo-effect is

$$\sigma = \kappa \frac{Z^a}{E^b}, \tag{3.1}$$

where E is the energy of the incident photon and Z is the charge number of the absorbing material. The factors a and b are energy dependent factors. For low energies a = 4 and b = 3, and a = 5 and b = 1 for high energies. This transition occurs because above material specific energies, excitation of electrons from the inner L-, M- and K-shell become possible.

For incident photon energies of $E_\gamma \approx 511\,\mathrm{keV}$, equal to the electron rest mass energy, the dominant interaction of photons with detector material is Compton scattering. The incident photon scatters inelastically of a charged particle, predominantly an electron, transferring energy and momentum to it. In this process the photon always retains energy and is not completely absorbed. The energy of the scattered photon can be determined from the laws of energy and momentum conservation:

$$E'_\gamma = \frac{E_{\gamma,0}}{1 + \frac{E_{\gamma,0}}{m_0 c^2}(1 - \cos(\theta))} \tag{3.2}$$

where E'_γ and $E_{\gamma,0}$ are the energy of the scattered and the incident photon, respectively. The rest-mass energy of the recoil electron is $m_e c^2$, and θ is the scattering angle with respect to the incident photon's direction. For small angles, only little energy is transferred while the maximum energy is transferred for back scattering ($\theta = 180°$). The differential cross section is given by the Klein-Nishina cross section (Klein & Nishina 1929):

$$\frac{d\sigma}{d\Omega} = \frac{r_0^2}{2}\left(\frac{E'_\gamma}{E_{\gamma,0}}\right)^2\left(\frac{E'_\gamma}{E_{\gamma,0}} + \frac{E_{\gamma,0}}{E'_\gamma} - \sin(\theta)^2\right) \tag{3.3}$$

where $r_0 = \hbar c\alpha/m_e c^2$ is the classical electron radius and α is the fine structure constant. With increasing energy the differential cross section shows an increasing tendency to forward scattering of the photons, especially for photon energies above 500 keV.

For photon energies above 1.022 MeV, i.e. twice the rest energy of an electron, pair production can occur. The name is derived from the process in which an electron-positron pair is produced when the incident photon interacts with an electric field. A third charged particle is required in the interaction as the conservation of both energy and momentum cannot be ensured in vacuum. In a detector, this role can be fulfilled by the nuclei with charge number Z of the detector material, where the photon interacts with the nucleus' Coulomb field. The cross section of the process can be approximated with

$$\sigma_l = \frac{1}{12}\alpha\pi r_0^2 Z^2\left(\frac{E_{\gamma,0}}{m_e c^2} - 2\right)^3 \tag{3.4}$$

in the low energy regime near the production threshold and with

$$\sigma_h = \alpha r_0^2 Z^2\left[\frac{28}{9}\ln\left(\frac{2E_{\gamma,0}}{m_e c^2}\right) - \frac{218}{27}\right] \tag{3.5}$$

in the high energy limit (Jauch & Rohrlich 1976). As a consequence of the cross sections Z^2 dependence, the pair production becomes increasingly important at high energies for detector material with large charge number Z.
An overview of the energy dependent interactions strengths in a Ge detector is given in Figure 3.1.

3.1.2 γ-ray Detectors

Detectors that are commonly used in γ-ray missions are either composed of a scintillator or semiconductor material. 1) In scintillators an excitation of an electron from the valence to conduction band is induced by the interaction with the incident photon. The produced electron-hole-pair recombines after a short period of time, emitting a less energetic photon. The energy of the photons can be outside the optical band. Impurities are injected into the pure scintillator crystals for more efficient and faster trapping of the electron hole pairs. The injected type of impurities is commonly chosen such that forbidden states in the energy gap of the pure scintillator crystal can be populated, which yields scintillation light in the optical or ultraviolet band. Due to the large band gap, the intrinsic light output of scintillators for γ-ray photons is comparably low. The efficiency for producing secondary photons varies between 7 and 10 photons per keV incident γ-ray energy which leads to a low energy resolution of scintillator detectors. The scintillators are coupled with photo-multiplier

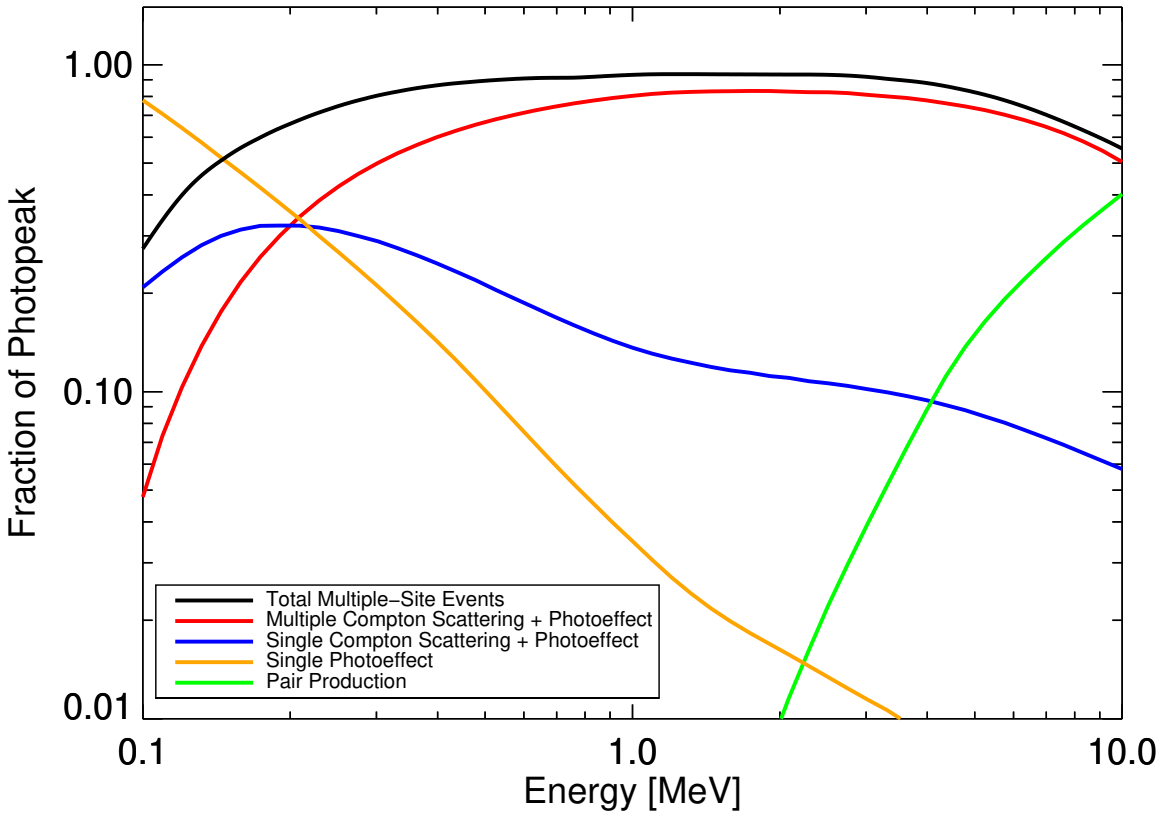

Figure 3.1: Relative strength of principal interactions of γ-rays with a Ge detector given as fraction of the full energy peak. Interaction probabilities are calculated from a Monte Carlo simulation of photon interaction with a 6 cm×6 cm high purity Ge detector. Image adopted from Roth et al. (1984). Single photo-effect is the dominant mechanism only below $\approx$ 140 keV.

tubes (PMTs), that translate the re-emitted photons into an electronic signal. The energy resolution of a scintillator detector is governed by the low light output and the statistical amplification of the primary signal in the first layer of the PMT, which typically result in a low energy resolution of $\approx$ 10% over the scintillators energy range. In addition to a poor energy resolution, organic scintillators have a low density, resulting in a small interaction probability of photons with the detector. The stopping power is low. Scintillator detectors are therefore not ideal for astrophysical high resolution spectroscopy. Nevertheless, due to the fast emission of fluorescence photons and amplification in PMTs, plastic scintillators are commonly used as anti-coincidence shields (Lichti & Georgii 2001) in combinations with semiconductor detectors. Beside the other commonly used scintillators NaI, CsI ,and PWO, BGO crystals ($Bi_4(GeO_4)_3$) have the advantage of having a high density of 7.2 g cm^{-3} and contain material with a charge number $Z_{Pb} = 75$, resulting in a high stopping power for γ-rays.

2) To achieve the desired high energy resolution, semiconductor detectors are utilized. The incident photon creates electron hole pairs in the depletion zone of a dopted semiconductor detector, that can be artificially enlarged by applying an external high voltage. The absolute amount of produced charge carriers is proportional to the energy of the incident photon.

Due to the small energy band gaps of semiconductor materials (1.1 eV for Si, 0.7 eV for Ge), the amount of produced charge carriers per unit of incident photon energy is increased with respect to scintillators, yielding an energy resolution improved by at least one order of magnitude. In addition to the small band gap, Ge also has a high density of 5.3 g cm^{-3}, providing a high stopping power for photons up to several MeV. The primary interaction of incident photons with the detector occurs dominantely in the surface layers of the detector. The secondary electron traverses further through the depletion zone, producing additional electron hole pairs along its way. In a semiconductor detector, the charge carriers are collected at the surface mounted electrodes by applying an external high voltage. Due to the small band gap, thermal excitation of charge carriers in the semiconductor is possible at room temperature, leading to a leakage current in the detector. Therefore, these types of detectors are cooled to $\approx$100 K to reduce thermal leakage currents. The amount of charge carriers, that reach the electrodes, can be affected by impurities and defects in the semiconductor lattice structure, introduced e.g. by impinging CRs. The impact of prolonged exposure to particle irradiation in a space environment on the detector energy resolution is further discussed in section 4.1.2.

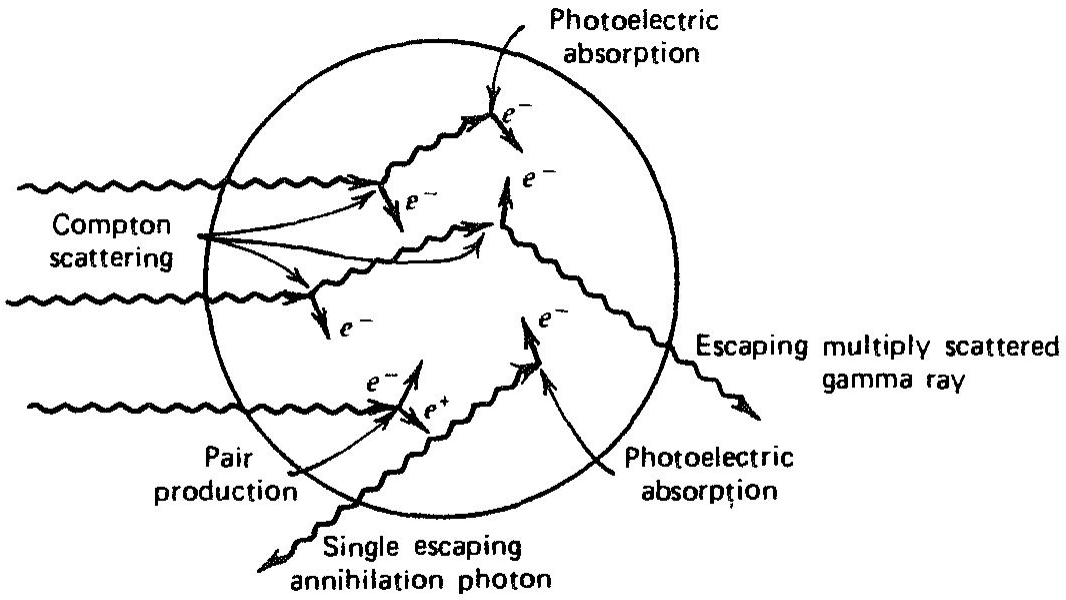

Figure 3.2: Interactions of photons with detector material. Probability for the various interactions depends on the volume of the detector and on the incident photon energy. Intermediate reactions such as emission and escape of secondary photons from electron synchrotron radiation are omitted. Image from Knoll (2010).

In a detector that utilizes the interactions of photons with absorber material described in the previous section, the energy of a single photon is not instantaneously deposited in the detector material in one interaction, but rather a cascade of interactions occurs, involving the primary photon as well as produced secondary particles. In an idealized, infinite detector energy deposition of a single photon is asymptotically complete, as the entire energy of the primary photon and all secondary particles remains within the detector volume, translating an incident energy spectrum exactly into the measured spectrum.

However, as indicated in the schematic diagram of the interaction and energy deposition of incident photons with the detector material in Figure 3.2, energy deposition can be incomplete, when the detection volume is finite. In general, the measured data can be described by the convolution of the incident energy spectrum with an energy dependent, detector specific response function with

$$D(E) = H(E) * R(E) = \int_0^\infty H(E')R(E - E')dE'. \tag{3.6}$$

Here D(E) is the measured photon spectrum at energy E, H(E) is the incident photon spectrum and R(E) is the detector specific response function. For semiconductor and scintillator detectors the response function in general contains three distinct features: a full energy peak, a Compton continuum and various escape peaks.

The full energy peak arises, when the entire energy of the incident photon is deposited in the detector volume. The entire energy is transferred to secondary charged particles in the detector volume, which in turn deposit their energy by production of subsequent electron hole pairs. The sharply defined energy of the incident photon is blurred by the detector response and appears as a broadened Gaussian in the measured spectrum. This broadening is the instrumental resolution at the incident energy and is solely governed by the stochastic process of charge carrier production in the detector.
The Compton continuum is produced by partial energy deposition of an incoming photon within the detector. The incident photon interacts only once with an electron in the detector and is scattered out of the detector volume, retaining the residual energy. The energy of the Compton electron can be derived from equation 3.2. No energy is transferred in forward scattering ($\theta = 0°$). Maximum energy transfer occurs during back-scattering ($\theta = 180°$), where the Compton electron's energy gain is

$$E_{e,max} = E_{\gamma,0} - E'_\gamma(\theta = \pi) = E_{\gamma,0}\left(\frac{\frac{2E_{\gamma,0}}{m_0c^2}}{1 + \frac{2E_{\gamma,0}}{m_0c^2}}\right). \tag{3.7}$$

In principle, this would lead to a sharp Compton edge in the measured spectrum, which is, however, again broadened by the instrumental resolution. The energy gap between the full energy peak and $E_{e,max}$ is given by

$$E_{gap} = E_{\gamma,0} - E_{e,max} = \frac{E_{\gamma,0}}{1 + \frac{2E_{\gamma,0}}{m_0c^2}} \quad . \tag{3.8}$$

For highly energetic photons with $E_{\gamma,0} \gg m_0c^2$ this reduces to $E_{gap} = m_0c^2/2$. The energy range between the full energy peak and the Compton edge is filled as multiple Compton scatterings of the same primary photon in the detector are possible, where each scattering deposits a partial amount of the total photon energy.
For incident photons energies above 1.022 MeV an electron positron pair can be produced in the vicinity of the Coulomb field of an absorber nucleus. The excess energy above 1 MeV of the photon is transferred into kinetic energy of the positron electron pair. Both particles deposit their kinetic energy in the detector within a confined volume close to the first photon interaction. However, the rest mass of both particles (511 keV c^{-2} each) is not deposited in

the detector. After the positron is thermalized within nanoseconds in the detector, it annihilates with an electron of the absorber material, producing two 511 keV photons. While these two γ-rays in most instances are reabsorbed in the detector, it is possible that one or both of them escape the detector. This produces the characteristic escape peaks in the spectrum, with a 511 keV and 1.022 MeV shift with respect to the full energy peak. Fig 3.3 shows the measured spectrum obtained for the interaction of monoenergetic 4.4 MeV and 6.1 MeV incident photons in a high purity Ge detector.
Both electrons and positrons lose energy via Bremsstrahlung in the detector, producing secondary photons. Depending on the interaction region in the detector and the energy of the secondary photon, partial energy information is lost when the secondary photons escape the detector, similar to the positron escape peaks.

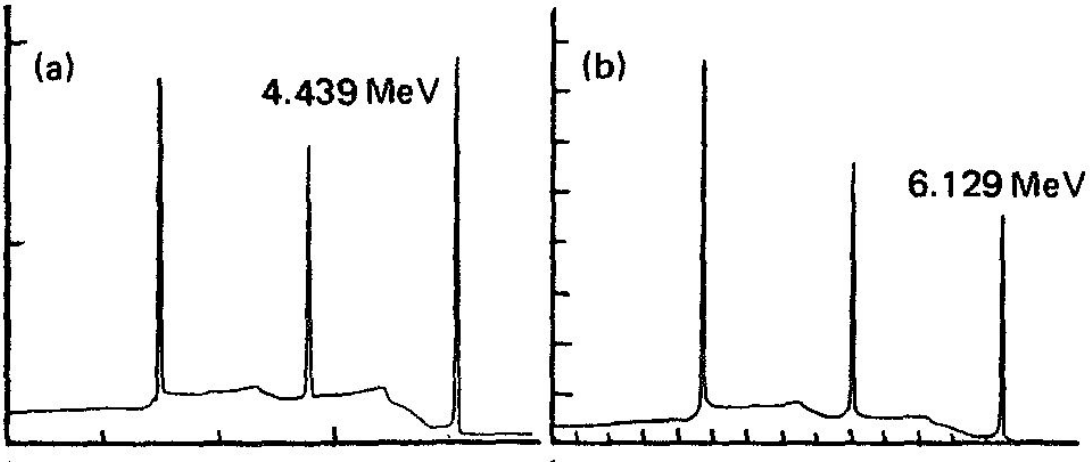

Figure 3.3: Energy response of a 100 cm^3 lithium doped Ge detector to mono-energetic photons of (a) 4.4 MeV and (b) 6.1 MeV. Mono-energetic lines are from ^{12}C and ^{16}O de-excitation. The full energy peak and both annihilation escape peaks are clearly visible. Counts between the Compton back scattering edge and the full energy peak is from multiple Compton interactions in the detector. From Berg et al. (1975).

3.1.3 Source Distinction in γ-ray Astronomy

There are a few dominant methods for gaining information on the incident direction of a measured photon in high energy astrophysics. Wolter-telescopes can achieve a high angular resolution by focusing X-rays with a combination of hyperbolic and parabolic, usually gold plated mirrors, as the refractive index of this material allows total reflections (Wolter 1952). Lensing systems at higher energies are, however, not feasible in this design. At energies above several GeV, Cherenkov detectors can be used to track the particle path of charged particles created in the interaction of highest energy γ-rays with the atmosphere. In the energy range of nuclear transitions, the most commonly used designs are Compton telescopes and coded mask apertures. In Compton telescopes the flight path of photons can be reconstructed from energy deposition in two or more subsequent layers. The incidence direction of the photon can be reconstructed by applying the energy dependent Compton scattering cross section. With regard to this work using the SPectrometer on INTEGRAL (SPI), specifically the principle of the coded mask aperture is explained.

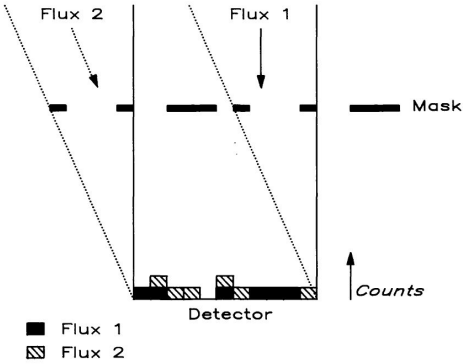

(a) This diagram depicts the working principle of a coded mask instrument. Bottom layer shows the counts in each detector pixel of the detector plane from two celestial sources. One source is aligned with the observation direction while the second one is off axis. The measured counts per detector pixel are the sum of both incident fluxes from two infinitely distant sources, modified by the mask pattern. Knowledge of the mask modulation (mask response) with respect to the aspect angle of the celestial source allows reconstruction of the two independent source contributions to the total measured counts. Image taken from Caroli et al. (1987).

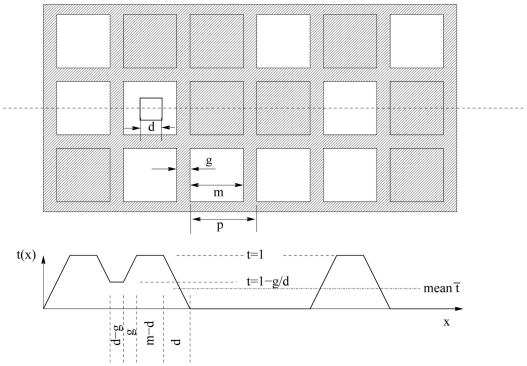

(b) Position dependent detector illumination when sliding the detector of pixel size d in the shadow of the mask. The structure of the mask is given by the size of the elements m and the width g of the support structure holding the opaque mask elements. Image adopted from Skinner (2008).

Figure 3.4: Working principle of coded mask aperture telescopes

A coded mask aperture, containing elements both transparent and opaque for γ-rays, is installed above the detector plane. A parallel beam of photons, entering the aperture of the instrument, is partially blocked by the opaque elements, imprinting a shadow-gram onto the detector plane specific to the incident-direction of the photons (see Fig. 3.4). Depending on the position of the celestial source with respect to the detector, only a partial amount of the detector plane is irradiated. The camera itself needs to be composed of a multitude of single detectors, where each receives a specific photon intensity with respect to one celestial source. These shadow-grams are very specific for point sources and become smeared out for spatially extended sources. The measured shadow-grams are then used to reconstruct the position of a celestial source in the field of view (FoV) of the telescope.

As the coded mask usually follows a specific geometric design, multiple celestial sources present in the same FoV can introduce similar shadow-grams on the detector plane, rendering a source discrimination ambiguous. To distinguish between different sources, coded mask telescopes commonly observe in a dithering mode. The satellite's and its co-alligned instruments observing direction are reoriented by a small angle between each observation period, creating a time dependent, alternating shadow-gram for each source per observation period. For INTEGRAL's instruments the typical observation periods, called pointings, last for ≈ 2000 s.

The angular resolution of a coded mask telescope is in general limited by the amount of separate pixels in the detector plane and the collimator length. However, increasing the total amount of detectors decreases the sensitivity of the camera as the sensitive detector volume

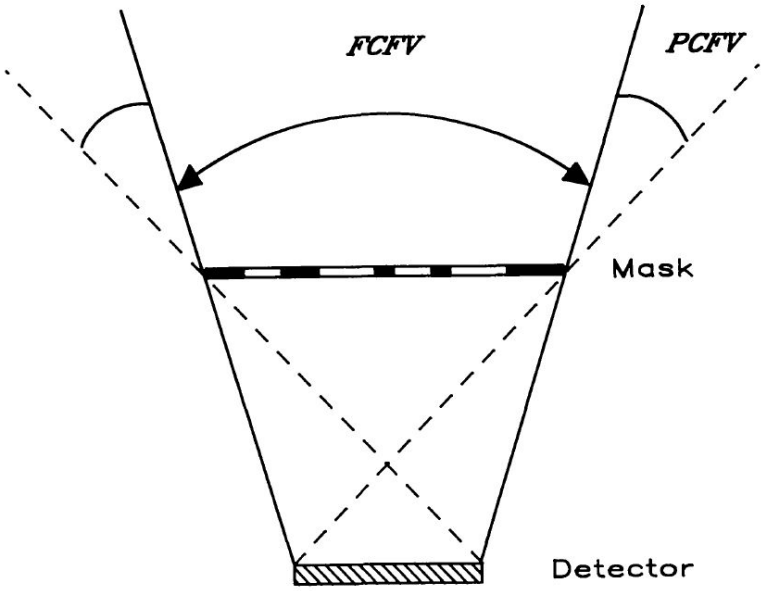

Figure 3.5: The angular resolution of the instrument, for a given distance between detector layer and coded mask plane, is determined solely from the pixel size of the detectors and the size of the transparent mask elements. Depending on the aspect angle of the celestial source, only a fraction of the detectors are illuminated, leading to partial coding of the detectors (PCFoV). The FoV of coded mask telescopes is given by the offset in angle, under which photons do not hit any detectors anymore through the mask. Image from Caroli et al. (1987).

per pixel for γ-rays decreases. The FoV of coded mask telescopes is governed by the size of the mask, which commonly larger than the detector plane. The angular resolution is given by the distance between the mask and the detector plane l_{mask}, the size of the transparent mask elements m_{mask} and the detector pixel size d_{mask}:

$$\theta = \sqrt{\left(\frac{m_{mask}}{l_{mask}}\right)^2 + \left(\frac{d_{mask}}{l_{mask}}\right)^2} \tag{3.9}$$

Skinner (2008) shows that the best angular resolution is achieved when both detector and mask elements have the same size, as is realized in SPI's coded mask system.

3.2 The INTEGRAL Mission and SPI

3.2.1 INTEGRAL

The mission of the INTErnational Gamma-Ray Astrophysics Laboratories (INTEGRAL) of the European Space Agency (ESA) is the observation of the *violent* Universe in the energy range from 15 keV to 10 MeV with good imaging and spectroscopic capabilities. γ-ray astronomy in this energy region encompasses a large variety of astrophysical phenomena: Neutron-Stars, black holes, CRs, supernovae or novae, to name only a few. γ-radiation from these sources can be emitted in continuum processes such as synchrotron radiation and

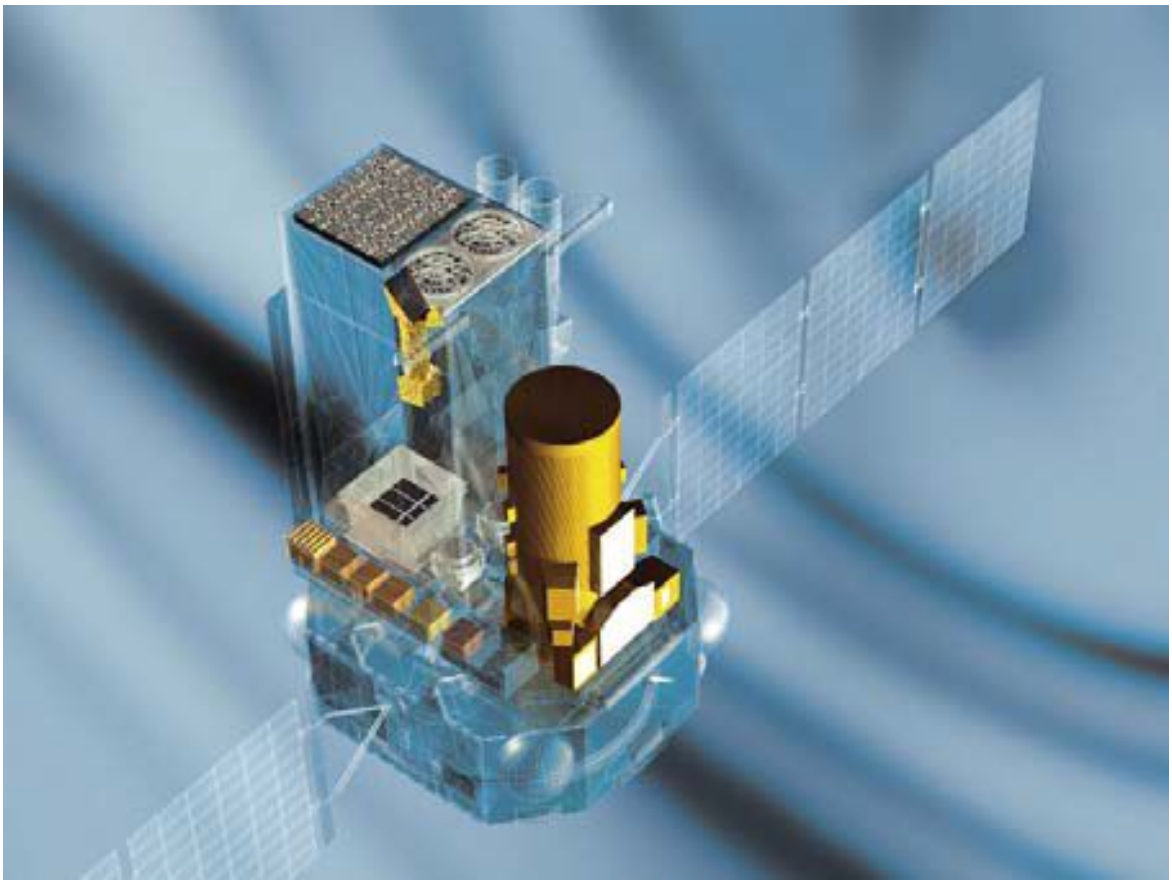

Figure 3.6: INTEGRAL spacecraft with lined out instruments. The spacecraft weighed 4 t at launch including 2 t of payload. Dimensions of the satellite are $(5 \times 2.8 \times 3.2)\,\mathrm{m}^3$. The solar panel span a width of 16 m when deployed. Image taken from Schanne (2006).

Bremsstrahlung of highly energetic particles but also in the form of γ-ray lines from radioactive decay and nuclear excitation. The mission was planned for a duration of two years with a possible extension to 5 years. Due to INTEGRAL's unique capabilities of observing and imaging the sky in the very specific energy range, it is still actively taking data after 17 yr in space.

INTEGRAL carries four co-aligned instruments. The two main instruments are the spectrometer SPI, optimized for high spectral resolution and the imager IBIS, optimized for high angular resolution. The setup is completed by the hard X-Ray monitor JEM-X and the optical camera OMC. All three high energy instruments employ the coded mask technique.

Data analysis in this thesis concentrates on data obtained from SPI. However a short overview of the additional instruments is presented here while SPI is described in detail in Sec. 3.2.2.

IBIS is the Imager on-Board the INTEGRAL Satellite (Ubertini et al. 2003), whose main objective is the observation of the Universe in the 15 keV to 10 MeV energy range with unprecedented angular resolution. The instrument consists of two detector layers 94 mm apart from each other. The upper layer (ISGRI; Lebrun et al. 2003) of the detection system comprises a matrix of (128×128) pixel elements with a total effective area of $2600\,\mathrm{cm}^2$. Each of the 16384 pixels is a separate CdTe detector with a thickness of 4 mm. Due to the small diameter of the detectors, the CdTe semiconductor array is only sensitive in the energy range between 15 and 150 keV. The bottom layer of the instrument (PICsIT; Labanti et al.

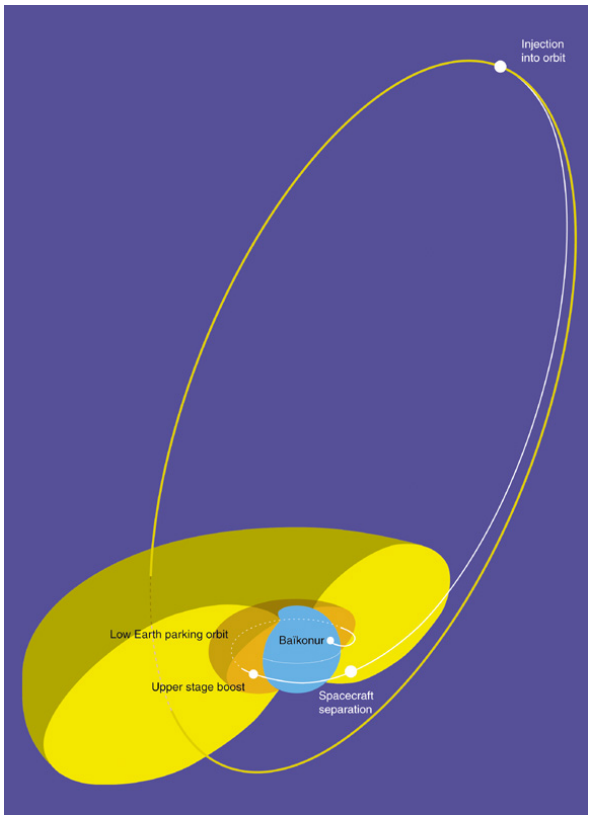

Figure 3.7: INTEGRAL's highly eccentric orbit and injection plan after successful launch from Baikonur/Kazakhstan on October 17, 2002. The orbits perigee is 9000 km and its apogee is 154000 km with an initial orbital period of three days. Due to de-orbiting maneuvers the orbital period was decreased to 2.5 days. The Earth is shown as a blue sphere. The Van-Allen radiation belts are included in yellow that are dominant below ≈40000 km altitude. Image from https://sci.esa.int/s/8aVny6A

2003) contains the high energy matrix with (64×64) pixels. Each pixel is a separate, square shaped CsI detector. The assemblies effective area is 2890 cm^2. IBIS utilizes both layers for particle path reconstruction, which achieves an angular resolution of 12', with a point source localization of 30" (Ubertini et al. 2003). The energy resolution of IBIS is $\approx$ 10% between 100 keV and 1 MeV, designed to observe continuum rather than (narrow) nuclear lines.
JEM-X (Joint European X-Ray Monitor; Lund et al. 2003) is utilized as a supplementary imaging monitor. Its main function is to distinguish the contribution from separate point-sources in crowded spatial regions. JEM-X consists of two identical, co-aligned micro-strip gas chambers with a 500 cm^2 effective area per detector. The two detectors are shadowed by a marginal layer of tungsten with 0.5 mm thickness, serving as coded masks. The detectors are sensitive in the energy range between 3–35 keV, with an energy resolution of 2.2 keV at 22 keV . The two detectors and their masks are rotated by 180° with respect to each other to avoid losses of angular information at the edges of the FoV. The instrument achieves an angular resolution of 3.5' and a point source localization of 15" for strong sources.
By integrating the Optical Monitoring Camera (OMC; Mas-Hesse et al. 2003) into the satellite design, INTEGRAL is capable of observing the Universe in multiple wavelengths simultaneously. OMC uses a classical refractive system for optical light with an entrance

aperture of 50 mm and a focal length of 154 mm. This optical design focuses light around 550 nm wavelength from a $5° \times 5°$ FoV onto a large format CCD chip. It achieves an angular resolution if 25" with a point source localization accuracy of 6". The high angular resolution is used to provide the precise direction of the entire spacecraft. Additionally, the camera provides brightness measurements and localization for variable optical counterparts to the γ-ray sources in the FoV of the main instruments.
INTEGRAL was launched on October 17, 2002 from Baikonur in Kazakhstan. The satellite was injected into a highly eccentric orbit with a perigee of ≈9000 km and an apogee of ≈154000 km and an inclination of 51.6°, yielding an initial orbital period of three days. Note that to comply with ESA's policy of minimizing space debris, the orbital period was decreased to 2.5 days in 2015, ensuring a reentry of the spacecraft in 2029. The highly eccentric orbit was chosen to avoid long periods in Earth's radiation belt. Charged particles mainly from solar winds become trapped by a mirroring effect of Earth's magnetic field. The inner radiation belts mainly consist of protons and reach an altitude up to ≈9000 km while electrons mainly constitute the adjacent outer radiation belts up to altitudes of ≈50000 km (Daly 1994). Extended periods within the radiation belts would lead to fast degradation of the detector arrays and malfunctions of the readout electronics from a significantly increased rate of charged particle interactions. In general, orbit phases between 0.1 and 0.9 are used in INTEGRAL data analysis, which means orbit phases above 50000 km altitude. SPI is switched to safe mode during belt passages to avoid radiation damage.

3.2.2 The Spectrometer on Integral SPI

Table 3.1: Design specifications of SPI. In-Flight performance can deviate. Values are taken from Winkler et al. (2003), Vedrenne et al. (2003).

Parameter	
Energy range	18 keV–8 MeV
Detector	19 Ge detectors, each (6 × 7) cm cooled @ 85 K
Detector area	500 cm^2
Spectral resolution (FWHM)	3 keV @ 1.7 MeV
Continuum sensitivity	5.5×10^{-6} @ 100 kev
[ph cm^{-2} s^{-1} kev^{-1}]	1.2×10^{-6} @ 1 MeV
(ΔE = E/2, 3σ, 10^6 s)	
Line sensitivity	3.3×10^{-5} @ 100 keV
[ph cm^{-2} s^{-1}]	2.4×10^{-5} @ 1 MeV
(3σ, 10^6 s)	
FoV (fully coded)	16° (corner to corner)
Angular resolution (FWHM)	2.5° (point source)
Source location (radius)	≤1.3° (depending on source strength)
Absolute timing accuracy (3σ)	≤200 μs
Mass	1309 kg

SPI was designed for spectral highly resolved observations of the high energy sky. Its camera covers an energy range from 20 to 8000 keV with a sub-percent energy resolution. The instrument is designed as a coded mask spectrometer with a fully coded field of view of

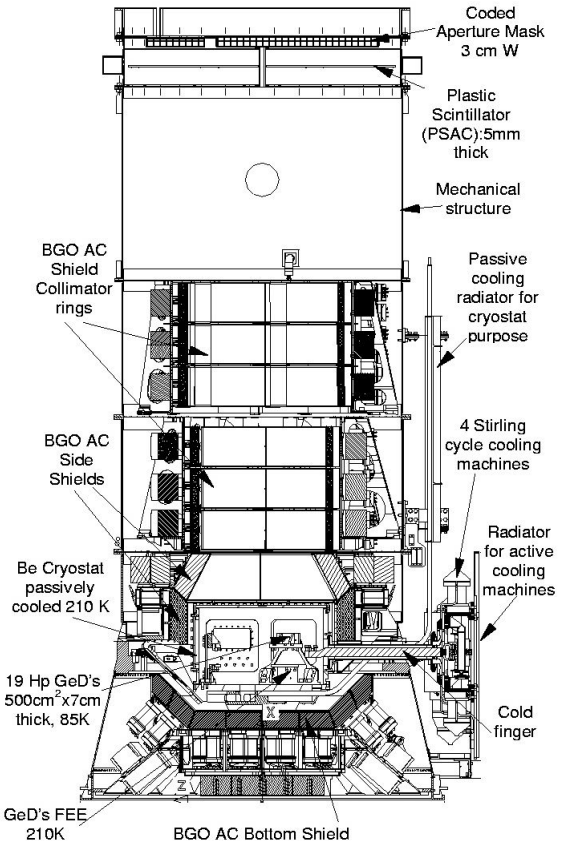

Figure 3.8: Transversal section of the SPI instrument including labeling of subsystems. Diagram taken from Vedrenne et al. (2003)

$16° \times 16°$ in which the detector plane is fully shadowed by the mask. This fraction gradually decreases towards no coding at $34° \times 34°$ FoV.

3.2.2.1 Camera

SPI's camera consists of an array of 19 hexagonally shaped high purity Ge detectors that are arranged in a hexagonal shape for optimal spacing and increasing the detector area (Fig. 3.9). Each detector has a base width of 6.2 cm and a height of 7 cm. A central bore contains the readout anode. The total effective surface area of the camera adds up to 550 cm^2. SPI's electronics are subdivided into two separate energies regions covering the energy range from 20 keV to 2 MeV (SPI's "low energy range") and from 20 keV to 8 MeV (SPI's "high energy range"). Both energy ranges are covered by a separate analog-to-digital converter with 16384 channels, yielding higher energy resolution in the low energy range. All detectors are encapsulated and cooled to 85 K by a beryllium finger to avoid thermal excitation of electrons in the depletion zone of the detector. A 4 kV high voltage has been applied to the detector to maximize the depletion zone and allow for fast pulse rise times in the readout electronics. The high voltage has been reduced to 2.3 kV within SPI's 17 yr of operation to increase the detector longevity.
The 19 detectors are numbered from 00–18 starting in the center of the detector array. However, additional pseudo detectors are defined for double events (numbering 19–60) and triple events (numbering 61–84), which account for the energy deposition of a single incident pho-

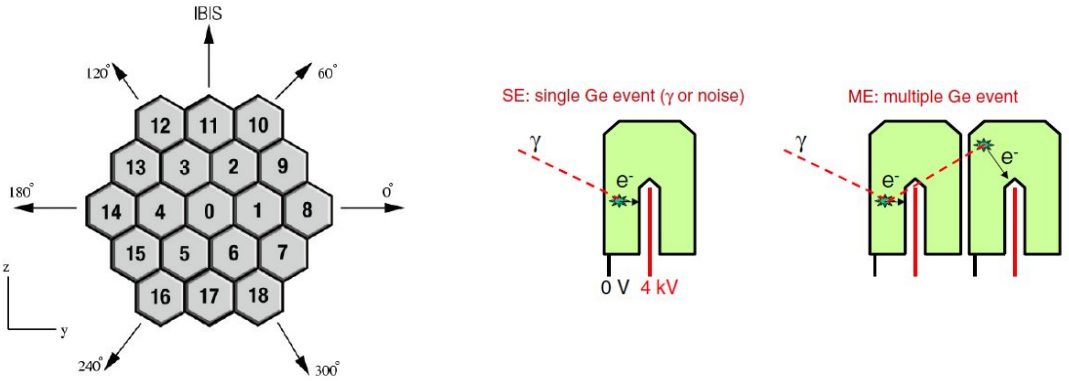

Figure 3.9: SPI's camera consists of 19 physical, hexagonally shaped detectors arranged in a honeycomb structure. The physical detectors are numbered from 00 through 18. Pseudo detectors are defined from the combination of multiple physical detectors accounting for interactions of single incident photons within multiple detectors.

ton within more than one detector. Multiple interactions, recorded in more than one detector within the light crossing time are summed up to form a single pulse called multiple events. Due to the increasing cross section for Compton scattering and pair production with increasing energy, multiple events become more important at energies above ≈1 MeV. Over the 17 yr mission duration a total of 4 detectors have failed, reducing the effective area for single events by 1/19 per detector failure to current ≈80% of the primary effective area.
Due to constant bombardment of the detectors with CRs, the Ge lattice structure suffers from production of defect sites that contaminate the lattice with additional charge carriers. This can lead to temporary charge trapping, decreasing the charge collection efficiency (Kretschmer 2011) and pulse shape in the readout electronics. This results in a shift in nuclear line peak positions and a degradation of SPI's energy resolution (see 4.2.3). To counter this effect, the camera is heated to 105° C semiannually to restore the Ge lattice structure, which is called an annealing period.

3.2.2.2 Anti-Coincidence Systems

The sensitivity of space born γ-ray missions with respect to the celestial objects of interest suffers from interactions of both photons and CRs with the detectors, that originate from sources outside the $34° \times 34°$ FoV, coded by the mask. To reduce the number of such interactions, that are considered background radiation, the detector array needs to be shielded in all directions outside the coded area. For that purpose, an anti-coincidence shield is installed in SPI (ACS), that consists of 91 BGO crystals arranged in 4 sub-units. Two collimator rings are placed between mask and detector plane, and the camera is surrounded by the side shield assembly. Each sub-element consisting of 18 BGO crystals with 16 mm thickness. A hexagonally shaped ACS array is placed below the SPI structure, consisting of 36 crystal with 50 mm thickness. Interactions of CR particles and photons, entering the detector from off observation axis directions, trigger a signal in the BGO crystals. Events that are simultaneously measured in the detector are rejected by the veto signal from the shield.
The deposited energy is transferred into photons with a wavelength of ≈400-650 nm. Each crystal is simultaneously monitored by two PMTs. This redundancy is intended to avoid the loss of readout information from BGO crystals. As the light output and amplification

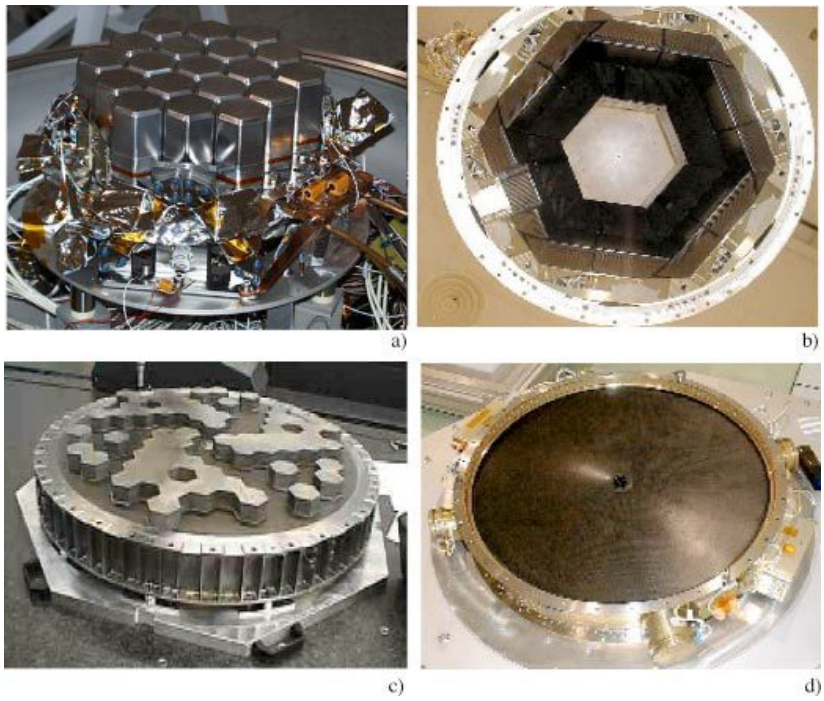

Figure 3.10: Subsystems of the SPI instrument. a) Ge detector area (the camera), b) ACS, c) mask, d) plastic scintillator (Vedrenne et al. 2003)

of subsystems are not identical, the threshold levels for each PMT readout electronics was set accordingly with a threshold level of ≈75 keV energy deposition in the BGO crystals. The threshold level was determined during commissioning phase to achieve an optimum between detector dead time and background reduction.
In addition, the ACS can be used as a γ-ray burst monitor. The large surface of the detector allows for a 4π monitoring, that was used in associating a neutron star merger with a γ-ray burst signal (von Kienlin et al. 2003; Savchenko et al. 2017).
A second veto signal is issued by a 5 mm thick plastic scintillator with a diameter of 80 cm that is installed directly below the tungsten mask. It is observed by a total of 4 PMTs of which two are installed redundantly. Pre-launch simulations (Jean et al. 1996) suggest that the additional layer of scintillator material could enhance the sensitivity by a factor of 1.4 at 511 keV, however, in fight performance of the additional layer is only 'modest' (Vedrenne et al. 2003).
In addition a pulse shape discriminator (PSD) is installed in the SPI electronics. Simulations of SPI background suggested, that the background in the 20–2000 keV range is dominated by the energy deposition of electrons. These electrons are emitted in the β decays from activated Ge, without the emission of a γ-photon. However, electrons deposit their energy locally in a single interaction, leading to a short rise time of the signal in the pre-amplifier. In contrast, highly energetic photons deposit their energy through multiple Compton scatterings in the Ge detectors. The summation of multiple interactions leads to a longer rise time and temporally broader pulse in the pre-amplifier. Information from the pulse shape discriminator is stored and used for rejection of single site events. Due to an overestimate of localized β events, sensitivity improvement from the PSD sub-assembly is negligible (Roques et al. 2003).

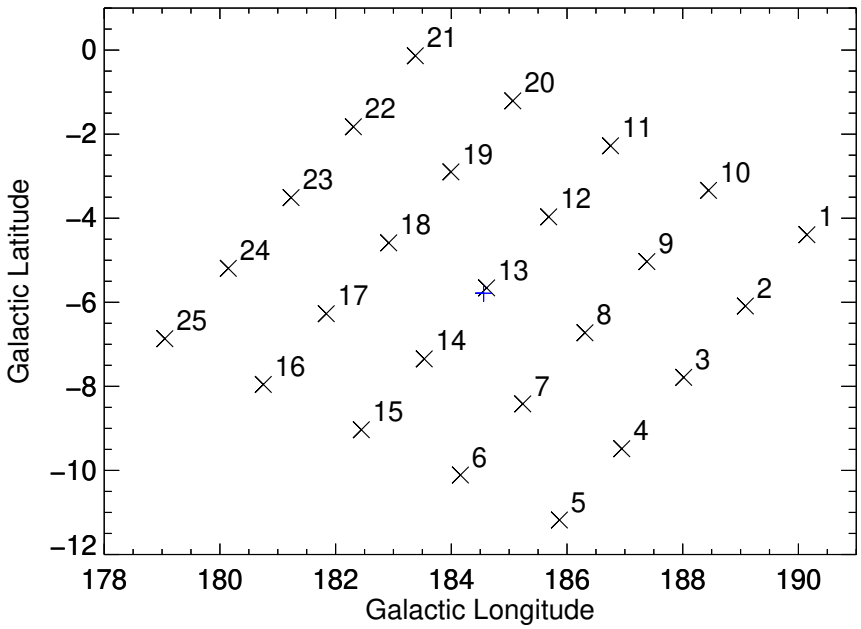

Figure 3.11: Dithering pattern of the SPI instrument for observations of the Crab nebular in Orbit 43. The blue cross in the center of the figure marks the location of the celestial source, at the position of the Crab Nebula at 184.6° Galactic longitude and -5.8° Galactic latitude. The numbered black crosses are the 25 positions in the rectangular shaped 5 x 5 dithering pattern. Each location is separated from the neighboring position by 2.1°. The FoV for each pointing is 16°x16°, i.e. the central blue celestial source of interest is always in the fully coded FoV of the instrument.

3.2.2.3 The Mask

Source localization is achieved through a mask placed 171 cm above the detector plane (Fig. 3.10). The mask consists of 127 hexagonally shaped mask elements with the same dimensions as the Ge detector blocks. 64 of these elements are transparent, while the remaining 63 blocks are made of tungsten to achieve a high stopping power for γ-rays. Roughly 50% of the detector area are thereby always shadowed by the mask, reducing the effective area. Localization is improved by virtually illuminating a higher number of detectors. This is achieved by rocking the instrument orientation by small 2° steps every 30 minutes while observing the same target, thus producing a different shadowing of the detector plane. Ground calibration with radioisotopes have shown that SPI has a PSF of 2.7°. Extending the coded mask principle to the SPI mask, the instruments response to a celestial signal is encoded in the mask pattern, which imprints a shadow-gram onto the camera containing all 85 physical and pseudo detectors. The shadow-gram is mainly dependent on the direction of the celestial source and the angle between the optical axis of the SPI detectors and the target. In addition, the relative detector intensity pattern, which are the convolution of the shadow-gram with the energy response of the camera, is dependent also on the incident energy of the photon, as higher energy photons are more likely to deposit energy in multiple detectors and the mask's transparency increases with increasing photon energy. Typical observations with SPI are conducted in intervals that last for 30 – 60 min each. Between these pointings, the instrument is reoriented by the 2.1° in a rectangular shaped grid (see Figure 3.11) consisting of 5 x 5 positions.

During one of these observation periods, the shadow-grams of the central source are gradually changing with each pointing due to the slight reorientation of the instrument. This change of the relative illumination of the detectors is shown in Figure 3.12 for the dithering pattern shown in Figure 3.11 for the combination of single and double detector events. The shadowing of the detector plane by the mask is dependent on the relative angle between the source position and the 120° point symmetric optical axis of the instrument. The behavior of the relative intensities for a specific pointing is best illustrated for the 19 physical detectors in the case, where the celestial source and the orientation of the instrument are almost identical (see Figure 3.12). As the size of the mask elements and the detector elements is identical, the shadow-gram is solely governed by the inner 19 mask elements (see Figure 3.10,c)) when the celestial source is directly faced. Therefore, groups containing three adjacent detector elements are either illuminated (numbers: [01,07,08],[03,11,12],[05,15,16]) or shadowed (numbers: [02,09,10],[04,13,14],[06,17,18]). Detector 00 is not covered by any mask elements and should therefore be in full light, however additional elements such as the supporting structure of the mask or screws occult the detector.

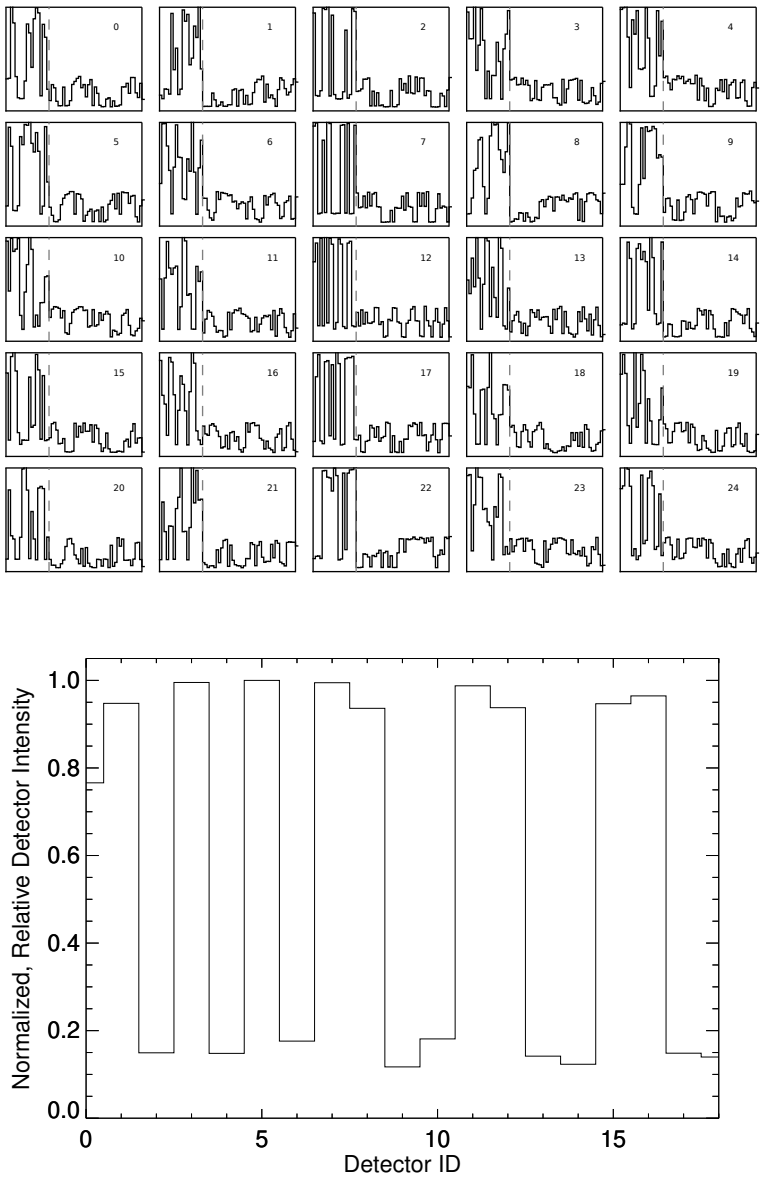

Figure 3.12: Detector pattern of SPI's coded mask. Upper panel contains the detector pattern for the combination of the 19 physical detectors (single events) and 42 virtual detectors (double events) at 4 MeV. The numbering of the sub figures is identical with the numbering of the dithering positions in Figure 3.11. The detector pattern change significantly with the reorientation of the space craft, which allows for the distinction between the celestial contribution and a time independent background behavior. The lower panel shows the magnified sub figure 12 of the upper panel for the 19 physical detectors. The relative intensity is normalized to detector 5, which is fully illuminated.

Chapter 4

Background Analysis of an Energetically Highly Resolved Spectrometer

4.1 SPI Data

4.1.1 SPI Data Structure

Measured SPI data can be best described as a three dimensional matrix. The coordinates of this matrix are energy, time and detector. Each element of the matrix contains a number of photons that are counted in one energy bin, per one detector, integrated over the time span of a specific observation period (e.g. one pointing). From this matrix it is possible to extract a photon count spectrum in energy by extracting the elements of one detector and totaling all entries in the time dimension for the inquired time span. In Figure 4.1 such spectra are shown for individual detectors (physical detector 0 and pseudo detector 35) on timescales ranging from one pointing to mission duration. In the lower energy range, double events only contribute on a subordinate level due to the small probability of scattering an incident photon from one detector into the adjacent detectors. However, at higher energies, where Compton scattering becomes more important, double events account for up to 40% of the overall measured counts.
The spectra are comprised of the contribution of celestial sources, either coded by the mask or shining through the shields at off observation axis positions, and a large, underlying instrumental background. As no coding information exists for the off-axis observations, contribution from these sources needs to be treated as celestial background. In total, the contribution of all background sources constitutes $\gtrsim 99\%$ of all measured counts. It is evident that no simple background suppression algorithm such as background subtraction can be applied to disentangle the on-axis celestial signal from the strong background. Instead, the Poisson statistics for the contribution of the celestial signal and the background, given by

$$P(d \mid m) = \frac{m^d e^{-m}}{d!} \tag{4.1}$$

have to be determined simultaneously. Equation 4.1 describes the probability for d events (measured photons) in a finite time (exposure time) and energy bin under the assumption that m events occur independently in the same time bin. In SPI data analysis the model for the predicted counts is also binned in energy. In both energy regions, a constant binning is used that oversamples the energy dependent instrumental resolution, shown in Figure 4.5.

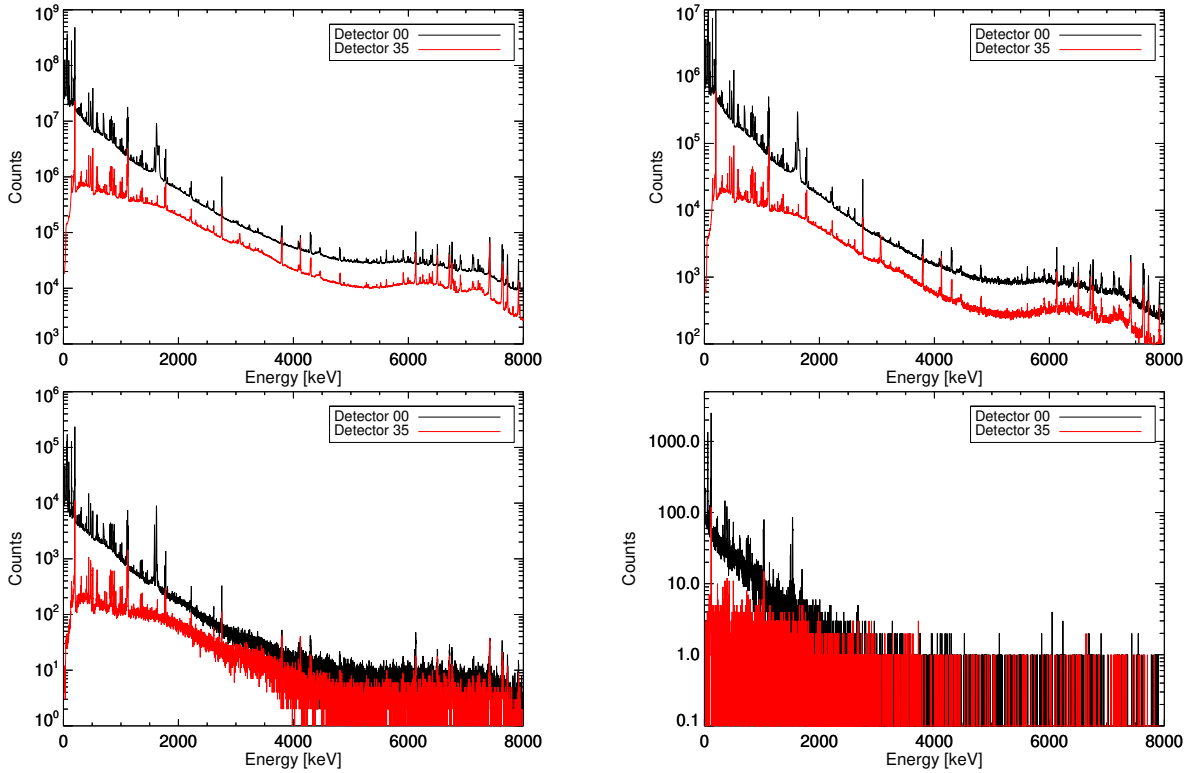

Figure 4.1: Measured photon spectra for detectors 00 and 35 (pseudo detector 3 + 11) integrated over different timescales. Integration timescales from left to right, top to bottom: Mission; Annealing, Orbit, Pointing. Double events have no crucial contribution below roughly 1 MeV. Above 2 MeV double events account for 40% of all measured events, while single events constitute roughly 60% of the measured background counts. In this thesis triple events are not included in the analysis. The ratio of double to single events is less than the aforementioned 40% per detector. However, the ratio of the detector integrated events, ranging over 42 pseudo double detectors in comparison to only 19 single detectors, is higher than the ratio for a single detector. On short timescales, the spectra are limited by count statistics.

The narrowest utilized energy binning is 0.5 keV below 2 MeV and 1 keV from 2 – 8 MeV. The specific model m_k for one energy bin is given as the sum of the contributions from all potential sources present over the entire exposure time. In our analysis the model for describing the data is given by

$$m_k = \sum_t \sum_j IRF_{k,j} \sum_{i=0}^{N_S} \theta_{i,t} S_{i,j} + \sum_t \sum_{i=N_S+1}^{N_S+N_{Bg}} \theta_{i,t} B_{i,k} \tag{4.2}$$

where m_k is the model for a specific energy bin k. The contribution of all celestial sources N_S is convolved with the image response function $IRF_{k,j}$, specific for every energy k and SPI's mask pattern. Each celestial source contributes to the model with a source specific number of image pixel parameters j, depending on the illumination of the detector by this source for a specific time interval. The number of background contributors $B_{i,k}$ is given by N_{Bg}. The background contributions are independent of the mask. The intensity parameters $\theta_{i,t}$ are the normalization constants for all individual (background) components. In general, they can be time dependent in each energy bin on different timescales. In this thesis, spectra

are derived per energy bin *k*, which means that no prior knowledge about the spectral shape is assumed.
In SPI data analysis the contribution from both point like sources and extended emission from diffuse sources is considered. For point sources the image parameter is j = 1, while the number of independent image pixels for an extended sources is dependent on the extension of the source and the size of each image pixel. For a given celestial location, defined by Galactic longitude/latitude ($l_{i,j}/b_{i,j}$), of the image pixel j the contribution is calculated by convolving this pixel through the image response function, which yields a specific detector pattern (shadow-gram) for this pixel. The detector pattern is specific for the relative angle between the location and the line of sight of SPI, which varies from pointing to pointing (cf. Figure 3.11). The model for each source is given by the sum of its individual pixel contributions. For a given set of N_S source morphologies the shadow-grams are known, and the absolute intensity needs to be determined. The intensity variations of the sources can be time dependent. The sources are assumed to be constant unless otherwise stated. The temporal intensity variation of the background is dependent on multiple external influences (cf. section 4.2.1).
The a priori unknown normalization parameters $\theta_{i,t}$ for all source contributions ($N_S + N_{Bg}$) are determined from statistical inference by maximizing the likelihood $\mathcal{L}(D \mid M)$. The probability for model M, given by equation 4.2, is maximized under the assumption of a measured data set D. As measuring photons follows the Poisson statistic, the likelihood is given by

$$\mathcal{L}(D \mid M) = \prod_{k=1}^{n} \frac{m_k^{d_k} e^{-m_k}}{d_k!} \quad . \tag{4.3}$$

In the statistical fit the negative logarithm of the likelihood is minimized which is given by

$$C(D \mid M) = 2 \sum_{k=1}^{n} (m_k - d_k \ln(m_k)). \tag{4.4}$$

This is called the Cash statistics (Cash 1979), multiplying the logarithm of the likelihood with a factor of 2. Note here that the factor $\ln(d_k!)$ is independent of model parameters $\theta_{i,t}$ and is therefore dropped from the minimization. In a likelihood ratio test, this factor will cancel out and can therefore be removed from the analysis.

4.1.2 Spectral Description of SPI Data

SPI data, in general, is comprised of an underlying continuum, upon which a finite number of nuclear de-excitation lines is present (cf. Figure 4.1). In the analysis in this thesis, the spectral shape in a finite energy range r is described by

$$\mathcal{S}(E) = C(E; A_{0,C_r}, \alpha_{0,C_r}) + \sum_{i}^{n} L(E; A_{0,L_{i,r}}, E_{0,L_{i,r}}, \sigma_{L_{i,r}}, \tau_{L_{i,r}}), \tag{4.5}$$

where the sum is over all *n* lines with individual lineshape L, present in the energy region r. The continuum function C is given by

$$C(E; A_{0,C_r}, \alpha_{0,C_r}) = A_{0,C_r} \left(\frac{E}{E_C} \right)^{\alpha_{0,C_r}} \tag{4.6}$$

where α_{0,C_r} is the power-law index and A_{0,C_r} is the amplitude, normalized to the pivot energy E_C of the energy region r. The structure of the line function is more complex with

$$\begin{aligned}
&G(E; A_{0,L_{i,r}}, E_{0,L_{i,r}}, \sigma_{L_{i,r}}) = A_{0,L_{i,r}} \exp\left(\frac{-(E - E_{0,L_{i,r}})^2}{2\sigma^2_{L_{i,r}}}\right) \\
&D(E, \tau_{L_{i,r}}) = \frac{1}{\tau_{L_{i,r}}} \exp\left(-\frac{E}{\tau_{L_{i,r}}}\right) \\
&L(E; A_{0,L_{i,r}}, E_{0,L_{i,r}}, \sigma_{L_{i,r}}, \tau_{L_{i,r}}) = \\
&G(E) * D(E) = \\
&\sqrt{\frac{\pi}{2}} \frac{A_{0,L_{i,r}} \sigma_{L_{i,r}}}{\tau_{L_{i,r}}} \exp\left(\frac{2\tau_{L_{i,r}}(E - E_{0,L_{i,r}})^2 + \sigma^2_{L_{i,r}}}{2\tau^2_{L_{i,r}}}\right) \times \\
&\operatorname{erfc}\left(\frac{\tau_{L_{i,r}}(E - E_{0,L_{i,r}})^2 + \sigma^2_{L_{i,r}}}{\sqrt{2}\tau_{L_{i,r}}\sigma_{L_{i,r}}}\right).
\end{aligned} \tag{4.7}$$

The total line function L(E) is a convolution of a symmetric Gaussian G(E) with an exponential tail function D(E). The symmetric Gaussian is specified by the amplitude $A_{0,L_{i,r}}$, the centroid energy $E_{0,L_{i,r}}$ and the intrinsic line width $\sigma_{L_{i,r}}$. The function D(E) accounts for the deterioration of charge collection efficiency caused by the trapping of charge carriers between their point of origin and the detector electrodes. As the absorption coefficient and the distance to the detector cannot be independently determined, an average degradation parameter $\tau_{L_{i,r}}$ is instead used to describe the partial charge trapping (Kretschmer 2011). The intrinsic line width can be expected to be almost constant with time, as it is dependent only on the band gap of the detector material. From the point of view of a physical interpretation, only the degradation parameter $\tau_{L_{i,r}}$ should increase due to the constant bombardment of the detector with CRs. However, as the two parameters $\tau_{L_{i,r}}$ and $\sigma_{L_{i,r}}$ are degenerate to some extent, their absolute values cannot be entirely discriminated in a statistical fit of the parameters. Therefore only the derived full-width-at-half-maximum (FWHM) of the line shows a consistent temporal behavior.
In Figure 4.2 the line shape L(E) from equation 4.7 is shown for an increasing degradation parameter τ in arbitrary units. The values for $A_{0,L_{i,r}}, E_{0,L_{i,r}}, \sigma_{L_{i,r}}$ are constant in all 5 cases, only the degradation parameter τ is altered. The physical parameters $A_{0,L_{i,r}}, E_{0,L_{i,r}}, \sigma_{L_{i,r}}$ do not correspond to the line amplitude, centroid energy and width of the spectral shape anymore. In particular, the peak position of the line is given by

$$E_{Peak} = E_0 - \tau, \tag{4.8}$$

determined from equating the derivative of the line shape with respect to the energy with zero ($\partial L/\partial E = 0$), for small values of τ. Consequently, the peak position of the lines can vary with time, however, the fitted positions E_0 should be stable over long periods of time, as these correspond to the laboratory energies of nuclear de-excitation lines.
The FWHM of the line is a combination of the two parameters τ and σ. According to Kretschmer (2011) the FWHM of the line is given by

$$\Gamma_L = \Gamma\left[a_0 + \sqrt{(1 - a_0)^2 + \left(\frac{a_1\tau}{\Gamma}\right)^2}\right], \tag{4.9}$$

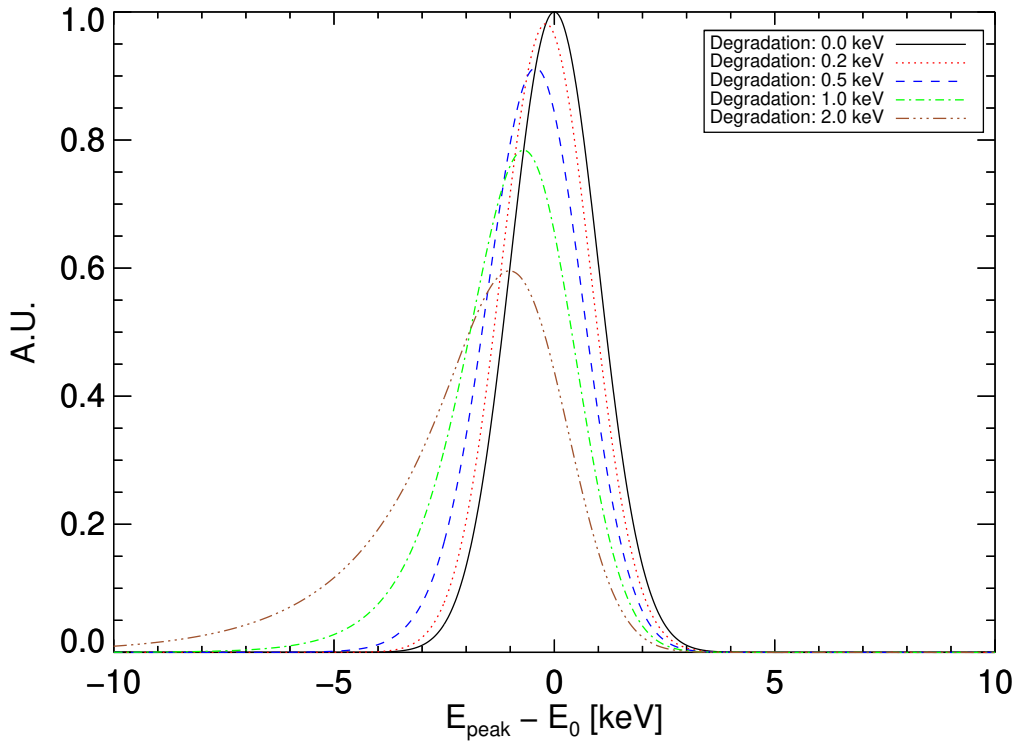

Figure 4.2: Degradation effects in the spectral shape of SPI lines. The centroid E_0 and amplitude A_0 do not correspond to the peak position and peak height of the physical line. Fitting the degraded spectral shape with a symmetric Gaussian leads to a spurious offset in the physical position of the line centroid towards lower energies.

where $\Gamma = 2\sqrt{2\ln(2)}\sigma$ is the FWHM of the symmetric Gaussian line. The parameters a_0 and a_1 are determined from a fit with $a_0 = 0.913735$ and $a_1 = 0.710648$ (Kretschmer 2011). The intensity of the line is given by the integrated counts, which is equivalent to the area under the line. For the analysis in this work this is one of the most important quantities, that is not affected by the degradation of the detectors. The integrated counts are given by the integral

$$\begin{aligned} \int_{-\infty}^{\infty} L(E)dE = \int_{-\infty}^{\infty} (G * D)(E)dE = \\ \int_{-\infty}^{\infty} G(E)dE \int_{-\infty}^{\infty} D(E)dE = \int_{-\infty}^{\infty} G(E)dE \\ = \sqrt{2\pi}A_0\sigma. \end{aligned} \tag{4.10}$$

The integrated counts are not effected by the degradation of the detectors. The deterioration of the charge collection efficiency leads to a prolonged rise time of the electronic signal and therefore shifts the absolute pulse height to lower levels. Nevertheless, the average amount of produced charge carriers per incident photon energy is still governed by Poisson statistics, and the information of an interaction of a photon with the detector is not lost, only distorted.

4.2 Time Integrated Background Model of a High-Resolution Spectrometer

4.2.1 Origin of SPI's Background

At the altitude of the INTEGRAL orbit the background is mainly introduced by the interaction of CRs with the satellite and instrument material. Close to Earth the composition of the CR flux is mainly protons (87%) and α-particles (12%). Particles heavier than αs only constitute $\leq 1\%$ of the total CR flux (cf. Figure 2.14). Interaction of these particles can lead to the excitation of nuclear transitions of the instrumental materials, that subsequently decay to the ground state under emission of γ-rays. Furthermore, interactions of highly energetic CRs can lead to the spallation of the impinged nucleus, during which neutrons are ejected from the nucleus. If these neutrons are sufficiently slow, they are subsequently captured by adjacent satellite nuclei, among others producing radioactive isotopes. Usually the new nucleus is not produced in its ground state but an excited, meta-stable state, which decays to the ground state under emission of photons with mono energetic energies specific to the decaying isotope. De-excitation can occur in a cascade with emission of more than one isotope specific line energy. The newly formed isotope can be unstable, further decaying to a new daughter nucleus under the emission of particle radiation and characteristic γ-ray lines.

The detected decay radiation is considered as either prompt event, when it occurs on time scales shorter than the coincidence window of SPI of 160 μs (Roques et al. 2003) after producing a veto trigger in the ACS system, and as delayed events otherwise. This can either occur when the half-life of the isotope or the live time of the meta-stable excited state is longer than the coincidence window. Besides the distinct nuclear de-excitation lines, an underlying continuum is present in SPI background counts, which consists of a Bremsstrahlung component from charged particles interacting with the satellite and the superposition of Compton tails due to partial energy deposition of nuclear de-excitation photons. The combination of all γ-rays from CR interactions constitute $\gtrsim 99\%$ of all events in an observation that can be estimated by the number of issued veto triggers by the ACS system of $\approx$ 70000 events s^{-1}. In contrast to that, the rate of the non vetoed events in the camera in the energy range 20 keV – 8 MeV is $\approx 40\,\mathrm{s}^{-1}$, i.e. the ACS reduces the background count rate by approximately three orders of magnitude.

In general, the intensity of the background follows the intensity of the background producing particle flux. In the case of SPI, the background intensity is correlated with the CR flux as modulated by the sun. During a solar flare, a significantly higher amount of CRs is ejected from the surface of the sun, leading to a leap in background intensity. However, the correlation between CR intensity and background intensity is only correct for isotopes for which the production rate is usually longer than the decay time. For isotopes with longer half-life times, a build-up effect can be observed. As the half-life of the newly produced isotope is considerably longer than the production rate, a reservoir of radioactive material is accumulated. An increasing number of radioactive nuclei of a specific isotope are present, increasing the flux of its specific decay lines. This increase only stops when the build-up of long lived radioactive isotopes and the decay rate equalize. Among others, the most prominent isotopes in SPI with long half-lifes are ^{22}Na and ^{60}Co with half-lifes of 2.62 and 5.27

years, respectively. They emit lines at the energies 1275, 1173, 1332 keV. Directly following solar flares, an increased flux for specific isotopes can be identified. These arise from isotopes with intermediate half lives of several hours to a few days. During solar flares, a large amount of these isotopes is produced, that decay within a few days until the normal intensity level from the equilibrium of production and decay is restored. One example is ^{48}V isotope with a half-life of 16 days. Additional to the increase in the flux of specific lines, solar flares can influence the spectral shape of the background in specific energy bands. In addition to the short term variations, the long term evolution of the background intensity is correlated with the 11 yr solar cycle (see section 4.2.3).

4.2.2 Background Modeling Approach

Data sets utilized in this thesis are composed of observations that are spread over several years and merged into one large data set to increase the typically low signal to noise ratio. To extract the spectral information per energy bin from these large data sets, the only information needed are the respective detector patterns (cf. equation 4.2), that are the input parameters for the statistical fit. The celestial patterns are known from the convolution of the celestial source positions and the image response function. In addition, the background patterns per observation time need to be determined as well in advance. In early SPI analyses, an on-off approach of modeling the background was adopted. In this approach the background contribution was determined from periods of time in which the satellite was oriented towards high Galactic latitude, as this region is considered as mostly *empty*, and no celestial sources imprint additional information onto the background. However, exposure on these regions is sparse and observation periods are scattered over extended periods of time, with observation gaps ranging up to hundreds of days. The degradation of the detector charge collection efficiency alters the spectral line shapes on a timescale of days, i.e. much shorter than the observation intervals for high latitude measurements. The background modeling approach in this thesis follows the description in Diehl et al. (2018); Siegert et al. (2019); Weinberger et al. (2020).

The background in this thesis is modeled according to the following assumptions. The detector pattern of the individual background components is constant in time. This assumption is justified, as the distribution of the background radiation emitting material in the instrument and satellite does not change during the mission time. As a consequence the direction dependent visibility of individual background components in the camera remains constant with time and is independent of the inter-pointing re-orientations of the satellite. It follows, that background counts, integrated over a prolonged observation period, produce a detector pattern that is representative for the background detector pattern on shorter timescales for energies. As the background, especially towards higher energies, is statistically limited (cf. Figure 4.1), the background cannot be determined on pointing timescales and integration of counts over several observation periods is required to provide sufficient statistics per detector for a precise modeling also of weak background lines. In addition, on timescales of single or several pointings, the celestial sources present in the FoV imprint their celestial pattern on the camera. This contribution, however, is smeared out by summing over a sufficient amount of pointings (Siegert et al. 2019). All measured counts in the respective observation time are attributed to the background. The time integration also requires the second, that

the temporal variation of the overall background intensity within the integration time can be traced by an external, independent measure. The correctness of the assumption is investigated in section 4.2.3. From this approach, the background components $B_{i,k}$ in equation 4.2 are determined. The absolute normalization $\theta_{i,t}$ of the background is determined in a statistical fit (cf. equation 4.2).

To further increase the statistical precision of the background model, the background is determined in adjacent energy bins by describing the background spectra per detector as a superposition of an underlying continuum on top of which a defined number of lines is present (cf. equation 4.5). The parameters of the continuum and line functions are determined in a statistical fit. To account for the order of magnitude variation in background strength, the total energy range is separated into smaller energy sub ranges.

In this thesis, the spectral information is extracted in fine energy bins, that are smaller than the intrinsic detector resolution. In these small energy bins the relative contribution of lines can vary with time, as the detector degradation influences the detector resolution. The background model in SPI's low energy range, adopted in this thesis, is modeled on a timescales that self-consistently accounts for the degradation of the detectors. The background is modeled per detector to obtain the required background pattern. In the ^{44}Ti/^{44}Sc specific energy sub ranges, the temporal evolution of the detector degradation is determined on a 3 d (one orbit) timescale, which is chosen as a trade-off between the integration time and the loss of information on the time dependent degradation. The number of instrumental background lines in each energy sub range is determined from the mission integrated background spectrum, i.e. the sum of 17 yr of data and all 19 physical detectors, in advance.

The fit background parameters, determined on a three day basis in the low energy range of SPI between 18 keV and 2 MeV are stored in a database per orbit and detector, from which the background model is built. The general trends in temporal and spectral properties of the background modeling approach are discussed in section 4.2.3.

4.2.3 Behavior of the Background in SPI's Low Energy Region

In Figure 4.3 the relative intensities of various background components are shown. These are similar to the detector pattern or shadow-grams of celestial sources but specific to the background. The parameters for the line strength per detector and orbit are extracted from the SPI line database. This also provides a validity check for the background model. While the intensities of the background components can change over time, the locations of the background sources within the satellite do not. Therefore, the relative intensities of the various components are expected to remain constant over long periods of time (see 4.3; upper four panels). Background intensity pattern only change when detectors fail. This is due to the fact that photons, that have a primary interaction in a dead detector and a secondary interaction in the adjacent detector (multiple event) are now seen as single events in the adjacent detector with potential missing energy. After a detector failure the pattern again remain constant until the next detector fails (see 4.3e). The continuum emission in the low energy range is largely a combination of Bremsstrahlung emission from charged particle scatterings in the satellite and Compton scattering of high energy photons from nuclear de-excitations.

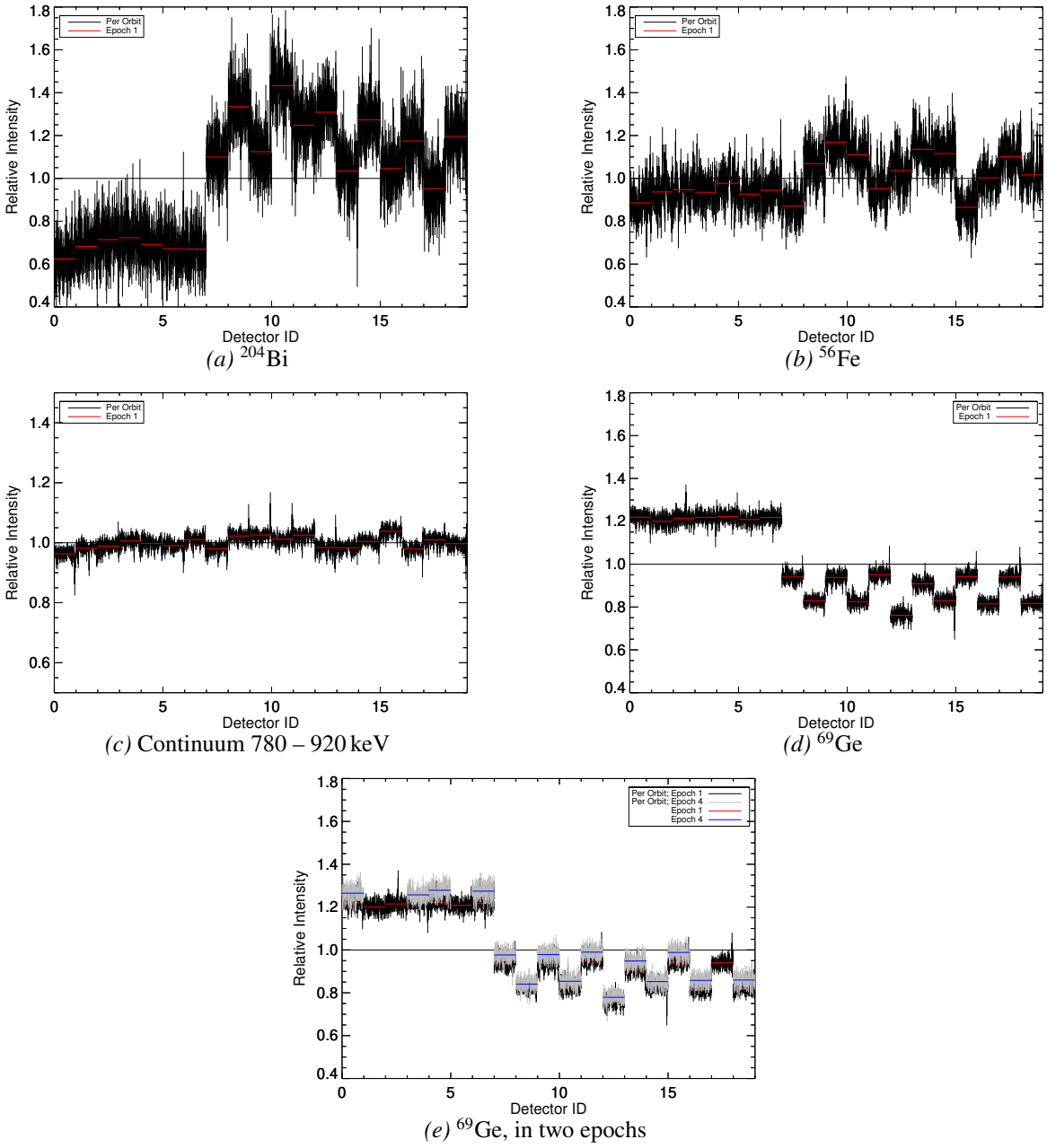

(a) ^{204}Bi

(b) ^{56}Fe

(c) Continuum 780 – 920 keV

(d) ^{69}Ge

(e) ^{69}Ge, in two epochs

Figure 4.3: Relative intensities of the background lines and continuum emission normalized to the number of working detectors. Top left panel: 752 keV line of ^{204}Bi, top right panel: 846 keV line of ^{56}Fe, center left panel: continuum 1100 – 1200 keV, center right/bottom panel: 1107 keV line of ^{69}Ge. This is similar to the detector pattern or shadow-grams, which would be imprinted from a celestial source on the detector plane. Black data points show the relative intensity of the detectors per orbits. The red line is the average over the first epoch (orbit 43 – 140). The relative intensities of the lines remain constant over long periods of time, and only change due to detector failures. The bottom panel includes the detector pattern of the ^{69}Ge line for the first and the fifth epoch (orbits 930-2100).

The continuum is largely isotropic and therefore produces a flat distribution in the camera. Minor deviations are introduced by the difference in effective detector volumes. In contrast,

contributions of the nuclear de-excitation lines produce a very specific background pattern induced by the position of the source in the satellite. The most prominent example of this behavior are the large number of Ge lines. As these lines are produced within the camera itself, the intensity of the lines is governed by the amount of surrounding detectors. The inner detectors (0,1,2,3,4,5,6) have six surrounding detectors each and therefore receive an equal amount of Ge irradiation (cf. Figure 4.3d). Detectors (7,9,11,13,15,17) at the edges of the honeycomb structured camera have four adjacent detectors, leading to a lower relative intensity of the Ge lines. Detectors (8,10,12,14,16,18) at the corners are connected to only three detectors and therefore have the least irradiation from the surrounding germanium. In contrast, background components with origins outside of the camera show the opposite behavior. Bismuth e.g. is mainly present in the ACS subsystem surrounding the camera. In this background line group the outer detectors provide a shielding for the inner detectors, which leads to a high line strength seen in the outer detectors and a lower intensity in the inner ones (4.3a). Similar behavior can be determined for the majority of instrumental background lines. Sources that have a directional dependence produce a peculiar detector pattern for their respective isotopes. Such a feature is produced by the presence of the IBIS telescope. Detectors facing IBIS show a significantly increased intensity in lines that originate in IBIS detector materials. On the other hand, lines emitted by copper isotopes have a rather flat intensity distribution due to the presence of copper in the cables connected to all SPI detectors.

In Figure 4.4 the camera-averaged variations in the absolute intensities of the background components are shown. The strength of the background increases linearly from the mission start and reaches a maximum in 2010 ($\approx$ MJD 55200). Afterwards, the background strength decreases and reaches a minimum between 2014 and 2015 (MJD 57000). The background then increases linearly again until 2020, with an absolute intensity close the maximum observed in 2010. The background strength is anti-correlated with the number of visible sunspots[1], shown in Figure 4.4 in gray. This number is an indicator of the solar emission strength, where a low sunspot number corresponds to weak magnetic fields on the solar surface. This reduces the magnetic shielding effect and leads to a high emission of charged particles. The solar cycle takes on average 11 yr, and approaches its second maximum in the INTEGRAL mission duration. The emission of prompt photons from CR interactions directly follows this trend in the strength of the solar cycle. Figures 4.4a–d show the temporal intensity variation of the continuum and three isotopes with a short half-life time that are considered prompt emission. Figure 4.4f shows the intensity of the ^{60}Co isotope with a half-life of 5.27 years. At the start of the mission no ^{60}Co is present in the satellite and the production of the isotope occurs faster than the decay. A reservoir of ^{60}Co is produced until the decay and production rate of ^{60}Co are equalized. The intensity of the line follows this trend and builds up until the solar maximum is reached. The amount of ^{60}Co remains stable during the solar minimum. However, it starts to increase again towards the end of the current mission duration due to the increase in the solar activity until it reaches a new equilibrium state. For medium lived isotopes (e.g. ^{48}V, see Figure 4.4e) the decay rate is higher than the production rate and only an insignificant amount of ^{48}V is present in equilibrium. The line intensity is mainly governed by the 11 year solar cycle. After the solar maximum is reached in 2013, the line intensity decreases to the level at the beginning of the INTEGRAL mission, and starts to rise again with the increasing solar activity. However, strong particles ejection from the sun during solar flares produces a large pool of ^{48}V

[1] Sunspot data taken from http://sidc.be/silso/datafiles

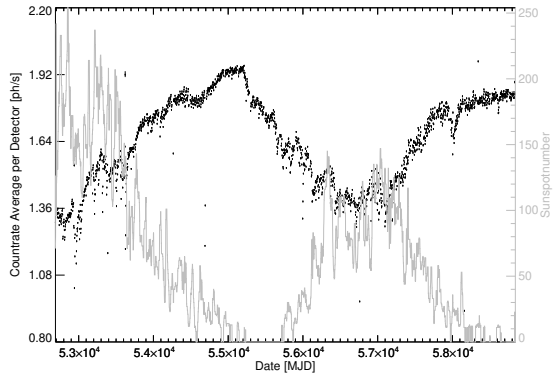

(a) 198 keV line of ^{71}Ge

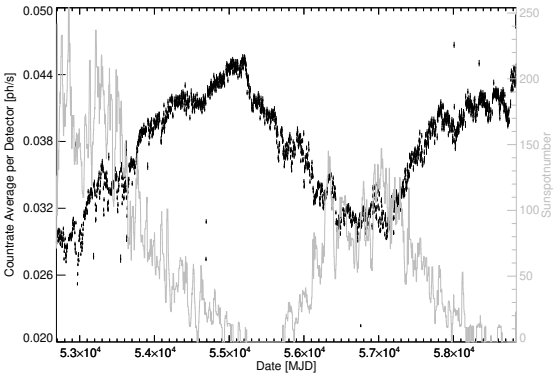

(b) 1107 keV line of ^{69}Ge

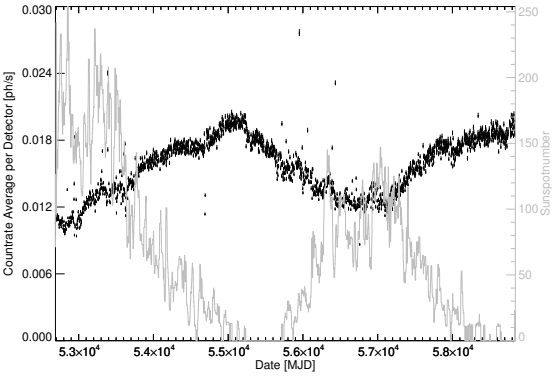

(c) 847 keV line of ^{56}Fe

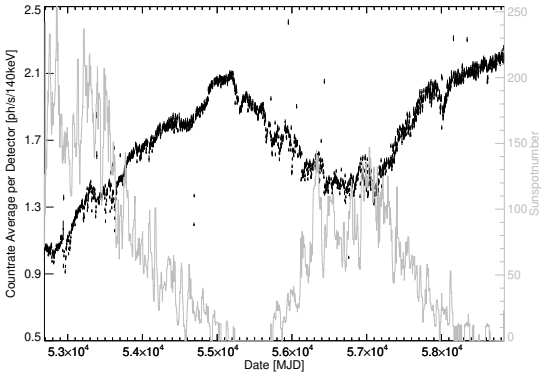

(d) Continuum intensity in the energy range 780 – 920 keV

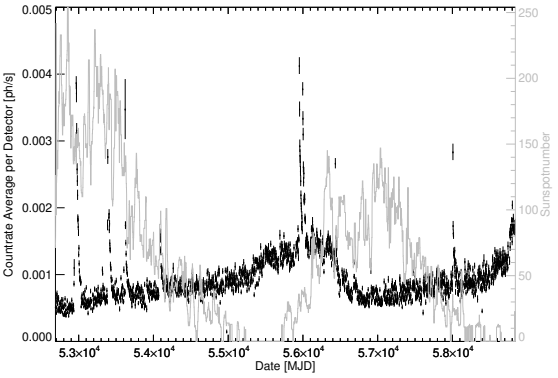

(e) 1308 keV line of ^{48}V

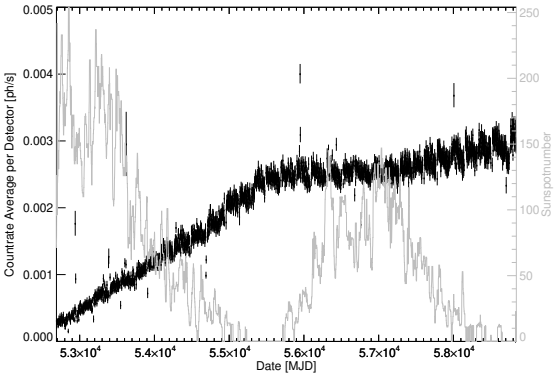

(f) 1332 keV line of ^{60}Co

Figure 4.4: Absolute intensity of background components. Black data points show the temporal variation in background intensity. The gray data points are the average number of sunspots seen per monthly period. This number is anti correlated with the emission of CRs from the sun. Upper two panels are from two Ge lines. The first at 198 keV (^{71}Ge) is the strongest background line in SPI. The second at 1107 keV is from ^{69}Ge. Central panels show intensity variation of the instrumental 846 keV ^{56}Fe line and the continuum intensity in the background range 780 – 920 keV. Continuum emission and de-excitation of these isotopes is prompt after interaction with CRs and follows the strength of the solar CR emission. The lower panels are from two isotope that do not decay promptly after production (see text).

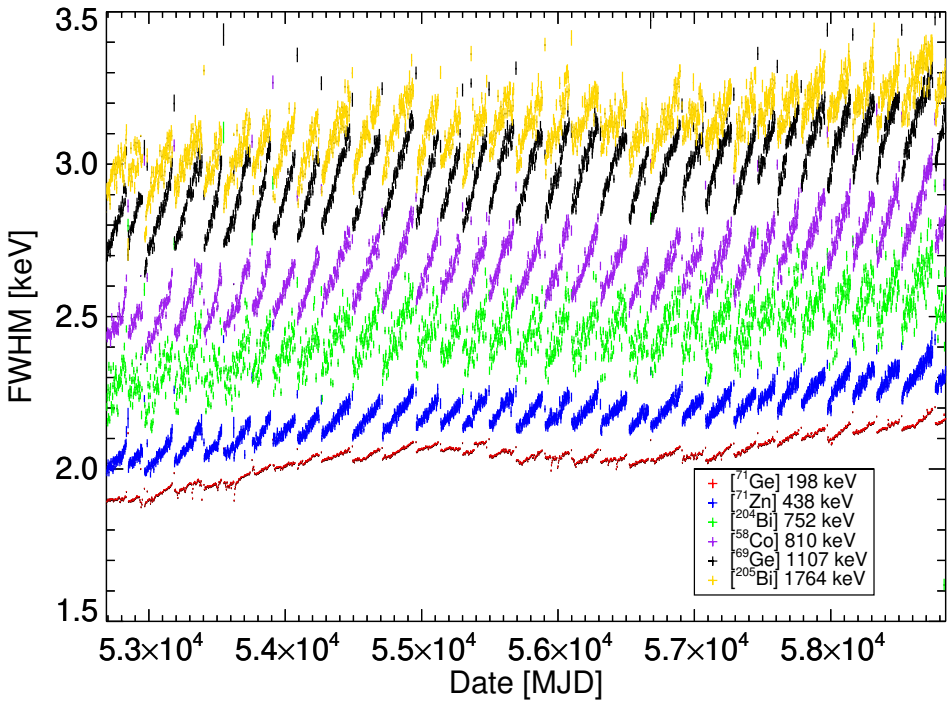

Figure 4.5: The FWHM averaged over all physical SPI detectors for lines in the energy range 20 – 2000 keV over time. The temporal saw-tooth shape is introduced by the degradation due to CR bombardment and the restoration of the detectors after the semiannual annealing phase.

nuclei. These decay according to their half-lifes until the stable equilibrium condition is restored, as demonstrated by fitting an exponential decay to the line intensity after a solar flare.

The evolution of the FWHM of the detectors is shown in Figure 4.5, which shows linear increases with cut-offs and restorations over time. The constant bombardment of the detectors leads to a degradation of the Ge lattice structure. This causes incomplete charge carrier collection and broadens the intrinsic line width of the detectors. Annealing phases, that are conducted ≈ twice per year, are intended to restore the Ge lattice structure and reduce the degradation effects. This restores the detector resolution and causes the sharp cuts in resolution (cf. Figure 4.5). As the resolving power of the Ge detectors is governed by Poisson statistics, the absolute values for the lines' widths increase with increasing line energy. However, the relative values $\Delta E/E$ decrease, which means a higher relative resolving power with increasing energy E. The line peak positions show the same saw-tooth behavior as the FWMH over time. This is again caused by the degradation of the detectors. The detectors are automatically calibrated in energy at the Integral Science Data Center (ISDC) per revolution, utilizing a symmetric Gaussian to fit the line peak position in channel space of SPI electronics. However, the energy degradation is not only visible in energy space but also in channel space. Therefore the centroid values for the lines used in determining the

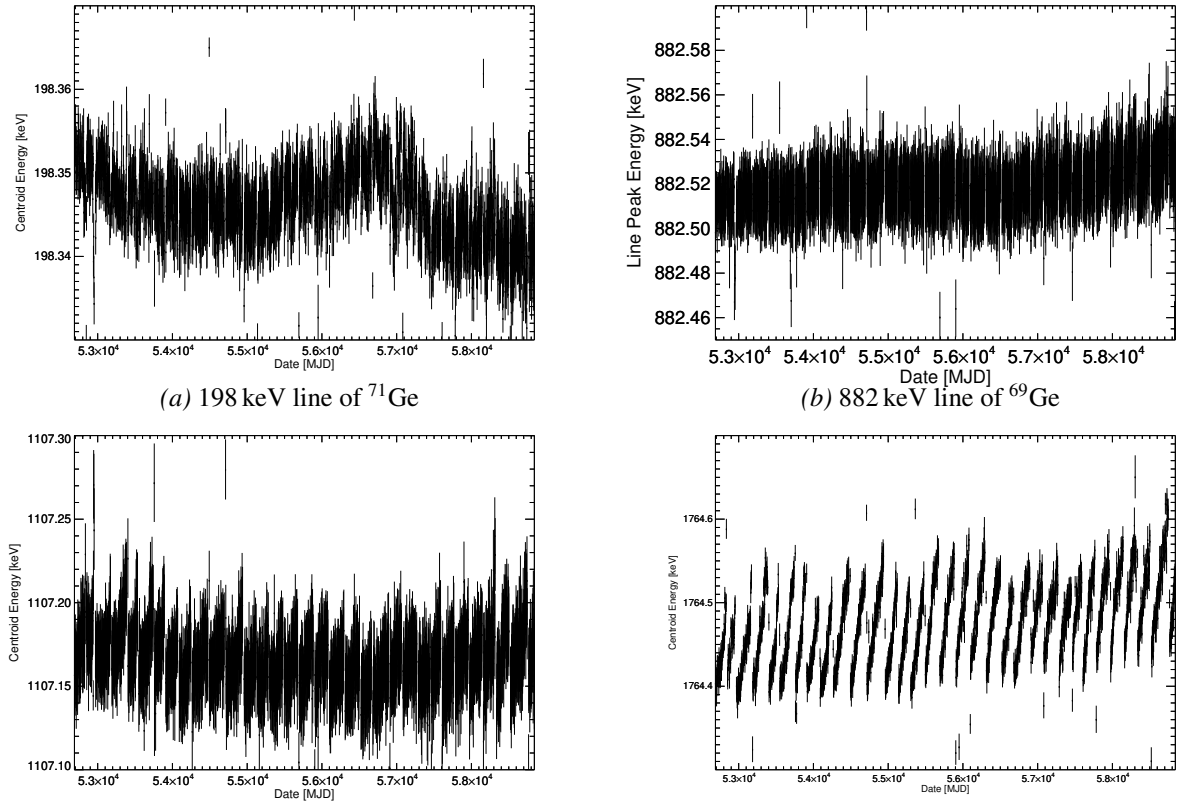

(a) 198 keV line of ^{71}Ge

(b) 882 keV line of ^{69}Ge

(c) 1107 keV line of ^{69}Ge

(d) 1764 keV of ^{204}Bi

Figure 4.6: Shift of the observed background line peak energies with time.

peak channel numbers at ISDC are shifted towards lower channels with increasing detector degradation. The peak position are aligned with the laboratory determined centroid energy of the calibration lines. However, calibrating with symmetric Gaussian lines shifts the peak positions by more than $E_0 - \tau$. Therefore the peak positions shift towards higher energies with increasing detector degradation, when determined by using an asymmetric Gaussian, which provides the correct, degradation adjusted peak positions (figure 4.6).

The drifts in spectral resolution and line peak positions are appropriately accounted for by fitting the database per orbit and detector. The variations of the background strength within an orbit are accounted for by an external measurement, which traces the variation of the incident CR flux on a sub orbit time scale. The variation of the CR strength within an orbit amounts to $\leq 5\%$. A first detailed list of characterized SPI background lines with their assigned isotopes can be found in Weidenspointner et al. (2003). An updated version of this list is available in Diehl et al. (2018). This also contains pattern characterization of lines and an in-depth description of the background. Viability tests for astrophysical measurements are given in Siegert et al. (2019).

4.2.4 Treating the Instrumental Background in the Vicinity of the ^{44}Ti Lines

In this section, the above described treatment of the instrumental background is shown in the vicinity of the three dominant ^{44}Ti lines. The background is modeled with 48 lines in the energy range 20 – 100 keV and 18 lines in the energy range 1115 – 1200 keV. In Figure 4.7 the background counts, integrated for all observation windows in orbit 43, are shown for detector 00. The spectrum is fit with equation 4.5, however, the high energy region is subdivided into smaller sub ranges, as indicated by the vertical gray lines in Figure 4.7.

In both displayed regions, a total of 66 individual background lines are necessary to adequately described the mission-integrated spectrum. In the description of the spectral shape for one orbit and one detector (cf. Figure 4.7) some of the lines are too weak to be recognized without a statistical fit. The background description is built on an empirical approach, not a physical one, i.e. the number of lines is not predetermined from the presence of isotopes in the instrument. The background line identification as stated in table 4.1 is mainly built on heuristic arguments. The main characteristic used in identifying the background lines are their abundance distribution in the satellite (e.g. the strongest lines are commonly produced by the abundant germanium group isotopes, cf. Figure 4.3e) and the background lines' detector pattern (see Figure 4.4f). However, multiple nuclear transition processes can lead to the presence of a single line composed of several overlapping, weak background lines.

From the background parameter database, the behavior of the background is predicted for the data sets. The most important predictions are the relative intensity patterns of the background components, which are different for the continuum and the line contributions as shown in section 4.2.3. These then are merged into a background pattern, which is scaled to an observation period on a sub orbit timescale. The short term variations in background intensity level due to varying CR activity are traced by an external measure. Here, the absolute number of saturated germanium detector events are used to scale the variation of the background level per observation period. Even though the background intensity fluctuations only amount to a few per cent over the period of one orbit, a re-normalization is necessary as the celestial signal only accounts for $\lesssim 1\%$ of the total counts in the respective energy bins. The absolute normalization of the background level are fit according to section 4.1, equation 4.2 simultaneously to the normalization of the celestial contributions. The observations, dedicated to the celestial point sources of interest, commonly last for periods of less than one orbit. Therefore the absolute background count rate per orbit can be offset from the count rate in the period during which the point source is in the instruments field of view.

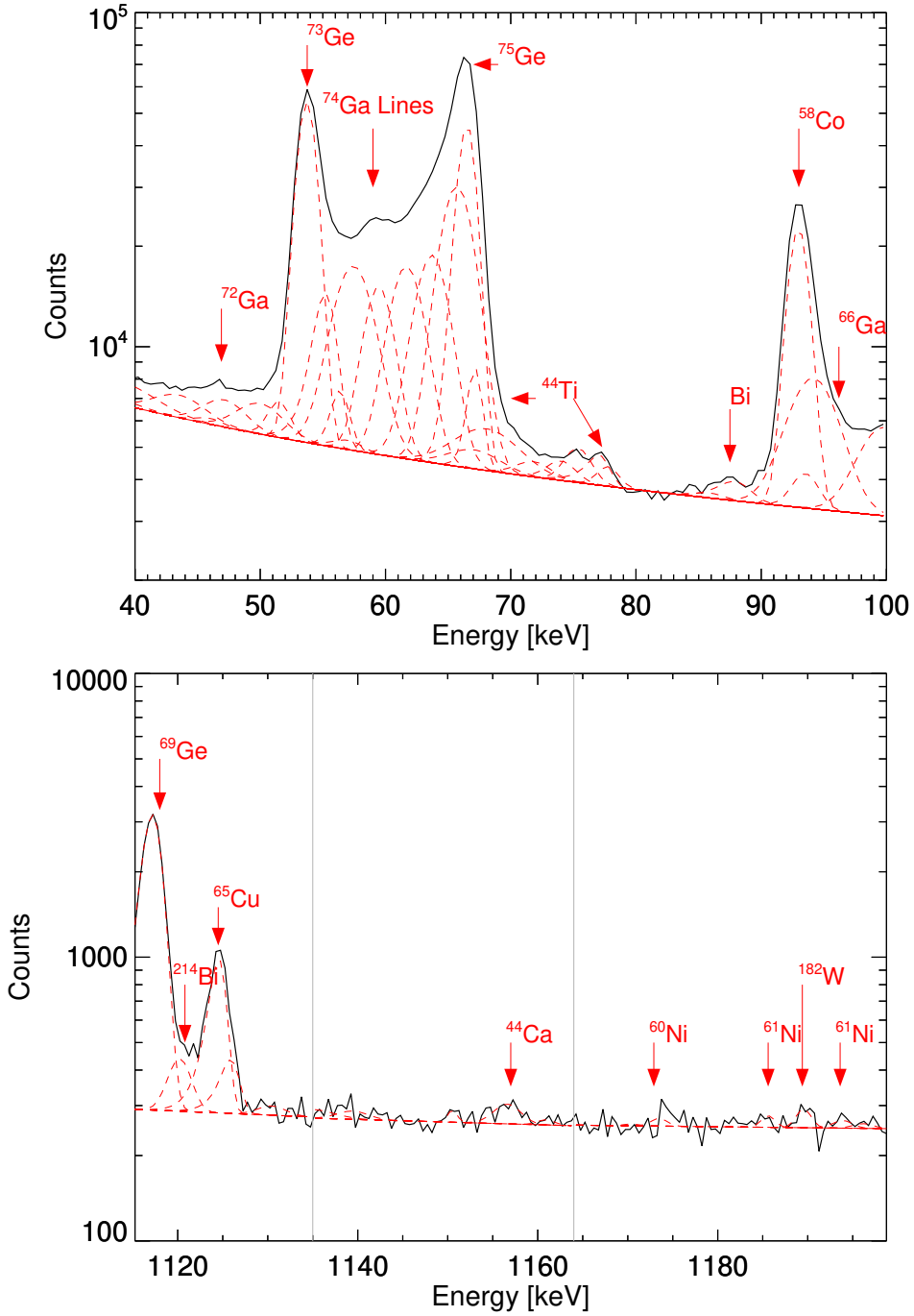

Figure 4.7: Background spectrum in the vicinity of the ^{44}Ti decay lines. The black spectrum are the integrated counts in the respective energy regions measured by the entire camera in the time span between orbits 43 and 131. The red dashed lines are the best fit models describing the background with equation 4.5. The gray vertical lines indicate the individual energy sub regions into which the background model is divided.

Table 4.1: Strong background lines in the vicinity of the ^{44}Ti decay lines. The table only contains lines dominating the background in Figure 4.7. Adopted from Diehl et al. (2018). Lab energies are the laboratory determined line energy of the respective nuclear de-excitation processes.

Energy [keV]	Rate [ph/s]	Process	Lab Energy [keV]
23.70(6)	0.28(6)	^{71m}Ge(IT)^{71}Ge	23.438(15)
25.10(3)	0.13(1)	^{58m}Co(IT)^{58}Ge	24.889(21)
30.6(4)	0.03(3)	^{28m}Mg(β^-)^{28}Al	30.6382(7)
53.75(1)	0.9(1)	^{73m}Ge(IT)^{73}Ge	53.440(9)
55.55(5)	0.23(3)	^{73}Ga(β^-)^{73}Ge	55.42(10)
56.71(2)	0.07(2)	^{74m}Ga(IT)^{74}Ga	56.559(10)
57.87(3)	0.20(3)	^{74m}Ga(IT)^{74}Ga + L	57.75
59.61(2)	0.32(4)	^{74m}Ga(IT)^{74}Ga	59.7
61.72(2)	0.30(4)	^{75m}Ge(IT)^{75}Ge	62.0(2)
63.61(3)	0.38(4)	^{73m}Ge(IT)^{73}Ge + K	63.33
65.82(5)	0.86(1)	^{75m}Ge(IT)^{75}As	66.00
66.65(7)	0.63(1)	^{75m}Cu(IT)^{75}Cu	66.2(4)
67.64(4)	0.19(4)	^{44m}Sc(IT)^{44}Sc	67.8679(14)
68.68(6)	0.10(2)	^{73m}Ge(IT)^{73}Ge	68.752(7)
74.96(4)	0.03(2)	Bi-Kα_2	(74.8157(9)
77.37(3)	0.02(2)	Bi-Kα_1	77.109(1)
87.46(4)	0.018(7)	Bi-Kβ_1	87.35
92.89(1)	0.38(5)	^{58}Co(IT)^{58}Co	92.41
94.27(5)	0.09(1)	^{67m}Zn(IT)^{67}Zn	93.311(5)
96.20(6)	0.09(1)	^{66}Ge(EC)^{66}Ga	96.34(2)
1116.9(1)	0.09(1)	^{69}Ge(EC)^{69}Ga + K	1116.90
1120.8(1)	0.0036(1)	^{214}Bi(EC)^{214}Po	1120.287(10)
1124.61(8)	0.047(9)	^{65}Zn(EC)^{65}Cu + K	1124.53
1157.04(6)	0.0012(2)	^{44}Sc(EC)^{44}Ca	1157.002(4)
1160.67(7)	0.0004(1)	^{44}Sc(EC)^{44}Ca + K	1160.77
1173.28(6)	0.0018(8)	^{60}Co(β^-)^{60}Ni	1173.228(3)
1185.63(7)	0.00035(8)	^{61}Cu(EC)^{61}Ni	1185.234(15)
1189.47(6)	0.0015(3)	^{182}Ta(β^-)^{182}W	1189.040(3)
1193.60(7)	0.0005(1)	^{61}Cu(EC)^{61}Ni + K	1193.57

4.3 Extending the Background Modeling Approach to SPI's High Energy Range

4.3.1 Readjustment of SPI Background Integration Time

In this thesis, I apply, for the first time, the general background modeling approach to SPI's high energy range above 2 MeV. This requires an adjustment of the background integration time. In this region double events, that only contribute a minor fraction of events in the low energy range, constitute up to 40% of all measured photons. Therefore, the double events are also included in the analysis of SPI's high energy range. Background for double events is modeled using the same approach as for single events.

The SPI background decreases monotonically with increasing energy up to ≈ 5000 keV (see Figure 4.1). Between 100 keV and 1 MeV the continuum's intensity decreases following a power law with an index of ≈ -1. The power law steepens above 1 MeV, with a power-law index of ≈ -3. At higher energies, the background continuum is dominated by Compton scattering of high energy photons emitted in the various nuclear de-excitation processes. As a consequence the background above 5 MeV flattens to a near constant behavior. In addition to the overall decrease in background intensity, the photo peak efficiency of interactions with the detector material decreases. As the background counts are measured without any prior knowledge of the spectral form of the background creating processes, the absolute measured counts per decay line decrease significantly due to the energy redistribution from Compton scattering and escape peaks (see section 3.1.2). Due to this decrease of photon count rate in SPI's high energy range of more than two orders of magnitude with respect to SPI's low energy range, the background cannot be determined on a revolution timescale. The high energy range constitutes an energy region of several MeV with background count rates varying by an order of magnitude. An integration time spanning the period between two annealing phases is used for determining the background parameters. As a consequence, temporal information on the degradation in the energy resolution and line peak shifts are lost. The obtained energy degradation and peak shifts only resemble the average degradation between two annealing phases.

In the low energy range the origin of strong background lines can usually be linked to the known decay energies of specific isotopes. In the high energy range, the production of positron-electron-pairs is a dominant process of photon interaction with detector material. Consequently, lines that are linked to the first and second escape peak start to arise (cf. section 3.1.2).

In general, prompt background lines follow the CR intensity of the sun (see section 4.4, ^{69}Ge,^{71}Ge). The normalization, when building the background model from the database, needs to take the variation of the CR strength between two annealing phases into account. In the high energy range, normalization of the background (equation 4.2, $\theta_{i,t}$) is commonly fit on an annealing phase timescale. Similar to the inter pointing variation during one orbit in the low energy range, the long term background intensity variation induced from the solar cycle over half a year need to be accounted for. In this thesis, the correct relative normalization between the beginning and the end of an observation period is achieved by scaling with the saturated germanium detector events (GeDSat). This tracer counts all events in the camera that deposit more than 8 MeV in the detectors. Such events originate from the interaction of energetic charged particles, that are also the origin of nuclear excitations in the camera. As the majority of high energy lines above 2 MeV is due to the prompt de-excitation of Ge-group isotopes in the camera (see Weidenspointner et al. 2003), the background intensity variations and GeDSat events are closely correlated. The GeDSat rate is sufficient to trace the inter pointing and inter orbit variations.

4.3.2 Consistent Trends in the High Energy Background Model

The high energy background database is constructed by fitting the spectral shape per detector, integrated over the time span between two annealing phases. While this causes a loss of information of the temporal degradation of the detector resolution and the shifts in line peak positions, the validity of extending the background modeling approach can still be inferred from the long term stability of the background detector pattern. In Figure 4.8 the stability of the detector pattern for strong high energy background lines is shown for epoch 5. This epoch spans the revolutions 931 – 2047, which starts after the last detector failure in revolution 930. This epoch is chosen as it provides the longest time span for which a stable detector configuration is present. As a comparison, the detector pattern for epoch 5 of the continuum at 780 – 920 keV is also included in Figure 4.8. As shown in Figure 4.3, background components that have an homogeneous source distribution in the satellite produce a flat intensity distribution in the detectors. However, due to detector failures, the flat distribution is distorted (compare Figure 4.8f and 4.4d). The continuum distribution at high energies (figure 4.8a, 4.8b) for epoch 5 follows the same behavior as the continuum in the low energy range (detector number 00 – 18). This is reasonable, as the sum of all processes producing continuum background still has an isotropic source distribution in the satellite. Also background lines, emitted from sources external to the detector array (figure 4.8c) follow the trend of a formally flat intensity distribution in the detectors. In general, the difference in relative intensity between the physical 19 detectors and the double detectors resembles the difference in effective detector areas. In contrast to that, the 3800 keV line of Ge shows the typical behavior of the Ge group lines. The inner 7 detectors see more flux than the surrounding detectors, and the detectors on the edges of the camera show the typical zig-zag-pattern, adjusted for the detector failures. No significant offset in the relative intensity of the double detectors is present for the Ge lines. This is because the intensity is not governed by the irradiation from an external source and is therefore not represented by the effective area under which the source is seen. The intensity distribution is rather governed by the effective detector volume from isotropic irradiation due the embedding in the camera array, which is almost uniform over detector range 00-60.

In general, the resolution of the Ge detectors is dependent on the detector temperature (Attié et al. 2003). During ground calibration, it was determined that the energy resolution (FWHM) follows the function

$$\mathrm{FWHM}_{\mathrm{Calibration}} = \mathrm{F}_1 + \mathrm{F}_2\sqrt{E} + \mathrm{F}_3\mathrm{E} \tag{4.11}$$

with $\mathrm{F}_1 = 1.54$, $\mathrm{F}_2 = 4.6 \times 10^{-3}$ and $\mathrm{F}_3 = 6.0 \times 10^{-4}$ at a temperature of 90 K. Values were determined for lines below 2 MeV. However, ground calibration does not resemble the in-flight performance of the Ge detector array and should only be used as consistency check. In Figure 4.9 the in-flight FWHM at different energies is shown in the extended range up to 8 MeV for the ground calibration and in-flight performance in gray and black, respectively. The best fit parameter for the calibration function determined from the time averaged (degraded) detector resolution are $\mathrm{F}_1 = 1.35$, $\mathrm{F}_2 = 3.4 \times 10^{-2}$ and $\mathrm{F}_3 = 3.0 \times 10^{-4}$. In contrast to the almost linear relation between energy and detector resolution seen during ground calibration, the extension to higher energies shows a clear tendency that the FWHM of the detectors is also proportional to the square root of the energy.

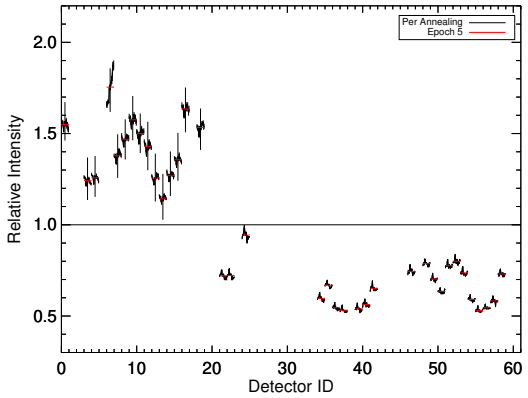

(a) Continuum in the energy range 3500 – 3600 keV

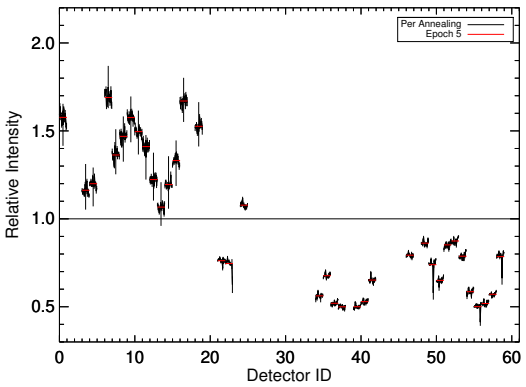

(b) Continuum in the energy range 6450 – 6550 keV

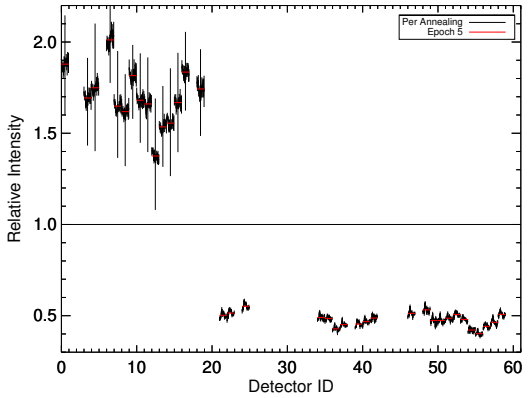

(c) ^{24}Na, 2754 keV

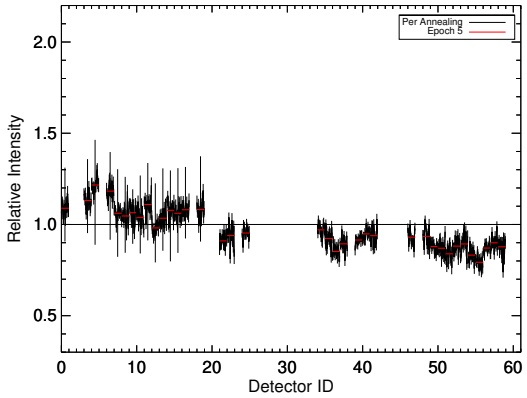

(d) ^{66}Ga, 3800 keV

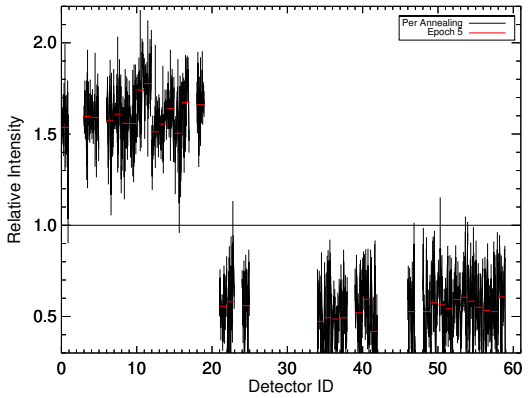

(e) ^{48}Ti, 6760 keV

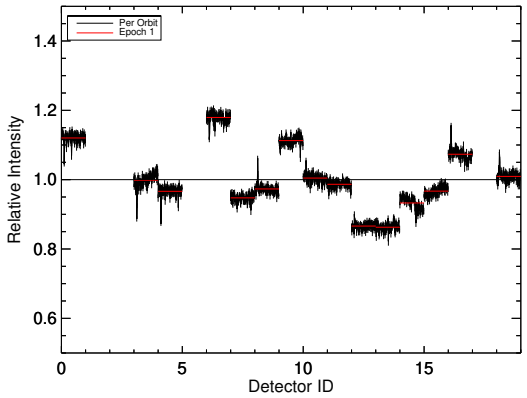

(f) Continuum 780 – 920 keV

Figure 4.8: Relative intensities of the background lines and continuum emission normalized to the number of working detectors for the physical (#00 – 18) and the pseudo detectors (#19 – 60). Black data points show the relative intensity of the detectors per annealing phase. The red line is the average over the fifth epoch (orbit 931 – 2047). The missing relative intensities of several detectors are caused by the failure of the respective physical and connected pseudo-detectors. Panel (f) shows the detector pattern of the continuum in the energy range 780 – 920 keV during epoch 5. For comparison, the continuum in this region produces a flat detector pattern in epoch 1, when all 19 physical detectors were still operational. Likewise, the continuum at high energy shows a pattern which is significantly offset from a flat distribution. This is, however, caused by the detector failures. The continuum pattern is still flat during epoch one where all detectors are operational.

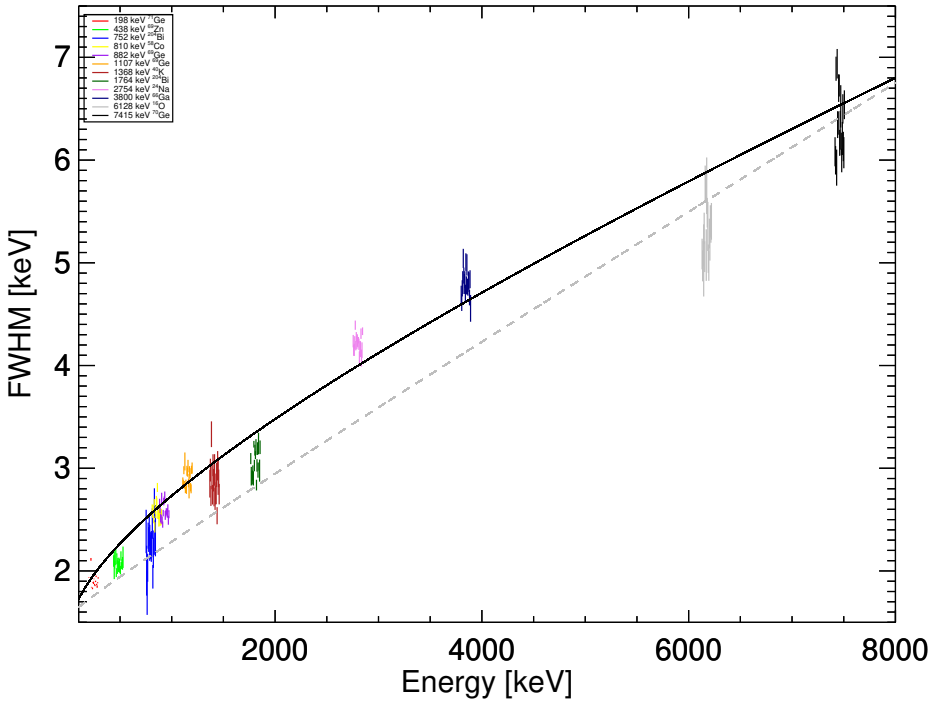

Figure 4.9: FWHM of background lines in the time period of orbits 43 – 92. In the energy region above 2 MeV the detector resolution can only be determined on an annealing timescale (i.e. half-year) and therefore resembles the average detector resolution per integration time period. The non degraded detector resolution can be obtained from the FWHM of background lines directly after an annealing. Below 2 MeV, the mean detector resolution of the inter annealing phase is included. The FWHM are shifted around their respective lines for illustration purposes only. Over the entire energy range, the FWHM can be represented by equation 4.11 with the exception of Doppler broadened lines (e.g. 511 keV positron annihilation, 4.438 MeV $^{12}C^{*}$ de-excitation), that are emitted by nuclei in motion with respect to INTEGRAL. The black line shows the in-flight calibration obtained for the time averaged detector resolution. The ground based calibration (Attié et al. 2003) is included in gray.

4.3.3 Sensitivity in SPI's High Energy Range

To derive the sensitivity of the instrument in the high energy range, a data set containing observations of the Galactic high latitude region, centered on (l/b) = (-70,70), is used. The sensitivity is estimated for epoch one in which all 19 detectors were operational, specifically revolutions 71, 72, 77, 78, 89 and 90 are used, accumulating a total exposure of 507 ks. The sensitivity is estimated for an exposure of 1 Ms at a 3σ sensitivity level from these high latitude observations. A conservative estimate is derived, where the sensitivity is estimated in a band around specific lines of astrophysical interest, that is twice the lines' FWHM at the respective energies. The sensitivity is estimated from the uncertainty of an arbitrary point source at the location (l/b) = (-70°,70°). No astrophysical counterpart that is detectable within SPI's sensitivity is present at this location, and the uncertainty of the fitted spectrum at this location should therefore only be introduced by statistics of the background counts.

The sensitivity is correlated with the strength of the background counts. Specifically, the decay line of ^{24}Na at 2754 keV and the de-excitation line of ^{16}O at 6128 keV are the strongest background contributions in the respective energy regions. In table 4.2 the energy bands of

Table 4.2: SPI sensitivity estimates based on background observations in the high energy range for narrow line emission. Sensitivity is given at a 3σ level for a 1 Ms observation in the energy band around relevant astrophysical de-excitation lines. Specifically ^{12}C, ^{15}N, and ^{16}O are de-excitation lines introduced by the interaction of CRs with the ambient medium.

	Centroid [keV]	FWHM at centroid [keV]	Energy band [keV]	Sensitivity (3σ) [10^{-5} ph cm^{-2} s^{-1}]
^{2}H	2224	4.5	2220 – 2228	8.9
^{24}Na	2754	4.2	2750 – 2758	10.1
^{12}C	4434	4.7	4429 – 4438	3.9
^{15}N	5298	5.4	5293 – 5303	3.7
^{16}O	6129	5.6	6122 – 6133	8.7
^{16}O	6917	7.3	6910 – 6924	5.4
^{16}O	7117	7.0	7110 – 7124	6.5

astrophysical interest and the estimated sensitivities are listed. For a data set containing observations past the first epoch, the sensitivity estimates listed in this table have to be scaled with the reduced collection area, accordingly. The launch of the INTEGRAL mission was coinciding with a solar CR flux minimum (cf. Figure 4.4a). Hence, the background level in orbits 70–90 is at a minimum, with respect to the rest of the mission. As the line sensitivity is governed by the background count rate, the sensitivity given in table 4.2 is the highest achievable sensitivity for a 1 Ms observation. For an observation, conducted later in the mission, the line sensitivity with the same exposure is reduced.

4.3.4 The Peculiar Behavior of the ^{12}C Background De-Excitation Line

Among other isotopes a feature is found in the line of the ^{12}C isotope, that is distinctly different from the normal background line behavior. For the entire mission duration, the lines FWHM is significantly higher than the instrumental resolution at the respective energy of 4438 keV. In Figure 4.10 the energy region covering the broadened ^{12}C line is shown for INTEGRAL revolution 150. The FWHM of the line is (66.5 ± 4.7) keV, while the detector resolution, determined from the ^{66}Zn decay line at 4470 keV, is (4.8 ± 0.8) keV. In general, instrumental lines are emitted in the rest frame of the satellite. Consequently, the FHWM of an instrumental line is given by the (degraded) resolution of the detector and shows no further line broadening. However, when photons are emitted, that are in motion with respect to the detector array, the measured line width is additionally Doppler broadened. The exact origin of this Doppler broadening is not known. Two possible explanations are discussed in the following:
First, I consider the possibility of broadening due to thermal motion assuming that the line is emitted in hot gas containing ^{12}C nuclei. In this case I consider the sun as the origin of ^{12}C line, where the excitation of ^{12}C is due to particle interaction in the stellar atmosphere. The FWHM of a thermally broadened line is given by

$$E_{FWHM} = \frac{2E_0}{c} \times \sqrt{\frac{kT}{m_{^{12}C}}} \tag{4.12}$$

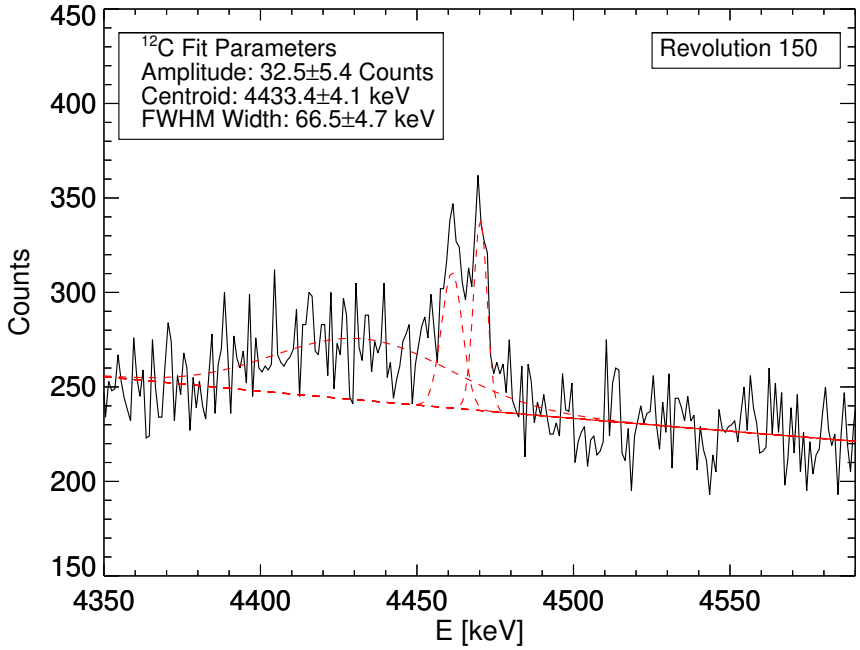

Figure 4.10: Background in the energy range containing the ^{12}C de-excitation line at 4438 keV. The spectrum shows the camera integrated counts per 1 keV bin in INTEGRAL orbit 150. Two additional lines are present at 4461 keV and 4470 keV, produced from an electron capture decay of ^{66}Ga. The parameters in the legend are the best fit values describing the ^{12}C de-excitation line.

where E_0 is the centroid energy of the carbon line, k is the Boltzmann constant, c is the speed of light, T is the gas temperature and $m_{^{12}C}$ is the mass of the carbon atom. Rearranging equation 4.12 yields a temperature for the thermal broadening of 66 keV at 4434 keV line energy of

$$T = \left(\frac{E_{FWHM} \times c}{2E_0}\right)^2 \frac{m_{^{12}C}}{k} = 2.9 \times 10^9 K. \tag{4.13}$$

While the temperature of the sun is $\approx 10^6$ K at the corona and 6000 K on the surface, even further in the solar interior, temperatures of maximum 15×10^6 K are reached. Thermal broadening can therefore be excluded as explanation for the broadening of ^{12}C line. I also exclude Doppler Broadening of the line due to the rotation of the sun as the average rotation velocity is 2 km s^{-1}, while velocities of more than 1000 km s^{-1} are required.
Secondly, I consider the case where the broadening is caused by the mechanism leading to the excitation of the ^{12}C. Inelastic scattering transfers recoil energy from the scattered particle to the nucleus, which remains in an excited state (cf. section 2.7). The nucleus emits a de-excitation photon before it is slowed down, which means that the nucleus is in motion with respect to SPI's camera. The dominant reactions for energy transfer that produce an excited ^{12}C nucleus are: ^{12}C(n,nγ)^{12}C, ^{12}C(p,pγ)^{12}C, ^{16}O(n,n$\alpha\gamma$)^{12}C, ^{16}O(p,p$\alpha\gamma$)^{12}C. Doppler broadening is also found for the nuclear de-excitation lines of ^{13}C and ^{27}Al. The location, where the interactions occur, can not be unambiguously identified. The sun is a potential source, as all three isotopes are present in the stellar atmosphere. Likewise, the excitation can also occur in Earth's atmosphere, which is composed of 20% oxygen and traces of carbon molecules. The satellite itself can also contribute to the emission in all three lines.

Carbon is present in the plastic components of the satellite, the ACS is an array of BGO crystals that contain oxygen and the detectors are embedded in aluminum.

The background lines of all three isotopes further show a peculiar behavior with respect to temporal variation of the incident CR flux. During phases of strong solar radiation (solar flares) the intensity of prompt background lines from satellite material scales with the elevated incident CR flux. The line strength of the peculiar background lines, however, is significantly increased, which cannot be explained by the influence of intense CR flux on the satellite alone. Figure 4.11 shows the background in the energy range 3850 – 4600 keV. During revolutions without solar flares (Figure 4.11, left panel) the broadened ^{12}C line produces a minor contribution above the underlying continuum. Furthermore, several other background lines are present in the spectrum. The double peaked background lines originate from isotopes in the Ge group. The first peak is at the energy of the respective decaying state in the excited daughter nucleus, following the EC decay on the parent isotope. This decay predominantly creates a vacant state in the innermost atomic shell of the daughter nucleus. The second peak is due to the simultaneous detection of X-ray photons, emitted when the vacant state is repopulated by an electron from a higher atomic shell. As the radioactive ^{66}Ga is produced by the neutron capture of ^{65}Ga, the background pattern for the ^{66}Ga decay is resembled by the background pattern of the Ge group lines. In addition, a background line of radioactive ^{24}Na, which decays via β^- decay, is present at 4122 keV.
However, during solar flares, the energy region is dominated by the ^{12}C decay line. In Figure 4.11, right panel, the energy range is shown for INTEGRAL revolution 1192, containing background modulation from a solar flare event. In the energy region 4400–4550 keV, the contribution from both ^{66}Ga lines is fully suppressed by the presence of the strong ^{12}C background line. The lines has a FWHM of (66 ± 0.8) keV and is centered at (4452.7 ± 0.3) keV. The integrated counts in the line are $(81.0 \pm 1.9) \times 10^3$. At (3945.8 ± 3.0) keV, an additional line is required to describe the spectrum. The line's FWHM is (84.3 ± 3.1) keV, and it contains $(14.1 \pm 0.8) \times 10^3$ counts. A second characteristic is approximated with a Gaussian line, which is centered at (4224.9 ± 1.9) keV. The integrated counts in the line are $(53.5 \pm 3.8) \times 10^3$.

The width of the ^{12}C line in a solar flare revolution is identical to the width in a quiescent revolution. I therefore conclude, that the line originates from the same, unidentified source in both cases. In addition, two distinct characteristics of energy redistribution (cf. section 3.1.2) to smaller energies due to partial energy deposition in the detectors are evident. The line, centered at 3946 keV is the first escape peak of the ^{12}C line at 4453 keV. The difference in energy peak position $\Delta_E = (507 \pm 3.0)$ keV is compatible with the rest mass energy of an electron. The second, additional line corresponds to the Compton edge. The description of the distorted Compton edge by a convolved Gaussian is only a coarse approximation. Nevertheless, the location of the line centroid at 4224 keV is compatible with the expected maximum energy of a backscattered electron of 4208 keV. In combination, the line of the first escape peak and the approximated Compton continuum contain $(67.6 \pm 3.9) \times 10^3$ counts. This suggests, that the fraction of photons counted in the full energy peak at 4438 keV with respect to all measured photons with incident energy of 4438 keV is

$$\mathrm{eff}_{\mathrm{Full}} \leq \frac{81.0}{81.0 + 67.6} = 54.5\%. \tag{4.14}$$

The effects of energy redistribution are approximately accounted for by the SPI IRF.

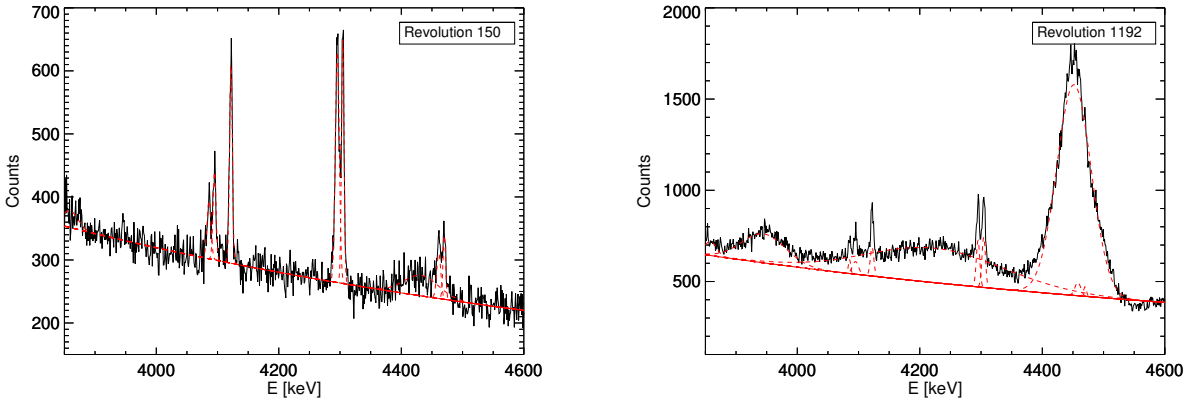

Figure 4.11: Background in the energy range containing the ^{12}C de-excitation line at 4438 keV. The left panel shows the camera integrated spectrum of the background during a revolution without increased CR intensity of the sun. The right panel shows the background in the same energy range during a solar flare. In the right panel, two additional lines are required to describe the spectrum. Both lines arise from the energy redistribution of the detectors with respect to an incident 4438 keV photon. One line accounts for the first escape peak at 3927 keV, and the second approximates the distorted Compton edge.

The presence of background lines, whose strength scales disproportionate with the incident CRs flux, implies an adjustment in the treatment of the high energy background. As the background parameters for the integrated counts are determined on the timescale between two annealing phases, the presence of a small number, i.e. one or two, of strong solar flares in this period produces a spurious detector pattern in the broad energy range 3850 – 4600 keV, dominated by ^{12}C. This detector pattern deviates from background pattern in a quiescent revolution, as it suppresses the correct background pattern of the ^{66}Ga and ^{24}Na decay lines. Likewise, the presence of other isotopes, whose lines flux is disproportionate to incident CRs flux, distorts the correct detector pattern in other energy regions. To restore the correct background pattern in all other revolutions, revolutions containing solar flares are removed from the data sets and the background modeling in the high energy range. Solar flares are defined by a 3σ deviation of the ^{12}C background line intensity from the median count rate in the adjacent ±20 orbits (see Figure 4.12).

4.4 Background Model Calibration on the Crab Nebula

In order to calibrate the above described extension of the background model to SPI's high energy range, observations of the Crab nebula are evaluated. With a diameter of ≈ 5', the Crab nebula can be considered as a point source in the analysis. It has a constant intensity spanning the mission duration of INTEGRAL with only small variations in the intensity level of $\approx 2 - 3\%\,\mathrm{yr}^{-1}$, that scatter around a stable mean (Wilson-Hodge et al. 2011). The spectrum at hard X-ray energies is well known and the source is bright enough to provide a high signal to noise ratio at orbit timescale. It is expected to be significantly detectable at MeV energies for prolonged exposure, estimated from the extension of the hard X-ray spectrum (e.g. Strickman et al. 1979; Pravdo et al. 1997; Kuiper et al. 2001; Ling & Wheaton 2003; Madsen et al. 2017). Commonly, the Crab nebula is observed twice per year with INTEGRAL following annealing phases. These observation campaigns are intended for

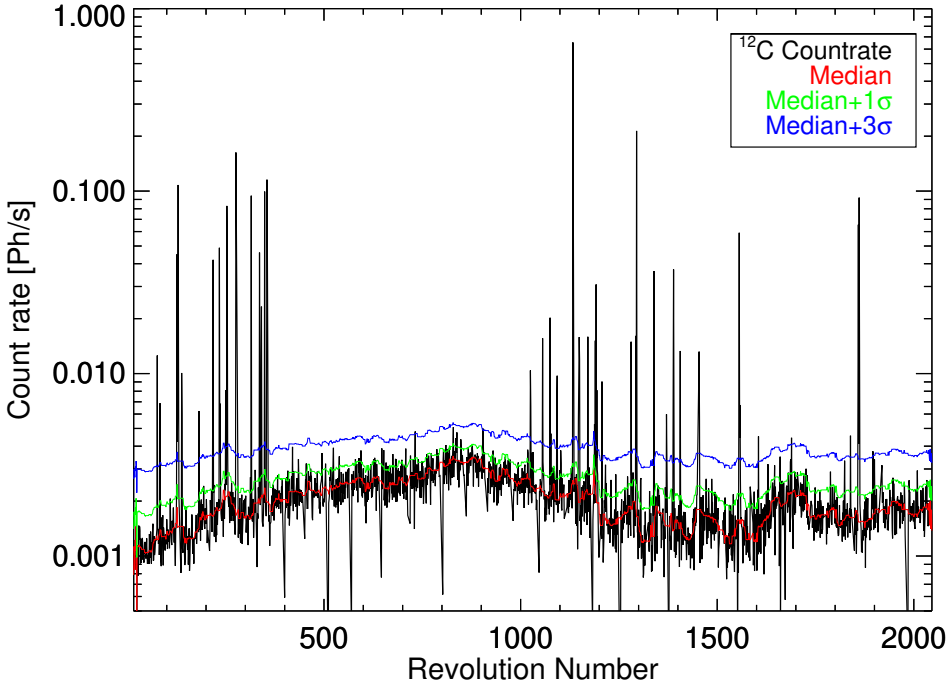

Figure 4.12: Temporal variation of the ^{12}C count rate. Also included are the 1 and 3σ deviation from the median values per 20 revolutions. The background intensity of the ^{12}C line follows the solar intensity, which is reasonable as this line can be considered as prompt background line. Deviations are found in revolutions with solar flare activity.

performance testing of the instruments. The instrument calibration itself was conducted on ground and with Monte-Carlo-Simulations. During 17 yr of operation a total exposure of 8.8 Ms on the Crab nebula was accumulated, composed of 3907 SPI pointings. Data from all observations campaigns are used and observations with exotic dithering patterns are not excluded.
To increase the signal to noise ratio, all data sets, albeit distributed over long periods, are summed into one large data set that contains the time series of all observations simultaneously. The spectrum is extracted from the time series of the count spectra according to equations 4.2 and 4.4. The spectrum is extracted in 0.5 keV bins in the energy region from 40 keV to 2000 keV and in 5 keV bins in the energy region 2 MeV to 8 MeV.

Before the extracted spectrum is analyzed, the performance of the newly developed high energy background model is evaluated. As figure of merit the Mighell χ^2 statistic (Mighell 1999), given by

$$\chi^2 = \sum_{i=1}^{N} \frac{(d_i + \min(d_i, 1) - m_i)^2}{d_i + 1} \tag{4.15}$$

is utilized to determine the quality of the fit per extracted energy bin. Here, d_i are the measured counts and m_i are the modeled counts per pointing i. The model includes the sum of the anticipated background and celestial counts. The non-modified Pearson χ^2_P statistic, which approximates the negative logarithm of the maximum likelihood, is only valid for data with Gaussian uncertainty, which is not the case for the Poisson distributed SPI data.

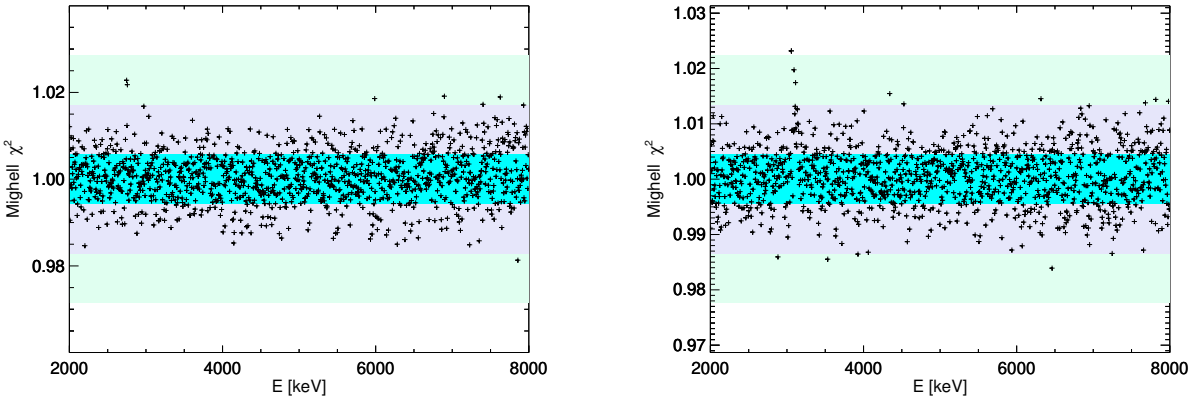

Figure 4.13: Evaluation of the high energy range background model performance. Reduced χ^2_{red} distribution for single events (left) and double events (right) in SPI's high energy range. The χ^2_{red} scatters around the desired $\chi^2_{\text{red}} = 1$ value. The 1,3, and 5σ uncertainty band are included as shaded areas. With the exception of the energy range 2900–3300 keV, the χ^2_{red} values (see text) are within the expected scatter.

Therefore, the Mighell χ^2 statistic is used as figure of merit, which is optimized to analyze Poisson distributed data. The chosen goodness-of-fit criterion is $\chi^2_{\text{red}} \stackrel{!}{=} 1$, given by χ^2/d.o.f. (degrees of freedom), which itself is subject to uncertainty (Andrae et al. 2010). In figure 4.13 the χ^2_{red} in the high energy range of SPI are shown, separated for an analysis of the single and double events. The majority of χ^2_{red} value lie within the 3σ uncertainty band around the ideal $\chi^2_{\text{red}} = 1$ value, indicating a good fit over the entire energy range.
Strong, clustered deviation from the ideal value are only given in the energy range 2900–3300 keV in the double events case. An analysis of this energy range shows, that this behavior is caused by the presence of excess counts in individual pseudo detectors. The spectral shape of the excess counts follows a line-like nature. However, no physical process that leads to the production of these lines can be identified, as the lines are detectable only in isolated revolutions, and typically only for individual pseudo double detector, not the entire camera. Furthermore, no counterpart in the involved single detectors can be identified. These lines are therefore treated as artifacts, and double events in the energy range are, in general, excluded from the analyses.

In addition to the reduced χ^2_{red}, the distribution of residuals, given by

$$\text{Res} = \frac{(\text{d}_\text{i} - \text{m}_\text{i})^2}{\sqrt{m_i}} \tag{4.16}$$

is analyzed. The distribution of residuals is shown in figure 4.14 for the 6 labeled energy regions. The distributions are shown for the combination of the background counts and the celestial emission. Since the celestial counts are accounted for, no deviation of the residuals towards positive values is expected. The residuals follow a normal distribution centered at 0, with a standard deviation $\sigma_{\text{Res}} = 1$, which indicates that the fitted model is a good description of the data, and the background model performs well.

In Figure 4.15 the spectrum of the Crab nebula is shown in the energy range 50 keV to 8 MeV. To increase the statistical significance at which the Crab is detected at high energy,

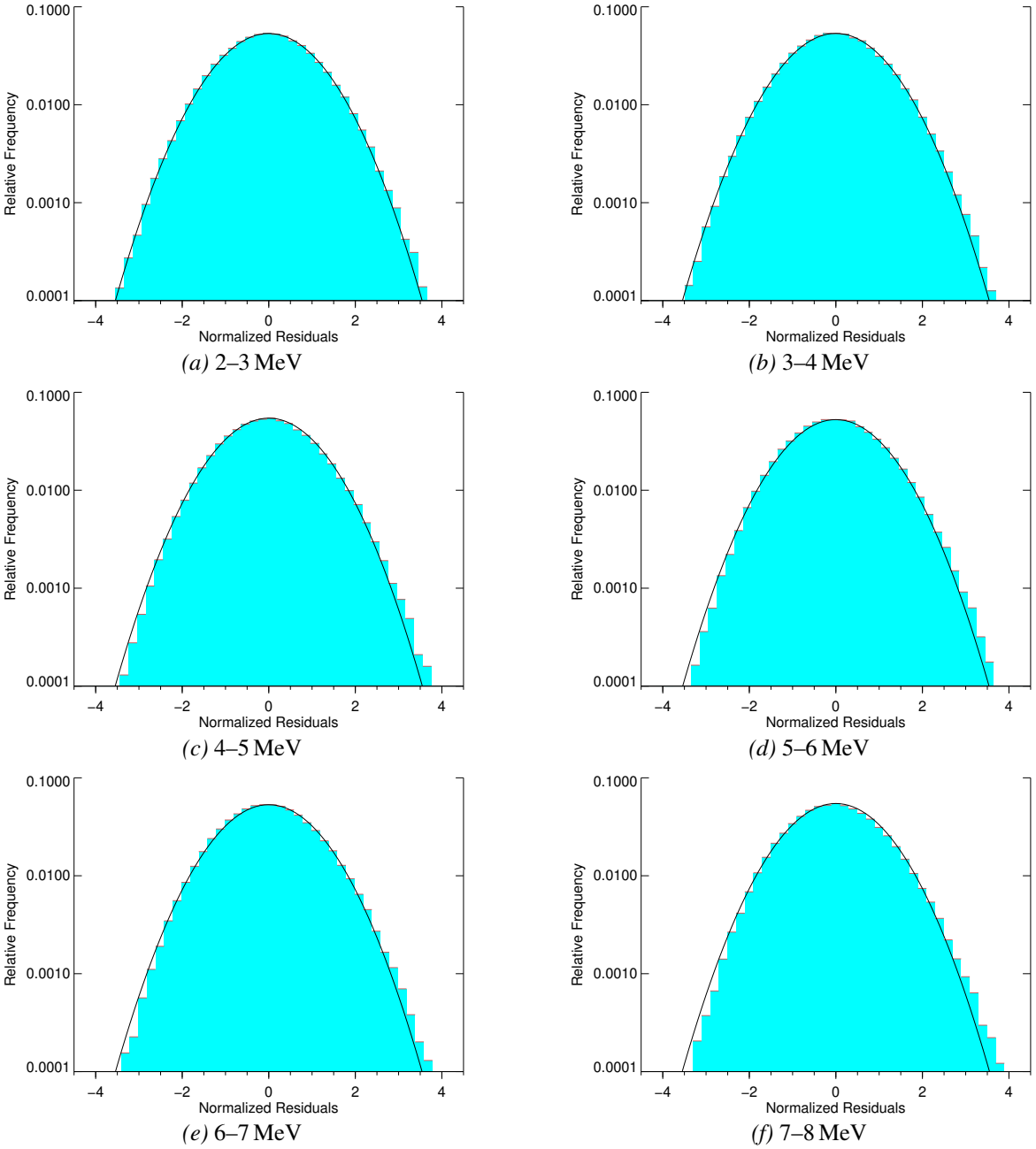

(a) 2–3 MeV *(b)* 3–4 MeV

(c) 4–5 MeV *(d)* 5–6 MeV

(e) 6–7 MeV *(f)* 7–8 MeV

Figure 4.14: Distribution of normalized residuals after fitting the high energy range background model and the celestial emission from the Crab nebula to the data. A normal distribution with expectation value $\mu = 0$ and standard deviation $\sigma_{\text{Res}} = 1$ is overplotted. The residuals are shown for the combined single and double events.

the two event types are combined and analyzed together. The spectral shape will be described by the two outlined models. Previous observations of the Crab nebula with various instrument in the hard X-Ray and γ-ray regime describe the spectral shape of the Crab nebula with a single power law. However, it has been pointed out, that the power-law index of the Crab electromagnetic emission is different in these two regimes. Typically, a broken power law is used to describe the spectral shape in both energy regions, with a hard break at

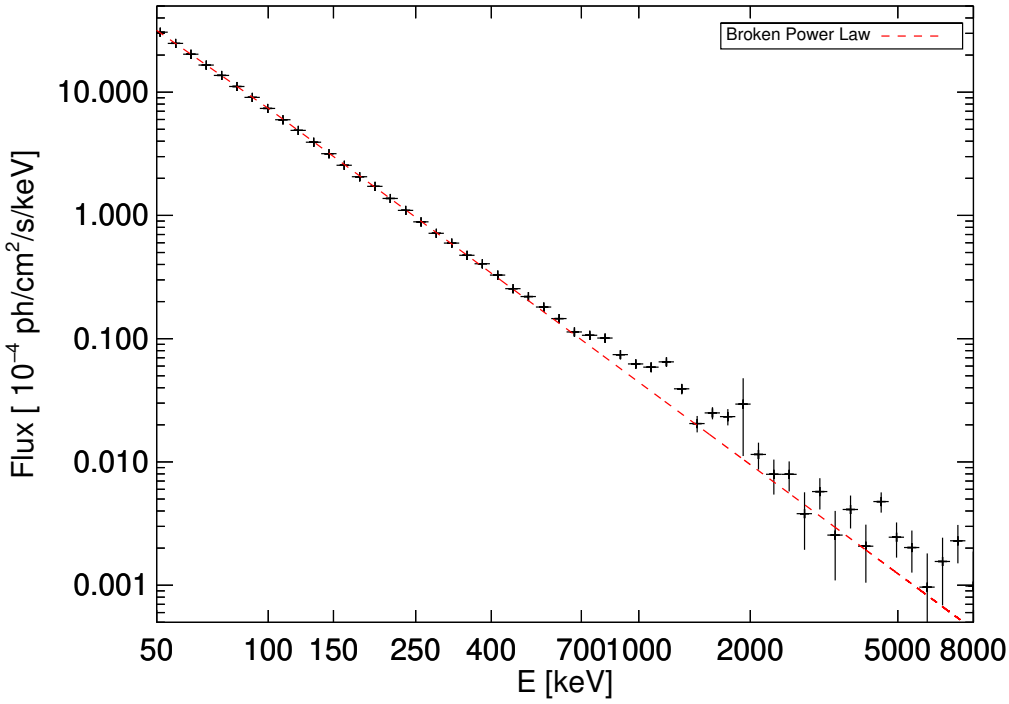

Figure 4.15: Crab spectrum over the energy range 50 keV to 8 MeV. The dashed line is the model representing the spectra with a broken power law. Parameters of the model are given in table 4.3

$\approx$ 100 keV (Strickman et al. 1979; Ling & Wheaton 2003). In general, the best fit values for models in spectral analysis of SPI data in this thesis are determined from a MCMC method, that minimizes the Pearson χ^2 as a test statistic (TS) by utilizing a Metropolis Hasting algorithm. The confidence intervals of all results are estimated from the 68th percentile interval of all sampled values. The best fit values for the model parameters are given in table 4.3.
When fitting the Crab spectrum with a single power law, the spectral shape of the entire emission is mainly fixed by the highly significant signal to noise bins below 100 keV. The single power-law index of $\alpha_1 = 2.13 \pm 0.17$ is therefore in good agreement with values determined in the hard X-ray regime alone with an index of $\approx 2.0-2.1$ (cf. compilation in Kirsch et al. 2005). However, a single power law does not provide a good fit ($\chi^2 = 6183$ for 4592 d.o.f.). When introducing a break in the power-law spectrum at a fixed energy of 100 keV, the fit quality significantly improves ($\chi^2 = 5353$ for 4591 d.o.f.). While the spectral index in the low energy range remains identical within uncertainty $\alpha_1 = 2.10 \pm 0.01$, the spectral index above the fixed break at 100 keV shows a softer spectrum with $\alpha_2 = 2.22 \pm 0.01$. The normalization at 1 keV is N = (11.8 ± 1.5) ph cm^{-2} s^{-1} keV^{-1}, compatible with the flux normalizations presented in Kirsch et al. (2005). The values of both spectral indices are in good agreement with the spectral shapes determined from instruments in the adjacent energy band and earlier SPI data (Jourdain & Roques 2009). Specifically at energies between 750 keV and 30 MeV, a power-law index of 2.23 was determined with COMPTEL data (Kuiper et al. 2001) for the nebula emission. The consistency provides good evidence, that our newly developed background model performs well over the entire high energy range of SPI.

Table 4.3: Crab model parameters. The normalization N is given at 1 keV.

Model Power Law	α_1	α_2	Break [keV]	N [ph cm^{-2} s^{-1} keV^{-1}]	χ^2	d.o.f.
Simple	2.13 ± 0.17			13.3 ± 0.4	6183	4592
Broken	2.10 ± 0.02	2.22 ± 0.03	100 (fixed)	11.8 ± 0.1	5353	4591

4.4.1 Influence of Continuum Sources

In the previous section the Crab nebula was used as persistent source to evaluate the performance of our background model. Besides this strong source, a multitude of hard X-ray sources exist that are detectable within SPI's sensitivity in the 50 – 100 keV energy region, especially in the crowded Galactic center region. Some of these sources are transient and only detectable during strong emission phases or flares. In addition to the Crab nebula (Jourdain & Roques 2009), the strongest continuum source in the spectral domain of SPI is the high-mass X-ray binary Cygnus X-1 (Jourdain et al. 2011). These two sources are also the only sources that can significantly influence the maximum likelihood estimate in section 4.1. The resolved spectra of both sources are shown in Figure 4.16.

The spectrum of the Crab nebula has already been discussed in the previous section 4.4. The broken power-law spectrum is otherwise featureless and detected with a total significance of 1390σ in the energy band 50 – 100 keV and 12σ in the energy band 1115 – 1190 keV, important for ^{44}Ti emission.

The spectrum of Cygnus X-1 is extracted by assuming a time averaged, constant $\theta_{i,t}$ in equation 4.2. The average spectral shape is best fit with a single power law with an index of $\alpha_{Cyg} = 2.00 \pm 0.07$. The averaged spectrum is detected with a significance of 996σ in the low energy band. However, in contrast to the Crab nebula, Cygnus X-1 is known to have a soft, a hard and potentially an intermediate emission state (Rodriguez et al. 2015; Grinberg et al. 2013; Jourdain et al. 2011). Due to the strength of Cygnus X-1 in the 50–100 keV energy band, neglecting a time variability of the source and adapting an averaged emission spectrum, however, results in an energy band-averaged, reduced $\chi^2 = 1.20$ for 134666 d.o.f., derived from the maximum likelihood values during the extraction of the spectrum from the raw data. I therefore adopted a time variability for Cygnus X-1, refitting the spectrum per 3 revolution period, which optimizes the maximum likelihood and results in a reduced Pearson $\chi^2 = 1.01$ for 134483 d.o.f.. Adopting a time dependency for the emission of Cygnus X-1 therefore seems justified.

When searching for the emission of a previously unknown ^{44}Ti bright source (cf. section 5.2), the increased sensitivity from larger statistics of a time-integrated observation are evaluated. However, test positions, for which the distance to the Cygnus X-1 source is smaller than the spatial resolution of SPI, are not independent of the flux contribution from Cygnus X-1, i.e. only one source can be measured at the same position at once. Fitting a constant source contribution from the Cygnus X-1 region does not provide a good fit. Analysis of grid points (cf. section 5.2) is excluded, whenever the angle between grid points and Cygnus X-1 is lower than the spatial resolution of the instrument.

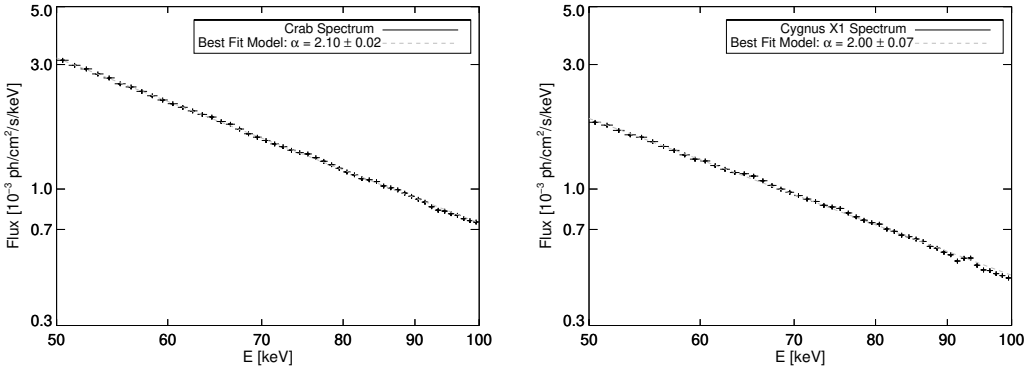

Figure 4.16: Spectrum of the Crab (left) and Cygnus X-1 (right) in the energy range 50 – 100 keV. Both spectra are fitted with a single power-law function. Best fit values are given in the Figure legends.

Chapter 5

^{44}Ti From Young Supernova Remnants

5.1 Emission From Recent Close-By Supernova Remnants

5.1.1 Sample Selection of Young Supernova Remnants

Since the beginning of systematic observation campaigns in the early 1920s, the field of SN research has progressed a long way. Yet, no uniform picture of their chemical imprint in the universe could be obtained. While theoretical descriptions have progressed to a level, where a handful of distinct scenarios are thought to be responsible for the majority of SN explosions (cf. sections 2.3 and 2.4), the increasing amount of observational data provides an ever increasing, varying parameter space, that needs to be accounted for. In addition to the mere description of the SNes' progenitors and explosive scenarios, also their impact on the chemical evolution of the universe and the physical evolution of galaxies needs to be understood. As such, the convolution of the various SN sub-type recurrence rates with their specific nucleosynthesis yields traces the history of chemical evolution in the Galaxy on a timescale of several billions of years. The precision of modeling this scenario is however limited by the accuracy of the SNe's theoretical description. As described in section 2, state-of-the-art simulations do not readily converge into uniform nucleosynthesis yields. The large parameter space of thermodynamic quantities, during which SN nucleosynthesis occurs, can be readily constrained by measuring γ-rays from individual SNe and their remnants, emitted from synthesized radioactive material.

Observing extragalactic SNe in γ-rays is mainly limited by the sensitivity of the current instruments, that allow for observations up to only a few Mpc for events that produce a large amount of radioactive ^{56}Ni, which is common for thermonuclear SNe, yet not for core collapse events. However due to the short half-life of ^{56}Ni the window for observation is limited to a few hundred days at those distances.
SN explosions occur only rarely in the Milky Way. For ccSNe, Diehl et al. (2006a) determine a rate of 1.9±1.1 events per century, and for type Ia SNe Cappellaro et al. (1999) find a rate of 4±2 SN per millennium. In the Milky Way, the youngest known core collapse event is the well studied remnant Cassiopeia A, which probably exploded in 1680 (Fesen et al. 2006). For type Ia explosions, G1.9+0.3 is the youngest remnant with an age of ≈ 120 yr, which is however ≈ 3 times more distant from earth (cf. section 5.1.1). With SNR ages of 100 yr upwards, nucleosynthesis during the explosion can be primarily studied by observing the decay γ-rays from the abundantly produced isotope ^{44}Ti with a half-life of (59.1 ± 0.3) yr

Table 5.1: The six youngest, close-by SNRs analyzed in this thesis. Astrophysical parameters, required for the mass determination, are taken from: (1) (Alarie et al. 2014), (2) (Reed et al. 1995), (3) (Krause et al. 2008a), (4) (Pietrzyński et al. 2019), (5) (Gall et al. 2015), (6) (Aschenbach et al. 1999), (7) (Hayato et al. 2010), (8) (Krause et al. 2008b), (9) (Sankrit et al. 2016), (10) (Reynolds et al. 2007), (11) (Reynolds et al. 2008), (12) (Borkowski et al. 2013). Observations of individual point sources with the SPI instrument usually span several years of mission time. Exposure on sources is given as dead-time corrected observation time, during which the target was at least in the partially coded field of view.

	Cassiopeia A	SN1987A	Vela Jr	Tycho	Kepler	G1.9+0.3
Distance [kpc]	3.3 ± 0.1	49.6 ± 0.5	0.2	4.1 ± 1	$5.1^{+0.8}_{-0.7}$	8.5
Year of Explosion	1681	1987	1320	1572	1604	1890
Age [yr]	330	24	690	438	406	120
Type	IIb	II-P	II	Ia	Ia	Ia
Exposure [Ms]	11.2	7.0	8.3	10.3	29.3	30.6
Gal. Longitude [deg]	111.7	279.7	266.3	120.1	4.5	1.9
Gal. Latitude [deg]	-2.1	-31.2	-1.2	1.4	6.8	0.3
References	1, 2, 3	4, 5	6	7, 8	9, 10	11, 12

(Audi et al. 2017). Depending on the SN type and the underlying mechanism driving the explosion, an ejected yield in the order of 10^{-6} – 10^{-4} $M_\odot$ of synthesized ^{44}Ti is expected per SN (cf. section 2). This amount is sufficient to be visible even after a few centuries up to a remnant distance of several kpc. Feedback from nucleosynthesis of SNe into the interstellar medium occurs on much longer periods than several half-lifes of the radioactive ^{44}Ti isotope. Diffuse emission of ^{44}Ti in the Galactic plane is not expected, as the majority of ^{44}Ti nuclei has long decayed before the SNRs ejecta are sufficiently mixed with the surrounding material. The decay time is comparable to the waiting time between SNe, so that the Galactic wide emission is dominated by only a few objects. This also means that along one line of sight, only the contribution from one SNR to the total emission is expected. During this early remnant phase the density of the ejecta has decreased to several atoms per cubic centimeter. On a timescales of one year, the density has sufficiently decreased so that SNRs become optically thin for hard X- and soft γ-rays, allowing for a direct conversion of detected flux to ejecta mass without major assumptions (see equation 5.4). In addition, the kinematics of the ^{44}Ti containing ejecta are still largely unaffected by the interaction with the reverse shock.

Here, I analyze the five young SNRs Cassiopeia A, Vela Jr., Tycho's SNR, Kepler's SNR and G1.9+0.3 located in the Milky Way galaxy. In addition, I search for emission in the ^{44}Ti decay chain in the SNR of SN 1987A, which is located in the Large Magellanic Cloud. Due to its very young age on astronomical timescales of 33 years, this remnant constitutes a promising candidate. In Tab 5.1 astrophysical parameters of these six remnants are listed, including age and distance measurements, necessary for translating the observed fluxes into ^{44}Ti ejecta masses of the respective remnant. As average observation date, 01.01.2011 is used. From this date the age of the SNR for equation 5.4 is defined as: age = 2011 - year of explosion. Exceptions are Tycho's and Kepler's SNe remnants. This analysis assumes a constant decay flux from all sources. In reality, 36% of the initial ^{44}Ti mass have decayed during the 19 yr of observation. However, the average amount of ^{44}Ti at the average obser-

vation date is 80% of the initial value. The offset from the true value is within the expected uncertainty of the measured fluxes, which justifies the assumption of a constant flux to maximize the sensitivity reached in the observation. The following considerations are based on and presented in Weinberger et al. (2020).

Cassiopeia A

Cassiopeia A (Cas A) is the youngest Galactic SNR attributed to a ccSN explosion with a remnant age of ≈ 340 yr. The young age and its proximity make Cas A one of the best studied SNRs in the Galaxy in all wavelength bands. The SN's optical transient might have been observed by Flamsted in 1680/1 (Green 2002), however, the transient was dimmer than expected for its close distance of only (3.3 ± 0.1) kpc (Alarie et al. 2014). Eriksen et al. (2009) infer from near infrared measurements, that the SN explosion was likely obscured by interstellar dust and that the early SN light curve was probably powered by $0.058 - 0.16\,M_\odot$ of ejected ^{56}Ni. Due to the presence of hydrogen and helium lines in a light echo of Cas A (Krause et al. 2008b), the SN is characterized as a type IIb event, commonly produced by progenitor stars of $15 - 25\,M_\odot$ (Young et al. 2006).

Cas A was the first remnant in which photons from the decay of radioactive ^{44}Sc could be measured (Iyudin et al. 1994) with the COMPTEL telescope in the 1157 keV emission line. Subsequent observations with various instruments (Vink et al. 2001) in the hard X-ray regime, especially with the INTEGRAL/IBIS imager (Renaud et al. 2006) and also the NuSTAR telescope (Grefenstette et al. 2014), substantiate the detection of photons from ^{44}Ti decay. The average mass of ejected ^{44}Ti was settled with results from previous observations and including results from the INTEGRAL/SPI spectrometer to be $(1.37 \pm 0.19) \times 10^{-4} M_\odot$ (Siegert et al. 2015).

This increased amount of ejected ^{44}Ti cannot be explained by typical 1D models, but is considered to arise from multidimensional asymmetries during the explosion (cf. section 2.3.3). This picture was complemented by more recent observations with the NuSTAR telescope (Grefenstette et al. 2017), that illustrated the asymmetric nature of the SN's ejecta. In Figure 5.1, the first spatially resolved image of Cas A in the hard X-ray regime depicts the distribution of radioactive ^{44}Ti in Cas A. This image also reveals, that ^{44}Ti containing material is apparently ejected in clumps, which is incompatible with a symmetric explosion. The parameters of the ejecta clumps are summarized in Table 5.2. These asymmetries in the ejecta structure of the SN are consistent with light echos of the SN explosion (Krause 2005; Krause et al. 2008a; Rest et al. 2011).

SN 1987A

SN 1987A exploded in the Large Magellanic Cloud on February 24, 1987. The SN's light curve showed a peculiar feature, with a plateau like, prolonged phase of intense light emission. It does not follow the commonly observed decline, correlated with the decay of ^{56}Co, the daughter nucleus of ^{56}Ni (Gall et al. 2015). Refinements of the distance to the Large Magellanic Cloud place SN 1987A at a distance of (49.6 ± 0.5) kpc (Pietrzyński et al. 2019). Due to its close distance, SN1987A was also the first SNR, in which the decay of radioactive ^{56}Co could directly be observed in the γ-ray regime (Matz et al. 1988; Tueller et al. 1990). This detection provided evidence that the early light curve of SNe is indeed powered by the

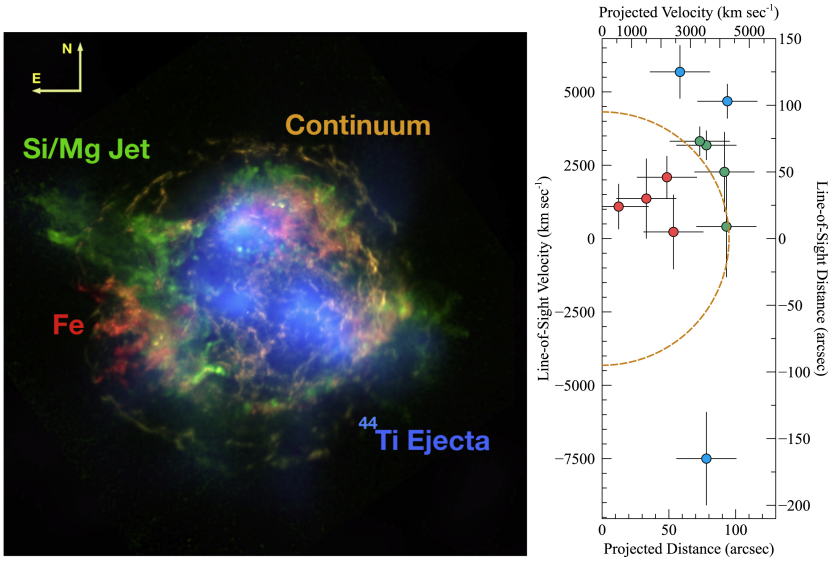

Figure 5.1: Left: False color image of the Cas A SNR. The continuum emission in the energy band 4 – 6 keV is colored in gold, the iron Kα emission is shown in red, mainly seen in the lower left corner. The silicon and magnesium rich ejecta are shown in green and the emission from the radioactive decay lines of ^{44}Ti are shown in blue. The ^{44}Ti distribution does not follow the distribution of iron in the ejecta. An explanation for this behavior could be that iron, interior to the reverse shock, is not shock heated yet and therefore not emitting radiation in the Kα line. A second explanation would be the misalignment of iron and ^{44}Ti in the ejecta. Right: Velocity distribution of the ^{44}Ti containing ejecta clumps in the SNR. Both images are adopted from Grefenstette et al. (2017).

Table 5.2: Properties of line emission from ejecta clumps in Cas A, determined with NuSTAR. Values are adopted from Grefenstette et al. (2017). The broadening of the lines is compatible with the instrumental resolution of 0.6 keV FWHM at 68 keV (Harrison et al. 2013) for most lines. Doppler shift velocity is calculated from the centroid shifts using equation 2.32.

Centroid keV	Shift Velocity km s^{-1}	1σ Width keV	Flux 10^{-7} ph cm^{-2} s^{-1}
67.35 ± 0.29	-2300±1300	≤0.3	8.8 ± 2.8
67.15 ± 0.2	-3200±900	≤0.3	12.3 ± 4.9
69.5 ± 0.6	7200±2700	$0.9^{+0.6}_{-0.4}$	$17.2^{+8.6}_{-7.4}$
66.6 ± 0.3	-5600±1300	$0.61^{+0.4}_{-0.25}$	$11.3^{+4.6}_{-3.8}$
67.6 ± 0.5	-1200±2200	≤0.92	7.8 ± 5.0
$67.8^{+0.4}_{-0.9}$	-330^{+1800}_{-4000}	0.7 ± 0.3	12.5 ± 5.5
67.8 ± 0.6	-330±2700	$0.73^{+0.4}_{-0.6}$	10.6 ± 5.5
66.8 ± 0.2	-4800±900	≤0.6	$6.4^{+4.1}_{-2.5}$
67.4 ± 0.3	-2100±1300	0.64 ± 0.3	14.4 ± 4.5
67.6 ± 0.3	-1200±1300	0.43 ± 0.3	9.6 ± 4
67.1 ± 0.2	-3400±900	≤0.34	$7.3^{+1.9}_{-3.2}$

decay of radioactive isotopes. The expansion velocity determined from the decay of ^{56}Co in the early SN explosion phase is 3100 km s^{-1}.

From the late time light curve Seitenzahl et al. (2014) infer a ^{44}Ti mass of (0.6 ± 0.2) ×

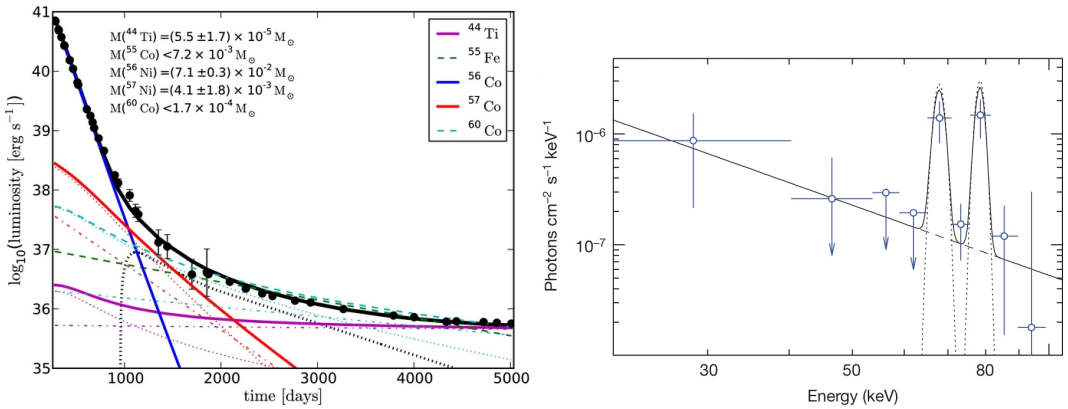

Figure 5.2: Left: Modeled bolometric light curve of SN 1987A. The various, radioactive isotopes (see legend) are responsible for the major energy input and light emission of the young SNR. The required radioactive ejecta masses are included. Black is the observed, bolometric, long term light curve of SN 1987A. Figure adopted from Seitenzahl et al. (2014). Right: ^{44}Ti emission lines in the IBIS spectral analysis. Image is adopted from Grebenev et al. (2012).

$10^{-4}\,M_\odot$. This value is in conflict with the direct detection of ^{44}Ti decay radiation, shown in Figure 5.2, with the INTEGRAL/IBIS imager and the NuSTAR telescope (Grebenev et al. 2012; Boggs et al. 2015). Both measurements constrain the expansion velocity to less than $4100\,\mathrm{km\,s^{-1}}$ and suggest an asymmetric explosion due to a Doppler shift in the ejecta bulk motion. In hard X-ray measurements of the SNR Boggs et al. (2015) find a best fit expansion velocity of $(700 \pm 400)\,\mathrm{km\,s^{-1}}$ for the ^{44}Ti decay lines, placing ^{44}Ti close to the center of the slowly expanding ejecta. This perspective is supported by the distribution of iron and silicon, determined from electronic shell transitions (Larsson et al. 2016; McCray 2017), suggesting that ^{44}Ti is contained within the velocity region of less than $1800\,\mathrm{km\,s^{-1}}$.

Vela Jr. / RX J0852.0-4622

A previously unknown SNR was discovered by its X-Ray emission in 1998, found in a detailed analysis in the direction of the Vela SNR (Aschenbach 1998). This emission was attributed to the remnant of a type II SN, which was called RXJ0852.0–4622 or Vela Jr. 20 years after the serendipitous discovery, the origin of the remnant is still not unambiguously identified. A significant flux excess was found in the energy region around 1157 keV with a flux of $(3.8 \pm 0.7) \times 10^{-5}\,\mathrm{ph\,cm^{-2}\,s^{-1}}$, that was attributed to the decay of radioactive ^{44}Sc (Iyudin et al. 1998). From the decay radiation, an age of ≈680 yr and a distance of ≈200 pc of the SNR was determined, which would make Vela Jr. the closest SNR in recent human history. Due to the close distance, the SNR has an apparent diameter of 2° (Aharonian et al. 2007).

G1.9+0.3

The SNR G1.9+0.3, is the most promising candidate for detecting ^{44}Ti in a thermonuclear SN. The remnant is located in the direction of the Galactic center. The SNR has been identified in a multi-wavelength analysis (Reynolds et al. 2008). Due to a high absorbing column density, the distance to the remnant is estimated to be 8.5 kpc, placing it close to the Galactic center. The optical transient was not observed in the northern hemisphere on

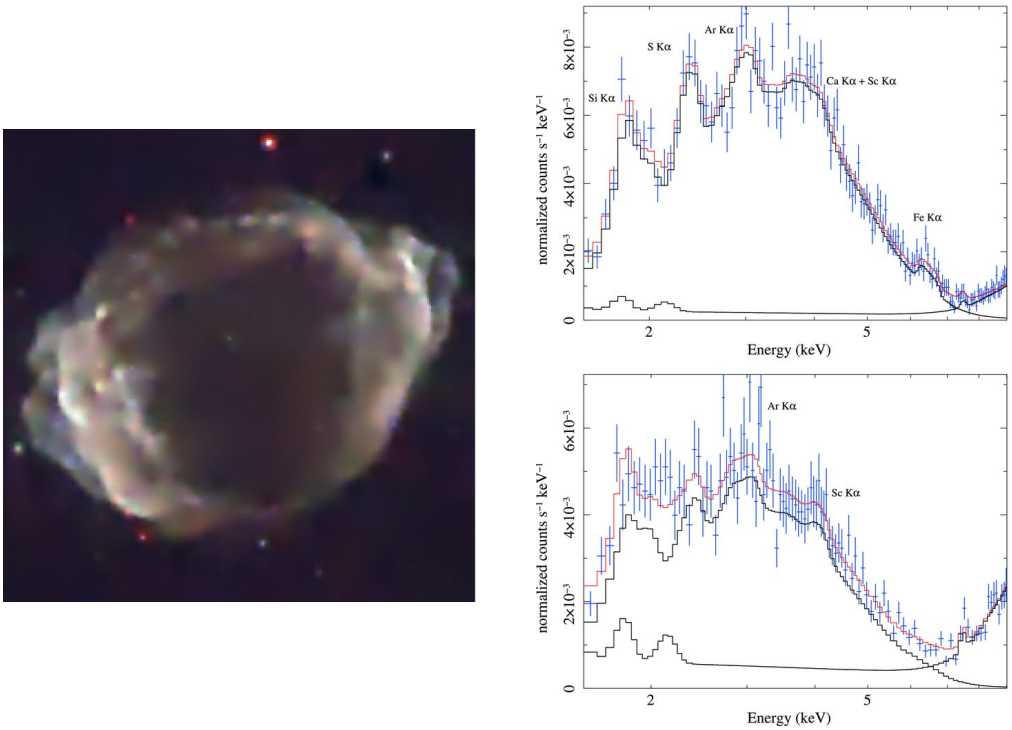

Figure 5.3: Left: False color Chandra X-ray image of the type Ia remnant G1.9+0.3. Color coding: red: 1–3 keV; green, 3–4.5 keV; blue, 4.5–7.5 keV. The image shows a celestial region of 127" × 121". Right: Chandra X-ray spectra for the northern rim of the remnant (top) and the interior region (bottom), including electron transition lines. Both images are adopted from Borkowski et al. (2010).

Earth as it was probably obscured by dust. From the apparent increase in size between 1985 and 2008 an age of ≈100 yr can be inferred, making G1.9+0.3 the youngest observed SNR in the Galaxy. The young age and diameter of roughly 2 pc requires a large SN shock front velocity of the order of 14000 km s^{-1}. Hints for the presence of radioactive ^{44}Ti in the remnant have been found in soft X-rays (Borkowski et al. 2010). The authors report the detection of a line feature at 4.1 keV in the analyzed Chandra data (figure 5.3), which they attribute to a fluorescence line in ^{44}Sc, emitted following the electron capture decay on ^{44}Ti. This interpretation suggests a ^{44}Ti ejecta mass of $(1 - 7)\times10^{-5}$ M$_\odot$.

Tycho's Supernova

The first observation of a SN (or stella nova) by European astronomers was made by Tycho Brahe in 1572, challenging the idea of an unchangeability of the stars. The remnant of SN1572 is called Tycho in the following. Measurements of the SN's light echo (Krause et al. 2008b) and comparison of measured X-Ray spectra with modeled light curves (Badenes et al. 2006) suggest, that Tycho is the remnant of a type Ia SN explosion. In close proximity to the center of the explosion, Tycho G was identified as a surviving binary to the exploded white dwarf (Ruiz-Lapuente et al. 2004). X-Ray measurements suggest that both iron group elements and intermediate mass elements (e.g. Ti) are distributed in clumps in the interior of the SNR (Miceli et al. 2015). Emission from the decay chain of ^{44}Ti has been reported in the interior region and the shocked shell of the remnant (SWIFT/BAT Troja et al. 2014), however, follow up measurements did not confirm this detection (Lopez et al. 2015). I adopt

a distance to the remnant of (4.1 ± 1.0) kpc (Hayato et al. 2010), while distance estimates range between 1.7 and 5.1 kpc (Albinson et al. 1986; Völk et al. 2008; Hayato et al. 2010; Slane et al. 2014). An expansion velocity of the ejecta of 5000 km s^{-1} is suggested by X-ray measurements with the Chandra satellite (Sato & Hughes 2017).

Kepler's Supernova

The SNR was discovered by Johannes Kepler in 1604. As Cas A and G1.9+0.3 have (probably) not been observed, Kepler's SN is the latest SN for which an optical transient was detected in the Milky Way. A distance of (5.1 ± 0.8) kpc was determined (Sankrit et al. 2016), which places the SNR at 460 – 600 pc above the Galactic plane. This rather large offset from the Galactic plane, the absence of a central compact object and the detection of strong iron lines in the ejecta (Reynolds et al. 2007) suggest, that Kepler is the remnant of a type Ia SN explosion. No detection of a ^{44}Ti decay signal has been claimed (Dupraz et al. 1997; Tsygankov et al. 2016).

5.1.2 Exploration of Spectral Extraction with Simulated SNR data

In this chapter, emphasis is put on the analysis of nuclear de-excitation lines, which are emitted following the radioactive decay of ^{44}Ti, not on broad band continuum emission. Here I aim to search for the emission of point like sources with respect to SPI's angular resolution. I analyze the emission of the nuclear de-excitation lines from specific sources with known celestial position and extent. This line emission can be spectrally resolved with SPI, as the extracted spectra are oversampling the instrumental energy resolution. As described in section 2.5, emission from as distinct region, such as a clump, in the ejecta creates an individual line at a specific Doppler shift and broadening. Under ideal conditions, such lines can be extracted from the overall spectral shape. However, the lines are expected to be weak with a commonly low signal-to-noise ratio per energy bin and narrower than any broad band emission. To increase the sensitivity for the total celestial emission signal, a model, describing the emission in the spectral domain, needs to be adopted. To evaluate the performance of the model, artificial data sets containing simulated emission from a SNR are created. The emission of the SNR is simulated with a given ejecta morphology, ^{44}Ti ejecta mass, SNR age and distance. From the simulated data sets, the spectrum is extracted, which is fit with a Gaussian model and the goodness of fit is tested against the correct, i.e. input, spectral shape. This additionally serves as evaluation for inferring ejecta kinematics from modeling the extracted spectral shape with a simple Gaussian.

The validity of this assumption is tested in the 1157 keV line. For both ^{44}Ti decay lines at 68 and 78 keV, kinematic effects only lead to a minor relative broadening and separation of the lines below the detector resolution. For the test scenarios considered here (see below), the separation of the lines is less than 0.3 keV at 78 keV, while the detector resolution is $\approx$ 1.6 keV FWHM. A distinction of different lines from the superposition is not feasible. The simulated data sets are created containing 4581 SPI pointings, equivalent to 10 Ms dead time corrected exposure. The background level of the data set is scaled to high latitude observations spread over the entire INTEGRAL mission duration, averaging over background level variations. For the spectral shape of the SNR's emission, three distinct scenarios are assumed.

Scenario one is a fully symmetric model. For the symmetric case, a homologously expanding sphere with a density profile exponentially decreasing with radius is assumed for the SNR's ejecta morphology. For this setup, the distribution of mass in Doppler shift velocity space approximately follows a normal distribution (Flörs 2020). This can be directly translated into a normal distribution in energy space. The Gaussian in energy space is centered at the laboratory decay energy of 1157.03 keV with a width of 3.85 keV (velocity space: 1000 km s^{-1}).
The second scenario considers a less homogeneous distribution of matter. It is assumed, that the total radioactive material is ejected in 5 clumps. The 5 clumps have a Doppler shift velocity of (-2000, -1000, 0, 1000, 2000) km s^{-1}, respectively. Each clump contains 20% of the total ejected mass.
The third scenario considers and even more inhomogeneous ejection of the matter. Here, the material is ejected in three clumps with Doppler velocities of (-2000, 0, 2000) km s^{-1}, respectively. Accordingly, each clumps contains 33% of the total ejected mass.

Initially, I investigate a SNR, that is located at a distance of 1 kpc from Earth and the age is set to 100 yr. The total ejecta mass of ^{44}Ti of the SNR is set to 10^{-4} M$_\odot$. At the assumed distance and age, this corresponds to an integrated flux of 2.56×10^{-3} ph cm^{-2} s^{-1}, that is distributed into the individual lines according to the above description of the ejecta structure. All individual lines of the ejecta clumps are broadened with the intrinsic detector resolution of 2.35 keV FWHM at 1157 keV. The spectral shape of the idealized emission is shown in Figure 5.4.

The simulated remnant is placed at the coordinates (l/b) = (-70°,70°). The convolved sky model of the artificial point source is normalized to contain the average required photon number per pointing and detector to reproduce the input flux in each energy bin. A poisson sample of this normalized, convolved sky model is drawn and added on top of the background counts. The spectrum of the SNR is extracted from the simulated raw SPI data following the formalism in section 4.1.

An analysis of the extracted spectra, ignorant of the input parameters, is performed by using a general continuum plus a certain number of Gaussian shaped lines, given by

$$F(E) = A_0\left(\frac{E}{E_C}\right)^{\alpha} + \sum_{i=1}^{N}\frac{F_{0,i}}{\sqrt{2\pi}\sigma_i}\times\exp\left(\frac{(E-E_{0,i})^2}{2\sigma_i^2}\right), \tag{5.1}$$

where A_0 and α describe the general continuum and $F_{0,i}$, $E_{0,i}$, and σ_i are the integrated flux, centroid energy and linewidth of the i'th Gaussian, respectively. The number i of lines is increased, until the fit model appears adequate (χ^2/d.o.f $\stackrel{!}{=}$ 1).

The extracted spectra and their appropriate description with the varying number of Gaussian lines is shown in Figure 5.5. In the following, the determined fit values and the derived χ^2 values are indexed with the number of their scenario.
The simplest assumption, representing the extracted spectrum with a single Gaussian line, only provides an good description of the data for scenario one. There, a reduced $\chi^2_1 = 227.1$ for 237 d.o.f. is derived for the Gaussian model, while the correct input model leads to $\chi^2_{1,c} = 227.1$. The Gaussian is detected with a significance of 135σ. The fit integral

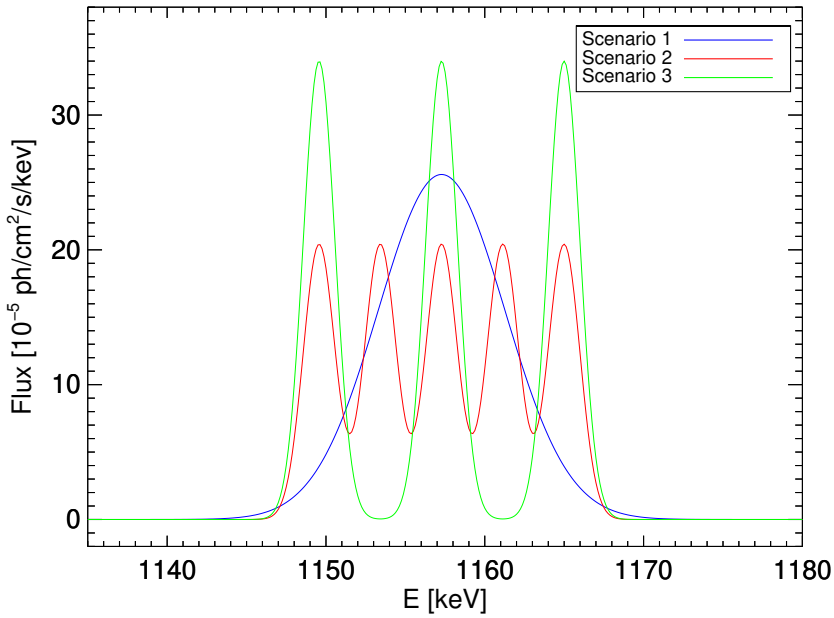

Figure 5.4: Idealized, simulated spectral shapes for the three discussed scenarios. All lines are broadened with the detector intrinsic resolution of 2.35 keV FWHM at 1157, except for the blue scenario, which is additionally broadened with a line width of 3.85 keV. Note here, that despite their significantly different appearance, all models contain the same flux.

flux, line centroid and line width of the Gaussian are $F_1 = (25.3 \pm 0.2) \times 10^{-4}$ ph cm^{-2} s^{-1}, $E_1 = (1157.07 \pm 0.03)$ keV and $\sigma_1 = (3.84 \pm 0.04)$ keV, which is a perfect reproduction of the input values. This is not surprising, as the input line shape is represented with the correct model at a high significance.

For all other scenarios, the single Gaussian representation provides a poor fit, with a reduced $\chi^2_2 = 3457$ and $\chi^2_3 = 14733$ for 237 d.o.f., respectively. The correct models are detected in the spectra with a significance of 126 and 156σ, respectively. For scenarios two and three, the increased inhomogeneity in the ejecta structure is reflected in an increasingly poor fit. The centroids of the Gaussian lines are $E_2 = (1157.96 \pm 0.28)$ keV, and $E_3 = (1157.05 \pm 0.32)$ keV, which is in agreement with the mean flux position of 1157.03 keV. Furthermore, despite the poor representation of the spectrum the reconstructed fluxes of $F_2 = (27.2 \pm 3.6) \times 10^{-4}$ ph cm^{-2} s^{-1}, and $F_3 = (26.0 \pm 3.4) \times 10^{-4}$ ph cm^{-2} s^{-1} in the Gaussian approximation are a good reconstruction of the correct value.
However, based on the poor fit quality of the one Gaussian representation, it is evident, that additional lines are required to describe the spectrum. For scenarios two and three, 5 and 3 lines are required, respectively, to provide a good description of the spectrum. This is identical with the number of input lines, and the reconstructed fluxes, centroid positions and line widths are identical to the correct input values within uncertainty. The general good reproduction is not surprising because of the high statistical significance of the lines.

To estimate the variance in the extracted results with varying remnant properties, the spectral analysis is repeated for a set of 3 cases. This study considers assumptions, where the remnant's distance and age are similar to the known astrophysical targets in this chapter

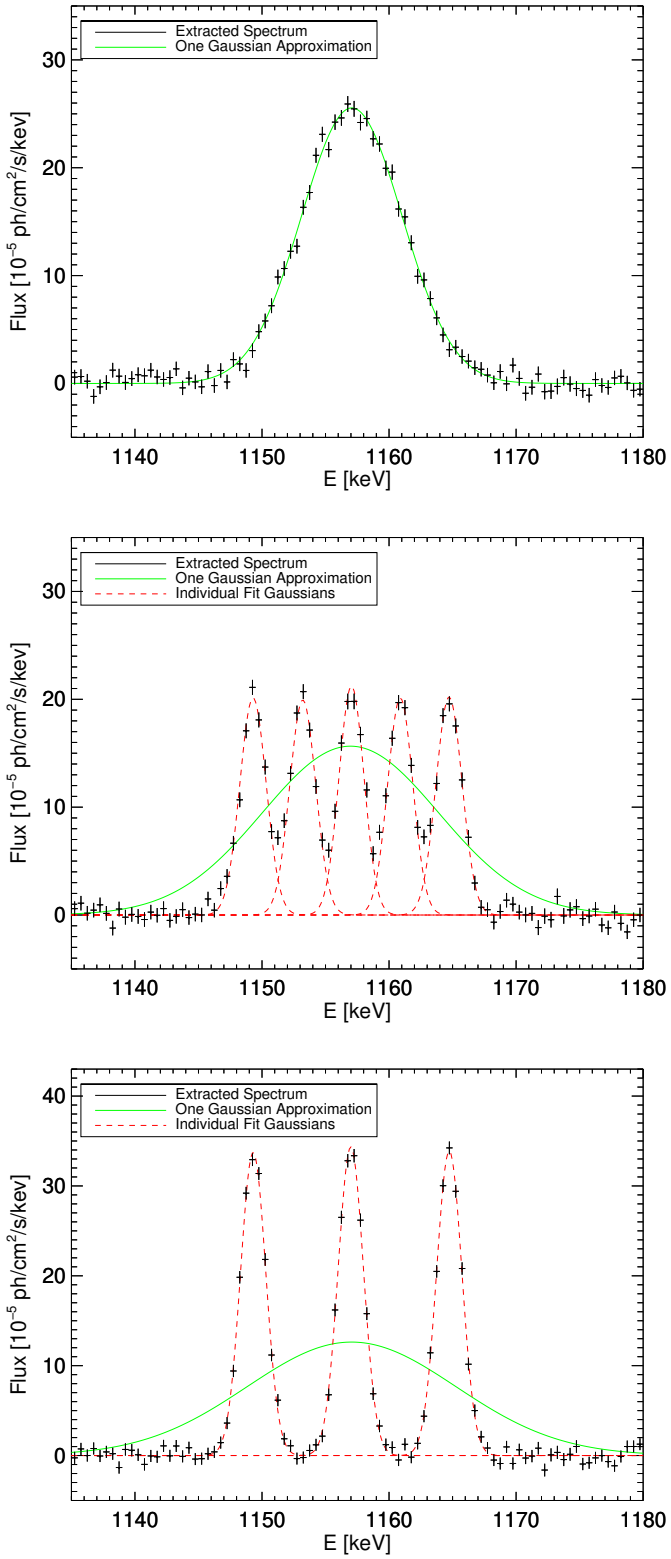

Figure 5.5: Extracted spectra of simulated SNRs. Top: Symmetric Input Model, Scenario 1. Center: Scenario 2. Bottom: Scenario 3. The fitted lines are the one Gaussian approximation (green) of the spectrum, which only provides an adequate fit of the spectrum in scenario one. For scenarios two and three, the number of lines for an adequate fit are five and three respectively. The individual fitted lines are indicated as red, dashed lines.

Table 5.3: Variance in representing extracted spectra with Gaussian lines. The first row indicates the input flux level, set to 100%, 10%, 3%, and 1% of the primary simulation. The number of lines row contains the required Gaussians for an adequate description of the spectrum. The table is separated with respect to the three scenarios. Fluxes are given in units of 10^{-5} ph cm^{-2} s^{-1}. The reconstructed centroids and line widths are for the one Gaussian approximation, given in keV. The extracted values are stable in the respective scenario. Also the reconstructed flux in the Gaussian line is mostly in agreement with the input flux. The detection significance is calculated from a likelihood ratio test, comparing the best fit line model with the null hypothesis (i.e. no flux). The significance is expressed in multiples of a normal distribution's standard deviation σ.

Input Flux	256	25.6	8.5	2.6
Detection Significance	135	12.8	5.1	3.4
Reconstructed Flux	254 ± 2	21.6 ± 2.1	10.4 ± 2.5	6.3 ± 2.3
Centroid	1157.0 ± 0.1	1157.4 ± 0.2	1156.9 ± 1.9	1154.8 ± 2.5
Line Width	4.0 ± 0.1	3.4 ± 0.3	4.4 ± 1.1	5.0 ± 1.7
Number of Lines	1	1	1	1
Detection Significance	126	13.7	4.1	3.7
Reconstructed Flux	272 ± 4	31.4 ± 4.6	8.6 ± 2.7	8.8 ± 2.5
Centroid	1157.0 ± 0.3	1156.0 ± 1.0	1154.0 ± 3.4	1158.2 ± 3.3
Line Width	6.9 ± 0.4	7.0 ± 0.9	6.5 ± 3.4	6.9 ± 2.1
Number of Lines	5	5	1	1
Detection Significance	156	17.4	5.9	Not Detected
Reconstructed Flux	260 ± 3	26.8 ± 4.8	10.4 ± 3.1	–
Centroid	1157.1 ± 0.3	1158.3 ± 1.5	1154.6 ± 3.4	–
Line Width	8.2 ± 0.5	8.0 ± 1.0	7.3 ± 2.3	–
Number of Lines	3	3	3	–

(see table 5.1). Increasing the age and distance of the artificial remnant both results in a decreased flux level, and thus a decreased signal significance. The accuracy of extracting the spectrum and representing it with a varying number of Gaussian lines is tested. The integral flux in the spectrum is decreased to 10, 3, and 1% of its original value, respectively. For a future SN in the Milky Way, that is detected when the remnant gets optically thin for γ-rays, the mentioned flux levels correspond to a SN distance of 5 kpc and 10 kpc for a ccSN (10%, 3%) and 1–5 kpc (1%) for a type Ia SN.

In table 5.3, the properties of the Gaussian representation for the extracted spectra are summarized. Also included are the number of required Gaussian lines to adequately describe the spectrum. As long as the remnant is detected with a high statistical significance, the input fluxes as well as several of the clumps can be adequately reconstructed. Only at a very low statistical significance of detecting the artificial SN above the background noise, the number of required Gaussians is reduced to one in scenarios 1–3. For the 3% flux level case, lines in scenario 2 are smeared into one line, while for scenario 3, it is still possible to distinguish between the individual clumps. In general, the trend suggests that the less uniform the flux is distributed in the spectrum, the more readily the individual clumps can be distinguished. In table 5.3, the reconstructed Gaussian widths and line centroids for the one Gaussian approximation are given. Even though this approximation is not a good representation of the spectrum in most cases, the extracted values remain stable. Even at a low detection level, where indeed only one line is required, the reconstructed values are in agreement with the

values determined for a high significance case. This suggests, that a value for the line shape and shift can be reconstructed, even when the correct spectral shape is only approximately described. In the majority of cases, where the line is detected with more than $\approx 4\sigma$, also the reconstructed flux is in agreement with the input flux. For the low significance detections the reconstructed fluxes are an overestimate of the true value.

To this point, the considered simulated spectral shapes emanate from the assumption of a highly idealized ejection of matter. All ejecta clumps are considered to have no intrinsic velocity spread. This is not necessarily true. As indicated in table 5.2, the majority of clumps found in a spatially resolved analysis of Cas A, do have an intrinsic velocity spread of the order of $v_{exp} \lesssim 1000\,\mathrm{km\,s^{-1}}$. To determine the influence on the detectability of individual components in a spectrally resolved analysis with expanding ejecta clumps, the above described simulations are repeated. In this second case, it is assumed that all ejecta clumps are again resembled as homologously expanding sphere. For scenarios 2 and 3, the lines of all individual ejecta clumps are broadened with 1.9 keV ($500\,\mathrm{km\,s^{-1}}$), additional to the detector resolution. For scenario one, the one Gaussian is additionally broadened with $500\,\mathrm{km\,s^{-1}}$, i.e. in total with $1500\,\mathrm{km\,s^{-1}}$, corresponding to a total line width of 5.87 keV. The simulated spectral shapes are shown in Figure 5.6. The simulated data sets are created with otherwise identical input parameters for flux and centroid shifts.
For scenarios 2 and 3, the broadening of the lines produces an overlap of the individual lines. In scenario 2, this leads to the appearance of an almost Gaussian shaped line profile with a flat top. In scenario three, ontop of the general offset the three peaks of the individual lines are still recognizable. In the following, it is investigated whether the individual lines can still be reconstructed.

Again, an agnostic analysis of the extracted spectra is performed. The extracted spectra and the best fit (multi-) Gaussian representation for the 100% input flux level are shown in Figure 5.7.

In scenario one, the spectrum is again perfectly represented with one adopted Gaussian. The extracted flux, centroid, and line width of $(25.8\pm0.2)\times10^{-4}\,\mathrm{ph\,cm^{-2}\,s^{-1}}$, (1157.01 ± 0.06) keV and (5.83 ± 0.06) keV are a perfect reconstruction of the input values. Again, this is not surprising as the spectrum is modeled with the correct line shape. For scenarios 2 and 3, the reduced $\chi^2_2 = 693$ and $\chi^2_3 = 2177$ for 237 d.o.f., respectively, are still a poor description of the spectrum. Nevertheless, in both cases, due to the broadening of lines, the one Gaussian approximation is a better fit to the data than in the highly idealized case above. The centroids of the lines are identical with laboratory energies within uncertainty. In both cases however, the reconstructed flux of $(26.9 \pm 0.3) \times 10^{-4}\,\mathrm{ph\,cm^{-2}\,s^{-1}}$ and $(27.0 \pm 0.3) \times 10^{-4}\,\mathrm{ph\,cm^{-2}\,s^{-1}}$ is significantly higher than the input flux. An adequate description of the data requires 3 and 3 Gaussians for scenarios two and three respectively. For scenario 3, it can be inferred that distinct clumps in the ejecta are still recognizable, despite their overlap. For scenario 2, the overlap of lines already leads to a reduction of distinguishable clumps.

The number of required lines and the reconstruction of the fluxes, centroid positions and line width is additionally investigated for lower level fluxes according to the above description. The extracted results, and especially the number of required lines for an adequate description of the spectra are summarized in table 5.4. Two major results are immediately evident. First, the overall detection significance of all lines at the respective fluxes is significantly

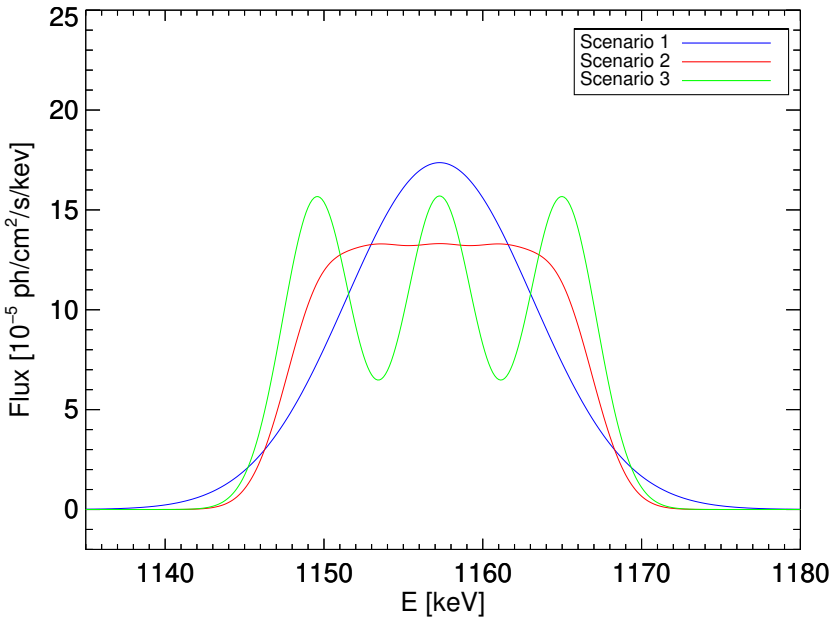

Figure 5.6: Broadened simulated spectral shapes for the three discussed scenarios. All lines are broadened with 1.9 keV, corresponding to an intrinsic clump expansion velocity of 500 km s^{-1} plus the detector intrinsic resolution of 2.35 keV FWHM at 1157 keV. Scenario one, indicated as blue line, is broadened with 5.78 keV, corresponding to a velocity spread of 1500 km s^{-1}, above the intrinsic detector resolution. In scenario 2, the overlap of the lines leads to an approximately Gaussian line shape with a flat top.

reduced compared to the non broadened case. This is not surprising, as the flux is spread over a larger range in energy. The signal per energy bin is reduced, while a larger amount of background needs to be accounted for. The second result is, that even at a relatively high detection significance, the required number of lines is always one. Due to the blurring from the overlap in the lines, the individual ejecta clumps cannot be distinguished above the general Gaussian approximation anymore. Again, the reconstructed centroid positions and line widths remain stable over the process of reducing the integral input flux.

In summary, the spectral analysis of a SNRs radioactive decay signature provides a diagnostic tool to infer the remnants ejecta structure.
For a future SN explosion in the Galaxy, with a very young age and a close by distance, a significant flux excess above the statistical background in decay channels of the primarily produced radioactive nuclii is expected. In such an event, the cumulative emission from the SNR in one specific decay channel can be segmented into individual Gaussian lines, from which the ejecta morphology can be readily inferred.
For a signal with a low detection significance, as expected for aged remnants, the cumulative emission in one specific decay channel can be adequately represented with a single Gaussian line to enhance the sensitivity for a celestial signal. The reconstructed values for the line centroids are generally in good agreement with the simulation input values. Constraints on the bulk motion of the ejecta can be drawn from the well constrained shifts in lines centroids from the laboratory determined line energy E_L. A significant blue or redshift of the line centroid indicates an ejection of matter by the explosion into one hemisphere.

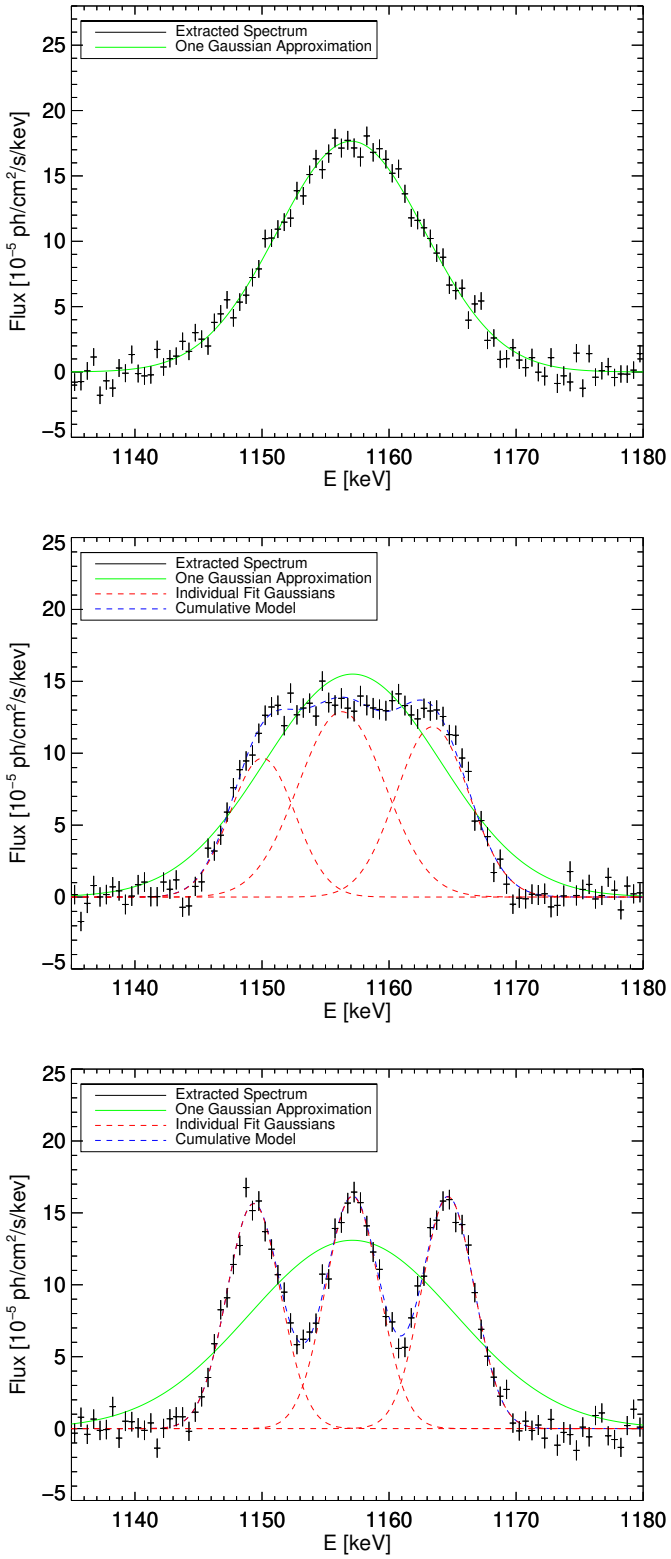

Figure 5.7: Extracted spectra of simulated SNRs with intrinsic clump velocity. Top: Symmetric Input Model, Scenario 1. Center: Scenario 2. Bottom: Scenario 3. The fit lines are the one Gaussian approximation (green) of the spectrum, which only provides an adequate fit of the spectrum in scenario one. For scenarios two and three, the number of lines for an adequate fit are respectively three. Due to the overlap of the broadened lines, two of the five input lines in scenario 2 are not distinguishable. The individual fit lines are indicated as red, dashed lines. The cumulative emission of all lines combined is shown in blue.

Table 5.4: Same as table 5.3, but for broadened eject clumps. The reconstructed centroids and line widths are for the one Gaussian approximation. The extracted values are stable during flux reduction. The reconstructed flux tends towards higher values with decreasing input flux level and increasing inhomogeneity in the spectral structure.

Input Flux	256	25.6	8.5	2.6
Detection Significance	116	14.8	3.0	Not Detected
Reconstructed Flux	258 ± 2	32.3 ± 3.4	6.8 ± 2.6	–
Centroid	1157.0 ± 0.1	1156.4 ± 0.5	1158.4 ± 3.5	–
Line Width	5.8 ± 0.1	5.8 ± 0.6	6.4 ± 3.7	–
Number of Lines	1	1	1	–
Detection Significance	113	8.9	3.7	2.9
Reconstructed Flux	270 ± 3	22.1 ± 3.1	9.4 ± 3.3	8.5 ± 2.6
Centroid	1157.1 ± 0.3	1157.4 ± 2.4	1151.3 ± 4.0	1159.6 ± 2.7
Line Width	6.9 ± 0.2	7.4 ± 1.4	7.9 ± 3.4	6.9 ± 2.1
Number of Lines	3	1	1	1
Detection Significance	111	11.7	4.3	Not Detected
Reconstructed Flux	270 ± 3	22.1 ± 3.3	11.7 ± 4.0	–
Centroid	1157.1 ± 0.1	1157.0 ± 0.9	1160.5 ± 4.4	–
Line Width	8.4 ± 0.1	7.5 ± 0.7	8.9 ± 2.8	–
Number of Lines	3	3	1	–

Similarly, the reconstructed flux in the Gaussian approximation is reproducing the input flux well. Deviation within the 2σ flux uncertainty are found for low level detections. Here it is concluded, that the deviation can be attributed to a fluctuation of a Gaussian distribution with a chance of $\approx 5\%$, which is still acceptable. In these cases, the reconstructed flux tends to be an overestimate of the input flux. This is especially true, when a non-uniform distribution of fluxes is modeled with an intrinsically symmetric Gaussian model. The extracted fluxes in the following section for the high energy line need to be treated with caution, when the detection level of the individual lines is low.

The reconstructed broadening of the line is investigated. Even though the Gaussian approximation is not a proper description of the line shape for spectra with high detection significance in scenario 2 and 3, the reconstruction of the line broadening appears to produce a *correct* value for the line width. Note that this is not a physically correct value, i.e. interpreting the line width with respect to the ejecta kinematics needs to be treated with caution. These reconstructed line widths, (8.2 ± 0.5) keV and (6.9 ± 0.4) keV for scenario 3 and 2, respectively, remain stable, on the one hand when the flux in the lines is reduced, but on the other hand also when the individual lines have an intrinsic broadening. The independence of the line broadening on the detection significance is promising, as it allows for a uniform interpretation of the line broadening in terms of ejecta expansion velocity. The difference in the line width values are due to the ejecta morphology. In scenario 2, the ejecta are more uniformly distributed. Therefore, the average energy spread, away from the centroid position, is small. For scenario 3, where two thirds of the ejecta are strongly blue or redshifted, the spread in the energy is higher. This is reflected in the increase of the line width.
In the symmetric case, the broadening of the line can be directly translated into an ejecta intrinsic velocity spread, such that 95% of the ejecta have line of sight velocities between

$[-2\sigma; 2\sigma]/(\mathrm{E_L}) \times \mathrm{c}$, where $\mathrm{E_L}$ is the laboratory line energy. For non uniform ejection, no equivalent interpretation of the remnant morphology is readily possible. However, it is estimated that the majority of the flux excess in the spectrum is covered within the $[-2\sigma + \mathrm{E_0}; \mathrm{E_0} + 2\sigma]$ range, where $\mathrm{E_0}$ is the fit line centroid. Therefore, the *expansion velocity* of the ejecta, i.e. velocity equivalent of the energy spread around the centroid, is uniformly calculated as $2\sigma/(E_0) \times c$ in the remaining thesis.

Linking the Lines in a Multi-Step Decay Cascade

According to the above evaluation, emission in all three lines can be described by assuming a single Gaussian for a signal with a low level detection significance, respectively. However, for such low significance detections, the line parameters are not well determined and carry a large uncertainty. To better constrain the SNRs kinematics with SPI data, the emission in all prominent lines of a specific decay chain are analyzed simultaneously by adopting a uniform flux and kinematic Doppler shift and broadening. In this case, the branching ratio corrected flux F_L is fitted as parameter of interest, while the individual line fluxes are calculated according to the branching ratios.
This approach is valid when the following two conditions are meet: a) The kinematics are identical for all subsequent decay steps. b) The activity of all decay steps is identical after correction for branching ratios.
Concerning the first criterion, the validity is discussed in the context of the ^{44}Ti isotope. The same argument is in general applicable for all decay chains, provided that the second decay step is significantly shorter than the initial decay. In the decay chain of ^{44}Ti, the activity of the sources at present date is governed by the long half-life of 60 yr of the initial decay step of ^{44}Ti. In contrast to that, the second decay step of ^{44}Sc occurs within a half-life of 4 hr, which is instantaneous with respect to the ^{44}Ti half-life. During the 4 h half-life of ^{44}Sc no acceleration or deceleration processes are expected to influence the kinematic behavior of the ^{44}Sc nuclei. Therefore the kinematic Doppler broadening of all three lines should be identical with respect to their centroid energies. A potential expansion velocity of 5000 km s^{-1} translates into a line broadening of $\approx$ 2 keV FWHM at 70 keV. However, the same expansion velocity translates into a FWHM of $\approx$ 25 keV Doppler broadening at 1157 keV. This effect is accounted for in the analysis.
Specifically, the model for each of the lines is given by

$$\begin{aligned} \mathrm{F_0}(\mathrm{F_L}, \mathrm{v_B}, \mathrm{v_D}) &= \mathrm{b_L} \frac{\mathrm{F_L}}{\sqrt{2\pi}\sigma(\mathrm{v_D})} \times \exp\left(\frac{(\mathrm{E} - \mathrm{E_0}(\mathrm{v_B}))^2}{2\sigma(\mathrm{v_D})^2}\right) \\ \sigma(\mathrm{v_D}) &= \sqrt{\left(\frac{v_D E_{0,L}}{2c}\right)^2 + FWHM_{0,L}^2} \\ \mathrm{E_0}(\mathrm{v_B}) &= (1 - \frac{\mathrm{v_B}}{\mathrm{c}})\mathrm{E_{0,L}}. \end{aligned} \tag{5.2}$$

Here, the line width and centroid, $\sigma(\mathrm{v_D})$ and $\mathrm{E_0}(\mathrm{v_B})$, are not determined in energy space, but the corresponding velocities for the Doppler broadening, $\mathrm{v_D}$ and bulk motion, $\mathrm{v_B}$ are fitted, as these create the conceptual link of the lines. The laboratory decay energy of each line is given $\mathrm{E_{0,L}}$, and the total broadening of the line is determined from the convolution of the instrumental energy resolution $\mathrm{FWHM_{0,L}}$ at $\mathrm{E_{0,L}}$ and the velocity and energy dependent $\sigma(\mathrm{v_D})$. The bulk velocity is defined such that a redshift of the ejecta corresponds to positive

bulk velocity.

The second condition can only be met, when the half-life of the second decay step is shorter than that of the first one. From the radioactive decay law it can be shown, that the activity of two subsequent decay steps 1 and 2 is given by

$$\lim_{t\to\infty} \frac{A_2(t)}{A_1(t)} = \frac{\lambda_2}{\lambda_2 - \lambda_1}, \quad \lambda_2 \geq \lambda_1 \tag{5.3}$$

where $\lambda_{1,2}$ are the decay constants. For the ^{44}Ti decay chain, this implies that the activity of both decay steps is identical to a precision of the order of 10^{-5}, which is significantly smaller than the statistical uncertainties of the measured fluxes. I therefore conclude, that both conditions are fulfilled.

When searching for the emission of radioactive decay in unstable isotopes (in this case ^{44}Ti), the measured flux can be translated into an activity of the source at the present date. This can further be translated into a mass of radioactive material, which was ejected in the SN explosion with

$$m_{ej} = F_L 4\pi r_{SNR}^2 Nu\tau \exp\left(\frac{t}{\tau}\right) \tag{5.4}$$

where N = 44 is the number of nucleons of ^{44}Ti, u is the atomic mass number, $\tau = 86.6$ yr is the decay constant of ^{44}Ti and t is the age of the SNR. The line flux $F_L = F_0/b_L$ is normalized to the branching ratio b_L of the line[1]. The distance to the SNR is given by r_{SNR}.

The power law in equation 5.1 describes a potential underlying continuum, which can be produced by synchrotron emission of charged particle scatterings in the SN ejecta or also from additional sources within SPI's PSF. Flux from sources, that are located close to the celestial point of interest (i.e. the SNR), cannot be separately determined due to SPI's modest angular resolution and contribute to the flux of the point source of interest.

5.1.3 SPI Measurements of Core Collapse Supernovae

5.1.3.1 Cassiopeia A

Detection of ^{44}Ti in Cas A

In this analysis, all available data up to 2019 were used, which amounts to a total dead-time corrected exposure of 11.2 Ms. I search for the emission of photons in the energy region 50 – 100 keV, containing both decay lines of ^{44}Ti and in the energy region 1090 – 1210 keV, containing the decay line of the subsequent decay of ^{44}Sc (see figures 5.8, 5.11). The spectra are described with an underlying power law, accounting for potential synchrotron emission of accelerated electrons in the SNR's magnetic field, and three Gaussian shaped lines, representing the three dominant decay lines of ^{44}Ti. The signal for the decay of ^{44}Ti is found with a combined significance of 5.4σ in all three lines. The separate significances per line are 2.2σ, 3.6σ and 3.3σ in the 68, 78 and 1157 keV line, respectively. Due to the presence of a

[1]The branching ratio describes the respective probability of photon emission per decay for the specific lines.

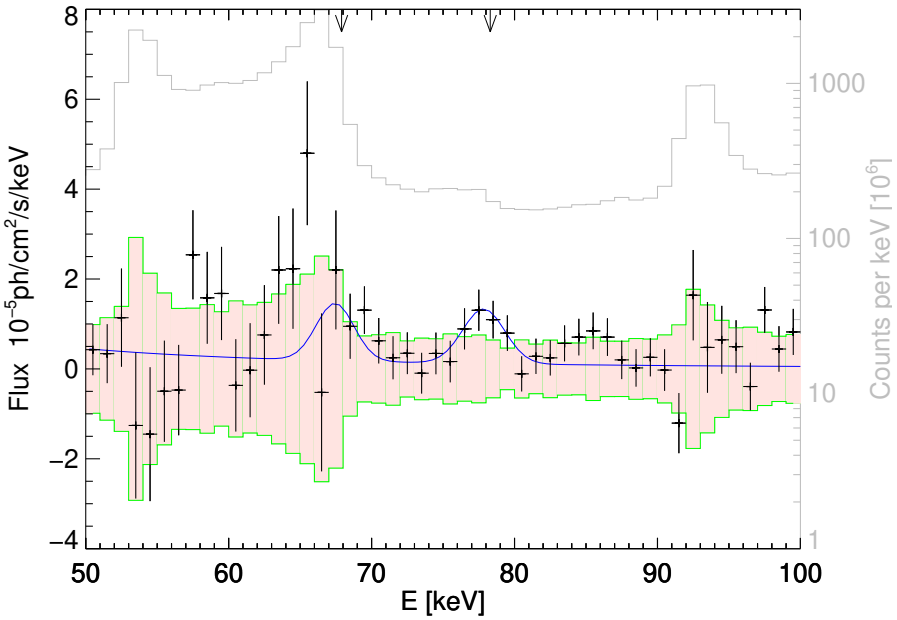

Figure 5.8: Uncertainty band determined from the statistical fluctuation of the 121 grid points in the celestial region of Cas A. The red shaded area, bracketed by the green line, marks the 1σ uncertainty band. The spectrum of Cas A is included in black, and represented by a power law and two Gaussian shaped emission lines at 68 and 78 keV in blue. The gray spectrum shows the mission integrated background counts of the 19 physical detectors. It is evident, that the statistical uncertainty and the variance of the extracted spectrum scale with the strength of background. Significant excess above the uncertainty band is only apparent at the 78 keV line. Emission of the 68 keV line is close to a strong background line complex.

strong background line complex (see section 4.2.4) in the region 50-70 keV, induced by the decay of Ge, Co and Pb, the decay signature at 68 keV is only marginally detectable above a large instrumental background.

To estimate the systematic uncertainties and validate that the signals are not spurious detections, I search for emission in the vicinity of the SNR, that could mimic the presence of a ^{44}Ti decay signal. This search for ^{44}Ti emission is conducted in a spherically square shaped grid, with edge length of $20° \times 20°$. Each individual location in the grid is separated by 2° distance from the adjacent grid point, which is compatible with the angular resolution of SPI. The grid is centered on the position of Cas A at (l/b) = (111.7°/-2.1°). This approach yields a total of 121 grid points. I extract the spectra in both energy regions of interest for each grid point and determine the significance of a ^{44}Ti decay chain signal above the instrumental background, combined for the 78 and 1157 keV line. Due to the complex of strong background lines, the 68 keV line is disregarded in this search. The spectral form for a combined line fit is shown in Figure 5.12 at the position of Cas A, however, including all three lines for illustration purposes.

The resulting point source significance distribution for the combined signal of the 78 and 1157 keV lines is shown in Figure 5.9. Each tile represents the surface area covered by the grid point at the center of the tile. Significant flux excess is only found at the central location, which coincides with the celestial position of Cas A, at the 4.9σ level. All other

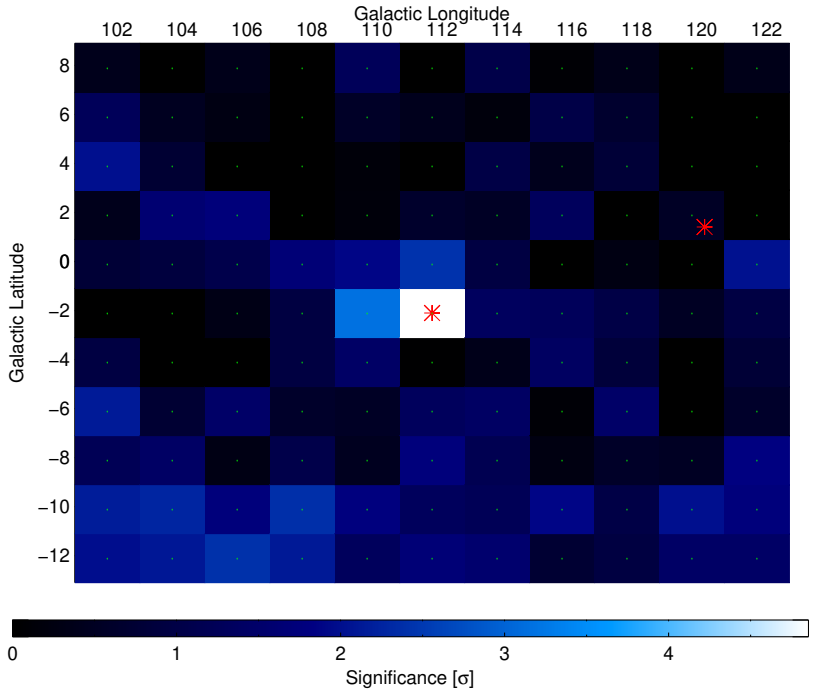

Figure 5.9: Significance map of the decay chain of ^{44}Ti. The color coding represents the detection significance of the combined 78 and 1157 keV signal. A significant signal at the 4.9σ level is only visible at the central tile, consistent with the location of Cas A. The second red star symbol in the upper right quadrant marks the position of Tycho's SNR at (l/b) = (120.1°/1.4°).

grid points do not show a significant signal. In the same grid, the position of Tycho's SNR is also marked with a red star symbol. No significant excess (0.3σ) is found at this location (see section 5.1.5.2).
A 1σ uncertainty band is determined from the statistical uncertainties in the spectra of the 121 grid points per 0.5 keV bin. I interpret the uncertainty band as the statistical fluctuation of a zero signal in the celestial region of Cas A with an integrated exposure of 11.2 Ms. The uncertainty band is slightly overestimated, as the exposure on all grid points is not uniform over the surface area of the grid. Less exposure naturally increases the uncertainty of the individual spectra at each grid point. The uncertainty band, shown in Figure 5.8, is a conservative limit, which encloses the Cas A spectrum with three simultaneously fit lines. Clear excess above the uncertainty band is only visible at the 78 keV line. The majority of the 68 keV line is covered by the statistical fluctuation of the uncertainty band.

Properties of ^{44}Ti from Separate Line Fits

In a first step, no prior knowledge of the processes, from which the decay signatures in the two energy bands arise, is assumed. The line shapes for the 78 keV and 1157 keV line are determined separately. In this process, a power law is fitted in addition (see equation 5.1) which is interpreted as continuum emission, introduced by synchrotron radiation in the SNR over the entire energy range spanning from 20 keV to 1.3 MeV. The best fit power-law index of the continuum is -2.6 ± 0.4.

The statistically most significant signal for a single line is identified in the region of the

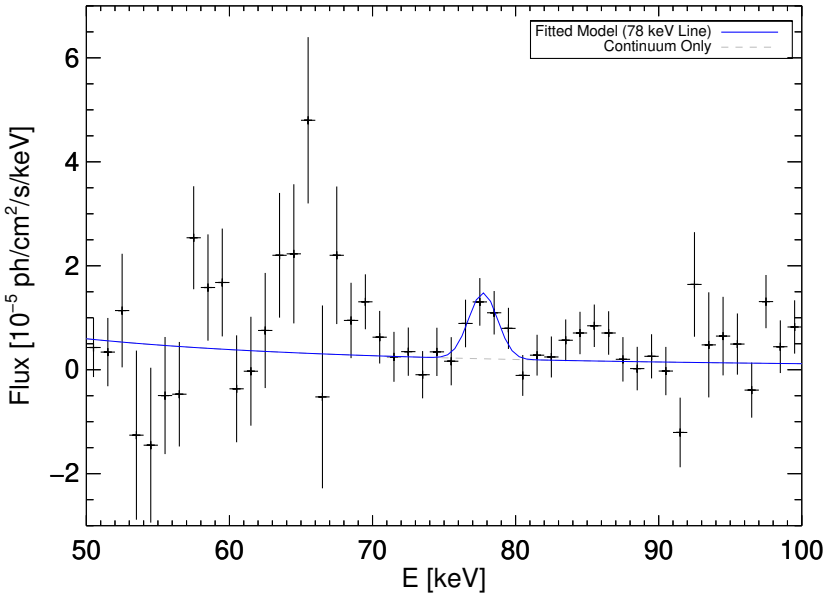

Figure 5.10: Cas A spectrum in the energy region 50 – 100 keV in 1 keV binning. The spectrum is represented by a synchrotron continuum (gray) on which a Gaussian shaped line is superimposed (blue). The blue spectrum shows the best fit values for an independent line on top of the best fit continuum, spanning the energy range from 20 – 1300 keV. The line is red shifted and broadened with respect to the instrumental resolution at 78 keV.

78 keV line with a significance of 3.6σ. The spectrum of Cas A in the 50 – 100 keV region including the fit spectral shape is shown in Figure 5.10. The line is represented by a Gaussian, containing a total, branching ratio corrected flux of $(3.3 \pm 0.9) \times 10^{-5}$ ph cm^{-2} s^{-1}. The line centroid is shifted by 0.8 keV to a centroid value of (77.5 ± 0.5) keV, which suggests a bulk motion of the ^{44}Ti containing ejecta of (2400 ± 1500) km s^{-1}. This means, that the bulk of the ejecta is receding from the observer. Additional broadening with respect to the detector resolution of 1.6 keV (FWHM) at 78 keV is observed. The best fit value for the FWHM of the line (i.e. instrumental and astrophysical) is (2.3 ± 0.8) keV. If interpreted as Doppler broadening of the line, this translates into an expansion velocity of the fastest moving ejecta of (5500 ± 2700) km s^{-1}. The integrated flux corresponds to a mass of $(2.1 \pm 0.6) \times 10^{-4}$ M$_\odot$ of ejected ^{44}Ti during the SN explosion, assuming a distance of (3.3 ± 0.1) kpc and a remnant age of 330 yr. The uncertainty in the ejecta mass is mainly introduced by the uncertainty in the determined flux, however, uncertainties in the distance to the SNR and decay constant of ^{44}Ti are also incorporated.

When represented by an independent Gaussian line, the decay line of ^{44}Sc at 1157 keV is detected with a significance of 3.3σ above the underlying continuum (see Figure 5.11). The line is significantly broadened with a FWHM of (40.0 ± 6.7) keV and the centroid is shifted to (1151.0 ± 7.9) keV, which is compatible with the laboratory determined line energy of 1157.0 keV. The line shift and broadening translate into an ejecta bulk motion of (1600 ± 2000) km s^{-1} and an expansion velocity of (8900 ± 1500) km s^{-1}. By assuming no prior knowledge, the integrated flux in the 1157 keV line is significantly higher with respect to the 78 keV line and contains $(9.5 \pm 3.0) \times 10^{-5}$ ph cm^{-2} s^{-1}. This translates into an ejecta mass of $(5.9 \pm 1.9) \times 10^{-4}$ M$_\odot$.

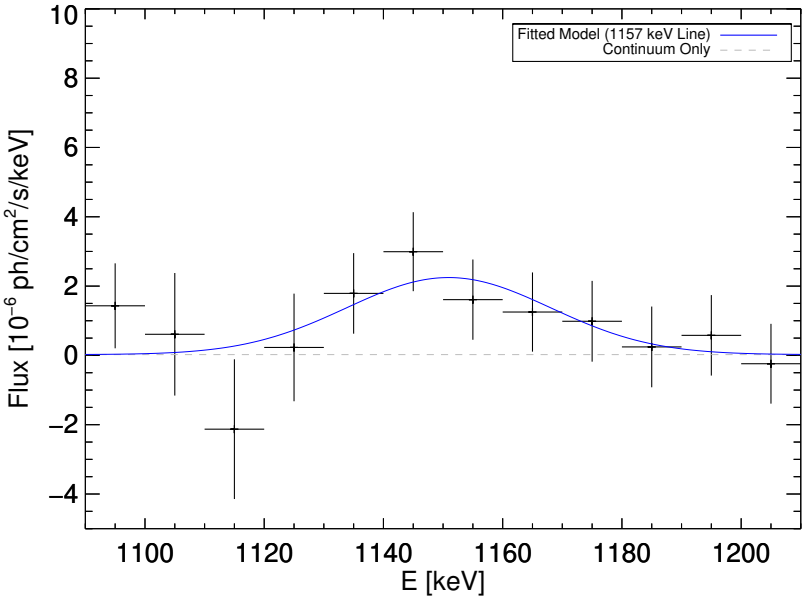

Figure 5.11: Spectrum of Cas A in the energy region 1090 – 1210 keV in 10 keV binning. The underlying continuum is determined over the broad energy range 20 keV to 1.3 MeV. The spectrum is fit with one Gaussian shaped line, centered at (1151 ± 7.9) keV and significantly broadened with respect to the detector resolution of 2.7 keV FWHM at 1157 keV.

Fitting a Combined Line Signal

All three lines are linked by a common origin, namely the decay chain of ^{44}Ti. This characteristic is used to search for a combined signal in the subsequent decay channels by determining the line flux and kinematic properties of the ^{44}Ti containing ejecta simultaneously. This introduces the assumption, that these values represent the signal purely introduced by the decay of ^{44}Ti. For possible additional contributions that can influence the ^{44}Sc line see section 5.1.4. The decay signal in the fit of a combined 78 and 1157 keV line is found with a significance of 4.9σ. Each line contains an integrated, branching ratio-corrected flux of $(4.2\pm1.0)\times10^{-5}$ ph cm^{-2} s^{-1}, which translates into a ^{44}Ti ejecta mass of $(2.6\pm0.6)\times10^{-4}$ M$_\odot$. The Doppler broadening of the lines is (2.4 ± 0.9) keV and (31.2 ± 6.6) keV respectively, which corresponds to an expansion velocity of the SNR of (6400 ± 1900) km s^{-1}. The bulk of the ejecta moves away from the observer with a velocity of (1800 ± 800) km s^{-1}. The corresponding determined line centroids are (77.9 ± 0.2) keV and (1150.5 ± 3.2) keV, respectively.
Due to the strong background lines complex in the low energy region, uncertainties are high when including the 68 kev line, which leads to an artificially broadened line. However, it is possible to include the 68 keV line in our analysis in a combined line fit of all three lines by adopting the kinematics determined from the 78/1157 keV line fit. The 68 keV line is then observed with a single line significance of 2.2σ. The significance for the detection of the decay signature of ^{44}Ti in all three lines in Cas A is in total enhanced to 5.4σ. The model for a combined fit is shown in Figure 5.12.
All measured values for the lines and the derived quantities are listed in Table 5.5.

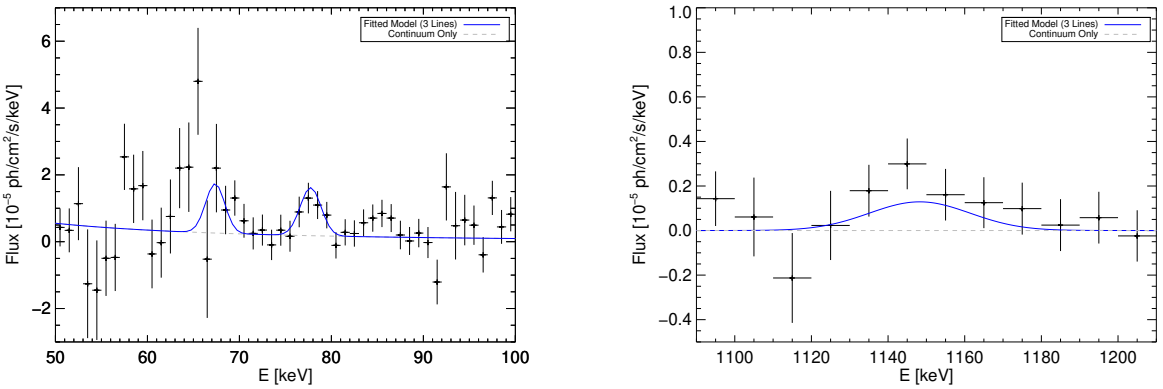

Figure 5.12: Spectra of Cas A in the energy regions containing the three dominant lines in the decay chain of ^{44}Ti. The blue curve shows the best fit model for a simultaneous multi-line fit of all three lines.

	Separate 78 keV	Separate 1157 keV	Combined 2 Lines	Combined 3 Lines
Detection Significance [σ]	3.6	3.3	4.9	5.4
Flux [10^{-5} ph cm^{-2} s^{-1}]	3.3±0.9	9.5±3.0	4.2±1.0	4.6±0.8
Centroid [keV]	77.7±0.5	1151±7.9	77.9±0.2; 1150.5±3.2	67.5 ; 77.9; 1150.5
Line FWHM [keV]	2.3±0.8	40.0±6.7	2.4±0.9; 31.2±6.6	2.3; 2.4 ; 31.2
Mass [10^{-4} M$_\odot$]	2.1±0.6	5.9±1.9	2.6±0.6	2.9±0.5
Shift [km s^{-1}]	2400 ± 1500	1600 ± 2000	1800 ± 800	1800 (fixed)
Expansion Velocity [km s^{-1}]	5500±2700	8900±1500	6400±1900	6400

Table 5.5: Best fit parameters of the Gaussian shaped lines and derived quantities for the ^{44}Sc and ^{44}Ti decay in Cas A. The first two columns give the values are given for individual, independent line fits of the 78 and 1157 keV line. Column three contains values for combined fits of the 78 + 1157 keV line. The last column contains the best fit parameters of a combined fit of all three lines, but with Doppler parameters fixed to the values determined for the 78 + 1157 keV line fit.

5.1.3.2 SN 1987A

Flux Limits In The Multi-Line Fit

SN 1987A was observed by SPI for a dead time corrected total exposure of 7 Ms. Due to the extra-Galactic origin of the source in the neighboring dwarf galaxy, several other X-ray emitting sources are present within SPI's FoV. Among them are the pulsar PSR B0540-69 and the high-mass X-ray binary LMC-X1, which are located less than 1° away from the position of SN 1987A. As this distance is below the angular resolution of SPI of 2.7°, the contribution of these two sources cannot be independently determined. The spectrum obtained for SN 1987A is therefore the superposition of three potential X-ray emitting sources. Fortunately, no signature mimicking the decay of ^{44}Ti is expected from both sources, additional to SN 1987A.
The spectrum is fit with one power law, accounting for the X-ray emission of the superim-

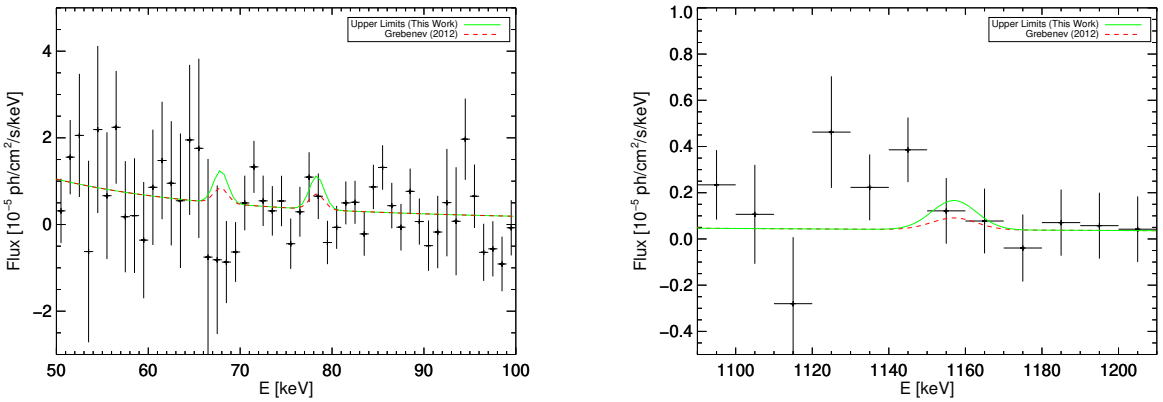

Figure 5.13: Spectra of SN 1987A in the energy regions 50 – 100 and 1090 – 1210 keV, relevant for the decay chain of ^{44}Ti. The flux in the low energy range is composed of the superposition of several celestial sources, that cannot be spatially separated within SPI's angular resolution of 2.7°. The superimposed continua are fit with one power law. No significant detection of decay lines is found in both regions. The green curve shows the 2σ upper limits obtained in our analysis. For comparison, the detection of ^{44}Ti decay with the INTEGRAL/IBIS telescopes is included in red (Grebenev et al. 2012).

posed continua radiation. No significant flux excess in the decay lines of ^{44}Ti is found in both energy regions, neither for the individual lines nor for the combined fit of all three lines at 68, 78, and 1157 keV, utilizing equations 5.1 and 5.2.
Upper limits at the 2σ level are determined from the search for the combined flux of all three lines, assuming that the flux F_L in equation 5.2 is identical in all lines. To determine the upper flux limits, the best fit continuum parameters are utilized. Ontop of this continuum, the combined line signal is added, assuming a fixed expansion velocity of the SNR. As test statistic, the χ^2 distribution is calculated. The flux of the superimposed line is increased until a $\Delta\chi^2 = 4$ for $\Delta d.o.f. = 1$ is reached as shown in Figure 5.14. The same procedure is utilized for all upper limits in the following sections. For the case of SN 1987A, the limits are determined for an expansion velocity of 3100 km s^{-1} (Tueller et al. 1990). Assuming co-moving ^{44}Ti ejecta, the upper flux limit is 2.0×10^{-5} ph cm^{-2} s^{-1}. With a remnant age of 24 years and a distance to the LMC of (49.6 ± 0.5) kpc, the flux translates into an ejecta mass upper limit of 7.5×10^{-4} M$_\odot$. The implication of the mass limits are discussed in combination with results for Cas A in section 5.1.4.

5.1.3.3 Vela Jr.

The SNR Vela Jr. has an apparent diameter of 2° due to its close distance to Earth (Aharonian et al. 2007). The extent of the SNR is slightly below the width of the SPI point spread function. However, the extended surface of the emission is modeled and folded through the image response function, yielding a more precise celestial detector response than assuming a simple point source emission. The SNR is modeled with a 2D Gaussian profile with a 1σ width of 0.6°. The 2° surface area then contains 90% of the expected SN decay flux. The spectra of both energy regions containing the dominant ^{44}Ti decay lines are shown in Figure 5.15.
No significant signal is found in any of the three decay lines. Upper limits are determined

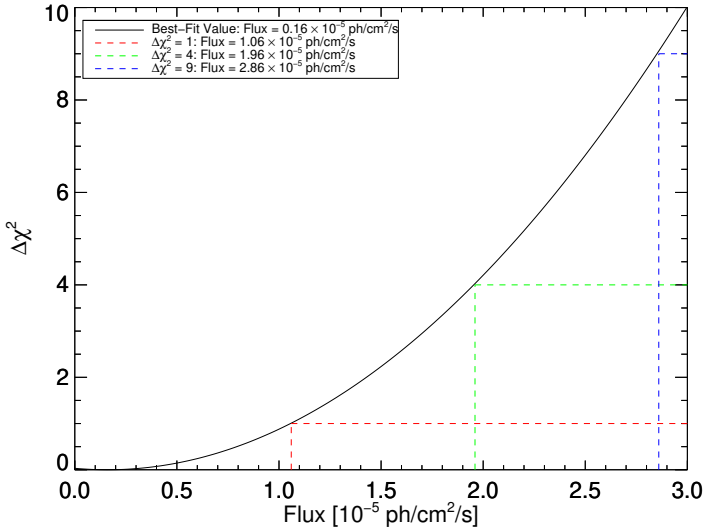

Figure 5.14: $\Delta\chi^2$ vs single line flux in SN 1987A. The values are calculated assuming a fixed expansion velocity of 3100 km s^{-1}, no ejecta bulk motion and the best-fit continuum parameters. The offset in χ^2 is given as the difference between the minimum χ^2 at the best-fit flux value and the increased flux value. The 1σ, 2σ and 3σ limits are indicated by the red, green, and blue dashed lines.

for an expansion velocity of 3000 km s^{-1} in agreement with expectations for ccSNe. The most stringent upper limit is found from a combined multi-line analysis of all three lines. The determined 2σ flux upper limit is 2.1×10^{-5} ph cm^{-2} s^{-1}. Assuming a remnant age and distance of 690 yr and 200 pc (Iyudin et al. 1998; Aschenbach et al. 1999), the flux translates into an ejected ^{44}Ti mass of 3.3×10^{-5} M$_\odot$.

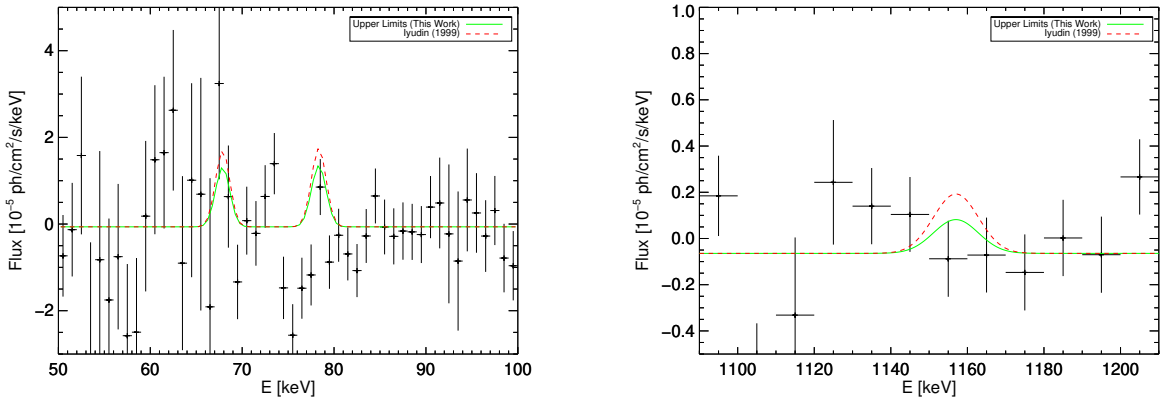

Figure 5.15: Spectra of Vela Jr. in the energy regions 50 – 100 and 1090 – 1210 keV. The green curve shows the 2σ upper limits obtained in this analysis. I show the estimation of ^{44}Sc decay with the COMPTEL telescope in red (Iyudin 1999).

5.1.4 Implication of Measured Parameters for CCSN Explosion Physics

Inadequacies of ccSN Simulations Concerning Ejected ^{44}Ti Masses

In the three analyzed ccSN remnants Cas A, SN 1987A, and Vela Jr. significant flux excess in the decay lines of ^{44}Ti is only found for Cas A. The ejected ^{44}Ti mass, determined from the measurements in this thesis, is $(2.6 \pm 0.6) \times 10^{-4}\,M_\odot$ when the signal from all three lines is combined. Similar ejecta masses are inferred by measurements with earlier SPI data ($(2.4 \pm 0.9) \times 10^{-4}\,M_\odot$; Siegert et al. 2015), INTEGRAL/IBIS ($(0.9 \pm 0.2) \times 10^{-4}\,M_\odot$; Tsygankov et al. 2016), NuSTAR ($(1.2 \pm 0.2) \times 10^{-4}\,M_\odot$; Grefenstette et al. 2017). Generally, the inferred mass for the ejected ^{44}Ti is $\gtrsim 10^{-4}\,M_\odot$. For SN 1987A, an ejecta mass upper limit of $7.5 \times 10^{-4}\,M_\odot$ is found, which is in agreement with observed ejecta masses in X-rays. Measurements with NuSTAR (Boggs et al. 2015) and INTEGRAL/IBIS (Grebenev et al. 2012) determined an ejecta mass of $(1.5 \pm 0.3) \times 10^{-4}\,M_\odot$ and $(3.1 \pm 0.8) \times 10^{-4}\,M_\odot$, respectively. The ejecta mass limit for Vela Jr.. determined in this thesis, is $3.5 \times 10^{-5}\,M_\odot$, however, the age and distance utilized for the calculation of this limit are uncertain and discussed in detail below.

Understanding the fundamental principles required for a successful explosion in ccSNe simulations is one of the major unresolved problems currently faced by the astrophysical community. Whether the explosion can be adequately described by two dimensional models, or a full set of three dimensional models is required, which traces the relevant hydrodynamic evolution of the explosion, is one of the open questions. I contribute to the solution of this problem by comparing the results of this thesis with the predicted ^{44}Ti ejecta masses of various scenarios. Conventional models for ccSNe, simulated only in one or two dimensional approaches, predict ^{44}Ti masses in the range of a few $10^{-5}\,M_\odot$ to a maximum of $\approx 10^{-4}\,M_\odot$ over the entire range of progenitor masses. The majority of nucleosynthesis calculations for ccSN rely on artificially inducing an explosion (see section 2.3.3 and e.g. Fryer et al. (2008)). Specifically for Cas A, which is the remnant of a progenitor with $15 - 25\,M_\odot$ (Fryer et al. 2008; Young et al. 2006), model calculations from piston driven explosions suggest an ^{44}Ti ejecta mass of $(1.4 - 8.7) \times 10^{-5}\,M_\odot$ (Timmes et al. 1996). Different mechanism to explode such a massive star (e.g. Woosley & Weaver 1995; Young & Fryer 2007; Fryer et al. 2008) all suggest ejecta masses below $10^{-4}\,M_\odot$ (Woosley & Weaver 1995; Young & Fryer 2007; Fryer et al. 2008). These models underestimate the production and ejection efficiency of ^{44}Ti in Cas A. Neither of these model calculations can explain the high ejecta mass observed in Cas A (and also in SN 1987A, see above).

One of the major drawbacks of 1D simulations is the introduction of the mass cut, an idealized zone separating the ejected material from the gravitationally bound material, falling back on the compact remnant. Hydrodynamic instabilities, induced from convective motion in the SN explosion, lead to direction dependent ejection of material. Only more recent models, evolved in multidimensional SN explosion simulations, self-consistently follow the directional dependence of the shock fronts multi-dimensional surface. Such simulations can reproduce the observed asymmetries in remnants such as Cas A (Wongwathanarat et al. 2013; Wanajo et al. 2018; Wongwathanarat et al. 2017). These simulations also suggest higher ejecta masses of ^{44}Ti of $\approx 1.5 \times 10^{-4}\,M_\odot$. A fully multidimensional treatment is required to explain nucleosynthesis and the ejection of freshly synthesized material in asymmetric ccSNe, indicating the importance of non radial flows above the PNS. In addition, nucleosynthesis in the SN explosion simulations is commonly represented by following a subset of tracer isotopes, representing only a small track of the nucleosynthesis pathway.

General nucleosynthesis yields, accounting for the entire set of isotopes in a nucleosynthesis network, is calculated from the thermodynamic quantities in the innermost SN explosion and post-processed in the simulation. Harris et al. (2017) point out, that this post processing can lead to the underproduction of intermediate mass elements, especially in the isotopes with mass numbers ranging from 36 – 52, by an order of magnitude. This could also explain the overproduction of the ^{44}Ti isotope in Cas A and SN1987A with respect to the simulated expectations.

Asymmetries in Cassiopeia A

In addition to the high ejecta mass, the asymmetric nature of the Cas A explosion can also be directly inferred from the observed kinematics.

Multidimensional explosion effects are also reflected in the kinematics of the SNR, as the ejection of freshly synthesized material in an asymmetric, clumped nature also suggests higher expansion velocities of the ejected material. In section 5.1.2, the interpretation of the line kinematics in the ^{44}Sc decay line with respect to the ejecta morphology was discussed. In 78 keV line, a significant shift of the centroid to (77.7 ± 0.5) keV is observed. A similar offset of the centroid is found for the 1157 keV line, however the centroid shift is compatible with the laboratory determined energy of the decay line. Nevertheless, by searching for a combined signal in both lines, the detected centroid shift is significant and the lines are centered at (77.9 ± 0.2) keV and (1150.5 ± 3.2) keV, respectively. This translates into a bulk motion of the ^{44}Ti containing ejecta with a velocity of (1800 ± 800) km s. This interpretation is consistent with the clumped nature of ^{44}Ti containing ejecta observed with the NuSTAR telescope (Grefenstette et al. 2017), shown in Figure 5.1. With the angular resolution of the NuSTAR instrument, 11 distinct regions containing ^{44}Ti clumps could be identified in the hard X-ray decay line of ^{44}Ti at 68 keV, that are distributed asymmetrically around the SNR. The majority of these clumps is seen to travel away from the observer. The bulk motion, calculated from the flux weighted mean velocity of the 11 ejecta clumps, is $\approx$ 1000 km s, consistent with the bulk motion determined in this thesis from the Gaussian line approximation. This agreement is a good indication that synthesized material was indeed preferentially ejected into one hemisphere during the explosion of Cas A.

Rayleigh-Taylor instabilities, introduced in the explosion of a type IIb progenitor lead to large scale mixing of the ejecta with the surrounding stellar shells and higher ejecta velocities than a spherically symmetric explosion would. In the 3D simulation, representing the Cas A remnant (Wongwathanarat et al. 2017), ^{44}Ti is present in the ejecta with velocities of $5000 - 9000\,\mathrm{km\,s^{-1}}$. In contrast, Nagataki et al. (1998) find ejected radioactive material only at velocities $\leq 4000\,\mathrm{km\,s^{-1}}$ in 2D. The observed Doppler broadening in the decay lines suggest an expansion velocity of $(6400 \pm 1900)\,\mathrm{km\,s^{-1}}$ from the combined multi line fit. From single line fits, an expansion velocity of $(5500 \pm 2700)\,\mathrm{km\,s^{-1}}$ and $(8900 \pm 1500)\,\mathrm{km\,s^{-1}}$ are observed in the 78 keV and 1157 keV line, respectively. The detection of ^{44}Ti at high velocities therefore further favors the asymmetric models for ccSN explosions with a ^{44}Ti signal.

In the separate analysis of the 1157 keV line in the Cas A remnant, a significantly higher flux is found than in the 78 keV line. Similar enhancement of the flux of the 1157 keV with respect to the 68 and 78 keV line have also been found in previous analyses with SPI (Siegert et al. 2015), albeit with less exposure, and with COMPTEL observations (Iyudin 1999). Considerations as discussed in section 5.1.2 support the interpretation that the increased

flux in the high energy line is due to an asymmetric ejection of matter in the remnant. However, before such conclusion can be drawn, other potential reasons for the elevated flux in the high energy line in SPI data are discussed:

1) First, an enhancement of the flux in the energy region of the 1157 keV line by an additional process, not accounted for in the present model, is investigated. Specifically, interactions of CR particles with the ambient medium in the SN shock are considered, which can produce two distinct features. Interaction of CRs with stable ^{44}Ca nuclei and spallation reactions on neighboring isotopes produce the excited ^{44}Ca state at 1157 keV. This effect only enhances the ^{44}Ca de-excitation line, but not the de-excitation lines in the scandium isotope. Due to the short half live of ^{44}Sc, the available equilibrium amount of ^{44}Sc is low. Therefore the excitation of ^{44}Sc only produces an insignificant influence on the line strength at both the 68 and 78 keV line. Summa et al. (2011) have modeled the spectrum produced from the interaction of CRs with the typical abundance distribution of isotopes in the ambient shock medium. They find that the most prominent lines of this process arise at 4.4 and 6.2 MeV from the de-excitation of ^{12}C* and ^{16}O*, respectively. A detailed analysis of the CR induced excitation of nuclear transitions in Cas A is presented in section 6.5.2.
In addition, the CR excitation of heavy elements in the remnant leads to a continuum-like emission from the superposition of the multiple de-excitation lines (cf. section 2.7.5). This continuum is distinctly different from the synchrotron continuum at low energies. Systematic effects of neglecting a second continuum emission by extrapolating the low energy synchrotron emission to high energies are considered. The flux intensity and the power-law index of the best fit synchrotron continuum spanning the entire energy range are mainly fixed by the spectral shape below 100 keV. In the energy region 1125 – 1175 keV, containing $\approx$ 90% of the decay line, the flux in the extended synchrotron continuum only accounts for $(1.0 \pm 7.0) \times 10^{-7}$ ph cm^{-2} s^{-1}, consistent with zero. The increases in the flux density from an additional continuum is further discussed in section 6.5.2. The best fit model of this continuum accounts for an additional flux of $(1.1 \pm 0.2) \times 10^{-5}$ ph cm^{-2} s^{-1} in the energy region 1125 – 1175 keV, which should be treated as systematic offset of the 1157 keV flux. When accounting for this systematic effect, the flux in the 1157 keV line is $(8.4 \pm 3.0) \times 10^{-5}$ ph cm^{-2} s^{-1}.

2) Absorption of the line flux in the 78 keV line is considered, which would make the mass estimates from the 78 keV line smaller and invert the problem. A recent study has shown that up to two thirds of the Galactic dust can be produced by the condensation of type II SN ejecta into dust grains (McKinnon et al. 2016). The attenuation length of dust grains is dependent on the wavelength of the incident photons, where shorter wavelengths suffer from higher attenuation. Depending on the composition of the absorbing dust, attenuation can be higher by one order of magnitude for the 78 keV line than for the 1157 keV line (see e.g. Iyudin et al. 2019). The presence of ^{44}Ti in newly formed dust grains or the presence of dust between the SNR and the observer can alter the relative line strengths of the 1157 keV to the 78 keV line beyond the laboratory branching ratio. Taking correction of the branching ratios into account, the flux ratio from my measurements is

$$\frac{F_{78}}{F_{1157}} = 0.35 \pm 0.14 \tag{5.5}$$

This would suggests, that between 51 and 79% of the line flux in the 78 keV line are absorbed. Assuming pure iron dust grains between Earth and Cas A, that have the highest ab-

sorption ratio between the 78 keV and 1157 keV line[2], an attenuation length of 2.38 g cm^{-2} is necessary to explain the observed flux ratio. This attenuation length is incompatible with dust observation towards Cas A (Lee et al. 2015), that suggest a column density of $\approx 10^{-4}$ g cm^{-2} iron along the line of sight.

Both considered processes cannot account for the overall flux elevation in the 1157 keV line. While the second mechanism fails to explain the observed discrepancy by several orders of magnitude, the first mechanism does not strongly reduce the flux in the line. The remaining discrepancy is $\frac{F_{78}}{F_{1157,red}} = 0.39 \pm 0.18$. In section 5.1.2, the low significance detection of a broadened 1157 keV line is considered for an inhomogeneous ejection of matter. The description of a non uniform flux distribution in the spectrum with an inherently symmetric model leads to an overestimate of the flux in the Gaussian representation. In the case of Cas A, a similar misrepresentation of the potential asymmetric ejecta morphology by a symmetric model will lead to a similar overestimation of the flux. This is additionally enhanced by an overestimate of the line width. Assuming that the combined analysis of the lines retrieves the correct value for the line broadening, it is evident, that the line broadening found in the high energy line is too high. A similar behavior was identified in section 5.1.2: The higher the asymmetry in the ejecta, the broader the fitted width of the Gaussian line. Therefore, the Gaussian contains even more artificial flux in the low and high energy flank, than inherently introduced by the false model assumption. Both effects lead to an elevated flux level in the high energy line, hinting towards highly asymmetric ejection of matter. An identification of individual ejecta clumps in the spectrum should resolve this ambiguity. Unfortunately, a spectrally resolved analysis of the 1157 keV is not feasible with the current SPI exposure on Cas A.

Absence of a ^{44}Ti Signal from Vela Jr.

In the analysis of the Vela Jr. SNR in this thesis no signal in both energy ranges, containing the ^{44}Ti and ^{44}Sc decay lines, could be found. The determined upper flux limit is 2.1×10^{-5} ph cm^{-2} s^{-1}. A similar limit was found with INTEGRAL/IBIS in the 68 and 78 keV line, with an upper limit of 1.8×10^{-5} ph cm^{-2} s^{-1}, however under the assumption of a point source. Both results show a discrepancy when compared to the serendipitous COMPTEL detection of the ^{44}Sc decay signal with a flux of $(3.8 \pm 0.7) \times 10^{-5}$ ph cm^{-2} s^{-1} (Iyudin et al. 1998) at 1157 keV. The significance of the line is contentious due to problems in the applied background modeling approach (Schoenfelder 2000). Similar doubts have been raised about the detection of the ^{44}Sc fluorescence line: While evidence for the detection of this line was identified (Tsunemi et al. 2000; Iyudin et al. 2004), follow-up observation (Slane et al. 2001; Hiraga et al. 2009) could not confirm these findings, which substantiates the idea, that the SNR age and distance are significantly higher than initially estimated.
From the SPI upper limit, the age and distance are inferred as outlined in the following. As neither the age nor the distance are uniquely determined, both quantities can only be determined in dependence of each other. To gauge the allowed parameter space for both

[2]See XCOM data base, https://physics.nist.gov/PhysRefData/Xcom/html/xcom1.html

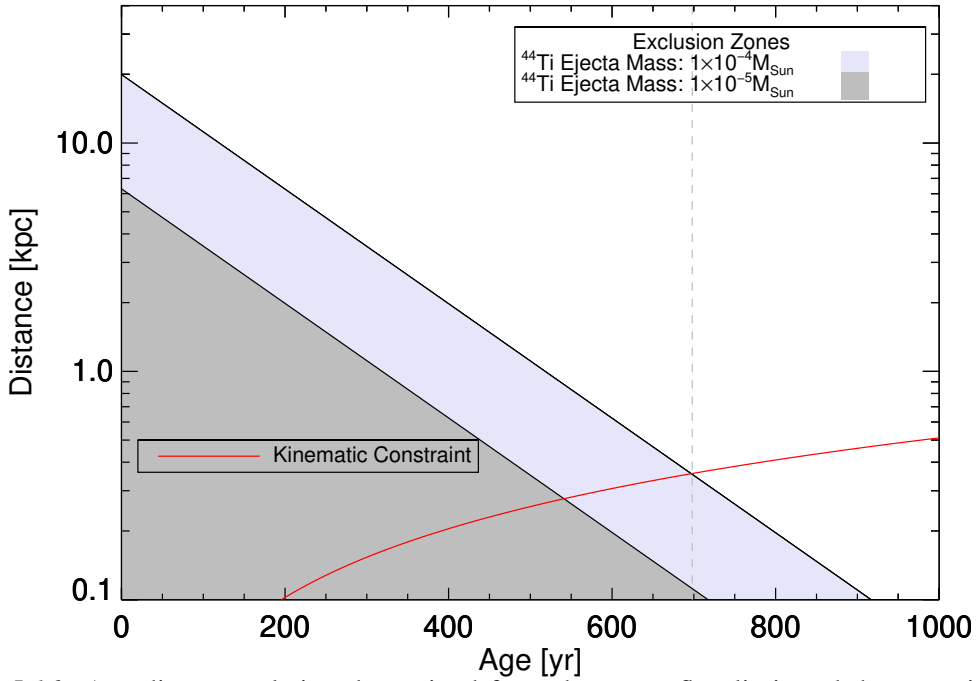

Figure 5.16: Age-distance relation determined from the upper flux limit and the canonical ejecta masses as indicated in the legend. The shaded areas indicate the parameter spaces that are excluded in this analysis. In addition, the red line indicates the age distance relation due to kinematic arguments (see text).

quantities, equation 5.4 can be rearranged to provide an age dependent distance by

$$d = \sqrt{\frac{m_{ej}}{F_0 4\pi N u \tau \exp\frac{t}{\tau}}} \tag{5.6}$$

$$= 19.9 \times \sqrt{\frac{m_{ej}}{10^{-4} M_\odot}} \times \exp\left(\frac{-t}{2\tau}\right) \quad \text{kpc}, \tag{5.7}$$

where m_{ej} is the ejected ^{44}Ti mass and d is the distance to the remnant. Since no emission in the decay chain is unambiguously detected in the remnant, the ^{44}Ti ejecta mass is assumed for equation 5.6. As a compact central object was linked to the SNR (Pavlov et al. 2001), the remnant is expected to originate from a ccSN, for which I assume a canonical ^{44}Ti ejecta mass between 10^{-5} and $10^{-4}\,M_\odot$. The excluded parameter spaces for the age and distance in both limits are indicated as the shaded areas in Figure 5.16. To further constrain the allowed parameter space, a kinematic argument is used, that relates the distance of the remnant to the age by the apparent size of the remnant. The diameter is given by

$$\tan\alpha = \frac{r_{dia}}{2d} = \frac{v_{exp} t}{2d} \Leftrightarrow d = \frac{r_{dia}}{\tan\alpha}, \tag{5.8}$$

where r_{dia} is the physical size of the remnant and α is its apparent size. The average expansion velocity of the ejecta $v_{exp} = 5000\,\mathrm{km\,s^{-1}}$ (Aschenbach 1998) is assumed to be constant during the evolution of the remnant. This relation is indicated in red in Figure 5.16. The intersection of the red line with the edges of the shaded areas would then provide a unique distinction of the remnants age and distance. In this analysis, a distance and age of $\approx 700\,\mathrm{yr}$

and of ≈ 300 pc are derived in the limit of the high ejecta mass. Interestingly, these values are consistent with the determination by Iyudin et al. (1998). I emphasize here that my estimate is solely based on an upper limit. Therefore, all parameter tupels to the right of the indicated grey line in Figure 5.16 remain allowed.
The analysis of the SNR's expansion rate using Chandra data determined a radial displacement of Vela Jr. northern rim between 2003 and 2008 of (2.40 ± 0.56)" (Allen et al. 2014). Assuming this region is representative for the entire SNR, they determined from a comparison with hydrodynamic simulations that the SNR's age is in the range of 2.4 – 5.1 kyr, and that it is at a distance of (700 ± 200) pc. This parameter space is in agreement with my analysis. Conversely, with these updated values I do not expect to detect any emission in the ^{44}Ti decay chain within SPI's sensitivity.

5.1.5 Observing ^{44}Ti in Thermonuclear Explosions with SPI

5.1.5.1 G1.9+0.3 Galactic Central Source

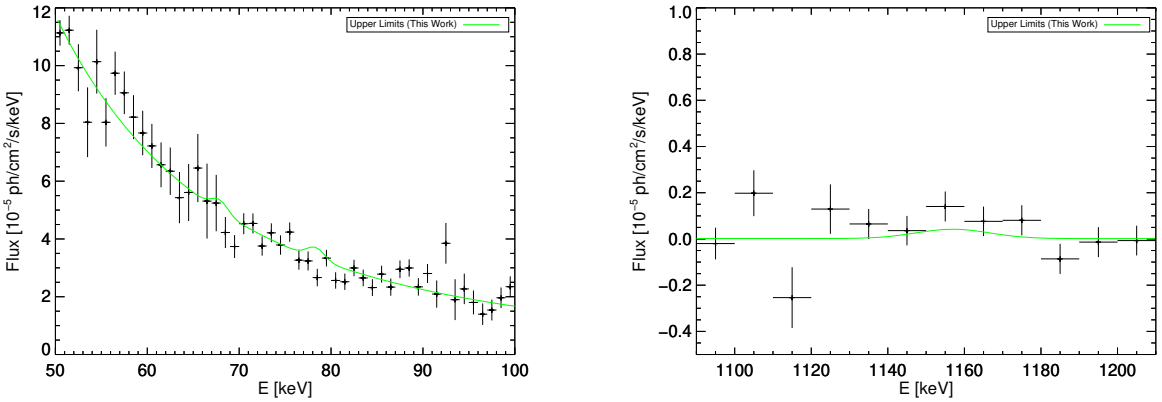

Figure 5.17: Spectra extracted from SPI data at the location of G1.9+0.3 in the energy regions 50 – 100 and 1090 – 1210 keV, containing the superimposed emission of several hard X-ray emitting sources. The spectrum is fit with one power law to account for the superposition of several hard X-ray continua, on top of which the signature for the ^{44}Ti decay chain is determined. The green curve shows the best fit power law and the 2σ upper limits obtained in our analysis.

The Galactic central region is a field of view crowded with a large number of X-ray emitting sources. In the direct vicinity of G1.9+0.3, several hard X-ray sources are present (Bird et al. 2016) within SPI's angular resolution of 2.7°, that are above the sensitivity limit of SPI in the energy range up to ≈100 keV. No emission in the decay chain of ^{44}Ti is expected in these additional sources, as neither of them is associated with recent nucleosynthesis. Therefore, potential flux excess above the continuum in the energy band surrounding the 68 and 78 keV line is attributed to the emission of G1.9+0.3. However, along the line of sight in a cone with 2.7° diameter, a volume of 1.4 kpc^3 is probed between Earth and the Galactic center. Such a large region can potentially host other SNRs that are not found in common SNR catalogs (Green 2014), but would be expected as a result of the high SN rate in the Milky Way (see section 5.3). The extracted, resulting spectra for the position of G1.9+0.3 are shown in Figure 5.17. The spectrum consists of the superposition of various continua, produced by the X-ray emitting sources and potentially also by the young SNR G1.9+0.3 from electron synchrotron emission. No distinction between the various contributors can be

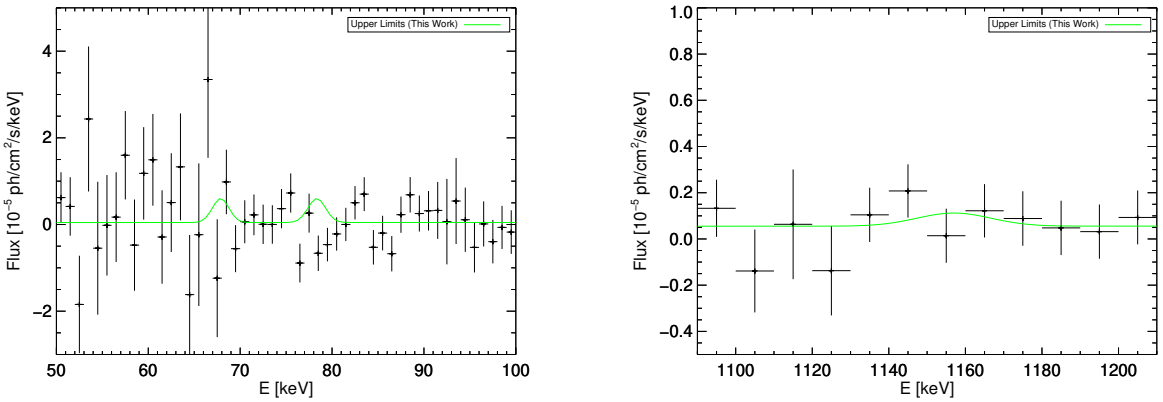

Figure 5.18: Spectra of Tycho's SN in the energy range 50 – 100 and 1090 – 1210 keV, relevant for decay chain of ^{44}Ti. Included in green are the upper limits for a multi-line fit (cf. text).

made based on the angular resolution of SPI, and the overall continuum spectral shape is fit with one power law, approximating the true shape of the continuum. I search for the imprint of the decay lines on top of the underlying continuum.

We find no flux excess in both energy regions for any of the three decay lines. The expansion velocity of the ^{44}Ti containing ejecta is not precisely known. While the SN's blast wave speed is $\approx$ 14000 km s^{-1} (Reynolds et al. 2008), expansion velocities around 5000 km s^{-1} are found for the type Ia SN2014J (Diehl et al. 2014; Churazov et al. 2015; Diehl et al. 2015) from the decay chain of the shorter-lived radioisotope ^{56}Co. As the distribution of the nucleosynthesis products in a thermonuclear SN is not precisely determined, ^{44}Ti can be located in the vicinity to ^{56}Co close the center, in a slower expanding medium or clumped as in the ccSNR Cas A. Therefore velocity dependent upper limits in the ^{44}Ti decay chain for expansion velocities between 0 and 15000 km s^{-1} are determined. The upper limits are in the range of $(0.3 - 1.5) \times 10^{-5}$ ph cm^{-2} s^{-1}.

5.1.5.2 Tycho SNR

SPI collected a total of dead time corrected exposure of 10 Ms on Tycho's SNR between 2002 and 2019. The majority of exposure was acquired while observing the neighboring ($\approx 8^\circ$ distance) remnant of Cas A, during which Tycho's SNR is in SPI's field of view. The extracted spectra are shown in Figure 5.18. I find no signal in any of the three de-excitation lines attributed to the ^{44}Ti decay (for comparison see Figure 5.9; Significance map in the vicinity of Cas A).

An upper flux limit is determined, assuming an expansion velocity of the ejecta material of 5000 km s^{-1}. The 2σ upper limit is 1.4×10^{-5} ph cm^{-2} s^{-1}, corresponding to an ^{44}Ti ejecta mass of 4.8×10^{-4} M$_\odot$ for a remnant age of 438 yr and a distance of 4.1 kpc.

5.1.5.3 Kepler SNR

The spectra obtained for Kepler's SNR are shown in Figure 5.19. No significant ^{44}Ti decay signal is found in either energy region. The 2σ upper flux limit is 1.1×10^{-5} ph cm^{-2} s^{-1}

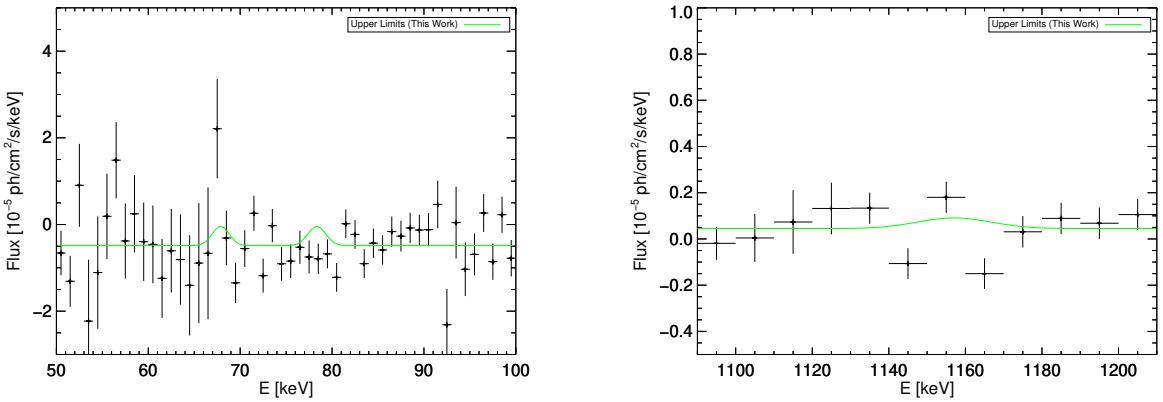

Figure 5.19: Kepler's SNR in the energy range 50 – 100 and 1090 – 1210 keV. Upper limits for a multi-line fit of the dominant lines in decay chain of ^{44}Ti are included in green.

assuming an expansion velocity of 5000 km s^{-1}, consistent with other thermonuclear SN explosions. The corresponding mass limit is 4.0×10^{-4} M$_\odot$ for an assumed remnant distance of 5.1 kpc and an age of 406 yr.

5.1.6 Exclusion of Type Ia Progenitor Models

G1.9+0.3

The upper flux limit determined for G1.9+0.3 translates into a ^{44}Ti ejecta mass of 0.3×10^{-4} M$_\odot$. The nucleosynthesis yields of the delayed detonation or pure deflagration model (e.g. Maeda et al. 2010) are compatible with our mass limits determined for this remnant. More exotic scenarios such as the double detonation scenario or the Calcium rich scenario (see section 2.4) are excluded, as the predicted ^{44}Ti ejecta yields for these scenarios are two orders of magnitude higher.

No detection for the decay lines in hard X-rays at the 68 and 78 keV lines has been claimed (Zoglauer et al. 2015; Tsygankov et al. 2016; Weinberger et al. 2020, this thesis) so far. Emission in the energy region at 4.1 keV was detected with Chandra (Borkowski et al. 2010), which was attributed to the emission of the ^{44}Sc fluorescence line, following the electron capture decay of ^{44}Ti. Correcting for the branching ratio, the detected flux in the 4.1 keV line corresponds to a flux in the 68 and 78 keV line of $(0.3-1.9)\times10^{-5}$ ph cm^{-2} s^{-1} per line. A ^{44}Ti decay as the origin cannot be excluded entirely over the assumed expansion velocity range. However, I argue, that the emission measured from the fluorescence line does not necessarily have to be produced by the electron shell transitions following the decay of ^{44}Ti. As this line is emitted by the transitions of de-exciting electrons in the scandium shell (Kα line), the preceding excitation can also be caused by thermal excitation in the shocked material. Furthermore, the difference in fluorescence line energy between the different isotopes of scandium is marginal, and the emission can therefore also be produced by transitions in the stable ^{45}Sc isotope, synthesized in the SN explosion.

Table 5.6: Values for the masses and fluxes of the six young SNRs. Fluxes are determined for the ^{44}Sc and ^{44}Ti decay separately and also with a combined fit for the most stringent constraints in the analysis. Fluxes are given in 10^{-5} ph cm^{-2} s^{-1}. Masses are given in 10^{-4} M$_\odot$.

	Cas A	SN 1987A	Vela Jr	Tycho	Kepler	G1.9+0.3
Flux ^{44}Sc	9.5±3.0	≤4.1	≤4.7	≤6.2	≤2.6	≤3.7
Flux ^{44}Ti	3.3±0.9	≤1.9	≤2.8	≤1.5	≤1.3	≤1.1
Flux Comb	4.2±1.0	≤2.0	≤2.1	≤1.4	≤1.1	≤1.0
Mass Comb	2.6±0.6	≤7.5	≤0.3	≤4.8	≤4.0	≤0.3

Tycho

Similar to G1.9+0.3, the more exotic progenitor models, that produce high yields of ejected ^{44}Ti, such as the double detonation and Ca-rich models, can be excluded for Tycho's SNR. The upper ejecta mass limit is in agreement with nucleosynthesis yields of the deflagration and delayed detonation models. The latter is also favored for this SNR by Badenes et al. (2006), as it best reproduces the observed X-ray spectra of Tycho's SNR.

Kepler

The determined upper mass limit excludes the majority of SN models, which predict high yields of ^{44}Ti. However, due to the somewhat uncertain distance to the SNR, ranging from 4.4 to 5.9 kpc (Sankrit et al. 2016), an upper mass limit of 5.4×10^{-4} M$_\odot$ is also possible. A minor part of the double detonation scenarios are therefore potential progenitor scenarios for Kepler's SNR.

5.1.7 Implications for Supernova Explosion Scenarios

5.1.7.1 Comparison of Measured ^{44}Ti Ejecta Masses With Model-Predicted Yields

In this comprehensive analysis of the six youngest, close by SNRs, a signal resembling the emission in the ^{44}Ti decay line was only found in the youngest ccSN remnant Cas A in SPI data. For all other sources, upper limits on the flux and corresponding ^{44}Ti ejecta were determined from SPI data. In table 5.6 the determined values for the six analyzed SNRs are listed. A comparison between the results from this thesis and the predicted nucleosynthesis yields from modeled SN explosions in Figure 5.20. Cas A's and SN 1987A's ejecta mass suggest, that both explosions are only compatible with the simulations of asymmetric, three dimensional SN explosion rather than axisymmetric, low dimensional models. This is also supported by the measured ejecta kinematics (see section 5.1.4). The small ^{44}Ti ejecta mass, determined for Vela Jr., may deviate, as the distance and age estimates (200 pc, 700 yr) underestimate the more likely, updated values determined by Allen et al. (2014) (700 pc, ≥ 2.4 kyr).

For the thermonuclear SNe, the models predicting high yields of ^{44}Ti such as the double detonation models or the Ca-rich scenarios, that might lead to peculiar type Ia SN such as SN 2005E or SN 1991bg (Mazzali & Hachinger 2012; Crocker et al. 2017), are not compatible

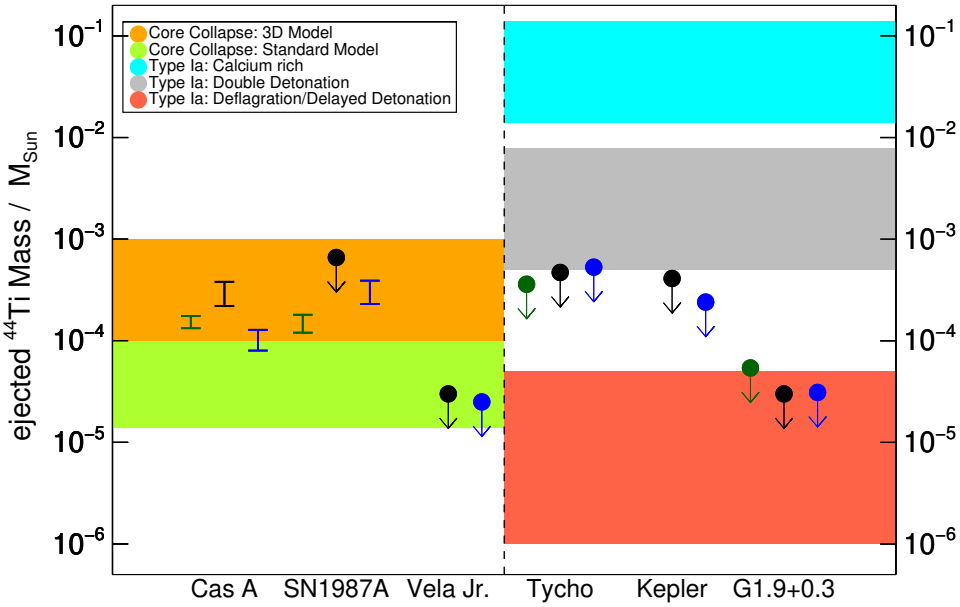

Figure 5.20: Comparison of the measured SN ejecta yields (black) or upper limits with predicted nucleosynthesis yields from SN explosion models. The left side show the three analyzed ccSN remnants Cas A, SN 1987A, and Vela Jr. The right side shows the remnants of the thermonuclear SNe G1.9+0.3, Kepler, and Tycho. The masses are determined for the age and distance values stated in table 5.1. The detection and upper limits determined from NuSTAR and INTEGRAL/IBIS are included for comparison in green and blue, respectively. The fluxes in the respective works are translated to ejecta masses assuming age and distances from table 5.1. Measured values are adopted from: (Cas A; Grefenstette et al. 2017; Tsygankov et al. 2016); (SN 1987A; Boggs et al. 2015; Grebenev et al. 2012); (Vela Jr.; Tsygankov et al. 2016); (Tycho; Lopez et al. 2015; Wang & Li 2014); (Kepler; Tsygankov et al. 2016); (G1.9+0.3; Zoglauer et al. 2015; Tsygankov et al. 2016).

with the measured upper limits of ^{44}Ti ejecta. Apart from Kepler's SNR, for which the distance determination is uncertain to some extent, the measured ^{44}Ti ejecta masses suggest that the observed three thermonuclear SN are part of the single degenerate progenitor branch. Nuclear fusion in this explosion type is triggered in the central regions of the WD, exceeding the Chandrasekhar mass limit. The predictions of both the pure deflagration and delayed detonation models are compatible with our results, and no further distinction can be made from SPI observations.

5.1.7.2 Galactic Calcium to Iron Ratio as Estimator for Supernova Rates

The detection of ^{44}Ti in only one Galactic SNR, however, also provides a peculiar picture for the production of ^{44}Ca in the Galaxy, which is solely attributed to the nucleosynthesis in SNe.

The solar abundance ratio of ^{44}Ca to ^{56}Fe, which are the end products in the respective decay chains of ^{44}Ti and ^{56}Ni, is used as an estimator for SN sub-type rates. I assume, that each sub-type is solely responsible for the solar content of ^{44}Ca and ^{56}Fe, with an abundance ratio of $[^{44}\mathrm{Ca}/^{56}\mathrm{Fe}]_{\odot} = 1.2 \times 10^{-3}$ (Anders & Grevesse 1989). In Figure 5.21 the solar abundance is shown as a function of ^{56}Ni in red as the reference value. I include the ^{44}Ti and ^{56}Ni for the

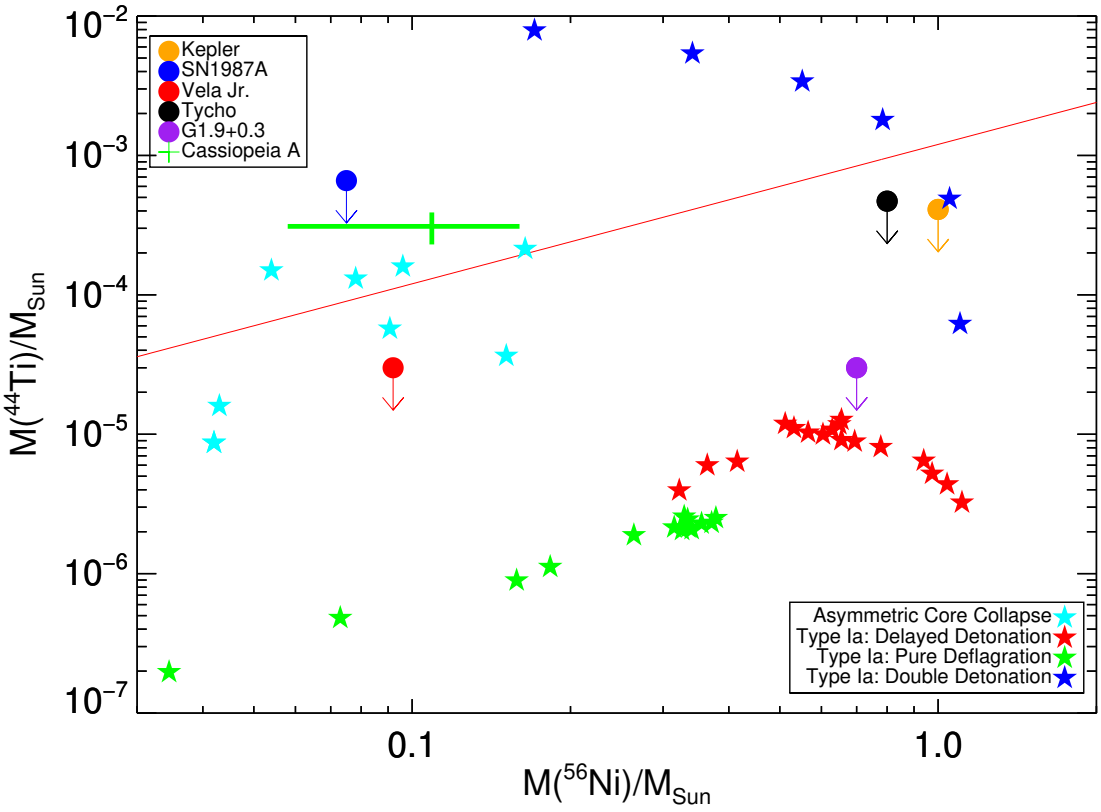

Figure 5.21: Abundance ratio of [^{44}Ti/^{56}Ni] for our mass estimates and several SN explosion models. The solar abundance ratio [^{44}Ca/^{56}Fe] = 1.2×10^{-3} (Anders & Grevesse 1989) is included in red and serves as a reference criterion to judge SN model sub-types. Inferred ^{56}Ni masses for Cas A, SN 1987A, Tycho, Kepler and G1.9+0.3 are taken from (Eriksen et al. 2009; Woosley et al. 1987; Badenes et al. 2006; Patnaude et al. 2012; Borkowski et al. 2013), respectively (see text for detail). Vela Jr.'s ^{56}Ni ejecta mass is taken from a modeled explosion of a 25 $M_\odot$ star (Maeda & Nomoto 2003). Model yields are from Wongwathanarat et al. (2017); Maeda & Nomoto (2003); Seitenzahl et al. (2013); Fink et al. (2014, 2010).

point sources, measured in our analysis, as dot symbols (upper limits). Cas A is shown as green cross symbol, accounting for the determined uncertainties. Modeled values for several SN types are shown as star symbols.

For Cas A, the only source with a detected ^{44}Ti signal, the ejected ^{56}Ni mass is inferred from a near-infrared spectral analysis (Eriksen et al. 2009). The ^{56}Ni ejecta mass for Vela Jr. was adopted from the explosion model of a 25$_\odot$ star (Maeda & Nomoto 2003). The ^{44}Ti to ^{56}Ni ratio in Vela Jr. may deviate from the solar abundance ratio of ^{44}Ca to ^{56}Fe due to the distance and age estimate. Woosley et al. (1987) infer an ejected ^{56}Ni mass of 0.075 $M_\odot$ from the early bolometric light curve of SN 1987A, which is adopted in this analysis. The ^{56}Ni ejecta masses of the three analyzed thermonuclear SNe are inferred from a comparison of measured X-ray spectra with long term simulations of SNR evolution (Badenes et al. 2006; Patnaude et al. 2012; Borkowski et al. 2013).

In Figure 5.21, the measured ^{44}Ti and ^{56}Ni ratio of both asymmetric ccSNe, Cas A and SN 1987A, are plausibly consistent with the [^{44}Ca/^{56}Fe]$_\odot$ abundance ratio. I infer, that asym-

metric SN explosion models can be responsible for the solar abundance ratio of ^{44}Ca and ^{56}Fe.
The majority of type Ia SN scenarios, on the other hand, significantly deviates from the measured solar abundance ratio of ^{44}Ca and ^{56}Fe. Observations suggest, that type Ia SNe consistently produce a ^{56}Ni mass of $0.1 - 1.0\,M_{\odot}$ (Stritzinger et al. 2006; Wang et al. 2008; Dhawan et al. 2016), which can be adequately reproduced by simulations.
Nucleosynthesis of ^{44}Ti and other intermediate mass elements in type Ia SNe is discussed in section 2.4. It is highly dependent on the physical conditions in the nuclear burning region. In the single degenerate scenarios of the delayed detonation and pure deflagration models, nucleosynthesis is limited to a high density regime in the WD, where the majority of nuclear fuel is burned completely to iron group elements (such as ^{56}Ni), and only a small amount of intermediate mass elements is produced (Seitenzahl et al. 2013; Fink et al. 2014). These two models can therefore not be major contributors to the solar ^{44}Ca content (5.21, green and red star symbols).
In contrast to that, nucleosynthesis in the double detonation scenarios does not solely occur in the central region, but also during the initial burning of the helium layer on the surface of the WD. Due to the significantly lower densities on the star's surface, large amounts of intermediate mass elements, especially ^{44}Ti, are produced in the initial detonation (Fink et al. 2010; Sim et al. 2012). Delayed detonation models therefore enrich the Galaxy in ^{44}Ti, overproducing the ^{44}Ca abundance in the solar system (5.21, dark-blue star symbol).
My results for thermonuclear SNe, constraining the explosion scenario to delayed detonation or pure deflagration models, show, that the three youngest Galactic type Ia SNe produce ^{56}Ni and ^{44}Ti with a ratio that is incompatible with ^{44}Ca and ^{56}Fe in the solar system.

Assuming that ccSNe are in general compatible with the solar $[^{44}\mathrm{Ca}/^{56}\mathrm{Fe}]_{\odot}$ ratio, I estimate the ratio of rates for type Ia SN sub-types. I use the constraints on the synthesized ^{44}Ti mass and the average yields of ^{44}Ti and ^{56}Ni from simulations. I find, that a ratio of $\geq 2.6 : 1$ of delayed detonation/pure deflagration to double detonation events is necessary to restore the solar $[^{44}\mathrm{Ca}/^{56}\mathrm{Fe}]_{\odot}$ ratio with respect to the ^{44}Ca overproduction introduced by a double detonation event.

5.2 Search for a Previously Undetected Galactic ^{44}Ti Source

5.2.1 Missing Galactic Supernova Remnants

SN explosions, in general, are a rarely occurring phenomenon in the Milky Way Galaxy. Indeed, only seven SNe during the last two millennia appear in historical records. In chronological order of their explosion dates, these seven encompass the remnants RCW 86 (SN 185), G11.2-03 (SN 386), SN 1006, the Crab (SN 1054), Tycho's SNR (SN 1572) and Kepler's SNR (SN 1604) (Stephenson & Green 2002). However, extinction in the optical band impose a major constraint on the detectability of SNe with the naked eye. The most famous case for this bias is the remnant of Cas A. In contrast to the other young SNe in the last millennium, no wide spread historical records are present in the 17th century for the explosion of Cas A. Another example is the youngest known, Galactic SNR, G1.9+0.3, detected in X-rays (Reynolds et al. 2008), whose explosion was apparently completely missed in optical observations some 100 yr ago.

Despite the low number of detected sources and an apparent overall rare occurrence of SNe, several explosions are on average expected per century in the Milky Way. Various estimates for the ccSN rate in the Galaxy are present in literature, based on the star formation rate in the Galaxy, volume integrated number of SNe, or by tracing the SNe's radioactive ejecta. Adopting an exponential disk like morphology for the distribution of SNe in the galaxy, Diehl et al. (2006a) infer a SN rate of 1 – 3 events per century. The estimate is based on the detected diffuse decay emission of radioactive ^{26}Al, synthesized in ccSNe and their massive star progenitors. Similar ccSN rates can be derived from other, Milky Way like galaxies or the number of Galactic pulsars (van den Bergh & Tammann 1991; Cappellaro et al. 1993; Keane & Kramer 2008). The ratio of ccSNe and type Ia supernovae is between 0.1 and 0.4 (Boissier & Prantzos 2009; Dufour & Kaspi 2013), suggesting a rate of 1 – 6 per millennium.

The observation window for detecting a SN in optical light is rather short, as the SN luminosity fades away on timescales of months to years within several half-life times of the radioactive isotopes powering the early emission. In contrast to that, the SNRs remain visible in X-ray and radio wavelength bands for several thousand years. Frail et al. (1994) suggest, that the shell of a SNR interacting with the ISM should be detectable for at least 60000 yr with the current radio telescopes. Assuming a SN rate of 2 events per century, this would suggest that at least 1200 SNRs should be detectable in the Galaxy. This disagrees with the observed number, as there are currently only about 300 detected SNRs (Green 2019). The low number of detected SNRs in the radio band surveys can be caused by various selection effects, one of them being that these surveys usually concentrate on the Galactic plane, neglecting higher absolute Galactic latitudes. While several additional SNRs have been detected in other wavelength bands (Aschenbach 1996; Pfeffermann & Aschenbach 1996; Asaoka et al. 1996; Reynolds et al. 2008; Acero et al. 2016, and references therein), there is still a significant discrepancy remaining.

All surveys mentioned above concentrate on detecting the electromagnetic emission of particles that are associated with the interacting shell of the expanding SNR with the surrounding medium. Here, I utilize the unique capabilities of SPI to search for the previously undetected SNRs in the Milky Way by tracing their emission of γ-rays in the decay chain of ^{44}Ti. While

providing a unique and independent way of searching, the detection of new sources would provide invaluable information on the history of SNe in the Galaxy over the last few centuries. Based on comparisons of the limiting sensitivity of the COMPTEL all sky survey (10^{-5} ph cm^{-2} s^{-1} at the 1σ level, 2.7×10^{-5} ph cm^{-2} s^{-1} at the 3σ level (Dupraz et al. 1997)) with models utilizing theoretical predictions of SN nucleosynthesis and Galactic distributions, The et al. (2006) determined that ^{44}Ti producing SNe might be exceptional events. Their simulations suggest, that on average five SNRs should be detectable in ^{44}Ti γ-ray observations in the Galaxy with the COMPTEL sensitivity. So far, ^{44}Ti decay radiation was only found in one Galactic SNR (cf. section 5.1.7). Even though more recent simulations (Dufour & Kaspi 2013) relax the constraints on the probability of detecting exactly one Galactic remnant emitting in ^{44}Ti, the probability of detecting it at the high Galactic longitude of Cas A is less than 2.7%. This suggests that several more ^{44}Ti bright SNRs should be detectable in the Milky Way.

5.2.2 Data Set

I search for the emission of previously unknown ^{44}Ti sources in the Galactic plane at latitudes $|b| \leq 18°$. The survey utilizes 17 yr of SPI data. This improves on COMPTEL's survey sensitivity by a factor of ≈ 5 (cf. section 5.2.4) , considering that the emission of the entire ^{44}Ti decay chain can be measured within SPI's broad energy range. I focus on the same energy regions as in section 5.1.

For the majority of observations INTEGRAL was oriented towards the Galactic plane. With the exception of a few time periods, during which INTEGRAL pointed to higher latitudes, the data set comprises 17 years of INTEGRAL/SPI observations between 2002 and 2019. As I am not searching for an integrated emission spread over the entire Galactic plane, but an emission of point like origin, the entire data set is separated into 10 spatially overlapping subsets, to reduce the size of the data set (number of data points), and to validate our findings by cross checks in the overlapping regions. Each subset is a Cartesian map projections of a square with dimensions of $40° \times 40°$ onto the Galactic plane. The data subsets are centered on the locations $l \in \{n \times 36°; 0°\} \forall\, n \in \{0, 1, ..., 8, 9\}$.
The entire data set consists of 68175 individual pointings, each with an average duration of ≈ 2000 s. For a continuously operating detector, this comprises a total dead time corrected exposure of 135.5 Ms. The exposure map of the Galactic plane is shown in Figure 5.22. The dead time corrected exposure for the individual subsets are listed in table 5.7.

5.2.3 Statistical Limits on Survey

I search for the emission of previously unknown sources in a mosaic pattern that is projected onto the sky. The center of each mosaic tile on the grid are separated by 1.5° from each other. The center for each tile is given by
$(l/b) \in (\{n \times 1.5°\} \forall\, n \in \{0, 1, ..., 238, 239\}/\{n \times 1.5°\} \forall\, n \in \{-12, -11, ..., 11, 12\})$.
The space covered by each mosaic tile is considered as a point source within the spatial resolution of SPI. To avoid potential degeneracy between the point sources, especially for adjacent grid points, the spectrum is extracted for each position in an individual fit, while spectra for all other positions are not extracted. This again describes the most conserva-

tive approach of a blind search. Within the latitude region |b| ≤ 18.75° the sky survey thus contains 6000 independent mosaic tiles, which in its own respect can be interpreted as an independent trial of finding a new source. The survey covers the energy region between 50 – 100 keV and 1115 – 1190 keV. In these regions, the spectra are extracted in 1 keV and

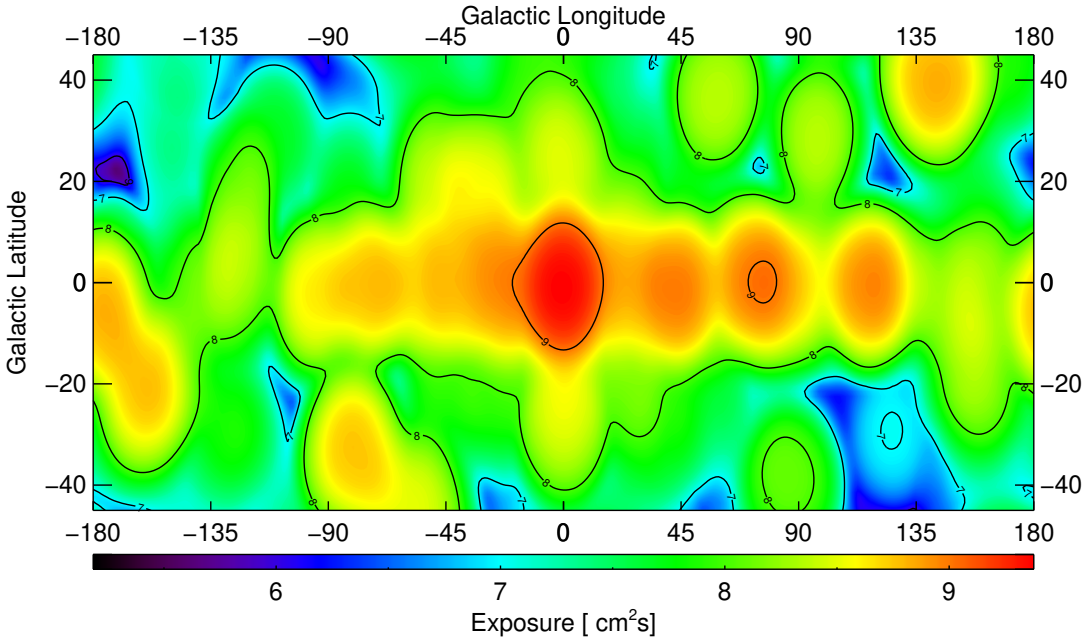

Figure 5.22: SPI sky exposure for $|b| \leq 45°$. The units of the exposure map are normalized to cm^2 s. The energy corrected exposure is calculated by dividing the exposure by the energy dependent, effective area for 19 working detectors, which is $\approx 130\,\mathrm{cm}^2$ at 70 keV and $69\,\mathrm{cm}^2$ at 1157 keV, respectively (Attié et al. 2003). The contours are given in decimal power. The minimum sky exposure in this region is $4.1{\times}10^5\,\mathrm{cm}^2$ s, the maximum is $2.4{\times}10^9\,\mathrm{cm}^2$ s.

Table 5.7: Dead time corrected exposure time of the 10 sub data sets. Note here, that the integrated exposure of the 10 data sets is 143 Ms. This slight offset with respect to the total exposure time is caused by the overlap of the individual sets of data.

Longitude [°]	Exposure [Ms]	Number of Pointings	Contains SNR
0	37.5	19825	G1.9+0.3 Kepler
36	19.3	10147	
72	16.8	8915	
108	13.0	5782	Cas A Tycho
144	6.5	3175	
180	9.1	4875	Crab
216	3.7	1745	
252	6.9	3169	Vela Jr.
288	11.4	4986	
324	19.2	10379	

2.5 keV binning, respectively. The spectrum for each mosaic tile is extracted separately, where the center of the mosaic tile is used as celestial source location in addition to known sources, that are present in the data subset.

A detection threshold is defined that does not allow more than one false detection, assuming pure photon counting statistics. For 6000 independent trials contained in the survey at $|b| \leq 18.75°$, one statistical fluctuation above a detection level of 3.75σ can be expected. It should be noted here, that the sensitivity of the survey (cf. section 5.2.4) is consequently also governed by photon count statistics. Figure 5.23 shows the signal to noise ratio for the fluxes in the 6000 analyzed tiles. The figure includes a normal distribution, representative for statistical noise. The noise distribution is separated for the energy range 65–80 keV including both ^{44}Ti decay lines and 1137–1177 keV including the potentially broadened ^{44}Sc decay line. As seen from the overall shape of the distribution, the measured fluxes in both energy bands are compatible with a normal distribution with a unit variance centered at zero. The positive tail, that is present in both energy regions towards positive signal to noise ratios, is introduced by the presence of continuum sources in the Galactic plane. Each tile covers the emission from a geometric area of $\approx 1.5° \times 1.5°$ projected onto the sky. Within the PSF of SPI, flux contribution from continuum sources, that are present in some tiles, cannot be determined independently from the contribution of the assumed point source at the center of the tile. The continuum sources differential flux distributions follow a power law with a negative index, and as a consequence, the sources are detected with a higher significance in the low energy range than in the high energy range, also after accounting for the reduced background at higher energies. This results in a more pronounced positive tail at lower energies. The left-hand distribution of Figure 5.23 is truncated at a signal to noise ratio of eight, however it extends to values of several hundred for strong sources such as the Crab nebula. The number of tiles with a signal to noise ratio above three, that are not introduced by statistical noise, is 198. This number is compatible with the number of sources in the general SPI source catalog, which contains 206 sources in the Galactic plane region at latitudes $|b| \leq 18.75°$. As some of these sources are transient or to dim to be detected in the narrow energy band, the observed number of tiles with signal to noise above three is reduced with respect to the INTEGRAL/SPI source reference catalog[3].

The number of potential ^{44}Ti emitting sources in both energy bands is influenced by the presence of continuum sources in the Galactic plane. To further investigate the properties of the sources, the extracted spectra of each mosaic tile are analyzed simultaneously for the emission of ^{44}Ti. The spectra are fitted with the model specified by equation 5.2, to search for a consistent emission in all three decay channels simultaneously. A uniform expansion velocity for the SN ejecta containing ^{44}Ti is assumed. In the low energy region, the Doppler broadening in energy space, corresponding to an expansion velocity of 4000 km s^{-1}, is of similar size as the energy resolution of the detector. However, at 1157 keV, the same velocity leads to a line broadening of 18 keV FWHM, significantly broader than SPI's energy resolution. The detection probability, i.e. the significance, for a combined signal is evaluated by fitting the combined line signal above a potential underlying continuum, modeled by a single power law (cf. equation 5.1).

[3]The reference catalog is obtained from https://www.isdc.unige.ch/integral/science/catalogue. The INTEGRAL source catalog contains all sources that are detected with 1mCrab above 1 keV. Specific flags are implemented if the sources are detected with the various INTEGRAL instruments.

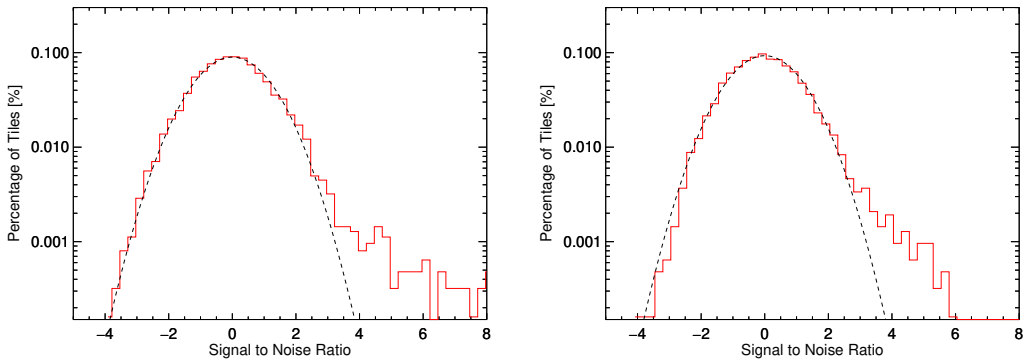

Figure 5.23: Distribution of signal to noise ratios in the plane survey in the energy bands containing both ^{44}Ti decay lines (left) and the ^{44}Sc decay line (right) indicated in red. The black dashed line represents a normal distribution with unit variance and zero mean. Both energy regions contain a positive tail, indicative for the presence of continuum sources in the survey. The distributions are truncated at signal to noise ratio equal to 8, truncating strong sources such as the Crab nebula.

The maximum-likelihood ratio λ (Neyman & Pearson 1933) is calculated between the model containing only the continuum emission and the model including the three emission lines for each mosaic tile. The test statistic is defined as

$$\lambda = \frac{\mathcal{L}(\mathrm{D} \mid \mathrm{M}_0)}{\mathcal{L}(\mathrm{D} \mid \mathrm{M}_1)} \tag{5.9}$$

where $\mathcal{L}(\mathrm{D} \mid \mathrm{M}_0)$ is the likelihood of best fit of the data by the power law (null hypothesis) and $\mathcal{L}(\mathrm{D} \mid \mathrm{M}_1)$ is the likelihood of best fit of the data including the power law and the three lines. The derived quantity

$$\mathrm{TS} = -2\ln(\lambda) = -2[\ln(\mathcal{L}(\mathrm{D} \mid \mathrm{M}_0)) - \ln(\mathcal{L}(\mathrm{D} \mid \mathrm{M}_1)] \tag{5.10}$$

is utilized to determine the statistical significance of the ^{44}Ti emission lines in each pixel. Here, TS follows a χ^2 distribution (Wilks 1938) with one degree of freedom which is the uniform flux $\mathrm{F_L}$ in the lines (cf. 5.1.2). The significance of the line is determined by deriving the p-value of observing TS by chance alone, if the null hypothesis were true. Commonly, the significance of a result is described as $n\sigma$, which is the integral of the standard normal distribution from n to ∞. The significance of detecting the lines at a specific location is given as $\mathrm{TS}^{1/2}\sigma$. For example, TS = 9 indicates, that the ^{44}Ti emission lines are detected with a significance of 3σ. The distribution of the test statistic is shown in Figure 5.24. The test statistic clearly follows a χ^2 distribution with one degree of freedom.

5.2.4 Sensitivity in the Galactic Plane

The sensitivity for ^{44}Ti emission in each pixel is defined as the flux upper limit at the 3σ confidence level. The upper limit is determined by varying the integrated flux in the lines until an offset of $\Delta\chi^2 = 9$ (for one degree of freedom) from the best fit value is reached (cf. Figure 5.14).
The sensitivity of the survey is not uniform in the Galactic plane nor throughout the 17 yr

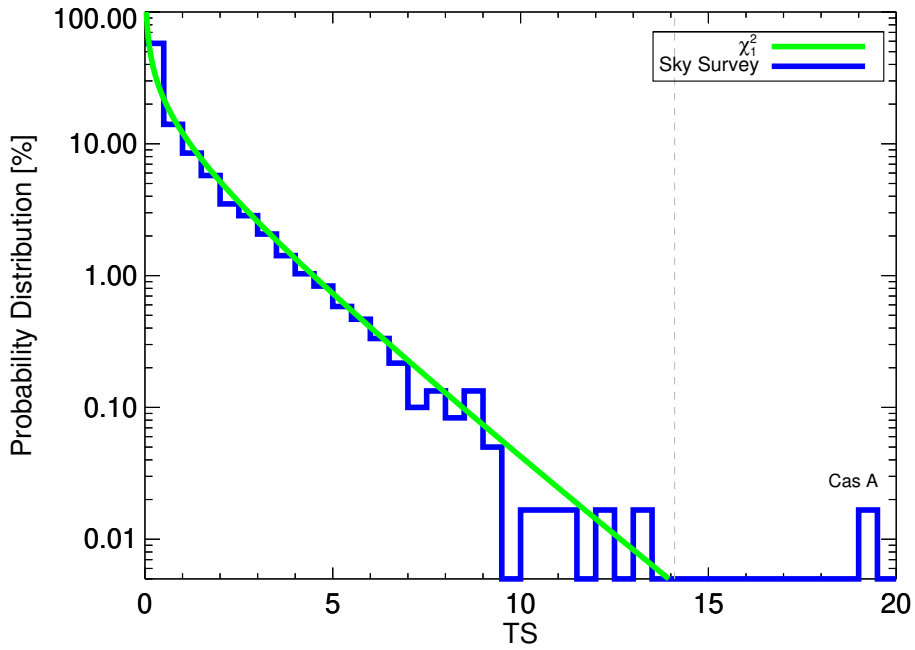

Figure 5.24: Distribution of the likelihood-ratio test statistic as defined in equation 5.10 for the 6000 celestial tiles. The model M_1 is given by a continuum ontop of which three lines are simultaneously fitted which are tested against the null hypothesis M_0, that the spectra are *celestial background* continuum only. TS follows a χ^2-distribution, indicated as the green line. The gray, dashed line indicates the defined detection threshold.

mission duration. The highest sensitivity is achieved around the center of the Galaxy which has the highest accumulated exposure time in SPI (cf. Figure 5.22). In Figure 5.25 the sensitivity in the Galactic plane in the latitude region $|b| \leq 18^\circ$ is shown.
The most sensitive region SPI can probe in this survey is located close to the Galactic center with a limit of 5×10^{-6} ph cm^{-2} s^{-1}. The limit is reached when no strong, hard X-ray emitting sources are coincident within the spatial resolution of the instrument. The sensitivity limit is better by a factor 5 compared to the COMPTEL survey. Compared to the survey in the Galactic plane with INTEGRAL/IBIS (Tsygankov et al. 2016), the sensitivity limit is better by a factor of 2.

Only 2% of the survey area is covered by a sensitivity limit below 1×10^{-5} ph cm^{-2} s^{-1} as shown in Figure 5.26. The survey covers 50% of its surface area at a sensitivity limit of $\leq 3.2 \times 10^{-5}$ ph cm^{-2} s^{-1} and 90% at $\leq 7.5 \times 10^{-5}$ ph cm^{-2} s^{-1}, thus comparable to the COMPTEL survey, however at higher spectral resolution.

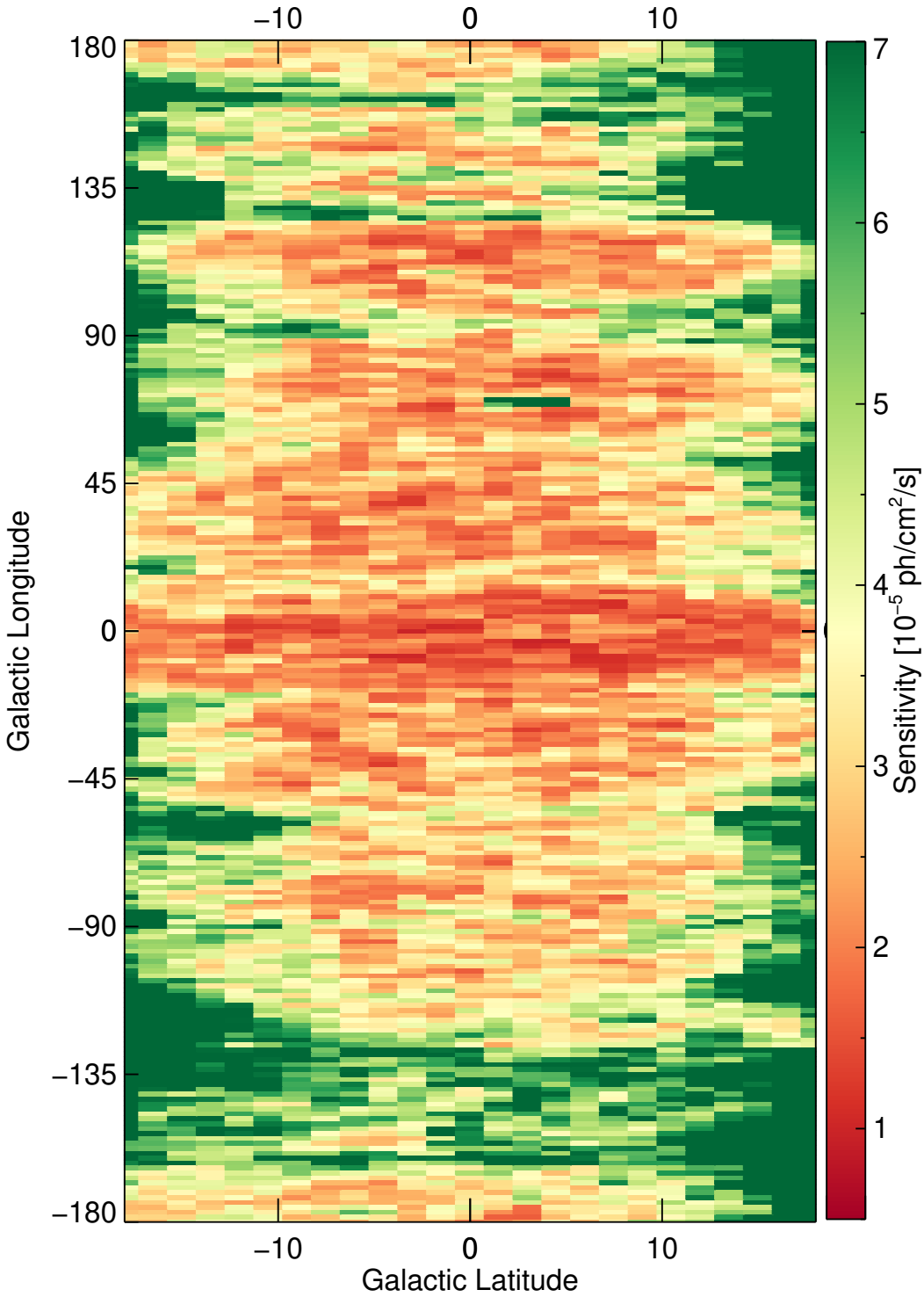

Figure 5.25: The map shows the sensitivity in the Galactic plane ($|b| \leq 18°$) for a combined signal in all three lines. The sensitivity is given as the 3σ flux limit (cf. text). The highest sensitivity is achieved in the Galactic center, that contains the highest exposure time. The fuzzy behavior of the sensitivity map is caused by the presence of continuum emitting sources within the spectral resolution of specific mosaic tiles. These influence the uncertainty of the extracted flux in the spectra per energy bin and consequently the achievable sensitivity.

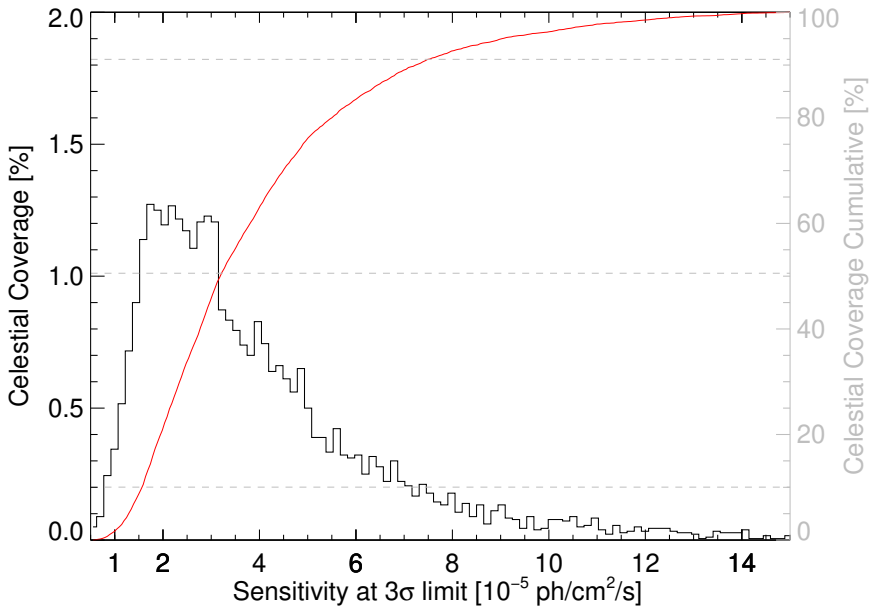

Figure 5.26: Fraction of the Galactic ^{44}Ti survey area that is covered by a specific sensitivity, given as function of the 3σ limiting flux. The black histogram shows the percentage of celestial tiles contained in a bin with width of 1.5×10^{-6} ph cm^{-2} s^{-1}. The red line is the cumulative coverage of the surface area in the latitude band $|b| \leq 18°$, where 100% corresponds to the entire survey's geometrical area. For $\approx 50\%$ of the survey area the sensitivity is better than 3×10^{-5} ph cm^{-2} s^{-1}. The horizontal gray, dashed lines mark the 10, 50, and 90% celestial coverage, respectively.

5.2.5 Evaluating the ^{44}Ti Survey

The detection significance of a potential ^{44}Ti signal on top of the power law is shown in Figure 5.27 for each pixel. In the survey, exactly one tile is found that fulfills the requirement for source detection. This tile is consistent with the location of Cas A (cf. section 5.1.3.1). I conclude, that with the exception of Cas A, no ^{44}Ti source is detected in the Galactic plane in the survey with SPI. Worth mentioning are the eight grid points in the survey, in which a potential ^{44}Ti signature is identified with more than 3σ significance. It is stressed here, that these are fully compatible with the expected number of tiles with high significance from statistical fluctuations, if the null hypothesis is true.

Excluding Cas A, the remaining high significance tiles are spread over the Galactic disk. In table 5.8 the locations of the excess sources are given. It is investigated, whether these sources might be associated with known SNRs and spuriously treated as statistical fluctuations. The positions of the sources are compared with the locations of established SNRs and young pulsars. For that purpose, I utilize the revised Green SN catalog (Green 2019), the Fermi/LAT catalog (Acero et al. 2016, and references therein for X-Ray emitting SNR

Table 5.8: Grid points containing a ^{44}Ti signature with more than 3σ significance.

Lon [°]	9.0	94.5	94.5	285.0	300.0	301.5	312.5	337.5	111.0
Lat [°]	-4.5	-16.5	-9.0	-12.0	-13.5	-12.0	18.0	6.0	-1.5
Significance [σ]	3.2	3.2	3.6	3.0	3.5	3.0	3.0	3.3	4.4

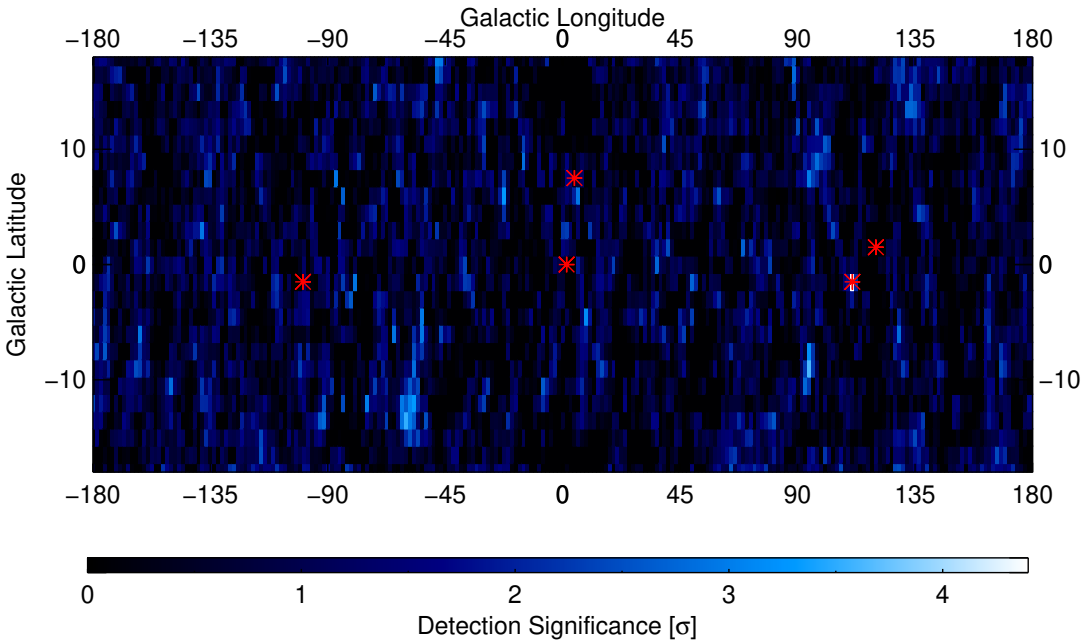

Figure 5.27: Galactic plane (|b| ≤ 18°) significance map of the ^{44}Ti decay chain signal. The color coding represents the detection significance of a combined decay chain signal. The highest significance for a combined signal is found at the tile coinciding with the location of Cas A at a level of 4.4σ. The red crosses mark the location of the five young, Galactic SNRs analyzed in section 5.1.

shells), and the positions of known pulsars with ages of less than 2000 yr (Manchester et al. 2005)[4]. The most comprehensive catalog of known sources contains 294 identified remnants (Green 2019) and encompasses the majority of remnants in the other catalogs.

The only counterpart for one of the source locations is found at the position (l/b) = (8.7°/-5.0°) (Green 2019), that is coincident with the survey location (l/b) = (9.0°/-4.5°) within SPIs angular resolution. This SNR is at a distance of 4.8 kpc (Pavlović et al. 2012). An apparent size of G8.7-5.0 of 26' was determined from radio band observations (Reich et al. 1990). No information on the age of the remnant is available, however, the lack of X-ray emission suggests an age of more than 2000 yr (Zhou et al. 2018). The best-fit flux in the decay lines of ^{44}Ti at this position is $(2.0 \pm 0.8) \times 10^{-5}$ ph cm^{-2} s^{-1}, determined from a combined line analysis at a Doppler broadening of 4000 km s^{-1}. This translates into a ^{44}Ti ejecta mass between $(1.8 \pm 0.7) \times 10^{-3}$ M$_\odot$ and $(6.0 \pm 2.2) \times 10^{4}$ M$_\odot$ for a SNR age of 500 yr and 2000 yr, respectively. While the latter is excluded in any model, the lower ejecta mass for the younger age would be compatible with a double detonation type Ia explosion, which would be in agreement with the latitude distribution of SNRs, suggesting that higher latitude remnants would more likely be the results of type Ia explosions (cf. section 5.1.1). However, the non-detection of an optical counterpart of a Galactic type Ia, close to the position of Kepler's SNR and approximately at the same age would be very unlikely. Furthermore, the emission is found with a red shift velocity of (5000 ± 1000) km s^{-1}, which would suggest an highly asymmetric ejection of ^{44}Ti into only one hemisphere of the explosion. The extracted spectra are shown in Figure 5.28. It is possible to attribute the feature at 66.7 keV

[4]https://www.atnf.csiro.au/research/pulsar/psrcat/

to a red-shifted ^{44}Ti decay line, however, the location is identical to the peak position of the background line complex between 64 and 67 keV, which is known to cause strong statistical fluctuations in the spectrum at that energy (cf. section 5.1.3.1). Due to the incompatibility of the ejecta mass in this analysis with age estimates of the SNR in other wavelength bands and the presence of the strong background lines at 65 keV, I consider the excess at (l/b) = (9.0°/-4.5°) as statistical fluctuation, which is not associated with the SNR G8.7-5.0.

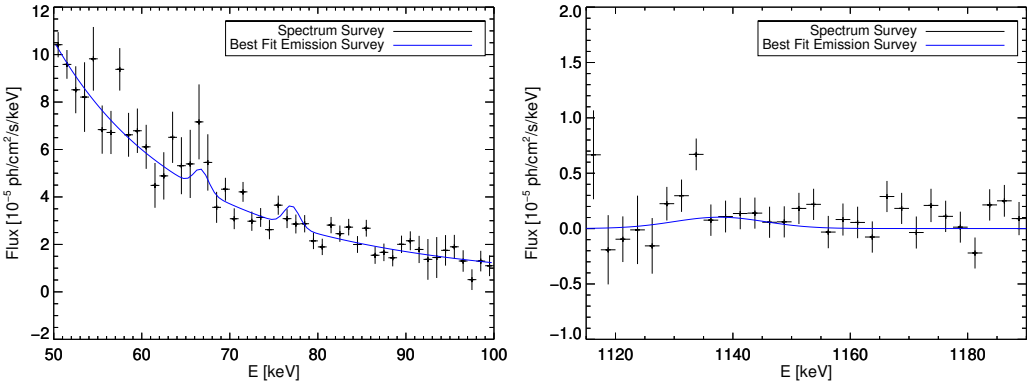

Figure 5.28: Spectra extracted for the source at (l/b) = (9.0°/-4.5°). The blue line is the best fit model of the survey spectrum (red). In addition, the high resolution spectrum, extracted in addition to the survey spectrum is included in black. In both spectra, a feature resembling a decay line on top of the power-law spectrum can be identified at 65 keV, consistent with the position of strong background lines in SPI.

The analyzed spectra for the remaining seven locations are shown in Figure 5.29. All other locations are regarded as statistical fluctuations, mimicking a ^{44}Ti signal due to the fluctuations in the vicinity of individual lines.

Whether a remnant can be detected in the SPI survey depends on the age and distance of the remnant. This relation is exemplified in a detailed analysis for the tile (l/b) = (337.5°/6.0°). The spectrum in the tile contains a flux of $(2.3 \pm 0.7) \times 10^{-5}$ ph cm^{-2} s^{-1} per line, revealed from a combined line fit. This flux is close to the sensitivity level, at which $\approx$ 50% of the tiles in the Galactic plane are covered. As no additional information on a SNR at that locations is available, the distance and age of the potential remnant cannot be separately determined. In Figure 5.30 the distance to the potential SNR in dependence on the age is shown under the assumption of specific ^{44}Ti ejecta masses of 10^{-5} M$_\odot$ (type Ia), 10^{-4} M$_\odot$ (ccSN), and 10^{-3} M$_\odot$ (peculiar Type Ia), respectively. The area in the lower left corner, below the lines, is the phase space in age and distance, in which SNRs can be detected with the respective ejecta masses. The figure also includes the ages and distances of the six SNRs discussed in section 5.1, excluding Vela Jr. Assuming a SN occurred in the direction (l/b) = (337.5°/6.0°) between 100 and 500 yr ago, it can only be speculated why an optical counterpart was not detected, since the distance to the SN can be considered close-by for a normal type Ia or a ccSN. A potential reason could be the extinction of optical light due to absorbing material in front of the explosion. On the other hand, the type Ia subclass, rich in ^{44}Ti, commonly only produces sub-luminous explosions (cf. section 2.4). In addition, a higher distance to the remnant would be possible due to the larger ^{44}Ti ejecta mass. The explosion might have been to dim to observe from Earth. This would also be in agreement with the remnants offset

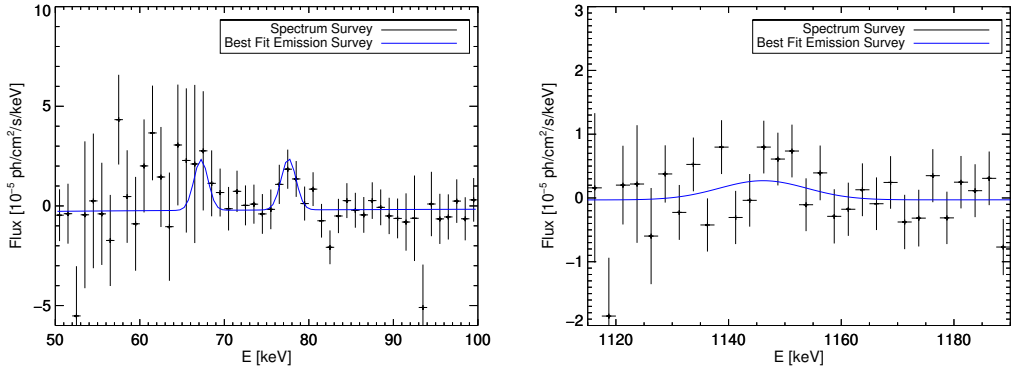

(a) Longitude 94.5°, Latitude -9.0°

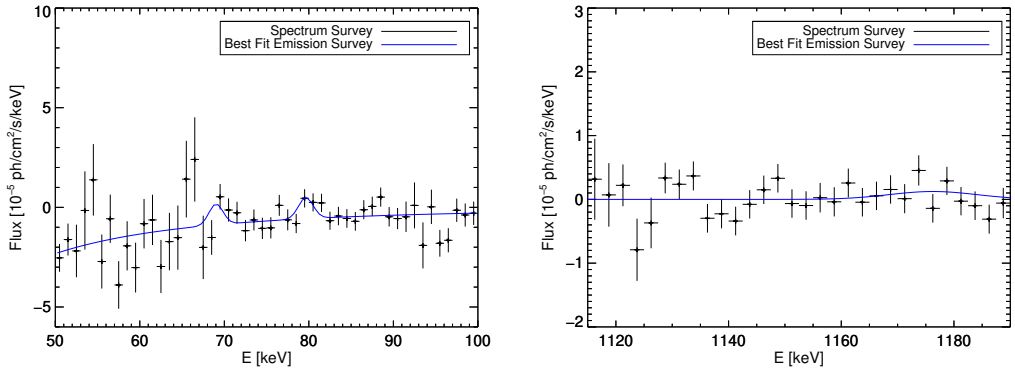

(b) Longitude 337.5°, Latitude 6.0°

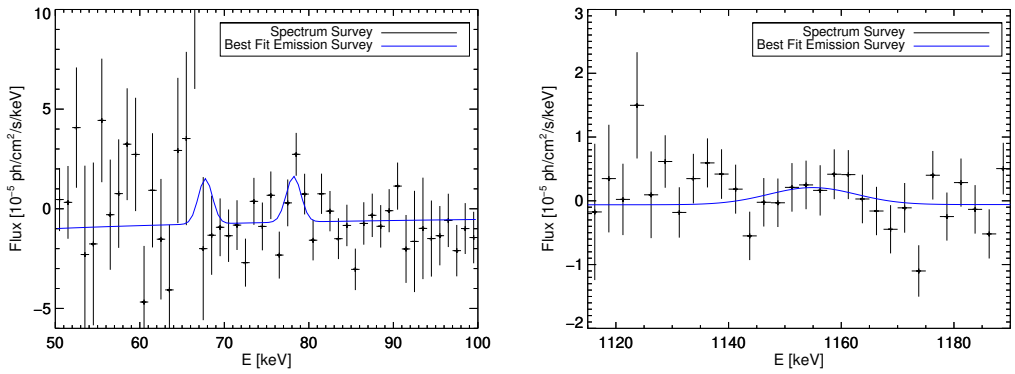

(c) Longitude 312.0°, Latitude 18.0°

Figure 5.29: Spectra of the sources showing significant excess in the survey (see text).

from the Galactic plane, commonly observed for this kind of peculiar type Ia (Perets et al. 2010; Lunnan et al. 2017).
Additional SPI exposure, dedicated to these locations, is required to confirm any potential low-level detections.

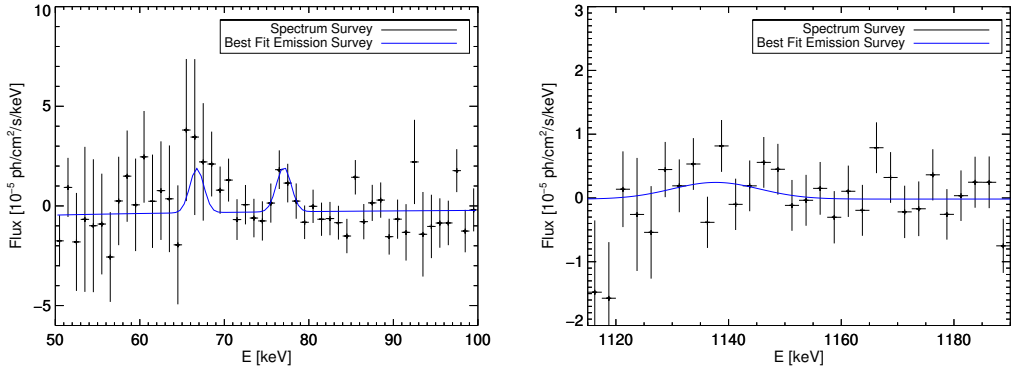

(d) Longitude 94.5°, Latitude -16.5°

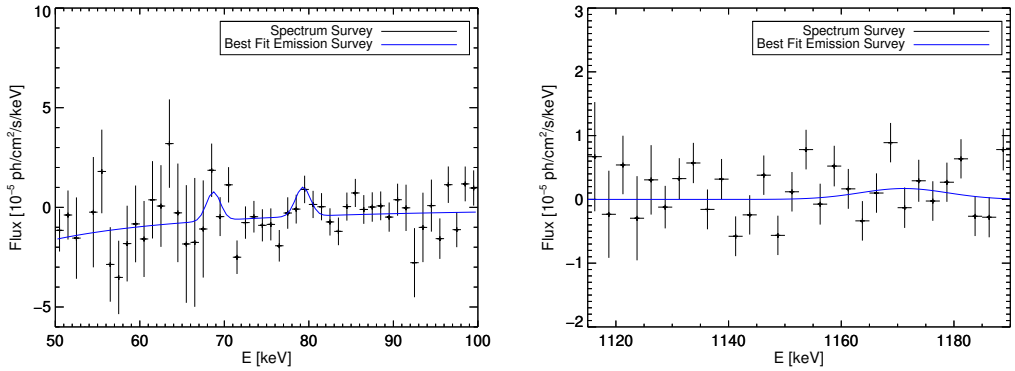

(e) Longitude 285.0°, Latitude -12.0°

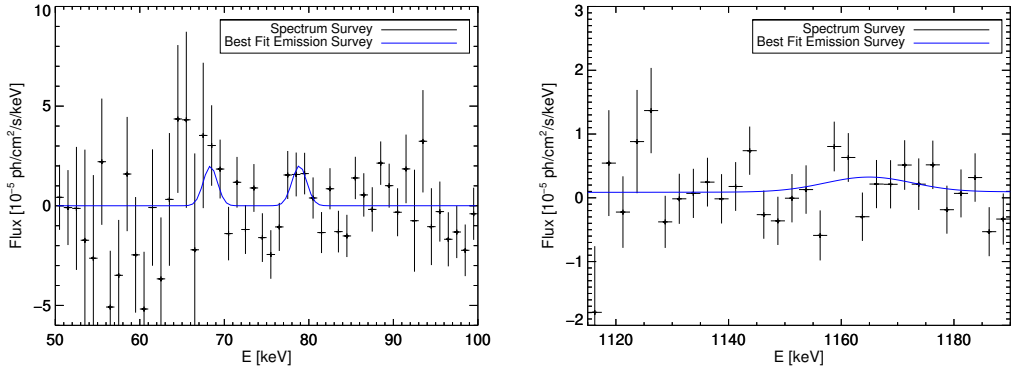

(f) Longitude 300.0°, Latitude -13.5°

Figure 5.29: Spectra of the sources showing significant excess in the survey (see text). Continued.

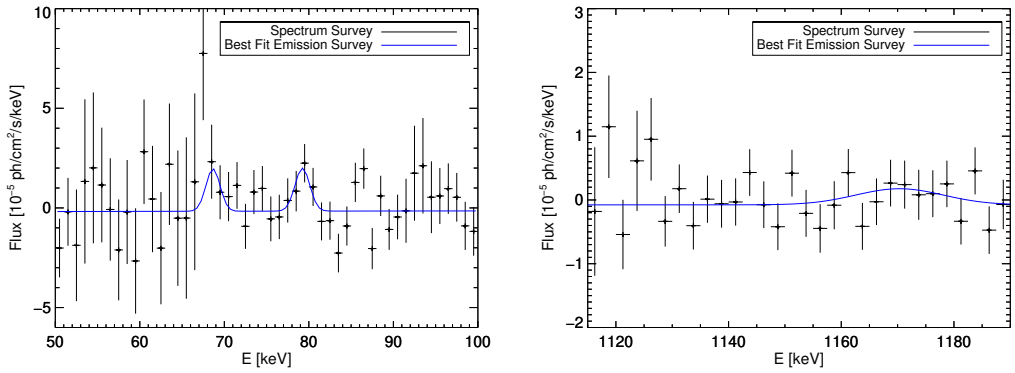

(g) Longitude 301.5°, Latitude -12.0°

Figure 5.29: Spectra of the sources showing significant excess in the survey (see text). Continued.

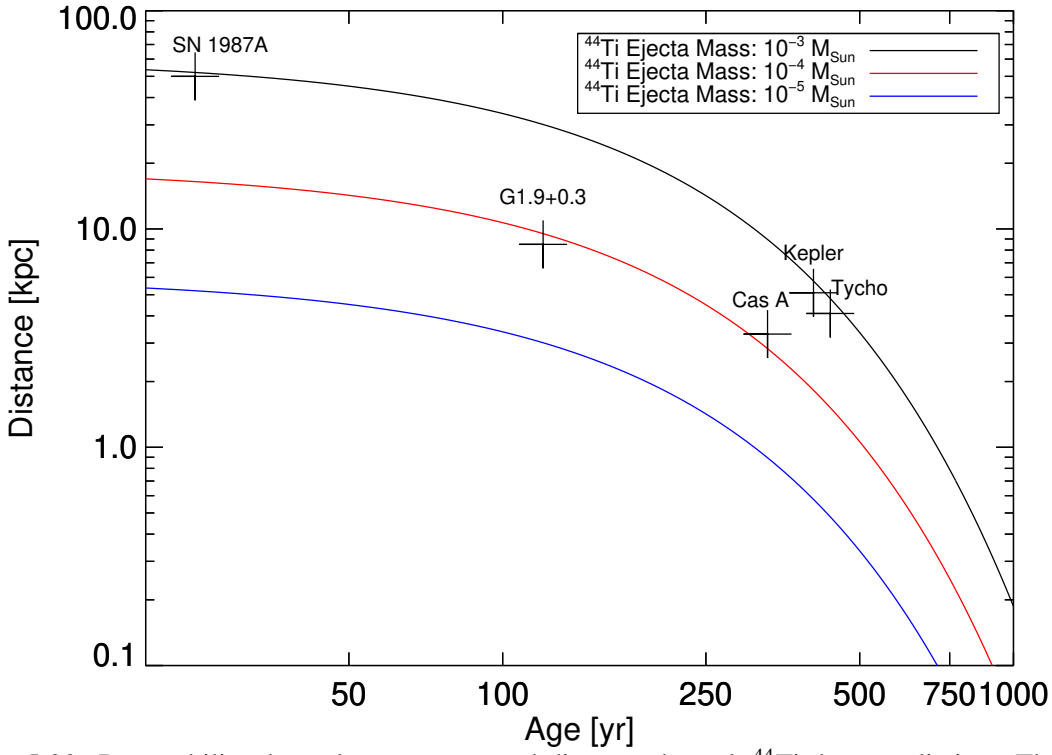

Figure 5.30: Detectability dependence on age and distance through ^{44}Ti decay radiation. The relationship is given for the assumed ^{44}Ti ejecta masses of $10^{-5}\,M_\odot$ (type Ia), $10^{-4}\,M_\odot$ (ccSN), and $10^{-3}\,M_\odot$ (peculiar Type Ia), respectively and calculated for a flux of 2.3×10^{-5} ph cm^{-2} s^{-1}. SNRs located in the lower left corner of the plot delimited by the three curves are detectable.

5.2.6 Estimating the Galactic ccSN Rate

The apparent scarcity of SNRs with ^{44}Ti fluxes above the detection threshold in this survey is peculiar. In simulated distributions of ^{44}Ti bright remnants in the galaxy, the existence of only one remnant above the detection level is highly unlikely ($\lesssim 5\%$, cf. The et al. 2006; Dufour & Kaspi 2013). Such predictions are typically based on the realization of a large number of simulations in a Monte Carlo framework, that sample a large range of potential remnant distributions in the Galaxy with predetermined ccSN recurrence rates (cf. table 2.3). Statistical fluctuations in these simulations allow for realizations, that predict a lower than average number of observable remnants, either because no SN occurred in the last centuries, or because the large distance to the young remnants results in a low number of sources with detectable fluxes at Earth.
However, the number of detectable SNRs in these simulations is determined by counting all remnants in the distribution that are above a fixed flux level. This flux level is typically set to the peak sensitivity of the COMPTEL all sky survey of 10^{-5} ph cm^{-2} s^{-1} at the 1σ level in the energy range of the 1157 keV line. This introduces a systematic effect in the number of detectable sources, which is overestimated, as the sensitivity for line emission is dependent on the exposure time and not uniform in the Galactic plane.

The detectability of a SNR is mainly governed by the age and distance to the remnant and the sensitivity of the survey in the direction of the remnant. The *completeness* of the survey, i.e. volume of the Galaxy in which SNRs should be detectable at a given age, is investigated. For that purpose, an active volume is defined to estimate the survey's coverage of the Galactic volume, however, by applying the spatially resolved sensitivity. The flux for a given age t, ejecta mass m_{ej} and distance r_{SNR} can be calculated by rearranging equation 5.4 to

$$F(m_{ej}, r_{SNR}, t) = \frac{m_{ej}\tau \exp\left(-\frac{t}{\tau}\right)}{4\pi r_{SNR}^2 Nu} = 175\left(\frac{m_{ej}}{M_\odot}\right)\left(\frac{kpc}{r_{SNR}}\right)^2 \exp\left(-\frac{t}{\tau}\right)\left(\frac{ph}{cm^2 s}\right). \quad (5.11)$$

In equation 5.11, τ and N are the ^{44}Ti decay constant and number of nucleons in the isotope, and u is the atomic mass unit. Equation 5.11 can further be rearranged to provide a distance up to which SNRs can be observed in each direction, given an age estimate, an assumed SN ^{44}Ti ejecta mass and the sensitivity limits given in Figure 5.25. In each direction, this maximum distance d_{max} defines a volume of a spherical pyramid with apex at Earth, in which SNRs can be observed. This is defined here as the directional *active volume*. The total active volume, as seen from Earth, is the sum of the separate active volumes for all celestial directions (pixels). As the majority of expected SNRs is expected to originate from ccSNe, I use a canonical (ccSN) ejecta mass of 10^{-4} M$_\odot$ ^{44}Ti. Furthermore a SNR age[5] of 0 yr and τ = 85 yr are assumed, respectively. The projected active volume for these parameters and the sensitivity at latitude b = 0 is shown in Figure 5.31. The spiral arm structure in the figure follows the description by Faucher-Giguere & Kaspi (2006) (cf. section 5.3.3). The active volume for a SNR age of 0 yr indicates the maximum coverage of the Galaxy in which ^{44}Ti decay emission can be detected with SPI. From that I conclude that even though very recent ccSNe should be observable in the majority of the Galaxy, the ^{44}Ti decay radiation in an explosion occurring in the outskirt area of the opposing Galactic hemisphere could be

[5]The age of the SN is the difference in time from the detection of the explosion on Earth and the present date. The age t = 0 implies, that the SN's light reaches Earth/SPI at the present date.

missed by SPI for a ^{44}Ti ejecta mass of 10^{-4} $M_\odot$. Since $d_{max} \propto m_{ej}^{0.5}$ the highest ^{44}Ti ejecta masses from the type Ia double detonation scenario would be seen by a factor of ≈ 3 further away, covering the entire Galaxy.

The Galactic ccSN rate is determined by extrapolating the local ccSN recurrence rate in the

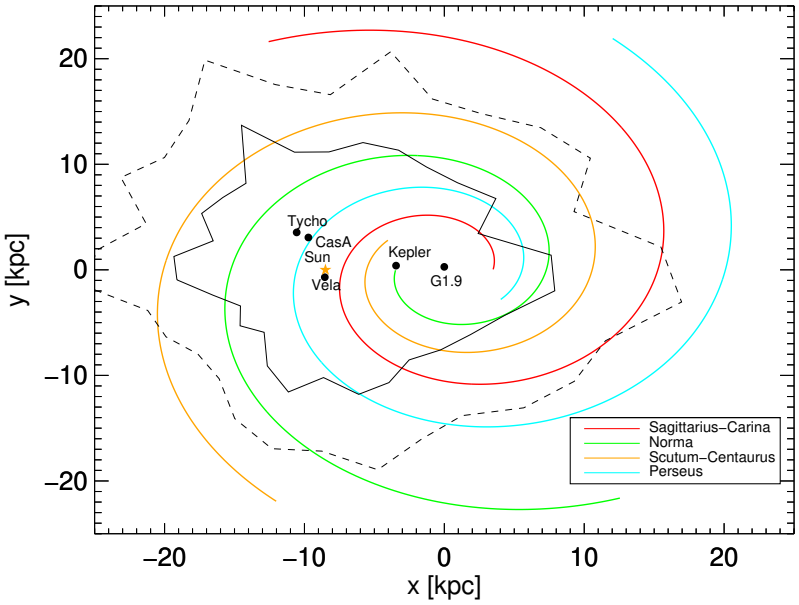

Figure 5.31: Galactic active volume for potential SN explosions. This volume is given by the maximum, direction dependent distance up to which a SN explosion is visible from Earth in ^{44}Ti decay photons. The volume is defined for a canonical ejecta mass and for the limiting ages of a recent explosion (dashed black line) and a SNR age of τ (solid black line). The active volume is centered on the Sun (orange star). The spiral arm structure is taken from a model (Faucher-Giguere & Kaspi 2006), which is intended to represent the Milky Way structure. The 5 black dots mark the location in the x-y-plane of the five Galactic SNRs analyzed in section 5.1.

observable Galaxy to the entire Milky Way. For this extrapolation, I marginalize over the height of the Milky Way, and only consider the surface density of SNRs (Sasaki et al. 2004), which is assumed to follow an exponential disk model with

$$\rho(r) = \rho_0 \exp\left(-\frac{r}{\sigma_r}\right), \tag{5.12}$$

where r is the absolute radial distance from the Galactic center, σ_r is the scale radius and ρ_0 is the central density (for further details see section 5.3.3). All parameters can be assumed constant in this calculations, as they do not change on the timescale of several centuries. The exponential disk model implies a rotational symmetry around the Galactic Center. The total number N_{SN} of SNe occurring in a specific surface area and time interval around the Galactic center is given by

$$N_{SN} = \int_0^{2\pi} \int_0^{r_{cut}} \rho(r) r dr d\phi, \tag{5.13}$$

where ϕ and r are the planar disc coordinates. The integration for r is from 0 to a cut-off radius r_{cut}, that can be considered the physical boundary of the Galaxy. The surface integral

yields a total number of Galactic SN

$$N_{SN} = \rho_0 2\pi\sigma_r^2 \left[1 - \left(1 + \frac{r_{cut}}{\sigma_r}\right) \exp\left(-\frac{r_{cut}}{\sigma_r}\right)\right]. \tag{5.14}$$

This integral can be approximated by

$$N_{SN} = \rho_0 2\pi\sigma_r^2 \tag{5.15}$$

for $r_{cut} \rightarrow \infty$, as the contribution from the surface beyond r_{cut} is less than 10% (4%) for $r_{cut}/\sigma_r \geq 4$ (5).
Likewise, the number of local SNe N_{loc} is given by the integral of the surface density over the projected, active surface area A_V framed by the black surface in Figure 5.27. This integral can be approximated by assuming a constant surface density in the vicinity of the sun at $r_\odot$, given by

$$\rho(r_\odot) = \rho_0 \exp\left(-\frac{r_\odot}{\sigma_r}\right) \tag{5.16}$$

which yields a local SN number of

$$N_{loc} = A_V \rho_0 \exp\left(-\frac{r_\odot}{\sigma_r}\right). \tag{5.17}$$

From these approximations, the ratio between the local and the Galactic number of SNe can be defined as

$$\frac{N_{SN}}{N_{loc}} = \frac{2\pi\sigma_r^2}{A_V} \exp\left(\frac{r_\odot}{\sigma_r}\right). \tag{5.18}$$

This reduces the estimation of the Galactic ccSN rate to the four parameters scale radius, solar position, active volume and local number of SNRs. In equation 5.18, I adopt a scale radius $\sigma_r = 5.8$ kpc (Pleintinger et al. 2019), from observations of ^{26}Al that traces SN activity. The distance of the sun from the Galactic Center is assumed $r_\odot = 8.5$ kpc (Kerr & Lynden-Bell 1986). The local SNR number in equation 5.18 is given by the numerical integration of the active surface area convolved with the complete density profile (equation 5.12). The active surface area is determined from the projection of the active volume (cf. section 5.2.4) onto the Galactic plane.

In Figure 5.32 the local observable Galaxy is shown, including the distribution of distances at which **all** SNRs can be detected with an age of τ. In equation 5.11, the expected flux $\langle F(t)\rangle$ of the radioactive decay law is given at the age $t = \tau$. This is equivalent to the expectation value of the radioactive decay law given by $\int_0^\infty t/\tau \exp(-t/\tau)dt = \tau$. Consequently, $\langle F(t)\rangle$ is

$$\langle F(t)\rangle = F(\tau) = 64 \left(\frac{m_{ej}}{M_\odot}\right) \left(\frac{kpc}{r_{SNR}^{l,b}}\right)^2, \tag{5.19}$$

which reversely defines the distance $r_{SNR}^{l,b}$ in each directional bin (l/b). The maximum distance in each longitudinal direction is calculated from the average sensitivity in the inner plane region (i.e. $|l| \leq 9°$, cf. section 5.3.5.1), the resulting active surface and the distribution of maximum observing distances is shown in Figure 5.32. The maximum observing

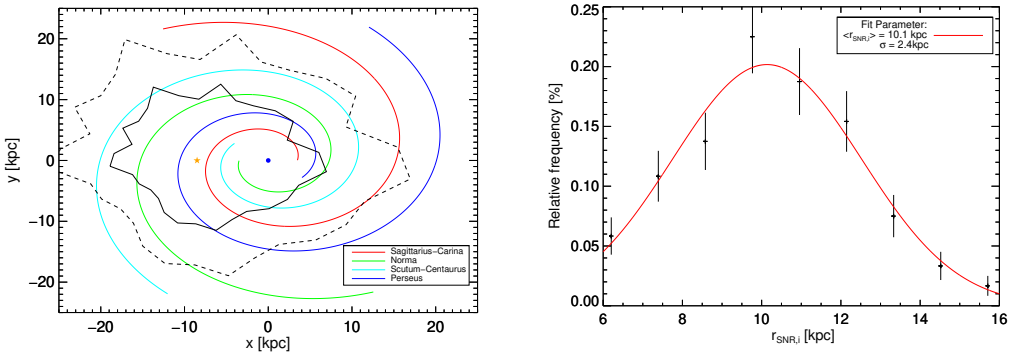

Figure 5.32: Left: Same as Figure 5.31, however, for the latitude averaged sensitivity. Right: Distribution of maximum observation distances (black data points) for the latitude averaged active volume defined by a SNR age of t = τ. The distribution can be approximated by a normal distribution with variance 2.4 kpc and mean 10.1 kpc.

distances are Gaussian distributed with a mean distance of $\langle r_{SNR,i} \rangle = 10.1$ kpc and a standard deviation of 2.4 kpc. I calculate the active surface with

$$A_V = \langle r_{SNR} \rangle^2 \pi, \tag{5.20}$$

which results in a ratio of $\frac{N_{SN}}{N_{loc}} = 2.78$.
In general, the ccSN rate can be determined by

$$\langle \dot{M}_{loc} \rangle = R_{loc} \times \langle m_{ej} \rangle \Leftrightarrow R_{loc} = \frac{\langle \dot{M}_{loc} \rangle}{\langle m_{ej} \rangle} \tag{5.21}$$

where $\langle \dot{M}_{loc} \rangle$ is the average injection rate of ^{44}Ti, R_{loc} is the local SN rate and $\langle m_{ej} \rangle$ is the average ^{44}Ti mass per explosion. The average injection rate in the local Galaxy is given by

$$\langle \dot{M}_{loc} \rangle = \frac{N_{loc} \times \langle m_{ej} \rangle}{\tau} \Rightarrow R_{loc} = \frac{N_{loc}}{\tau}. \tag{5.22}$$

Consequently, the Galactic SN rate is given as

$$R_{Gal} = \left(\frac{N_{SN}}{N_{loc}}\right)\left(\frac{N_{loc}}{\tau}\right) = 2.78\frac{1}{\tau} = \frac{3.21}{\text{century}}. \tag{5.23}$$

The ratio for the Galactic to local number of SNe is estimated from the surface densities, given as $\frac{N_{SN}}{N_{loc}} = 2.78$. The second term is estimated from the one known ccSN in the active volume, Cas A, such that $\frac{N_{loc}}{\tau} = \frac{1}{86.6a}$. One of the major assumptions in this estimate is, that the probability for the occurrence of a ccSN in a finite volume, weighted by the surface density, is considered to be identical for a similar, finite volume, weighted by the surface density. For example, a spiral arm structure would reflect in a higher density of remnants in the direction of the Galactic anti-center (l = 180°). It cannot be excluded that the one observed SN is not just the only SN in the active volume, but also the only SN in the entire galaxy for the specified period. Therefore, the active volume, as it is defined here, can only be considered the lower limit for an active volume and consequently the overall Galactic ccSN rate can be lower. Given the above assumptions, the ccSN rate in the Galaxy cannot

be higher than 3.2 explosions per century, as otherwise more than one remnant would be expected to be detectable in the Milky Way.

The data set for the survey in this thesis comprises the first 17 yr of INTEGRAL/SPI observations. Thereby, the satellite was mainly oriented towards the Galactic plane, accumulating the highest exposure in the Galactic center region. However, this observing strategy neglects the higher absolute latitudes of the Milky Way. For example, the position at which potentially a previously unknown SNR is observed in the survey at b = −9°, is only covered by 2.6 Ms of SPI exposure. A further increase in exposure on regions, that have been observed for tens of Ms cannot readily improve the sensitivity in these directions any further. However, a different observation strategy, that concentrates on the low exposure regions or higher Galactic latitudes could provide valuable information on yet undetected SNRs. A recent example of a newly discovered SNR is the Hoinga SNR (Becker et al. 2021), detected at (l/b) =(249.5°/24.5°). An observation strategy could e.g. be developed from a modeled SNR remnant distribution, described in the following section.

5.3 Modeling the Core Collapse Supernova Remnant Distribution in the Galaxy

5.3.1 The ^{44}Ti Sky

As shown in the previous sections, the only known SNR for which emission in the ^{44}Ti decay chain is measured with SPI is the SNR Cas A. Also in the Galactic survey, no emission from previously unknown SNRs in the ^{44}Ti decay chain is found with high significance. This result reaffirms the results of previous Galactic surveys with COMTPEL (Dupraz et al. 1997) and INTEGRAL/IBIS (Tsygankov et al. 2016). All three surveys find no significant emission from any new, previously unknown sources. The small number of visible SNRs, however, appears to contradict the expected number of visible remnants in the Galaxy (The et al. 2006; Dufour & Kaspi 2013), that are based on a presumed known SN rate and additional models constraints, that are inferred from ^{44}Ti dependent quantities.

To gain an independent measure for the SN rate and the inferred production rate of ^{44}Ti, a different approach is utilized to model a synthetic distribution of SNRs in the Galaxy and their associated ^{44}Ti fluxes.

The model investigates the contribution of ccSNe to the production of ^{44}Ti in the Galaxy. This confinement is based on two arguments: First, the occurrence of type Ia SNe is a rather rare phenomenon with respect to their core collapse counterpart. In general, estimates based on the observations of SNe in the Milky-Way and extragalactic spiral arms suggest, that in total ccSNe of all types constitute 80 – 90% of all occurring SN events (van den Bergh & Tammann 1991; Cappellaro et al. 1999). Second, the majority of type Ia simulations suggest only a minor amount of ^{44}Ti to be ejected per explosion, which is commonly one to two orders of magnitude lower than expected for the typical ccSN events. Therefore, the time average of the typical type Ia ^{44}Ti production rate can be considered negligible in comparison to the core collapse rate.

The modeling approach utilized in this thesis is specifically intended to avoid the biases, that can be introduced by locally occurring phenomena or the introduction of a fixed SN rate, that has proven to yield an apparent spatial distribution of SNRs incompatible with observations. Instead, the modeling approach in this thesis is built on a *bottom up* approach, utilizing parameters that are independent off the hypothetical, predicted observables, which should be compared with the observations. This approach traces the history of star formation, from the formation of single stars in stellar clusters (cf. section 2.2) to their eventual demise as a potential ccSN, over the duration of the last $t_{sim} = 50$ Myr. This simulation time is considerably longer than the half-life of ^{44}Ti. Nevertheless it is necessary to a) reach a steady state production of long lived isotopes (^{26}Al, ^{60}Fe) in the Galaxy and b) have a sufficient amount of clusters evolved to a point where all stars with $M_* \geq 8\,M_\odot$ have exploded. The essential ingredients are the masses of the individual cores in GMCs (see section 2.2) in which the stars are born, the masses of the individual stars in the clusters and the Galactic star formation rate (SFR). The entire model is based on the evolution of massive stars in clusters, that is dominated by the physical parameter of a long-term stable SFR. The advantage of utilizing the SFR as a key parameter here is, that it is a quantity that can be determined independently from γ-ray measurements, decoupling the modeling from the investigated observables. Following the distribution and evolution of the clusters, the nucleosynthesis feedback into the Galaxy is determined from the properties of the individual star clusters.

The distribution of SNRs from these ingredients is modeled within the framework of the PSYCO code, a tool that is specifically designed to model the distribution of radioactivities within the Galaxy (Pleintinger 2020). PSYCO modeling follows three essential steps.

Mass distribution The available total mass in the simulation for star formation is governed by the long term rate of star formation in the galaxy, hence given as $M_{tot,sim} = t_{sim} \times$ SFR. In a first step, this mass is distributed into individual clusters (according to an ECMF) and, within the clusters, distributed into stars according to an IMF, as will be described in section 5.3.2.

Spatial distribution In the subsequent step, the clusters are distributed randomly in a simulated galaxy. While the cluster formation time is randomly chosen from a uniform distribution in the time interval [0,50] Myr, the spatial distribution of the SNRs follows a doubly exponential disk distribution and a spiral arm distribution given in section 5.3.3, respectively.

Tracing the nucleosynthesis In the final step, the production and decay of radioactive ^{44}Ti in each individual cluster is traced. While only explosions in the last $\approx$1000 yr are relevant with respect to the visibility of a ^{44}Ti signature in the sky, the entire 50 Myr are traced to constrain the average ^{44}Ti production history.

5.3.2 Star Formation

The distribution of masses into both the star clusters as well as the individual stars in the cluster follows a physically motivated approach. As discussed in section 2.2, the population of stars in a specific cluster follows the IMF and the distribution of the total star forming mass into clusters of stars should be determined by the ECMF. Within the framework of the PSYCO tool, an optimal sampling approach is applied, that is intended to closely resemble

a given, continuous distribution function by discretized values, without distorting the slope of the distribution function nor producing major gaps between the sample intervals. The sampling technique follows the description in Kroupa et al. (2013) and Schulz et al. (2015). In general, the total mass of a cluster or the star forming mass in the Galaxy is given by

$$M_{Tot} = \int_{M_{Min}}^{M_{Max}} M\theta(M)dM \tag{5.24}$$

under the assumption, that the distribution function $\theta(M)$ is integrable in the mass interval $[M_{min}, M_{max}]$. This condition is commonly fullfilled for the IMF and the ECMF, as both distributions follow a power law

$$\theta(M) \propto c\left(\frac{M}{M_{max}}\right)^{-\alpha} \tag{5.25}$$

with a normalization constant c, and a power-law index α. Optimal sampling of the given, analytical parent distribution $\theta(M)$ is achieved, when the condition is fulfilled, that the mass M occurs exactly once above the mass limit M_{Max} in the interval $[M_{Max}, M_{Tr}]$. In analytical terms this implies that

$$\int_{M_{Max}}^{M_{Tr}} \theta(M)dM = 1 \tag{5.26}$$

It is immediately evident that this object with mass M is unphysical, as it extends to a theoretical truncation mass M_{Tr} beyond the physically motivated mass range M_{Max} and is, consequently, removed from the population. However, the integration very well serves to provide the normalization c of the mass distribution, by combining equations 5.25 and 5.26:

$$c = \frac{1-\alpha}{{M_{Tr}}^{1-\alpha}{M_{Max}}^{\alpha} - M_{Max}} \tag{5.27}$$

Including the normalization in equation 5.24, the expressions for the total mass and the truncation mass can be derived

$$M_{Tot} = \frac{1-\alpha}{2-\alpha}\frac{M_{Max}^{2-\alpha} - M_{Min}^{2-\alpha}}{M_{Tr}^{1-\alpha} - M_{Min}^{1-\alpha}} \tag{5.28}$$

$$M_{Tr} = \left[\frac{1-\alpha}{M_{Tot}(2-\alpha)}(M_{Max}^{2-\alpha} - M_{Min}^{2-\alpha}) + M_{Max}^{1-\alpha}\right]^{\frac{1}{1-\alpha}} \tag{5.29}$$

With these analytic expressions, the parental distribution function can be discretized into individual mass elements m_i, fulfilling the integral condition that

$$\int_{m_{i+1}}^{m_i} \theta(M)dM = 1 \quad , \tag{5.30}$$

which is the same condition as in equation 5.25. As the value for the highest mass bin, m_1 is determined by the physical condition of a maximum mass in the system M_{Max}, the following integration limits can be determined in an iterative approach in decreasing mass order, given by

$$1 = \int_{m_{i+1}}^{m_i} c\left(\frac{M}{M_{max}}\right)^{-\alpha} dM = \frac{c}{1-\alpha}\left(\frac{m_i^{1-\alpha} - m_{i+1}^{1-\alpha}}{M_{Max}^{\alpha}}\right) \tag{5.31}$$

$$m_{i+1} = \left(m_i^{1-\alpha} - \frac{1-\alpha}{cM_{Max}^{\alpha}}\right)^{\frac{1}{1-\alpha}} \quad . \tag{5.32}$$

Consequently, the mass M_i contained in each stepwise integration can be determined from the integration limits via

$$M_i = \int_{m_i}^{m_{i+1}} M\theta(M)dM = \frac{c}{2-\alpha}(m_i^{2-\alpha} - m_{i+1}^{2-\alpha})M_{Max}^{\alpha} \quad \forall \alpha \neq 2 \tag{5.33}$$

The physical parameter of M_{Max} is given as boundary condition from the input parameters. The approach can then be applied to distribute the initial total star forming mass into separate clusters following equation 2.7 and the cluster masses into separate stars following the IMFs in Table 2.1. For the models in this thesis, the mass is distributed according to the Chabrier (2005) IMF. The fundamental Salpeter IMF (Salpeter 1955) overproduces stars in the lower mass end due to the missing bend at $1\,M_\odot$ and is not utilized. Both the Chabrier (2005) or Kroupa (2001) IMFs distribute a significantly higher fraction of mass in the mass range above $8\,M_\odot$.

5.3.3 Density Distribution of Star Forming Regions

Two models that describe the distribution of ccSN progenitors in the Milky Way are adopted. The first model is a doubly exponential disk model, that was introduced to describe the ^{26}Al emission in the Milky Way, as this isotope is a tracer for massive stars (Diehl et al. 1995; Diehl et al. 2006a). The density distribution function is given as

$$\rho(r,z) \propto \exp\left(-\frac{|z|}{\sigma_z}\right) \times \exp\left(-\frac{r}{\sigma_r}\right) \tag{5.34}$$

where σ_z and σ_r are the scale height and radius of the Milky Way disk, respectively. The parameters r and z are the radius from the Galactic center and the elevation above the Galactic plane. Updated values for the scale radius of 5.8 kpc and the scale height of 770 pc (Pleintinger et al. 2019) were adopted, as determined from diffuse ^{26}Al emission in the Milky Way.

In addition, a spiral arm model is used, that follows the distribution of pulsars in the Milky Way from Faucher-Giguere & Kaspi (2006). As pulsars are the direct result of stellar core collapse, the distribution of pulsars can be considered a tracer for the distribution of massive stars in the galaxy. The model assumes four spiral arms, and is intended to qualitatively reproduce the major features of the Milky Way. The centroid positions of the four spiral arms in cylindrical coordinates are described by

$$\theta(r) = k_i \times \ln\left(\frac{r}{r_{0,i}}\right) + \theta_{0,i} \tag{5.35}$$

where r is again the planar radius from the Galactic center. The values for k_i, $r_{0,i}$, and $\theta_{0,i}$ are given table 5.9. The parameter k_i is the pitch angle of the i'th arm, $\theta_{0,i}$ are the Galactocentric angles of the arms at their starting points given by $r_{0,i}$. The probability for the formation of a cluster in each arm is assumed to be identical. The radial position of a specific cluster j is chosen from a radial distribution following a Gaussian ring density distribution between the radial positions $r_j \in [0, 20]$ kpc. The centroid and width of the Gaussian disk are $E_0 = 7.0$ kpc and $\sigma_r = 1.83$ kpc, respectively. From the radial positions, the angle $\theta(r)$ is calculated according to equations 5.35. However, to spread the cluster positions around the centroids of the respective spiral arms, the azimuth is corrected by an offset off

$$\theta_{off} = \theta_{corr} \times \exp(-0.35 r_j/\text{kpc}). \tag{5.36}$$

θ_{corr} is randomly chosen in the interval $[0, 2\pi)$, which mainly effects the clusters in the vicinity of the Galactic center. Furthermore the clusters are spread around the centroids of the Galactic arms by adjusting the radius with an offset of r_{off}, which is randomly chosen from a normal distribution with a width of $0.07 r_j$. In contrast to the angular correction, the radial offset increases with distance to the Galactic center, increasing the radial spread of the arms in the outskirts of the galaxy.
The distribution of clusters in the simulated galaxies is shown in Figure 5.33.

Table 5.9: Parameters describing the spiral arm model. The pitch angel is denoted k, the radial starting point is r_0 and the Galactocentric angle is θ_0.

Name	k[rad]	r_0[kpc]	θ_0[rad]
Norma	4.25	3.48	1.57
Carina-Sagittarius	4.25	3.48	4.71
Perseus	4.89	4.90	4.09
Crux-Scutum	4.89	4.90	0.95

5.3.4 Implementation of Nucleosynthesis Yields from Simulations

Within the PSYCO environment, the ejecta of a single stellar explosion are not randomly distributed in a set time interval. Nucleosynthesis feedback is traced from the entire star content in a cluster over the course of several millions years . Therefore, the mere knowledge about the ejected masses of radioisotopes is not sufficient to trace the clusters nucleosynthesis history. In addition, the temporal information, i.e. the delay time between the formation of a star cluster and the explosion of its content stars, is required. Depending on the initial mass of the individual stars, this delay time can range up to ≈ 40 millions years for the lowest mass star ($\approx 8\,M_\odot$) that still explodes as ccSN.

In general, the highest mass stars burn through their fuel on timescales much shorter than their low mass counterparts (cf. section 2.2). However, above a certain mass, stars might not explode in a SN following the collapse of their respective core, but a black hole is directly formed (cf. Figure 2.4). The third required parameter in the calculation of the nucleosynthesis yields is therefore the explodability of stars, that determines the mass range in which material is ejected after core collapse. Here, the explodability from the nucleosynthesis models of Limongi & Chieffi (2018) are adopted, that suggest explosions solely in initial stellar mass range of $8 - 25\,M_\odot$. This also sets the timescale for the first SN explosions. In these models, the first ejection of ^{44}Ti occurs after 9.8 Myr, following the explosion of a $25\,M_\odot$ star.
The ejecta masses of ^{44}Ti for ccSNe are commonly calculated from parameterized models. However, these models usually do not encompass a large variety of SN progenitor masses, but produce ejecta values for subset of progenitors with a coarse spacing in initial mass. The ejecta masses vary drastically with the progenitor mass and also with the adopted explosion physics.
Extensive lists for the nucleosynthesis in the ejecta of ccSNe are given by Woosley & Weaver (1995); Thielemann et al. (1996); Tur et al. (2010). More recent results are given by Limongi & Chieffi (2018) for a variety of stars with different rotational and metallicity parameters in the mass range $13 - 120\,M_\odot$. The nucleosynthesis results of the latter are utilized in the

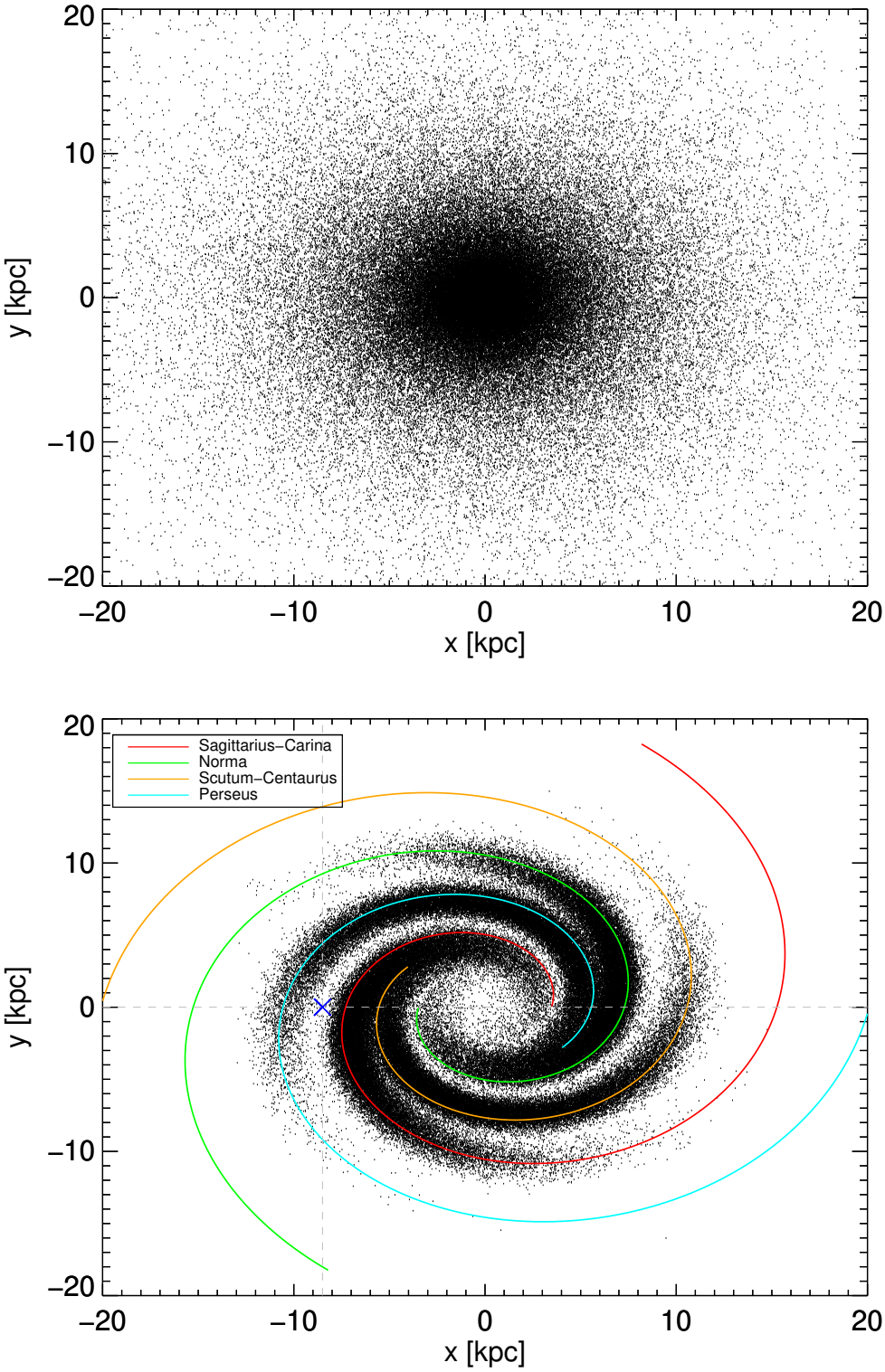

Figure 5.33: Examples of cluster distributions in the Milky Way. Upper panel shows an exponential disk distribution in the x-y-plane. Due to the small scale length, the majority of clusters are distributed in the Galactic center region. Lower panel shows the distributions of clusters along the spiral arms representing the Milky Way structure. The lack of clusters in the Galactic center is caused by the Gaussian disk profile, adopted for the radial distribution of remnants with a centroid at a distance of 7.0 kpc from the Galactic center. Colored lines indicate the centroids of the arms. The blue cross marks the location of the Sun.

model calculations. The models also include the necessary delay times between the star formation and explosion. However, the list of progenitors in Limongi & Chieffi (2018) is rather incomplete concerning the explosions of less massive stars with an initial mass of $\leq 13\,M_\odot$. Following the IMF for single stars, the majority of ccSN explosions is produced by stars less massive than $13\,M_\odot$. The list is therefore extended by the results from Wanajo et al. (2018), that also contains fiducial ejecta masses for three evolved stars in the mass range $8 - 10\,M_\odot$, possibly resembling ECSNe.
In general, the initial stellar masses in the clusters are discretized in much finer binning than any nucleosynthesis simulations can offer. To reach the level of binning used in the modeling, values for the ^{44}Ti ejecta masses as well as the explosion delay time are interpolated in between the coarse bins given by the simulations. The same approach is adopted to extrapolate values at both edges of the explosion mass range.
The present day content of ^{44}Ti in each cluster is then calculated according to the radioactive decay law. However, due to the very short half-life of 59.1 yr (Audi et al. 2017) of the ^{44}Ti isotopes in comparison to the modeling timescale of 50 Myr, the majority of individual clusters only contains a negligible amount of ^{44}Ti, producing only a very faint decay signal (see section 5.3.5.2).

5.3.5 Model Results: Flux Distribution of SNRs

5.3.5.1 Galactic Distribution of SNRs

In Figure 5.34 and 5.35 the distribution of SNRs in Galactic latitude and longitude coordinates are shown.

The distribution of remnants in latitude for both morphologies is rather uniform. This is governed by the initial, exponential profile of the cluster distribution. It is worth noting here, that the brightest SNRs with fluxes above 10^{-5} ph cm^{-2} s^{-1}, are concentrated in the Galactic plane at $|b| \leq 10°$. The width of the distribution in the exponential model is broader with respect to the spiral arm model as the initial scale height of the cluster distribution is 0.7 kpc

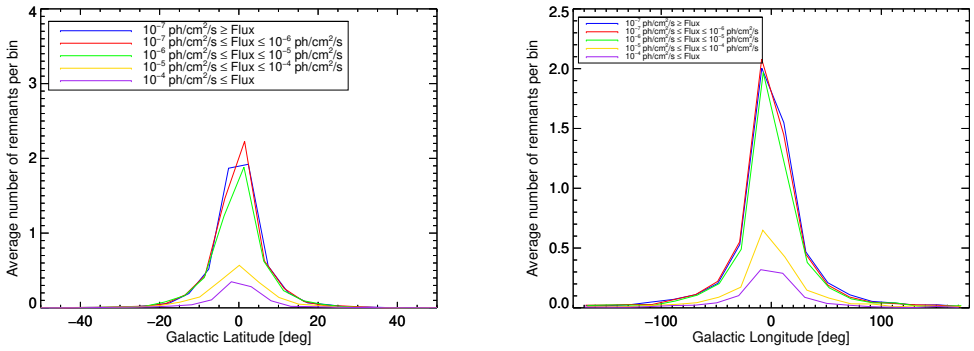

Figure 5.34: Spatial distribution of SNRs for the simulated galaxies, each realized with a SFR of $4\,M_\odot\,yr^{-1}$ for the exponential distribution model. The distribution shows the average number of remnants per coordinate bin. Left panel: Latitude distribution in 5° bins. Right Panel: Longitude distribution in 20° bins. The different color codings represent the distribution of SNRs in the specified flux intervals as seen at Earth. The ordinate gives the average number of SNRs per bin for the set of 1000 simulated skies.

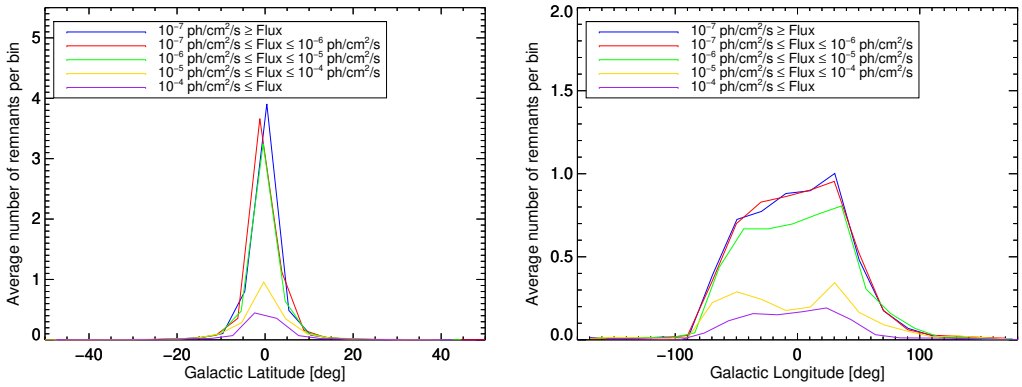

Figure 5.35: Same as Figure 5.34 for the spiral arm model.

instead of 0.3 kpc. However, it is possible that the scale height of 0.7 kpc is overestimated due to the exponential disk model used in Pleintinger et al. (2019). This might be owed to possible foreground emission in ^{26}Al, that artificially increases the scale height. This would suggest that the distribution of SNRs in latitude for the exponential disk model might, in fact, be narrower as assumed in this analysis. Consequently, the remnants would be more concentrated in the Galactic plane, where the sensitivity of SPI is, in general, higher due to an increased exposure.

A significant difference can be observed in the distribution of bright remnants in the Galactic longitude. For the exponential disk model, the amount of remnants is exponentially correlated with the distance to the Galactic center. Therefore the brightest remnants are expected to be visible in the Galactic center. The situation is, however, very different for the spiral arm model. The distribution of bright SNRs is determined by the convolution of density distribution of cluster formation (see Figure 5.33) and also by the distance (see Figure 5.36) to the respective SNR. The amount of SNRs in each direction is simply the result of summing the remnants in the consecutive spiral arms. As Earth is located at a distance of 8.5 kpc from the Galactic center (Kerr & Lynden-Bell 1986), the majority of dense spiral arms is located towards the Galactic center and extends to $\approx 100°$ longitude. In the direction of the Galactic anti-center (i.e. longitude = 180°), no more spiral arms exists in the spiral arm model in addition to the one inhabiting the Sun. Due to the lack of cluster formation in the Galactic center, given by the Gaussian ring model for the distribution of clusters in the Galactic plane, the average number of bright SNRs peak at $|l| \approx -50°$ and $|l| \approx 30°$ parallel to the tangents of the adjacent spiral arms. While there is a significant difference in the distribution of SNR distances between the two models as shown in Figure 5.36, the average distance to the SN explosions is 10.1 kpc (spiral) and 10.0 kpc (exponential). However, in the spiral arm model, the fraction of close-by SNe with distances below 5 kpc is significantly higher than in the exponential disk model.

5.3.5.2 Observability of SNRs

The most direct link between the simulations and the observations is the comparison of the flux distributions of the individual SNRs for the simulated galaxies with the observed sky in the radioactive decay lines of ^{44}Ti. So far, only the spatial distribution of the SNRs has

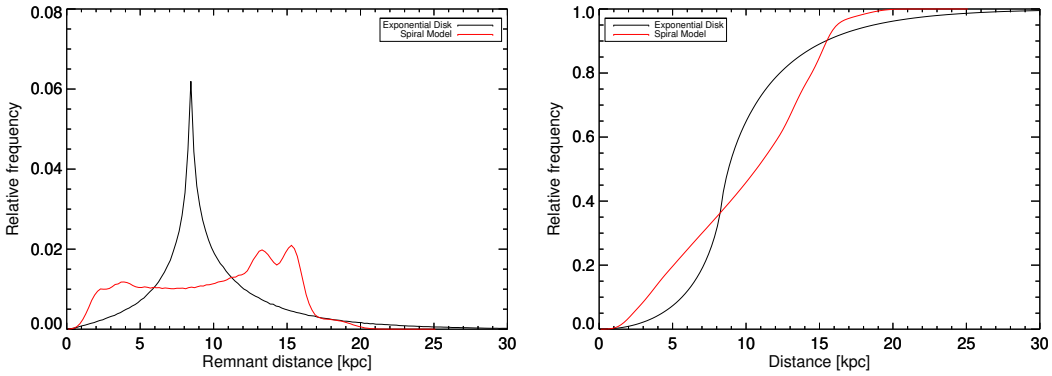

Figure 5.36: Distribution of SN explosion distances to the sun for the exponential disk (black) and spiral arm (red) model. Left: Relative frequency. Right: Cumulative relative frequency. The average distance to the remnants in both cases is 10 kpc. However, the relative frequency of close-by SNRs is higher in the spiral arm model.

been considered. However, the masses of ejected, radioactive ^{44}Ti at the time of explosion are known. From these masses, the temporal information, and the distance to the SNRs the observable decay flux at the location of Earth can be calculated (see equation 5.4) and projected onto a 2D map. Four maps, containing the location of ccSN remnants that shine in ^{44}Ti decay emission, are shown in Figure 5.37. These maps depict distributions for the exponential disk model and the spiral arm model with an initial SFR of $4\,M_\odot\,yr^{-1}$. From these maps, it seems evident that the simulated skies are not compatible with only detecting one source in ^{44}Ti decay flux. This seems especially true towards the Galactic center region in the exponential disk model, where the presence of several SNRs with ^{44}Ti decay fluxes above $10^{-6}\,ph\,cm^{-2}\,s^{-1}$ are present within the field with the highest sensitivity in the SPI survey in this thesis (cf. section 5.2).
The absolute number of ccSN remnants above a specific flux threshold of $10^{-9}\,ph\,cm^{-2}\,s^{-1}$ is correlated with the SFR. This behavior is expected, as the SN rate is likewise correlated with the SFR (cf. Figure 5.41a), and hence a higher SN rate leads to the existence of a higher average number of SNRs in the galaxy. The cumulative probability for the detection of SNRs above a given flux levels is stable within the two assumed morphologies. This serves as a good test for the stability of the modeling approach. While the absolute number of SNRs can change with the SFR, the distribution of the flux levels, which is mainly determined by the distance and age of the SNRs, should only depend on the morphology of the remnant distribution. This interrelation also becomes evident from the bend in the flux distribution above $10^{-6}\,ph\,cm^{-2}\,s^{-1}$. While the distribution of remnants below this threshold show a similar behavior, the probability for high fluxes declines faster in the exponential disk model than in the spiral arm model. This behavior is due to the distance distribution of the SNRs. While the average distance is identical in both morphologies, the probability for close-by (distance ≤ 5 kpc, s. Figure 5.36) SNe is higher in the spiral arm model. As, according to equation 5.4, the flux produced by an individual ejection of radioactive material is dependent on the distance r^{-2}, the presence of young, close-by SNRs in the spiral arm model produces, on average, more SNRs bright in ^{44}Ti decay flux.

The average number of detectable ccSN sources is, in addition to the input parameters of

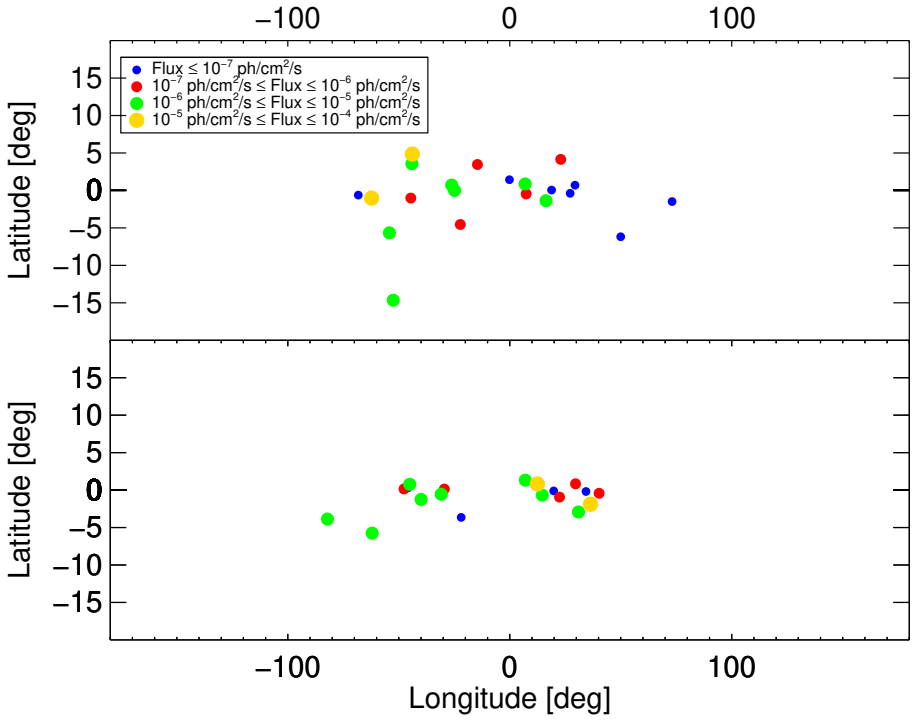

(a)

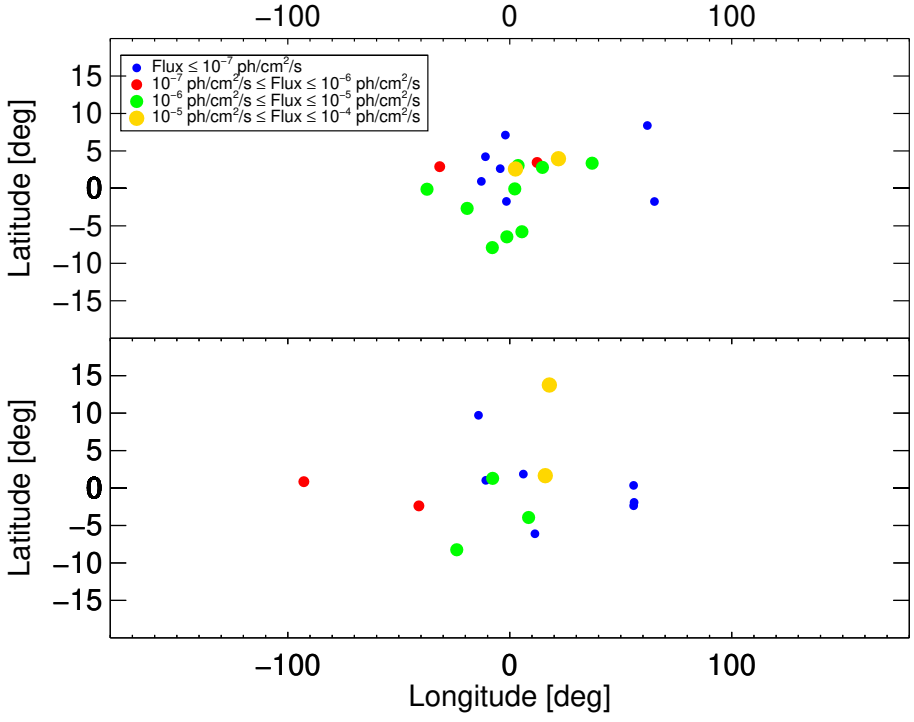

(b)

Figure 5.37: Flux distribution for four simulated galaxies, each realized with a SFR of $4\,M_{\odot}$ per year. Panel a) shows the distribution of remnants for to the spiral arm model in the Galactic plane region. Panel b) shows the distribution of remnants for the exponential distribution model. The color coding distinguished the fluxes, with which the SNRs are seen at Earth. In addition, the size of the plotting symbol for the SNRs is representative for their flux level, and does not relate to the remnants apparent size on the sky. The celestial surface area of all remnants is compatible with or below SPI's angular resolution.

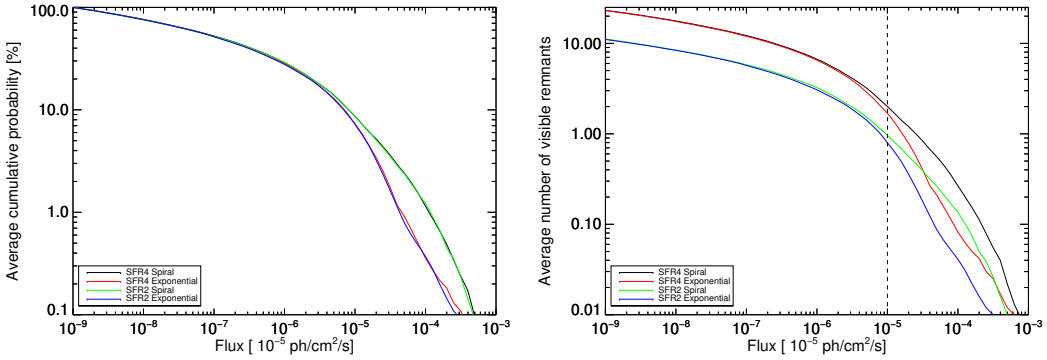

Figure 5.38: Cumulative distribution of fluxes for the modeled SNR distributions, considering only individual SNRs with a minimum flux level of 10^{-9} ph cm^{-2} s^{-1}. Each distribution is determined from 1000 MC runs, yielding a total of 4000 simulated galaxies. Left: Cumulative average detection probability. Right: Average number of sources above the specified flux level. The dashed line marks a flux of 10^{-5} ph cm^{-2} s^{-1}, the canonically assumed limiting flux in SNR surveys (see e.g. The et al. (2006); Dufour & Kaspi (2013))

the simulation, also dependent on the sensitivity of the measuring instrument. In a first step, the detectable number of sources is determined from the fluxes of the sources alone, disregarding their spatial distribution on the sky. The number of detectable sources follows a Poisson distribution (see Figure 5.39). In Table 5.10, the expected number of detectable sources for a limiting sensitivity of 10^{-5} ph cm^{-2} s^{-1}, 10^{-6} ph cm^{-2} s^{-1}, and 10^{-7} ph cm^{-2} s^{-1} are listed. These are determined from fitting a Poisson distribution to the probability mass function of detectable sources. While the first value is compatible with the limiting flux of COMPTEL all sky survey in the 1157 keV band (Iyudin 1999; The et al. 2006), the surveys conducted more recently with newer instruments such as INTEGRAL/IBIS (Tsygankov et al. 2016) or INTEGRAL/SPI (this work) reached higher maximum sensitivity levels close to 10^{-6} ph cm^{-2} s^{-1} at a 3σ level. Future X- and γ-ray telescopes should be able to probe an order of magnitude higher sensitivity levels at a flux of 10^{-7} ph cm^{-2} s^{-1}. For the conservative estimate at a 10^{-5} ph cm^{-2} s^{-1} flux level, 1.68 ± 0.03 ccSN remnants are expected to be detectable in the exponential disk model and 2.01 ± 0.04 in the spiral arm model assuming an average SFR of 4 M$_\odot$ yr^{-1}. These numbers are fully compatible with the detection of only one SNR in the galaxy. For a SFR of 2 M$_\odot$ yr^{-1} and 1 M$_\odot$ yr^{-1}, the detection of one remnant is compatible with the low number of expected, detectable sources. However, a higher SFR of 8 M$_\odot$ yr^{-1} would, on average, suggest a number of detectable ccSN remnants incompatible with observations. The probability for detecting 0 or 1 sources are 0.04 and 0.13 in the exponential disk model and 0.03 and 0.10 in the spiral arm model. This means that in more than 80%, two or more remnants are expected to be detectable.

In a second step, the spatial information of the modeled ccSN remnant distributions is also taken into account by comparing them with SPI observations. For that purpose, the 3D spatial coordinates of the remnants are projected onto a 2D Galactic longitude and latitude map with coordinates l' and b'. The locations of the remnants are randomly selected in the model from the spatial distributions given in section 5.3.3. In order to compare the fluxes from the modeled distributions to the SPI observations, the remnants coordinates l' and b' are re-

Table 5.10: Average number of ccSN remnants detectable above the limiting ^{44}Ti decay flux for several morphologies and star formation rates. The SFRs are given in units of $M_\odot\,yr^{-1}$. The table contains average number of observable ccSN remnants integrated over the entire sky, disregarding potential sensitivity variations in the direction of the Galactic anti-center. The spatially resolved average number of detectable sources is given in the last two rows, calculated from the sensitivity map of the SPI plane survey. All numbers are determined from a fitted Poisson distribution. Uncertainties on the expected value are given at the 1σ level.

Morphology	SFR1	SFR 2	SFR 4	SFR 8
	sensitivity limit 10^{-5} ph cm^{-2} s^{-1}			
Exponential disk	0.34 ± 0.02	0.79 ± 0.02	1.68 ± 0.03	3.20 ± 0.15
Spiral Arm	0.59 ± 0.03	0.96 ± 0.03	2.01 ± 0.04	3.57 ± 0.17
	sensitivity limit 10^{-6} ph cm^{-2} s^{-1}			
Exponential disk	1.56 ± 0.12	3.04 ± 0.04	6.52 ± 0.06	13.41 ± 0.42
Spiral Arm	1.35 ± 0.07	3.24 ± 0.05	6.74 ± 0.06	13.39 ± 0.34
	sensitivity limit 10^{-7} ph cm^{-2} s^{-1}			
Exponential disk	2.90 ± 0.13	5.73 ± 0.07	12.02 ± 0.09	25.51 ± 0.51
Spiral Arm	2.88 ± 0.15	5.79 ± 0.07	12.22 ± 0.09	24.43 ± 0.57
	Spatially resolved map sensitivity; 17 yr SPI data			
Exponential disk	0.14 ± 0.03	0.46 ± 0.02	0.92 ± 0.03	1.82 ± 0.13
Spiral Arm	0.20 ± 0.04	0.54 ± 0.02	1.15 ± 0.03	2.21 ± 0.13

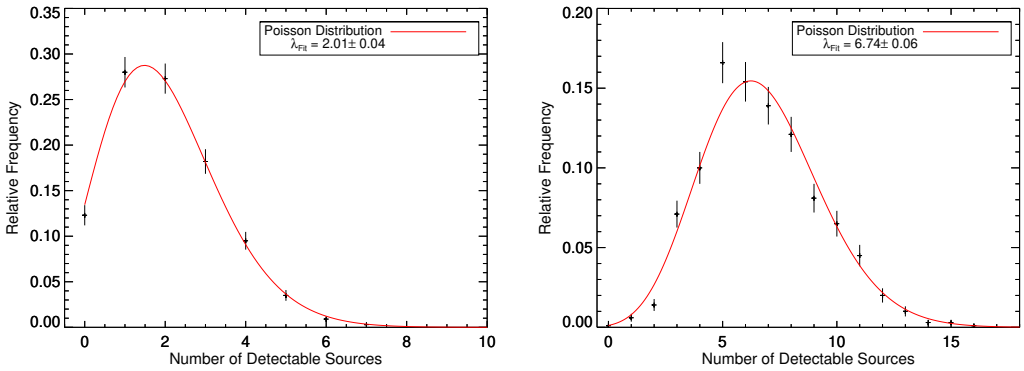

Figure 5.39: Probability mass function of detecting the specified number of SNe with a flux above the sensitivity limit 10^{-5} ph cm^{-2} s^{-1} (left) and 10^{-6} ph cm^{-2} s^{-1} (right) in 1000 simulated remnant distributions with SFR = $4\,M_\odot\,yr^{-1}$ in the spiral arm model. The expected values λ_{Fit} of the fitted Poisson distribution are given in the legend.

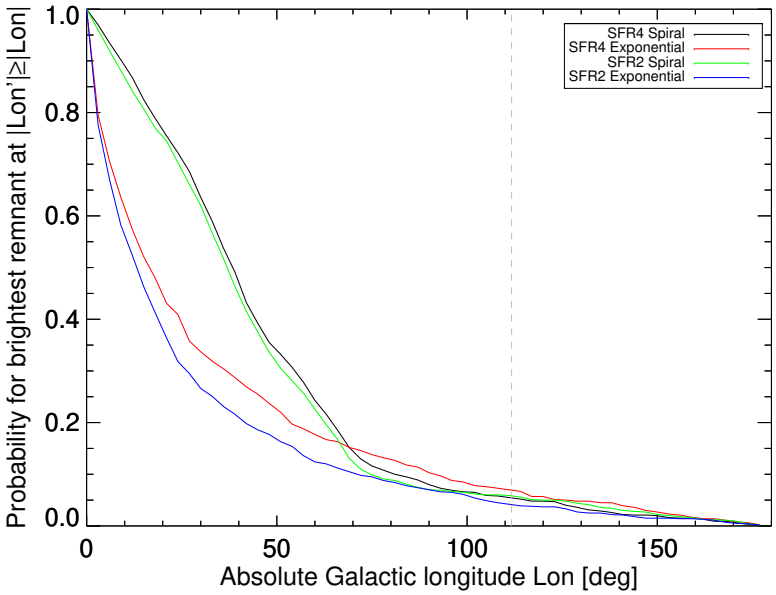

Figure 5.40: Detection probability for the ^{44}Ti decay emission brightest SNR above the given absolute longitude. The absolute brightness of the SNR is not taken into account, i.e. the brightest remnant is not necessarily detectable in the respective MC run. The gray dashed line indicates the absolute longitude of the Cassiopeia A SNR at l = 111.7°.

binned into a grid, that is consistent with the coordinate grid introduced in section 5.2.2. Each point in the grid is assigned the flux from the ccSN remnants it contains. In the unlikely event of two coinciding SNRs, the flux in the grid point is the sum of both SNRs, i.e. the celestial position is treated as if containing only one remnant instead of the superposition of several remnants. The number of detectable SNRs is determined as the number of grid points, in which the modeled flux is higher than the 3σ sensitivity limit, determined in the survey of the Galactic plane. This method only allows for the detection of ccSN remnants at latitudes $|b| \leq 18°$. As shown in figures 5.34 and 5.35, the majority of modeled ccSN remnants is confined to the Galactic plane. As this analysis approach utilizes a non idealized, celestial sensitivity distribution, the lack of uniform exposure on the Galactic plane becomes evident. As a consequence, the average number of detectable sources is smaller, albeit still compatible with the numbers from the idealized, spatially unresolved analysis. The average number of expected ccSN remnants is in agreement with the non-detection of any source additional to Cassiopeia A. The only exception is for the very low SFR of $1\,M_\odot\,yr^{-1}$, where the probability for detecting one sources is 0.13 and the probability for detecting two or more sources is 0.18, respectively, i.e. no detectable sources are expected in 69% of all simulations.

This picture changes immediately, when the location of the detected Cas A SNR is considered in addition. From figures 5.34 and 5.35 it is evident, that the majority of SNRs is accumulated in either the center of the Galaxy or the inner $\approx \pm 100°$ Galactic longitude. The probability for finding the brightest SNR, on average, above an absolute Galactic longitude is shown in Figure 5.40. Here the brightest SNR is not necessarily defined as a detectable remnant, but only as the brightest remnant in the respective MC run of the model simulation. The probability of finding the brightest SNR at an absolute longitude above 112°, which is the location of Cas A, is below 8% in both tested remnant morphologies. This can

be explained by the following assumptions. First, it is possible that the assumed spatial distribution of SNRs does not adequately describe the true celestial situation. This would also suggest that the distribution of star forming regions need be spread over a larger longitudinal space than assumed. While it is possible to artificially increase the density of star forming regions beyond absolute longitudes of 100°, this would mean that the distribution of massive stars and star forming regions would shift from the direction of the Galactic center towards the Galactic anti-center. This is inconsistent with the observed distribution of massive stars in the Galaxy (e.g. Urquhart et al. 2013). I conclude, that the position of Cassiopeia A at high longitude as the only detectable SNR is due to statistical fluctuations, originating from the position of the Sun with respect to the currently brightest visible remnant, as the position is not excluded with high significance ($\leq 2\sigma$).

5.3.6 Discussion of the CCSN Rate and CCSN Feedback

5.3.6.1 Core Collapse Supernova Rate

The method, as described in the search of previously unknown, ^{44}Ti bright remnants (cf. section 5.2.6), is one way of estimating the Galactic ccSN rate. Within the simulations conducted in this thesis, the ccSN rate can be calculated from the SN explosions during the time scale of the simulations. The rate itself depends on the explodability and the IMF, as these two quantities determine the amount of stars that are in the mass range for a potential ccSN. Within the Limongi & Chieffi (2018) models, the maximum mass for an exploding star is $25\,M_\odot$, which explodes 9.8 Myr after formation. The dependence of the ccSN rate on the SFR is shown in Figure 5.41a. In the figure an almost linear relation between the ccSN rate and the star formation rate can be identified. The ccSN rate is linked to the SFR with $R_{ccSN} = \alpha \times SFR$, where $\alpha = (0.57 \pm 0.04) \times 10^{-2}\,M_\odot^{-1}$. The gray shaded area in the left panel of Figure 5.41a indicates the allowed region of ccSN rates and SFR rate taking into account the upper limit of the ccSN rate determined in section 5.2.6. With the linear relation between ccSN rate and SFR, this also limits the allowed SFR rate to values of less than $5.7\,M_\odot\,yr^{-1}$.

In my analysis, regarding the emission of ^{44}Ti in the Galactic plane, emission was found in only one, previously known SNR. In the entire Milky Way, no additional ^{44}Ti bright sources could be found with high statistical significance. This limits the number of observable SNRs in the Milky Way to ≈1, where the one detected source is at a peculiarly high Galactic longitude, considering the distribution of ^{44}Ti bright SNRs modeled with PSYCO. Within the PSYCO framework, this low number is consistently modeled by assuming an initial SFR ranging between 2 and $4\,M_\odot\,yr^{-1}$. Within these models, the expected number of ^{44}Ti bright remnants ranges between 0.46 and 1.15. Overall, the inferred SFRs of $2-4\,M_\odot\,yr^{-1}$ seem to be compatible with the commonly assumed SFRs of $\approx 1-4\,M_\odot\,yr^{-1}$ (cf. table 2.3). Higher SFRs, especially in the range $\geq 8\,M_\odot\,yr^{-1}$, would lead to a number of SN observable in γ-ray emission, that is incompatible with the low number of observed sources.

With the linear relation between SFR and ccSN rate, this translates into a ccSN rate in the Milky Way of 1.1–2.3 explosions per century. The ccSN rate is in good agreement with literature values, that suggest a ccSN rate ranging between 0.8 and 5.2 explosions per century (cf. figure 5.42). These rates are based on various estimation techniques, including the count

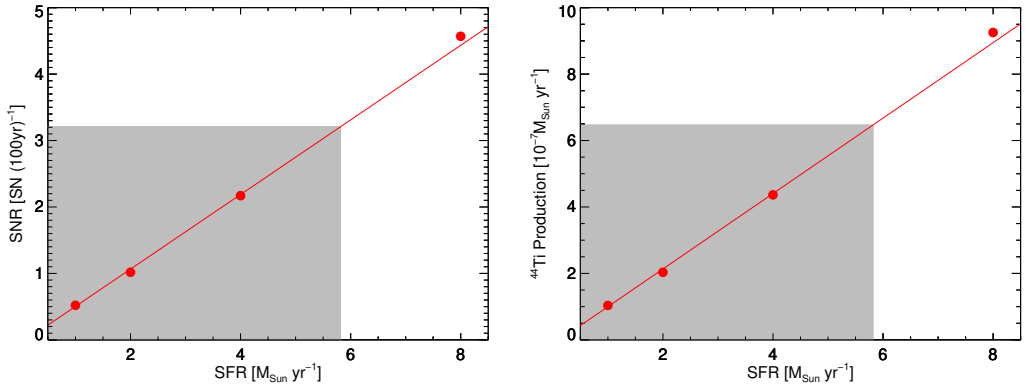

(a) *(b)*

Figure 5.41: Left: CcSN rate per century in dependence of the star formation rate per year. All stars between 8 – 25 $M_\odot$ contribute to the ccSN rate. The determined sampling variance of the ccSN rate is too small to be distinguishable from the plotting symbols. The gray shaded area shows the allowed range of the ccSN rate and SFR considering the upper limit determined in section 5.2.6 Right: ^{44}Ti production rate in dependence on the SFR. The gray shaded is similar to left panel, however for ^{44}Ti production rate and SFR.

of massive stars (Reed 2005), number of radio remnants and historical SN records (van den Bergh & Tammann 1991; Tammann et al. 1994; Adams et al. 2013), and extrapolations of extragalactic ccSN rates (Cappellaro et al. 1993; Li et al. 2011). Furthermore, my ccSN rate is consistent with the ccSN rate of (1.9 ± 1.1) events per century (Diehl et al. 2006a), based on observations of the γ-ray signature of radioactive ^{26}Al, a direct tracer of massive star activity, in the Milky Way.

The various estimates of the ccSN rate in the Galaxy suggest that ≈ 2 ccSNe should occur per century. Since the explosion of Cas A about seven SNe should have exploded within the Galaxy in the last 350 yr. However, no explosion has been observed within this time span. CcSNe explode within the dense birth clouds of their massive progenitor stars. Large column densities of absorbing hydrogen gas in these clouds (cf. section 2.2.1) as well as the presence of molecular clouds between the SNe and the observer at Earth lead to a large extinction of optical light. Therefore, ccSNe could have been hidden from the optical instruments of the observers in the last few centuries. The best example for this is Cas A, whose transient was not observed in the respective era.

In contrast to optical light, the Milky Way is transparent to γ-rays. The compatibility of missing all potential ccSN explosions in ^{44}Ti decay radiation within the last 400 yr with SPI with the assumed canonical ccSN rate is investigated. To miss all explosions requires that all explosions during this time span have occurred outside of the active volume (cf section 5.2.6) at the respective time of the explosion. For ccSNe in the last century, 64% of the Galactic SN activity are covered by the survey at a ccSN age of 0 yr and 31.2% at a ccSN age of 100 yr. On average, i.e. at a ccSN age of 50 yr, the survey encompasses 49.6% of the Galactic SN activity. For the estimate it is assumed, that the occurrence of SNe in the Galaxy follows Poisson statistics with an expectation value of two events per century. The probability of all 20th century ccSNe occurring outside the active volume, is 37.1%.

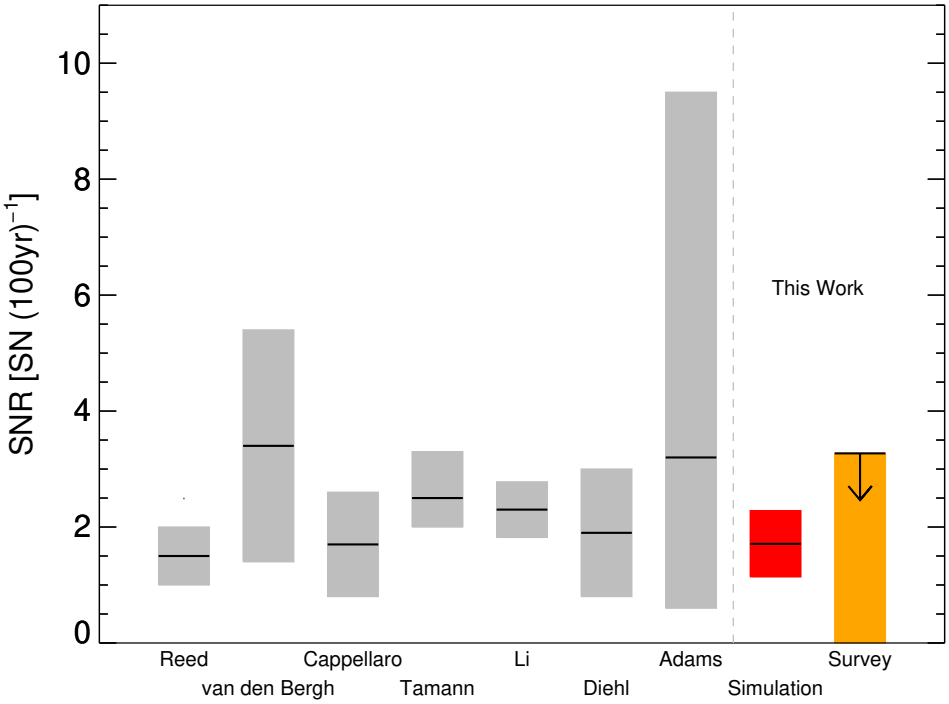

Figure 5.42: Compilation of ccSN recurrence rates. Gray shaded areas are ccSN rates from the existing literature (cf. table 2.3). The black lines in the center represent the determined value, the gray shaded ares the uncertainty as given in the referenced works. Cited works are from left to right: Reed (2005); van den Bergh & Tammann (1991); Cappellaro et al. (1993); Tammann et al. (1994); Li et al. (2011); Diehl et al. (2006a); Adams et al. (2013). On the right side of the graph, the ccSN rates, determined in this thesis, are given. Red is the rate determined from the comparison of the simulated ^{44}Ti bright remnant distribution with observations, orange indicates the survey determined limit.

With increasing age of the ccSN explosions, the active volume, i.e. the completeness of the survey with respect to the Galaxies full area with potential SN activity, decreases. Within the last four centuries, the coverage of the total SN activity decreases to 17.6%, 5.4%, and 1.7% at the respective ccSN ages of 150, 250 and 350 yr. Consequently, the probability of missing explosions from the respective centuries in a present day survey increases. Assuming Poisson statistics for the occurrence of ccSNe as above, the probability of missing all explosions in the 19th, 18th and 17th century is 70.4%, 89.7% and 96.7%, respectively.
The probability for all ccSN occurring outside the time dependent, active volume within the last four centuries is 22.7%. Also for a higher ccSN rate of 3 explosions per century, the probability for all potential ccSNe to be missed in the survey is 10.8%. The non-detection of sources with an age of less than 350 yr is consistent with canonical ccSN rates and the instrument sensitivity.

As indicated in sections 5.2.6 and 5.3.3, the spatial probability distribution for the occurrence of a ccSN is not uniform in the Galaxy. Following the assumed density profiles for massive star formation and the surface density of SNRs, the probability for the occurrence of a ccSN in the Galactic center region is significantly higher than in the vicinity of the Sun. This

effect has been incorporated in the probability estimate above. For a hypothetical observer, located at the Galactic center, the probability of missing all ccSNe, that occurred within a time span of 400 yr, reduces to 9.5% and 2.9% for a ccSN rate of 2 and 3 events per century, respectively. The fact, that the majority of ccSNe in the Galaxy can be missed in a present day ^{44}Ti survey is partially introduced by the position of the Sun at 8.5 kpc from the Galactic center.

5.3.6.2 Extraordinariness of ^{44}Ti Rich Supernovae

Now that the ccSN rate in the Galaxy has been established and linked to the general SFR, another conceptional link between the modeling of a SNR distribution and the observable Galaxy is investigated: The production rate of ^{44}Ca, the end product in the decay chain of ^{44}Ti. While this quantity needs not necessarily be constant over the life time of the Milky Way galaxy, I assume that the average ^{44}Ti production rate during the last 40 Myr is representative for the steady state production of ^{44}Ca today. Likewise to the ccSN rate, the ^{44}Ca production rate is almost linearly dependent on the SFR as shown in 5.41b. The determined SFR upper limit of $5.7\,M_\odot\,yr^{-1}$ translates into a ^{44}Ti production rate limit of $6.5 \times 10^{-7}\,M_\odot\,yr^{-1}$

A discrepancy however arises, as the resulting production rate of the radioactive ^{44}Ti isotope and the stable ^{44}Ca nucleus at the end of the decay chain, is significantly incompatible with the production rate inferred from Galactic chemical evolution models. These models infer a production rate of ^{44}Ca of $5.5 \times 10^{-6}\,M_\odot\,yr^{-1}$ (Leising & Share 1994; The et al. 2006). The models presented here, however, constantly fall short of this rate by approximately one order of magnitude, varying between 2.0 and $9.3 \times 10^{-7}\,M_\odot\,yr^{-1}$ in the modeled SFR range between 1 and $8\,M_\odot\,yr^{-1}$. To relax the constraints on the production rate of ^{44}Ca, following Timmes et al. (1996), it is assumed that only half of the ^{44}Ca content is produced as ^{44}Ti, while the other half is synthesized directly as ^{44}Ca. The required ^{44}Ti production rate is then $\approx 3 \times 10^{-6}\,M_\odot\,yr^{-1}$. To solve the discrepancy, three potential solutions are suggested:

1. **Increasing the SFR**
2. **Increasing the SN ^{44}Ti ejecta yields**
3. **Introducing a ccSN independent ^{44}Ti production site**

The first hypothesis is to artificially increase the SFR to an extent, such that the modeled ^{44}Ti production rate matches the observed rate. The ^{44}Ti production rate is almost linearly dependent on the SFR, i.e. $R_{^{44}Ti,prod}(SFR) = \eta \times SFR$ with $\eta = 1.13 \times 10^{-7}$. The extrapolated, required SFR is $26.7\,M_\odot\,yr^{-1}$, exceeding the observed SFR rates of $0.8\,M_\odot\,yr^{-1}$, $\approx 4\,M_\odot\,yr^{-1}$, and $13.0\,M_\odot\,yr^{-1}$ (cf. table 2.3). In addition, with the linear relation between the SFR and the ccSN rate, the increased SFR suggest a ccSN rate of 15.0 events per century, incompatible with observations. The first hypothesis is rejected on this basis.

The second solution, increasing the ^{44}Ti ejecta yields of ccSNe, seems justified. The adopted 1D models from the Limongi & Chieffi (2018) consistently suggest ejected ^{44}Ti masses of $\leq 5 \times 10^{-5}\,M_\odot$ per explosion with the exception of a few specific parameter combinations. For the low mass end of the simulations, the ^{44}Ti ejecta masses from Wanajo et al. (2018)

are $\approx 2 \times 10^{-6}$ $M_\odot$. When comparing these ejecta masses to the observed masses of Cassiopeia A or SN1987A, one immediately notices, that the simulated ejecta masses of ^{44}Ti are insufficient. The measurement based ejecta mass is $(2.6 \pm 0.6) \times 10^{-4}\,M_\odot$ (Cassiopeia A Weinberger et al. 2020). Assuming that the explosion is the result of a $\approx$20 $M_\odot$ star (Young et al. 2006), the ^{44}Ti ejecta masses in the PSYCO models can be underestimated by almost an order of magnitude. No observations of the ejected ^{44}Ti masses in ccSN explosions at the low mass end below 10 $M_\odot$ are available. However it is assumed here that the models by Wanajo et al. (2018) also underproduce the ^{44}Ti ejecta masses by up to one order of magnitude. This region of uncertainty in the ejecta masses allows to increase them in the models to the extent, that the time averaged production of ^{44}Ti in the models is identical with the ^{44}Ti production suggested by the Galactic chemical evolution models. The adopted increase in the ^{44}Ti ejecta masses is dependent on the initial SFR of the models. Specifically, the ^{44}Ti ejecta masses are increased by a model dependent production factor. All ejecta masses are uniformly multiplied by this production factor, independent of the mass of the exploding star. These factors are 14.75, 6.87, and 3.24 for the SFR of 2, 4, and 8 $M_\odot\,yr^{-1}$. The increase by a factor of almost 15 suggests very high ejecta masses, exceeding the observed masses, however it is necessary to satisfy the production condition. The increase in ejecta masses also influences the appearance of detectable sources in the sky. As the observable fluxes of SNRs are directly proportional to the ejecta masses as shown in equation 5.4, the number of bright sources above the detection threshold consequently increases. For the spatially unresolved analysis, the detectable number of SNRs at a flux level of $10^{-5}\,ph\,cm^{-2}\,s^{-1}$ increases to 3.65 ± 0.06, 5.82 ± 0.09 and 8.72 ± 0.32 in the spiral arm model and to 3.47 ± 0.06, 5.70 ± 0.09 and 8.03 ± 0.29 in the exponential disk model for the SFRs of 2, 4 and 8 $M_\odot\,yr^{-1}$, respectively. The problem arises, that while satisfying the production rate of ^{44}Ti in the galaxy, the celestial distribution of SNRs becomes incompatible with conducted ^{44}Ti surveys (cf. chapter 5.2). Also in the spatially resolved analysis, comparing the sensitivity map of SPI to the modeled maps, the average number of detectable sources increases to 2.84 ± 0.05, 4.26 ± 0.06, and 5.82 ± 0.24 in the spiral arm model and 2.84 ± 0.05, 4.27 ± 0.07, and 5.82 ± 0.24 in the exponential model for the aforementioned SFRs. These results are again largely inconsistent with the detection of only one remnant as the probabilities of detecting less than 2 remnants is between 10 and 20% in all cases. Considering the location of Cassiopeia A, the probability is reduced to below 2%.

The first two hypothesis can therefore not be self-consistently modeled to be compatible with the celestial distribution of ccSN remnants. However, the model results from the PSYCO code only take ccSN explosions into account, following the formation and evolution of massive star groups. Due to this deficiency, a second population of SN explosions can be added to the simulation results in order to explain and fill the discrepancy in the ^{44}Ti production rates. To this point, the influence of type Ia SNe have been disregarded in the context of creating a significant impact on the observable sky in ^{44}Ti decay lines, due to their assumed small ^{44}Ti ejecta mass as well as their rare occurrence (see section 5.3.1). The overall type Ia to ccSN ratio is 0.1 (Dawson & Johnson 1994; Hatano et al. 1997; The et al. 2006), while updated values (Mannucci 2005; Boissier & Prantzos 2009; Smartt 2009) suggest a ratio between 0.2 and 0.4. In context with the PSYCO simulations, this translates into a type Ia SN rate between $0.1 \times 10^{-2}\,yr^{-1}$ (lower limit) and $0.9 \times 10^{-2}\,yr^{-1}$ (upper limit) in the moderate SFR range of 2 – 4 $M_\odot\,yr^{-1}$.

For classical type Ia SNe (i.e.delayed detonation and deflagration model, cf. section 2.4.3), the combination of the low occurrence rate and the small ^{44}Ti ejecta mass does not provide any significant contribution to the Galactic ^{44}Ti abundance. On the other hand, as introduced in section 2.4 and 5.1.7, specific type Ia progenitor systems exist, that lead to the production of a very large amount of ejected ^{44}Ti. While the double detonation model (Moll & Woosley 2013; Leung & Nomoto 2020) produces up to several 10^{-3} $M_\odot$ ^{44}Ti, the rare subtype of calcium rich gap transients (CRGT) (cf. section 2.6.2 and might (Filippenko et al. 2003; Perets et al. 2010; Kasliwal et al. 2012; Valenti et al. 2013)) produce 50% of its ejecta mass in ^{44}Ti and is considered as one solution to solve the abundance issues of ^{44}Ca in the intra-cluster medium (Mulchaey et al. 2013).

In section 5.1.7, a ratio $\geq 2.6 : 1$ for classical type Ia SN explosions to the double detonation scenario was determined. This means, that the estimate for the highest possible rate of double detonation type Ia explosions in the Galaxy is $0.3 \times 10^{-2}\,\mathrm{yr}^{-1}$, which uses the most optimistic ccSN rate and type Ia to ccSN ratio. For the CRGTs, the progenitor system is not well understood yet, but assumed to be of a thermonuclear origin. Kasliwal et al. (2012) suggest a ratio of CRGT to the other type Ia scenarios of 2.3%, which leads to a waiting time for these special type Ia explosions of several 10^4 yr. Even though the waiting time of both extraordinary event types is orders of magnitude higher than the typical ccSN waiting time, the high ^{44}Ti yields lead to a ^{44}Ca production rate that is consistent with the expected rate from chemical evolution scenarios. In this case, due to the long waiting time between individual events, the celestial distribution of detectable SNRs is also not significantly affected. Covering the Galactic surface between Earth and the Galactic center, i.e. a radius around Earth of 8.5 kpc, and assuming an ejected ^{44}Ti mass of $\approx 10^{-2}\,M_\odot$ (Kromer et al. 2010), a double detonation event would be visible up to an explosion age of 500 yr for a sensitivity limit of $10^{-5}\,\mathrm{ph\,cm^{-2}\,s^{-1}}$. Assuming an average double detonation recurrence time of $1.0 \times 10^{-3}\,\mathrm{yr}^{-1}$, the probability that no explosion occurred during the past 500 years is 60%. Therefore, the observed sky is compatible with the expected double detonation (and also CRGT) celestial distribution.

While the estimates of the recurrence time and the ^{44}Ti ejecta masses of all SN types can still not be adequately modeled and observations of SNRs in ^{44}Ti decay γ-rays are sparse, it appears safe to assume that the majority of the Galactic ^{44}Ca content is produced in the rare, peculiar, ^{44}Ti rich SN explosions. This would allow a rather low recurrence rate of ccSNe, compatible with the observed sky distribution of ^{44}Ti bright remnants, while still achieving the required production rate of ^{44}Ca in the Galaxy due to an additional, rarely occurring scenario.

Chapter 6

Cosmic Ray De-Excitation Lines

The sites of Galactic CR acceleration are still a matter of debate. While particles with highest energies above 10^{18} eV are expected to originate from outside of the Galaxy, it is widely accepted that the bulk of the CRs up to the *knee* in the CR spectrum originates in the Galaxy (cf. section 2.7). As, however, the trajectories of the CRs in the Galaxy are constantly altered by the presence of magnetic fields, CRs detected at Earth cannot be linked to their acceleration sites. Besides other potential sources, SNRs are considered as the dominant accelerators for the majority of Galactic CRs based on their power to solely replenish the losses of CRs escaping the Milky Way. Considering the residence time of CRs in the Galaxy, the power required to sustain a constant CR energy density in the Galaxy can be estimated to be $\approx 10^{41}\,\mathrm{erg\,s^{-1}}$ (Strong et al. 2010). This value is consistent with the power of depositing 10–20% of SNe's kinetic energy of 10^{51} erg into CRs, assuming a SN rate of 2–3 events per century.

The acceleration of particles can be linked to SNRs by observing the emission of electromagnetic radiation at the SNR's location. The radiation is produced by the interaction of CRs with the ambient medium. The four dominant processes are synchrotron radiation, bremsstrahlung from a non-thermal distribution of particles (NTB), inverse Compton scattering and the production and respectively decay of neutral pions. A detailed description of these processes is given in sections 2.7.2 and 3.1.1.
The detection of synchrotron radiation in the radio wavelength band and up to several hundred keV hints towards the acceleration of particles in SNRs (Parker & Shakeshaft 1968; Ballet 2006; Reynolds 2008; Vink 2011; Helder et al. 2012). Strictly speaking, however, this synchrotron radiation is only evidence for the acceleration of electrons in the shock. Similarly, the detected emission of high energy γ-rays with energies between GeV and several TeV could be produced by electron interactions (leptonic model), either via inverse Compton scattering on ambient low energy photons or by the emission of electron NTB. However, also the decay of pions, that are produced from the interactions of protons with ambient hydrogen, produces emission in the GeV to TeV range (hadronic model). Recent observations indicate, that the decay of pions is most likely the dominant contribution to the high energy radiation detected in several remnants (Morlino & Caprioli 2012; Ackermann et al. 2013; Zirakashvili et al. 2014; Ahnen et al. 2017). This provides direct evidence for the acceleration of protons in several SNRs. However, the γ-ray spectrum can potentially also be explained by a leptonic component with a complex parental electron spectrum. While the hadronic model is favored, the ambiguity between the leptonic and the hadronic model

is difficult to solve. Several remnants apparently lack the pion component, and the highest energy emission can be fully explained by the leptonic model (Abdo et al. 2011).

Additional direct evidence for the acceleration of hadrons can be gained by observing electromagnetic radiation of SNRs in the low MeV range. Inelastic scatterings of energetic particles result in the production of excited nuclear states and radioactive nuclei, which decay under the emission of photons with energies typically ranging between tens of keV and $\approx$ 20 MeV (cf. 2.7.4). Specifically low energy CR (LECR) protons and ions with energies of $\lesssim$ 100 MeV per nucleon can be ideally observed through their production of nuclear de-excitation lines. In this energy range nuclear excitations are expected to be the dominant process for CR energy loss (Meneguzzi & Reeves 1975). An increased flux in the high energy line of the ^{44}Sc decay at 1157 keV with respect to the 78 keV line of the parent nucleus ^{44}Ti might be a hint towards hadron acceleration in the Cas A remnant (cf. section 5.1.4).

In the following sections the broadband energy spectrum in SPI's full energy range between 20 keV and 8 MeV is analyzed for the emission of CR-induced nuclear de-excitation lines in Cas A ontop of an electron NTB and synchrotron continuum, with special focus on the strongest expected de-excitation line of $^{12}C^{*}$ at 4.4 MeV. Non-thermal bremsstrahlung, that is emitted by the interaction of electrons with ambient medium electrons and ions contributes to the broadband spectral energy distribution (SED) as measured with Fermi-LAT and MAGIC (cf. Figure 2.16; Ahnen et al. (2017)). This emission should extend towards $\approx$ 1 MeV below which the spectrum becomes harder with a smaller power-law index. The data set used in this analysis is identical with the data set in section 5.1.3.1 with the exception of the extended energy range. The data set comprises 11.2 Ms of dead time corrected exposure during which Cas A was at least in the partially coded FoV of SPI.

6.1 Spectral Energy Distribution of Cassiopeia A with SPI

In Figure 6.1 the measured broadband spectrum of Cas A as observed with SPI is shown. Over the entire energy region, the spectrum can be characterized into three distinct regions. Below $\approx$ 100 keV, the spectrum contains a strong continuum component. The continuum extends down towards the NIR region (e.g. Rho et al. 2003) and is consistent with a synchrotron radiation origin from a population of accelerated electrons in the remnant (Abdo et al. 2010). Above $\approx$ 2 MeV, an additional continuum-like emission appears to be present in the spectrum. In the energy region between the two apparent continua, the spectrum approaches an apparent local minimum in differential flux.

In an initial attempt to describe the spectrum, the emission is modeled with two distinct power-law functions: One accounting for the synchrotron emission below $\approx$ 100 keV, the second accounting for the high energy continuum. The shape of the model needs to smoothly connect the low energy synchrotron emission with the high energy continuum tail. The model is given by $F = \sum_{i=1}^{2} N_{PL,i}(x/x_{0,i})^{-\lambda_{PL,i}}$. The contributions of the 68, 78 and 1157 keV decay lines of ^{44}Ti and ^{44}Sc are modeled with Gaussian shaped lines (cf. equation 5.2). In addition, the spectrum could potentially contain the signatures of nuclear de-excitation lines. These are further discussed in section 6.2. The chosen goodness of fit criterion is $\chi^2 = 7264$ for 6655 d.o.f. The second continuum is found with a significance of 6.7σ ($\Delta\chi^2 = 49$ for

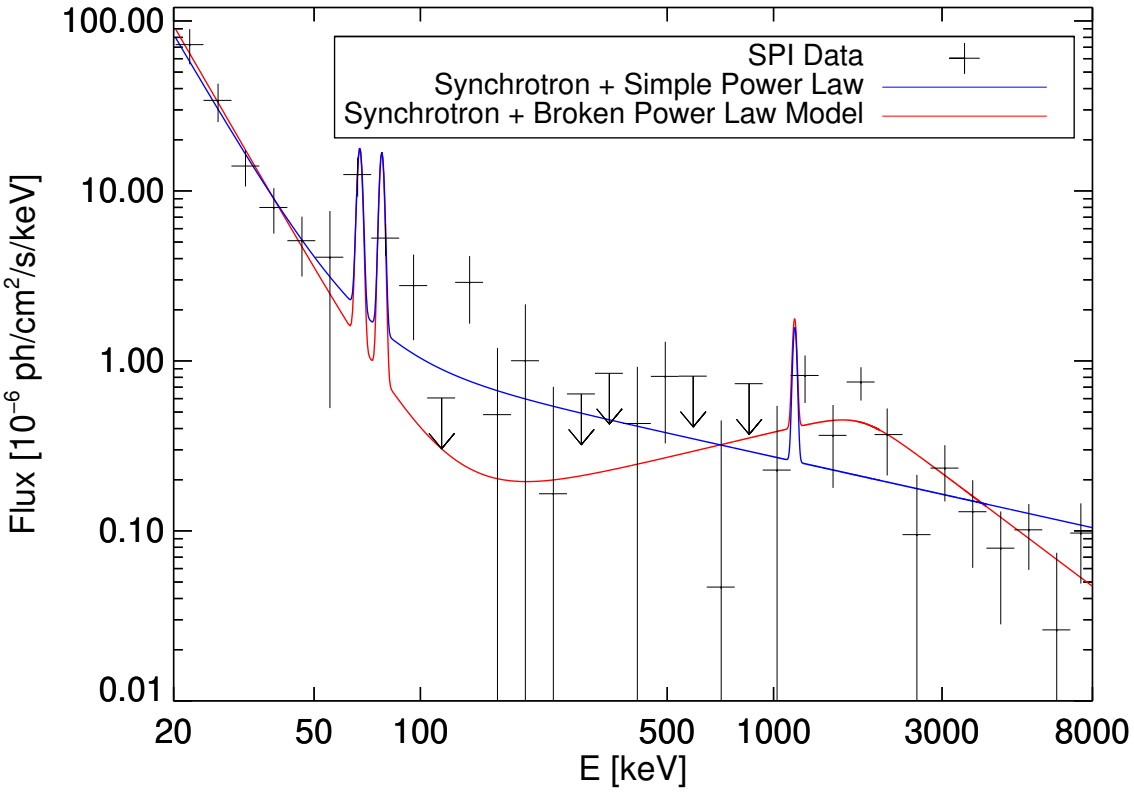

Figure 6.1: Broadband spectrum of Cassiopeia A between 20 keV and 8 MeV. The spectrum is logarithmically binned in energy for illustration purposes. The spectrum is evaluated at high resolution. Arrows indicate the 2σ upper flux limit in the respective bins. The best fit models (see text) are included in blue and red. The spectrum is fit with a varying number of power laws to account for a previously undetected continuum component with a break at $\approx$ 1.7 MeV and Gaussians to model the contribution from the ^{44}Ti and ^{44}Sc decay lines at 68, 78, and 1157 keV. The model is fit to the energetically highly resolved spectrum, correctly accounting for the strong excess in the narrow lines.

Δd.o.f = 2). The best fit power law has an index $\lambda_{PL,2} = 0.5 \pm 0.1$, and a normalization of $(2.7 \pm 0.4) \times 10^{-7}$ ph cm^{-2} s^{-1} keV^{-1} at $x_{0,2} = 1.0$ MeV. While the rather flat continuum ($\lambda_{PL} \stackrel{!}{=} 0$) is a reasonable description of the spectrum in the energy range between 200 keV to $\approx$ 1 MeV, a potential continuum-like emission above 1.5 MeV is not well represented with the flat continuum.

In addition, the entire continuum emission is described with a simple power law accounting for the synchrotron emission plus a smoothly broken power-law model instead of the second continuum, given by

$$F_{SBP} = N_0 \left(\frac{E}{E_0}\right)^{-\lambda_1} \left[\frac{1}{2}\left(1 + \frac{E}{E_b}\right)^{\frac{1}{\beta}}\right]^{(\lambda_1-\lambda_2)\times\beta} \tag{6.1}$$

where N_0 is a normalization parameter and E_0 is the pivot energy set to 1.0 MeV, λ_1, λ_2 are the indices of the broken power-law function before and after the break and $\beta = 0.1$ is a parameter describing the smoothness of the transition at the break energy E_B. The chosen goodness of fit criterion is $\chi^2 = 7255$ for 6653 d.o.f. The broken power-law model is found with a significance of 6.8σ ($\Delta\chi^2 = 58$ for Δd.o.f = 4). Fitting a smoothly broken power law to the spectrum improves the quality of the fit by $\Delta\chi^2 = 9$ for Δd.o.f = 2 (λ_2 and E_b)

with respect to the model with two simple power laws. The significance of the break is 2.5σ. The best fit parameters for the smoothly broken power law are a normalization constant of $N_0 = (3.3 \pm 0.6) \times 10^{-7}\,\mathrm{ph\,cm^{-2}\,s^{-1}\,keV^{-1}}$. The power-law index after the break is $\lambda_2 = 1.6 \pm 0.4$, describing the high energy tail of continuum emission. The power-law index before the break is $\lambda_1 = -0.5 \pm 0.3$, which describes an increase in the flux below the energy break point at $(1760 \pm 70)\,\mathrm{keV}$.

Non-Thermal Bremsstrahlung?

The nature of the broadband continuum emission is investigated. Previous observations of Cas A focused on the remnants emission in the radio to X-ray band and on the above GeV energy range (Parker & Shakeshaft 1968; Hales et al. 1995; Rho et al. 2003; Renaud et al. 2006; Maeda et al. 2009; Abdo et al. 2010; Ahnen et al. 2017). With SPI, emission in the energy gap between the two previous energy regions can be observed (cf. Figure 6.3). The possibility is assessed that the electromagnetic broadband emission originates from bremsstrahlung of a non-thermal population of electrons, accelerated in the SNR's shock. The determined spectral shape is evaluated with an analytical expression for bremsstrahlung from a non-thermal parent distribution of electrons that follows $\mathrm{dN_e(E)/dE} = \mathrm{K_e E^{-q}}$ with the normalization constant $\mathrm{K_e}$. A detailed derivation of the analytical expression for the photon energy spectrum can be found in Zeković et al. (2013). They describe a spectral break in the γ-ray emission at photon energies of $\approx 2\mathrm{m_e c^2}$, where $\mathrm{m_e}$ is the electron rest mass. The emissivity dW per volume dV, frequency $\mathrm{d}\omega$ and time dt below and above the break are given by

$$\begin{aligned}\frac{\mathrm{dW}}{\mathrm{dt d}\omega \mathrm{dV}} &= \frac{16 Z^2 e^6}{3 m_e^2 c^4} n_i K_e (2 m_e c^2)^{1-q/2} \frac{1}{4} \exp\left[-\left(\frac{1}{q} + \frac{1}{q-1}\right)\frac{q-2}{2}\right] \\ &\quad \times (\zeta_e E_\gamma)^{-q/2} \left[\ln(0.684 \cdot 2\zeta_e) + \frac{1}{q} + \frac{1}{q-1}\right] \qquad (6.2) \\ \frac{\mathrm{dW}}{\mathrm{dt d}\omega \mathrm{dV}} &= \frac{16 Z^2 e^6}{3 m_e^2 c^4} n_i K_e \frac{1}{2} \exp\left[-\left(\frac{1}{q} + \frac{1}{q-1}\right)\frac{q-3}{2}\right] \\ &\quad \times (\zeta_e E_\gamma)^{1-q} \left[\ln\left(1 + \frac{\zeta_e E_\gamma}{2 m_e c^2}\right) + \ln(0.684 \cdot 2\zeta_e) + \frac{1}{q} + \frac{1}{q-1}\right] \qquad (6.3)\end{aligned}$$

where Z is the charge number of the interacting ions, $E_\gamma = \hbar\omega$ is the photon energy, and ζ_e relates the kinetic energy of the electrons to the photon energy with $E_{kin} = \zeta_e E_\gamma$. In general, ζ_e is required to be larger than unity and can be energy dependent. In the simplification here, it is assumed to be constant over the narrow energy range of SPI between the break at 1760 keV and 8 MeV. Further, equation 6.3 shows that above the break the photon spectrum in energy follows the parental electron distribution with the spectral index $1 - q$, i.e. $F_\gamma(E_\gamma) \propto E_\gamma^{1-q} \propto E_\gamma^{-\lambda_2}$. Below the break energy, the spectral index of the NTB emission is given by $F_\gamma(E_\gamma) \propto E_\gamma^{-q/2}$.

Equation 6.3 states, that the index of the photon emission is related to an electron distribution with spectral index q. From the analysis of the continuum emission in the 200 keV to 8 MeV range, no uniform electron spectral index can be determined. Above the break energy at 1760 keV, the spectral index of the electron distribution would be $q = \lambda_2 + 1 =$

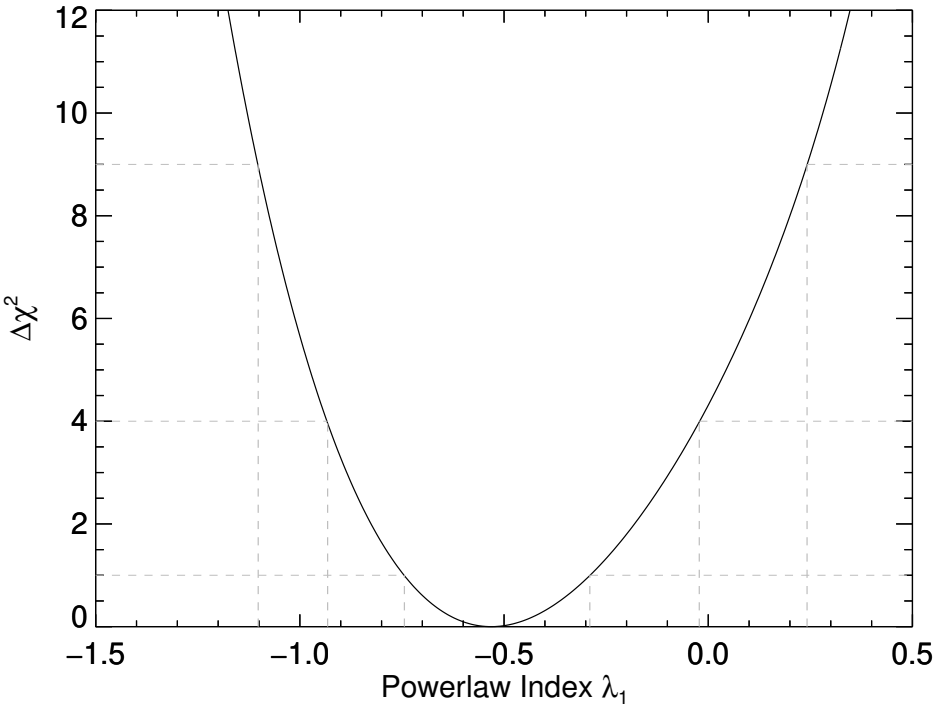

Figure 6.2: $\Delta\chi^2$ over broken power-law index λ_1. The values are calculated assuming the best fit values for all other model parameters, only letting λ_1 vary. The gray dashed lines indicate the 1, 2 and 3σ limits.

2.6 ± 0.4. Below the break the spectral photon index would suggest an electron parent index of $q = 2\lambda_1 = -1.0 \pm 0.6$. With the definition of the power-law indices as given in equation 6.1, the slightly negative value indicates an increases in the differential γ-ray flux (cf. Figure 6.1). This infers, that the electron distribution contains a break in energy, below which the population of accelerated electrons becomes increasingly depleted with decreasing energy. However, the γ-ray spectral index below the break is not well constrained due to the low signal to noise ratio in the majority of energies bins between 200 keV and 1 MeV. The low energy power-law index is mainly affected by the position of the minimum flux in the spectrum between 200 keV and 1 MeV. Figure 6.2 shows the 2 and 3σ upper limits of λ_1, assuming the best fit values for all other parameters. Both a constant offset ($\lambda_1 = 0$) as well as a decreasing flux ($\lambda_1 \geq 0$) are compatible with the observed SPI γ-ray spectrum. Still, the translation of the γ-ray power-law indices into the power-law indices of the parental electron distribution leads to two mutually excluding values of q.

The inferred shape of the electron distribution is incompatible with the shape of the electron distribution inferred from IR observations. The spectral shape of the IR to X-ray ($\lesssim$ 100 keV) emission in Cas A suggests, that it is produced by electron synchrotron radiation. The parental accelerated electron distribution was determined to follow a uniform power law with $dN_e(E)/dE \propto E^{q_{IR}} \exp(-E/E_m)$, with $q_{IR} = -2.34$ and an exponential high energy cut-off at 200 GeV (Rho et al. 2003; Abdo et al. 2010). NTB in SPI's energy range would be produced by the same population of electrons. The high energy γ-ray index $\lambda_2 = 1.6 \pm 0.4 = q_h - 1$ would suggest an electron distribution compatible with the spectral shape of the IR determined electron distribution. However, the break in the SPI γ-ray

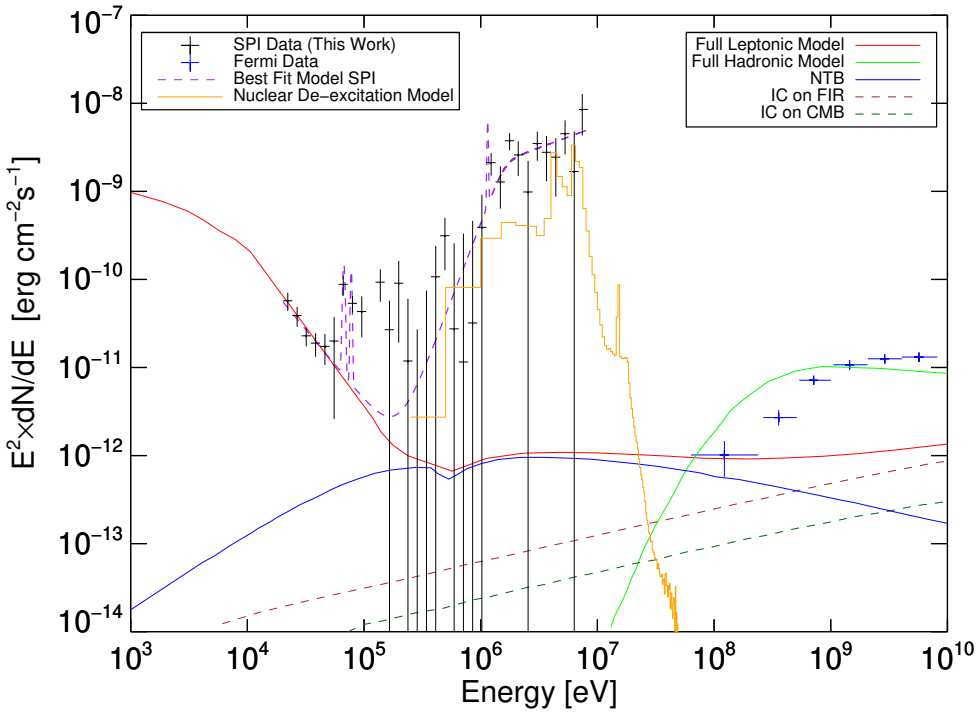

Figure 6.3: Reconstructed multiwavelength photon SED of Cas A. SPI data points (black) are taken from this thesis. The purple dashed line is the best fit model of the SPI data. In addition to the continuum-like emission, modeled with a broken power law (cf. eq 6.1), the model contains a synchrotron component, detectable up to $\approx 100\,\mathrm{keV}$ and the three emission lines of the ^{44}Ti decay chain. The orange spectrum describes the emission detected with SPI with a nuclear de-excitation spectrum. For further discussion of the nuclear de-excitation spectrum cf. section 6.4. Additional data and models are adopted from (Ahnen et al. 2017). Fermi data is added as blue data points. The different lines show the contribution of the various processes of emitting radiation from accelerated particle interaction in the SNR, modeled assuming a leptonic or hadronic origin of the GeV-TeV emission. The red model is the sum of all leptonic components in the spectrum. Below $\approx 100\,\mathrm{keV}$ the leptonic emission is dominated by synchrotron radiation that extends down towards the NIR region (e.g. Rho et al. 2003). The kink in the red/blue spectrum around 511 keV is a numerical artifact, introduced by the fitting routine utilized in (Ahnen et al. 2017).

spectrum at 1760 keV would require a break in the parental electron spectrum towards lower electron energies. Such a break is not supported by IR data. As the parental electron distribution is expected to follow a uniform power law over the entire energy range, a NTB origin of the γ-ray continuum in SPI's energy range is unlikely.

In addition, the energy content between several hundred keV and 8 MeV in SPI data, if it originated from NTB, is several orders of magnitude higher than expected from GeV-TeV measurements. In Figure 6.3, the broadband spectral energy distribution (SED) of SPI data is shown. The figure includes a description of the data with a nuclear de-excitation spectrum, further discussed in section 6.4. Additional SEDs and data points from Fermi/LAT observations in the figure are adopted from Ahnen et al. (2017). In the latter study, the NTB contribution is modeled to be consistent with the synchrotron emitting electron population. The NTB SED consistently contributes $\approx 10^{-12}\,\mathrm{erg\,cm^{-2}\,s^{-1}}$ to the full SED in SPI's

energy range. The SED is translated into a differential flux model in SPI's energy range, which ranges between 1×10^{-11} ph cm^{-2} s^{-1} keV^{-1} at 8 MeV and 5×10^{-9} ph cm^{-2} s^{-1} keV^{-1} at 1 MeV. The model is fit to SPI data and can be excluded with a significance of 6.2σ.

From inconsistencies in both the spectral shape and the energy content, the hypothesis of an NTB origin of the flux in SPI's data above several hundred keV is rejected.

6.2 Nuclear De-Excitation Lines in Cassiopeia A

As NTB cannot explain the high energy continuum in the Cas A between several hundred keV and 8 MeV, its origin due to the interaction of CRs with the ambient medium is considered. As discussed in section 2.7.5, the interaction of accelerated protons and ions produces a large number of nuclear de-excitation lines in the energy range of $\approx$ 300 keV to several MeV. While some of these nuclear de-excitations produce distinct lines in the spectrum (cf. Figure 2.18), a large number of weaker, superimposed lines lead to an underlying, continuum-like emission (cf. Figure 6.3, orange model).

The emission above 300 keV is described by the model spectrum in Figure 2.18 (Summa et al. 2011). This model is intended to account for the continuum emission in SPI data above several hundred keV and potential superimposed CR de-excitation lines. This means, that only the synchrotron continuum below 100 keV and the three ^{44}Ti lines are fit additionally, however the broken power-law model is not. The best fit normalization of the CR de-excitation model spectrum is 0.32 ± 0.15. The goodness of fit is $\chi^2_{\mathrm{red}} = 1.1$ ($\chi^2 = 7310$ for 6654 d.o.f.). Clearly, representing the continuum with a (broken) power law provides a significantly better fit of the data (cf. section 6.1).
In Figure 6.4 the residual fluxes of the model are shown. The model faces a caveat when describing the SPI spectrum, as it cannot simultaneously account for the continuum and the lines. The model contains the bulk of the continuum emission from superimposed lines in the energy region between 500 keV and 2.5 MeV. This part of the model needs to be increased to account for the bulk continuum emission in the same energy region in the SPI spectrum. Increasing the normalization of the continuum leads to a simultaneous significant overestimate of the strongest lines in the spectrum, specifically the de-excitation lines of ^{12}C, ^{15}N, and ^{16}O in the energy region above $\approx$ 3 MeV, visible in form of the negative, clustered residuals in the vicinity of e.g. the 4.4 and 6.1 MeV lines.

As the continuum emission and the line emission cannot be jointly modeled, I search for the imprints of the strongest emission lines above the continuum separately. The continuum is described with the broken power-law model in equation 6.1. The strongest de-excitation lines are listed in table 6.1. All model components are fit simultaneously, including the normalization and power-law indices of the broken power law. The model is given by

$$\mathrm{F_{tot}} = \mathrm{F_{Synchro}} + \mathrm{F_{SBP}} + \mathrm{F_{44,All}} + \sum_{\mathrm{i=1}}^{12} \mathrm{F_{i,CRL}} \tag{6.4}$$

where $\mathrm{F_{Synchro}}$ and $\mathrm{F_{SBP}}$ are the low energy synchrotron continuum below 100 keV and the broken power law (cf. above), $\mathrm{F_{44,All}}$ are the contributions from the ^{44}Ti decay lines and $\mathrm{F_{i,CRL}}$ are the 12 strongest CR-induced de-excitation lines indicated in table 6.1.

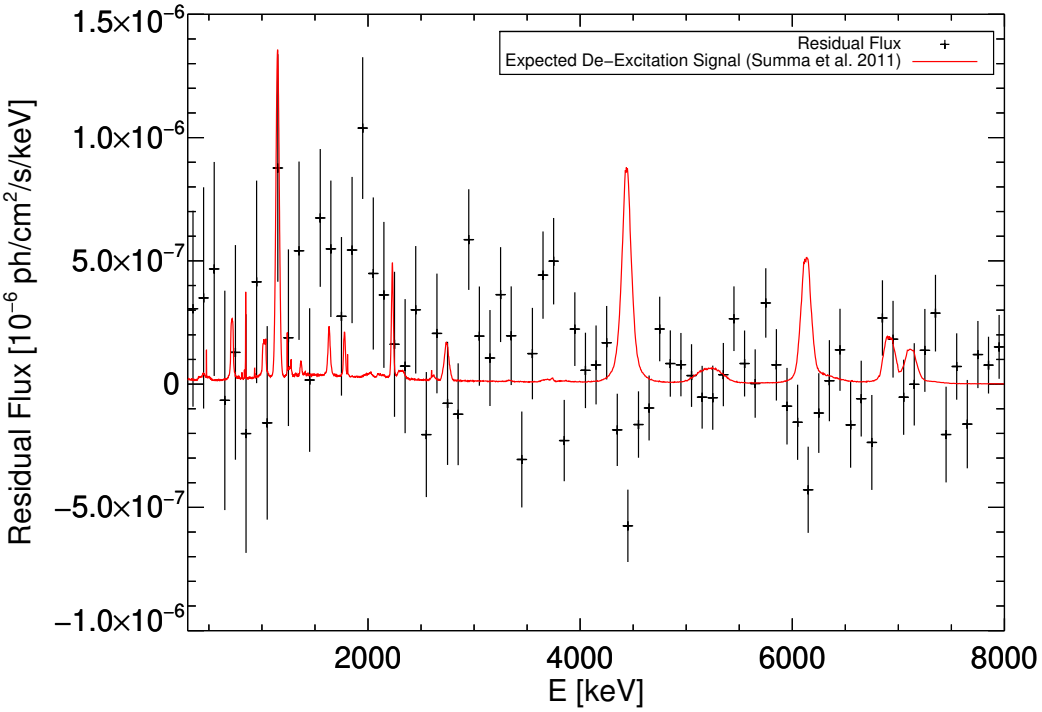

Figure 6.4: Residual flux in SPI spectrum of Cas A (black data points) in 100 keV bins between 300 keV and 8 MeV when modeling the emission with the simulated CR de-excitation spectrum of Summa et al. (2011). The red line shows the model. The strongest lines are visible as negative residuals, as the model cannot adequately describe the spectrum (see text).

In Figure 6.5 the spectrum of Cas A is shown, including the broken power law to account for the unresolved line components. The goodness of fit is $\chi^2 = 7237$ for 6640 d.o.f, suggesting that including all strong de-excitation lines does not significantly improve the fit. A likelihood ratio test between the model without the lines and the model with lines suggest a detection significance of all lines of 1.7σ ($\Delta\chi^2 = 19$ for Δd.o.f. = 12).
The broken power law is not affected by the presence of additional lines in the fit. The best fit normalization is $N_0 = (3.7 \pm 1.0) \times 10^{-7}$ ph cm^{-2} s^{-1} keV^{-1} at 1000 keV. The power-law index after the break is $\lambda_2 = 1.6 \pm 0.3$, describing the high energy tail of continuum emission. The power-law index before the break is $\lambda_1 = -0.9 \pm 0.8$. These parameters are consistent with the values determined when fitting only the continua (cf. section 6.1).

For each line, a likelihood ratio test is conducted to assess the significance of the individual lines. The full model is tested against the model containing all other components except the one specific line. No line, that could be attributed to de-excitation of nuclei in the shock region, is detected with high significance.
The line with the highest individual significance is found at the 2.6σ level above the continuum. The centroid of the fit line is at (6882 ± 19) keV. The integrated flux in the line is $(4.5 \pm 2.2) \times 10^{-5}$ ph cm^{-2} s^{-1}. The line is broadened with a width of (90 ± 18) keV (FWHM). The energy resolution of SPI at 6.9 MeV is 6.1 keV (cf. section 4.3), i.e. the resolving power of SPI at 6.9 MeV is $R_{6.9\,\mathrm{MeV}} = 6900/6.1 = 1131$. The line is significantly broadened with respect to the instrumental resolution.
The possibility is explored, that the line could be produced by the de-excitation of $^{16}O^*$

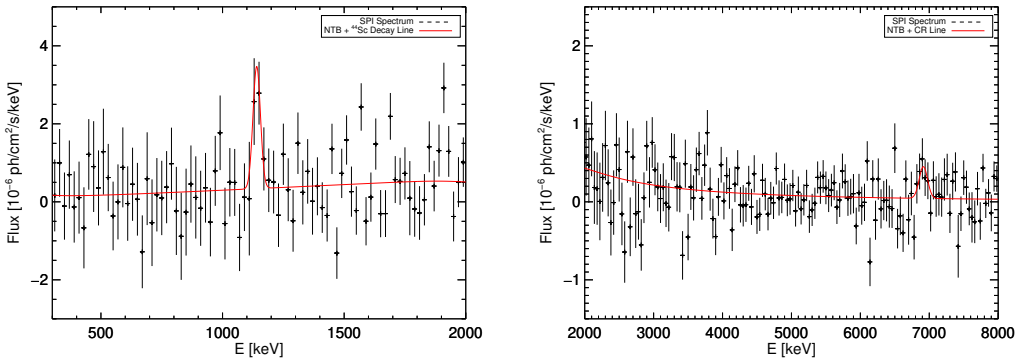

Figure 6.5: Left: Cas A spectrum between 300 keV and 2 MeV in 20 keV binning. Right: Cas A spectrum between 2 MeV and 8 MeV in 40 keV binning. Binning is for illustration purposes only. The continuum is modeled with a simple power law account for synchrotron radiation at low energy and a broken power law for the high energy continuum. A search for emission from CR-induced nuclear de-excitations shows a potential line at 6.9 MeV with an integrated flux of $(4.5 \pm 2.2) \times 10^{-5}$ ph cm^{-2} s^{-1} at a 2.6σ significance level.

in the SNR. During high energy background modeling, the precision of SPI's energy calibration at 6.9 MeV was determined. The strongest background line close to the ^{16}O* de-excitation line is the de-excitation line of ^{71}Ge at 6915.7 MeV. During background modeling, the centroid position of the background line was consistently found at (6915.8 ± 0.5) keV, suggesting that the energy calibration at 6.9 MeV is correct within 0.5 keV. The laboratory energy of the ^{16}O* de-excitation line is 6917 keV, while the centroid position of the fit line is (6882 ± 19) keV. The line is significantly red-shifted with respect to the laboratory energy. Assuming, that the kinematically induced Doppler shift of the remnant also applies to the CR de-excitation lines, the bulk of the ejecta is moving away from the observer with a velocity of (1500 ± 800) km s^{-1}. This would be in agreement with the bulk ejecta motion determined from the ^{44}Ti decay lines. In contrast to the bulk motion shift of the line centroid, the line width in this case does not inherently carry information corresponding to the expansion velocity of the SNR's shock wave. The broadening of the line is instead caused by the superposition of the ejecta expansion velocity and the nucleus' recoil velocity, added from the interaction of protons and ions to the target nucleus.

The intriguing line at 6.88 MeV is evaluated assuming that this line indeed is emitted by the de-excitation of the 6.92 MeV excited ^{16}O level. The proton spectrum in the initial estimate follows literature values given by Ahnen et al. (2017). The proton spectrum at Cas A is assumed to follow a power law in kinetic energy with $Q_p(E_p) = Q_0 E_p^{-\gamma_p}$ with an index of $\gamma_p = 2.2$. The production of π^0 requires a threshold energy of 280 MeV (cf. section 2.7.2). It is assumed here that the same proton distribution extends down towards the low MeV region, in which nuclear transitions are efficiently excited by CR interactions (cf. Figure 2.17). The total energy content of protons above 100 MeV is $\Omega_p = \int_{100\mathrm{MeV}} Q_0 E^{-\gamma_p} dE = 9.9 \times 10^{49}$ erg (Ahnen et al. 2017), which corresponds to $\approx 5\%$ of the ejecta's kinetic energy.

The flux in the 6.92 MeV line is estimated with (Summa et al. 2011)

$$F_\gamma = \frac{n_O}{4\pi d^2} \int Q_p(E_p)\sigma(E_p)v(E_p)dE_p \tag{6.5}$$

where $\sigma(E_p)$ is the energy dependent excitation cross section, v(E_p) is the proton velocity with respect to the target nucleus, d = 3.3 kpc is the distance to Cas A and $n_O \approx 0.5\,cm^{-3}$ is the target density of oxygen atoms in the interaction region. This target density of oxygen atoms is adopted from literature values (cf. Table 6.2 and Laming & Hwang (2003); Willingale et al. (2002); Lodders (2003)) and accounts for a homogeneous distribution of oxygen in the entire interaction region. It is noted here, that dense ejecta knots can have a higher oxygen particle density (e.g. Micelotta et al. 2016). The excitation cross section for $^{16}O(p,p)^{16}O^*$ is taken from Kiener et al. (1998). In this estimate, the line broadening effects of the recoiling target as well as the atomic substructure of the nucleus are disregarded, i.e. the potential excitation of other nuclear transitions in ^{16}O. The resulting flux in the $^{16}O^*$ de-excitation line at 6.92 MeV, estimated with this method, is $F_{6.92\,MeV} = 5.5 \times 10^{-6}\,ph\,cm^{-2}\,s^{-1}$. In this simplified approach of estimating the γ-ray fluxes from CR interactions in Cas A, the resulting flux in the line is roughly an order of magnitude lower than in SPI data (cf. Figure 6.5). Based on this estimate, the origin of the 6882 keV line from ^{16}O excitation, assuming interaction in the smooth post reverse shock region of Cas A (Micelotta et al. 2016), seems not plausible.

If the line is due to the excitation of ^{16}O by CRs in the shock region of the Cas A SNR, other lines should be visible as well, given the sensitivity of SPI. It is stressed here again, however, that the argument is based on a line with a low significance. In Figure 6.6, a simulated nuclear de-excitation spectrum on top of the continuum-like emission is shown.

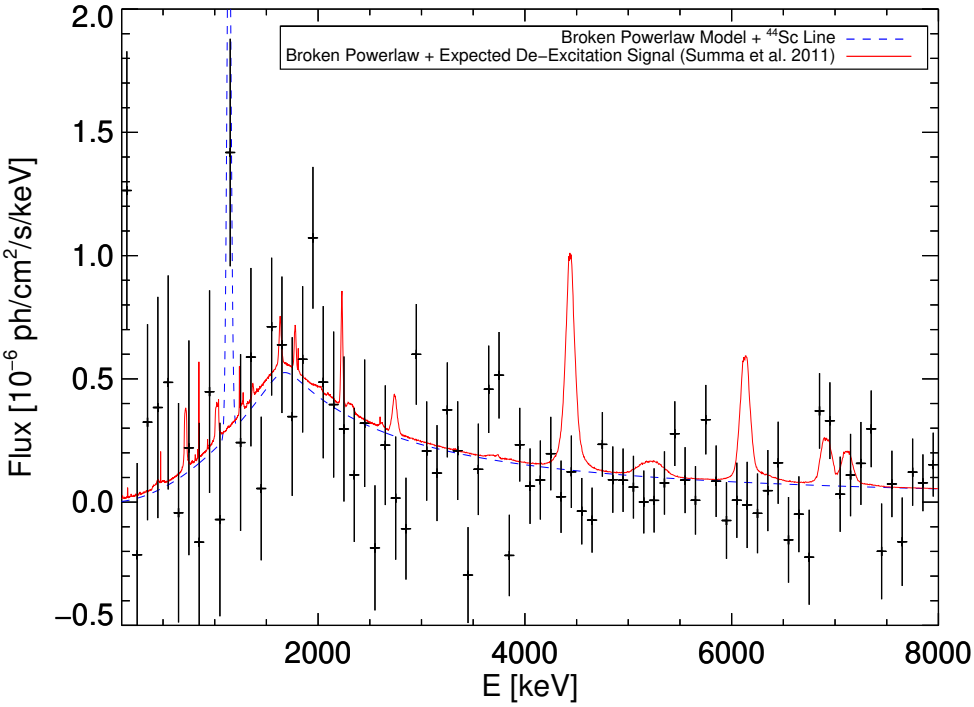

Figure 6.6: High resolution SPI spectrum of Cas A including simulated nuclear de-excitation lines. The de-excitation spectrum was modeled with the chemical composition of the Cas A remnant (Summa et al. 2011). The blue line indicates the best fit model of the continuum component. The simulated nuclear de-excitation spectrum is added on top of the broken power-law model. Significant excess is expected in the region around 4.4 and 6.1 MeV.

Table 6.1: Flux limits on strongest CR de-excitation lines at the 3σ level. The line FWHM and integrated, extracted fluxes are extracted from the simulated spectrum (Summa et al. 2011). Some of the lines are a blend of various de-excitation processes, that cannot be separated due to the strong kinematic broadening. Within the sensitivity of SPI, only the two strongest lines at 4.4 and 6.1 MeV are expected to be detectable.

Isotope	Line Energy [keV]	Line FWHM [keV]	Flux Limit [10^{-5}ph cm^{-2} s^{-1}]	Expected Flux [10^{-5}ph cm^{-2} s^{-1}]
^{10}B	718	26	9.5	0.7
^{56}Fe	847	4	4.6	0.1
^{10}B	1022	32	8.8	0.5
^{20}Ne	1634	27	5.8	0.6
^{14}N	1635	Blend		
^{28}Si	1779	20	6.7	0.4
^{30}Si	2235	21	5.5	1.0
^{24}Mg	2742	50	7.1	0.8
^{16}O	2754	Blend		
^{12}C	4434	94	4.9	10.2
^{15}N	5269; 5298	230	7.7	1.6
^{16}O	6129	120	5.2	5.8
^{16}O	6917	125	6.3	2.5
^{16}O	7115	125	7.1	1.8

The spectrum is adopted from Summa et al. (2011). In the remaining chapter, this simulated spectrum is referred to as model 1. The CR excitation of all lines is from a CR spectrum, that extends down to LECR with a power-law index of $\gamma_p = 2.3$. For particle interactions the composition of the ambient medium in Cas A was assumed. Upper flux limits for candidate strong emission lines and their respective expected fluxes in model 1 are listed in table 6.1.

6.3 4.4 MeV De-Excitation Line as Reference Line for the Cosmic Ray Excitation

Assuming the same composition of the ejecta and CR spectrum at low energies as in model 1, the $^{12}C^*$ de-excitation line at 4.4 MeV is expected to contribute the highest flux to the CR-induced γ-ray spectrum. Contributions to this line are from the reactions

$$^{12}C(p, p')^{12}C^* \quad (6.6)$$

$$^{12}C(\alpha, \alpha')^{12}C^* \quad (6.7)$$

$$^{16}O(p, x)^{12}C^* \quad (6.8)$$

$$^{16}O(\alpha, x)^{12}C^*, \quad (6.9)$$

which are those CR interactions with the two most abundant isotopes heavier than He in the acceleration region (cf. Table 6.2) with large cross sections for LECR excitation. The 4.4 MeV line is therefore used as benchmark to gauge the detectability of the lines in the SPI spectrum. In my analysis, no flux excess at 4.4 MeV is detected ($F_{4434} \leq 4.9 \times 10^{-5}$ph cm^{-2} s^{-1}

at 3σ) in the Cas A spectrum (c.f. Figure 6.5). In model 1, the line at 4.4 MeV is expected to contain an integrated flux of 10.2×10^{-5} ph cm^{-2} s^{-1}. The reason for this significant discrepancy between flux limit and expectation is investigated.

First, the possibility is assessed that the line flux is drowned by a large statistical background noise. For that purpose, the detectability of the line is investigated in an artificially created data set, similar to the approach described in section 5.1.2. The length of the data set is chosen to be identical to the length of the Cas A data set. The background count level of this data set is chosen from high latitude observations, spread over the INTEGRAL mission duration to avoid utilizing data with specifically low background. An artificial source contribution is added by normalizing the IRF convolved sky model of a point source at location (l,b) with the flux per keV bin, extracted from the simulated spectrum around the 4.4 MeV line (Figure 6.10). A Poisson sample of the renormalized sky model is drawn and added to the background SPI counts. 100 samples of a simulated sky are realized. The spectrum of the point source is then extracted from the artificial data sets (cf. section 4.1). An example of the extracted spectra is presented in Figure 6.7. The 4.4 MeV emission is modeled with a simple Gaussian on top of a constant offset. In all simulated data sets, the de-excitation line is detected with an average significance of 4.5σ. The integrated flux in the best fit Gaussian model is $(9.7 \pm 3.0) \times 10^{-5}$ ph cm^{-2} s^{-1}, which is in agreement with the input flux of 10.2×10^{-5} ph cm^{-2} s^{-1}.

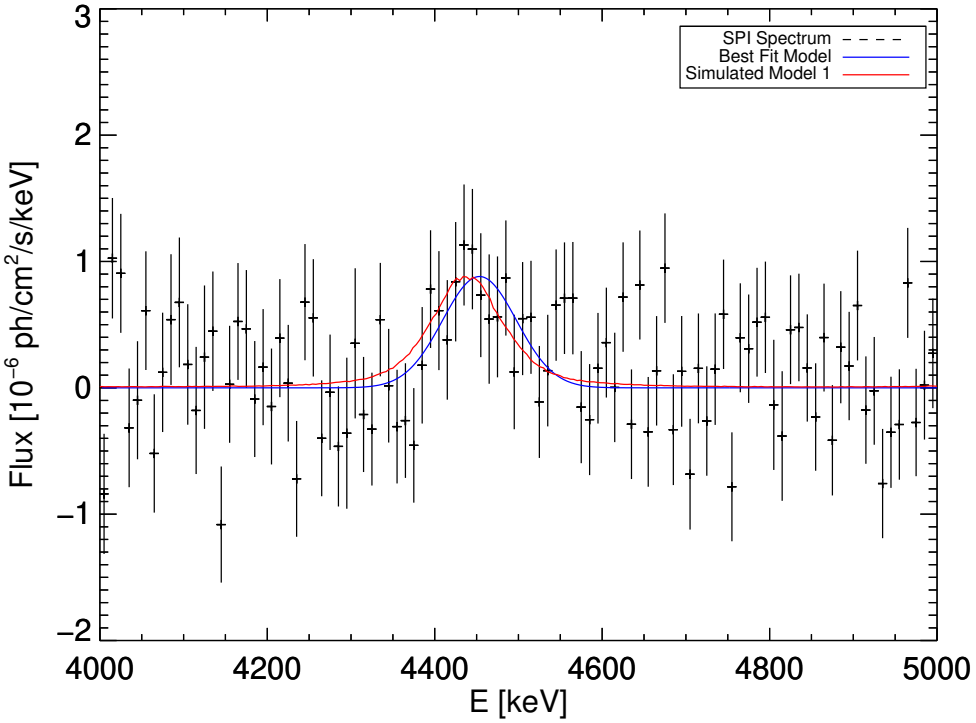

Figure 6.7: Extracted spectrum from simulated CR de-excitation spectrum (cf. Figure 6.6, red line), assuming a flux normalization of the expected 4.4 MeV line flux given in Figure 6.6. The extracted spectrum is fit with a simple Gaussian ontop of a constant offset. The simulation would predict a detectable signal (4.5σ) in the SPI detectors. This is not seen in the real data. For details see text.

Additionally, the effect of energy redistribution of incident photons of energy E_{in} to scattered, lower energy photons $E_{measured}$ on the detectability of the strongest emission lines is investigated. While this effect is subdominant in the low energy region, where only a low percentage of the incoming photons are redistributed to lower energies, the efficiency of the process significantly increases with increasing energy. As estimated in section 4.3.4, less than 50% of the incident γ-rays at 4.4 MeV are detected at 4.4 MeV, while the remaining photons are measured with lower energies. As the applied extraction procedure in SPI data analysis extracts the spectrum per individual energy bin, photons, that are redistributed into these individual bins from higher energies, could spuriously be attributed to the flux in the bin. This additional continuum-like flux (cf. Figure 6.9) could potentially drown the line flux. To gauge the effect on the CR de-excitation spectrum, especially the influence of the redistributed strongest lines, the cameras energy response for incident photons with 4.4, 5.2, 6.1, 6.9 and 7.1 MeV was simulated. The energy response for the 5 distinct incident energies is shown in figure 6.8. Each energy response is constructed from $\approx 5 \times 10^5$ photons. All events included in the response are non vetoed events, i.e. incident photons that deposit more than the respective threshold energies in the anti coincidence systems are not included in the energy response. In observations these events generate a veto trigger. The energy redistribution contains single events and multiple events, i.e. the deposited energy of consecutive interactions in more than one detector are summarized into one event with energy equal to the sum of the consecutive energy depositions.

All energy responses contain the same distinctive features. The intensity of the full energy peak at the respective incident photon energy gradually decreases with increasing photon energy. The first escape peak, redshifted by 511 keV with respect to the full energy peak, only contains $\approx 1\%$ of the incident photons. The second escape peak is highly suppressed, as the probability of at least one of the escaping 511 keV photons generating a veto trigger in the shielding is high. Each energy response also contains a 511 and 1022 keV line. Primary interactions of photons with the satellite material lead to the production of positron electron pairs. Their annihilation radiation is subsequently detected in the camera. The plateau between the first escape peak and the full energy peak is the Compton backscatter peak. The probability for detecting a photon with energies between the Compton edge and the full energy peak does not decrease to zero. Multiple, subsequent interactions of one incident photon in the detectors are counted as one event. Therefore, the cumulative energy deposition of one photon can be higher than the energy deposited in one Compton backscattering.

The energy redistribution is applied to the spectrum in Figure 6.6. In SPI data analysis, the spectrum is extracted per separate energy bin. For the incident flux in each energy bin the effect of energy redistribution is accounted for by utilizing a pseudo effective area, which is the convolution of the physical detection area of each detector with the full energy peak efficiency. The full energy peak efficiency is therefore already accounted for in SPI data analysis. For the calculation the full energy peak efficiency is scaled to unity. The redistribution spectrum is calculated for the 5 strongest lines in the spectrum at 4.4, 5.2, 6.1, 6.9 and 7.1 MeV with the respective energy responses. First, the integral flux of each line is convolved with the energy response to produce a redistribution spectrum per 5 keV energy bin. In this spectrum the full energy peak and the escape peaks appear as sharply defined fluxes in one bin (cf. Figure A.1). To account for the kinematic broadening of the lines in the input spectrum (model 1), the flux per energy bin is re-distributed according to a Gaus-

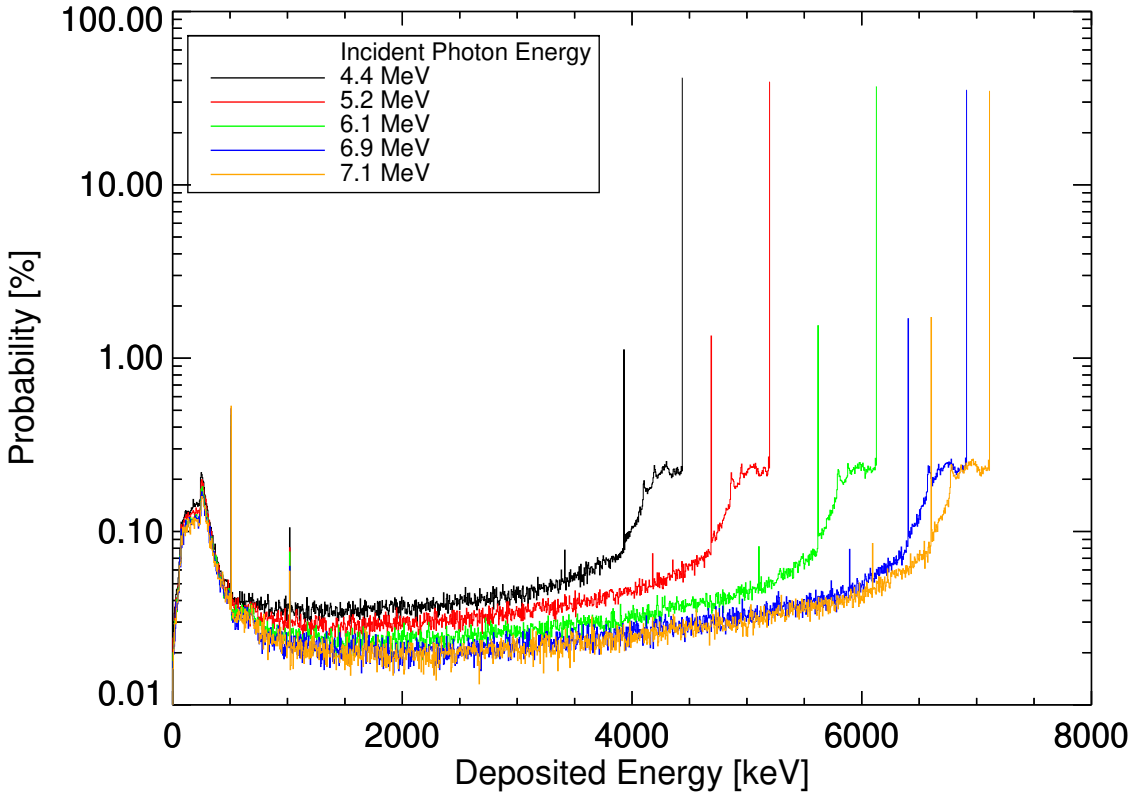

Figure 6.8: Energy response of SPI's camera in 5 keV bins. Each response was simulated with $\approx 5\times10^5$ photons. The ordinate shows the probability for each of the incident photons to be measured in the range of the energy bins respective 5 keV width. The energy response was simulated for the 5 incident photon energies of 4.4, 5.2, 6.1, 6.9 and 7.1 MeV. The narrow 511 keV line is present in all responses, similar to the 1.022 MeV line. For the simulated incident photon energies, the full energy peak efficiency varies between 35% (7.1 MeV) and 41% (4.4 MeV).

sian distribution with the width of the input line (e.g. 40 keV for the 4434 keV line). The redistributed flux is added to the primary spectrum, shown in Figure 6.9. For illustration purposes, the redistributed spectrum of each line is shown without the flux contained in the full energy peak. The first and second escape peaks, which are sharply defined characteristics in Figure 6.8, in each spectrum are blurred with the width of the respective de-excitation line.

The redistribution of photons to lower energies has a distinct effect on the simulated spectrum. Each of the strong, high energy lines produces a Compton continuum that extends down to several hundred keV. The sum of these continua increases the strength of the primary continuum. The superposition of the broadened escape peaks and the Compton backscatter plateaus lead to an increase of the total continuum by a factor of a few with respect to the primary continuum (cf. Figure 6.9, red vs. black line) specifically in the energy range above $\approx$ 3 MeV. This effect partially fills the valleys between the individual strong lines. The peak fluxes of the strongest de-excitation lines at 4.4, 6.1 and 6.9 MeV, respectively, remain at a level approximately one to two orders of magnitude above the increased continuum. The detectability of the strongest lines above the continuum is not impaired.
It is pointed out, that the flux in the 6.9 MeV line can be enhanced by the redistributed photons. The position of the Compton edge of scattered 7.1 MeV photons is similar to the

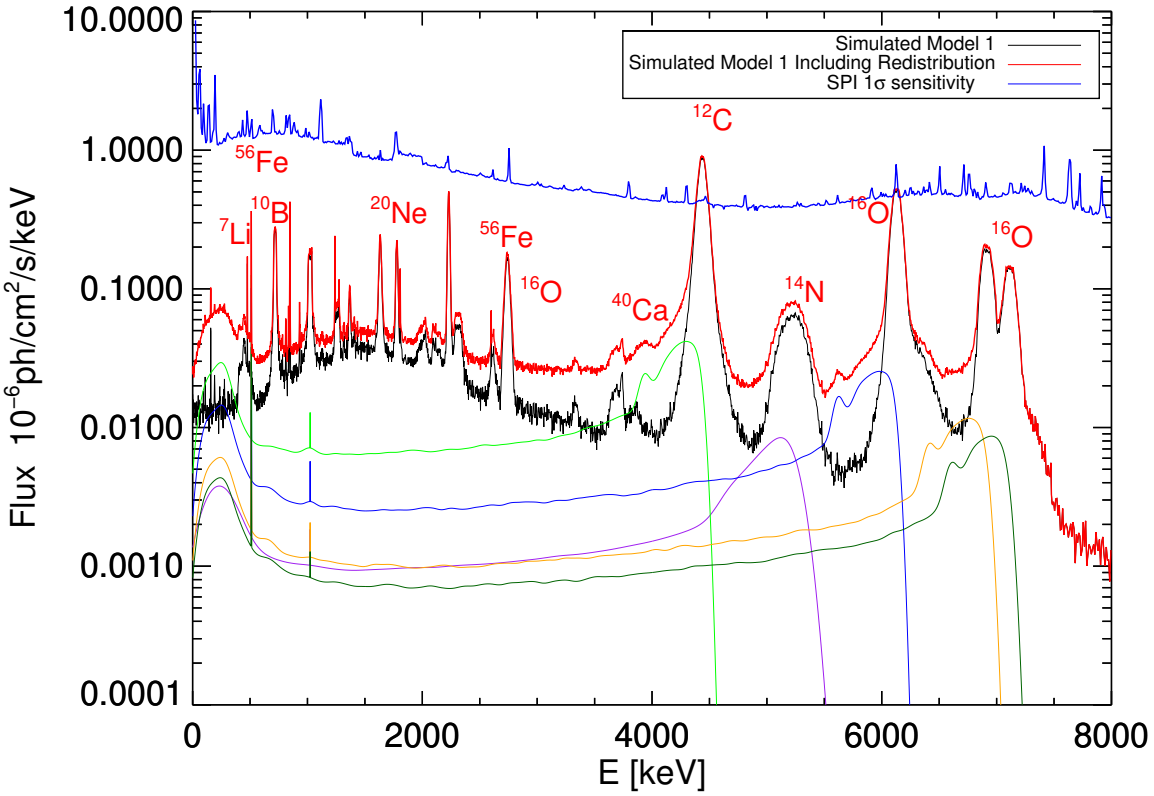

Figure 6.9: Similar to Figure 6.10. The five strongest lines in the spectrum are convolved with the energy dependent energy response of the camera. The individual contribution of each line to the flux at lower energies because of flux redistribution are indicated in green (4.4 MeV), purple (5.2 MeV), blue (6.1 MeV), orange (6.9 MeV) and dark green (7.1 MeV). The total spectrum, which is the sum of the simulated spectrum and the redistributed spectra is shown in red. The total spectrum fills the gaps between the individual lines.

peak position of the 6.9 MeV line. As the effective area and the celestial detector pattern at 6.9 and 7.1 MeV are similar, scattered 7.1 MeV photons can spuriously be attributed to the 6.9 MeV line. For the spectrum in Figure 6.9, the impact of this effect on the 6.9 MeV line is estimated to be $\approx 10\%$.

The apparent line at 6.9 MeV in the SPI spectrum is further discussed. As indicated above, the energy dispersion of the 7.1 MeV line to the 6.9 MeV line has no significant effect on the flux ratio between the 6.1 and the 6.9 MeV and 4.4 MeV lines, respectively. If the 6.9 MeV line were emitted in Cas A, both other lines necessarily would be above the detection threshold within SPI's sensitivity. An astrophysical origin of the 6.9 MeV line is therefore unlikely. This is in agreement with the low significance of the line of 2.6σ, suggesting that the apparent emission around 6.9 MeV is due to statistical fluctuations.

Neither of the above discussed hypotheses can explain the discrepancy between the non-detection of the lines and the high expected flux in model 1. Other environmental issues at the SNR's location could lead to a blending of the broadened lines into the statistical noise. These effects are investigated by modeling the CR nuclear de-excitation spectrum in the following section.

6.4 Modeling the De-Excitation Flux

To further investigate the discrepancy, the entire nuclear de-excitation spectrum in SPI's energy range is re-simulated. For this purpose, the Monte-Carlo code (cf. section 2.7.5), developed by Ramaty et al. (1979)[1] and revised for updated interaction cross sections (Kozlovsky et al. 2002), is used. The code is applied to the specific case of Cas A.

As the code's setup is one-dimensional, the distribution of the ejecta in the interaction region with CR particles is assumed to be homogeneous in Cas A. Inhomogeneities and variations in the chemical abundances of the ejecta are initially not taken into account. The obtained spectra are representative for the average fluxes produced by a smooth ejecta distribution. To obtain a highly resolved photon spectrum, the Monte Carlo simulation is conducted with 10^7 photons. The resulting photon spectrum is binned into 2300 individual energy bins, with an energy dependent bin width between 2 and 5 keV. On average, each bin contains ≈ 4000 photons.

Besides the above mentioned considerations, the code is further based on the following assumption. The abundance ratios of the elements mainly contributing to the de-excitation emission are normalized to hydrogen as ambient gas in the input file. Here, the composition of the interacting medium consists of material ejected during the progenitor stars Wolf-Rayet phase and synthesized during the SN explosion (Lingenfelter 2019). The remnant's elemental abundances are determined from X-ray data (Willingale et al. 2002) of Cas A, which are normalized to the silicon abundance with respect to the solar values of the silicon to hydrogen ratio. Optical measurements (Chevalier & Kirshner 1979) of the solar abundance ratios are used to obtain the required abundance ratios of the elements with respect to hydrogen in Cas A (see Table 6.2). Acceleration of electrons to TeV energies is assumed to occur mainly at the reverse shock (Helder & Vink 2008; Ahnen et al. 2017). The reverse shock at a radius of 1.71 pc (1.52–2.01 pc; Micelotta et al. 2016) is assigned as the location of proton and ion acceleration as well as the interaction region for nuclear excitation. The elemental abundances of the accelerated CRs are normalized to the accelerated proton abundances. The chemical composition of the CRs are inferred from Engelmann et al. (1990). The velocity distribution of the accelerated particles is assumed to be isotropic in the interaction region.

In the SPI spectrum, no line that could be attributed to the de-excitation of $^{12}C^*$ at 4.4 MeV is found, even though this line is predicted to contribute the strongest flux in model 1. It is pointed out here, however, that the de-excitation spectrum in model 1 was simulated assuming highly favorable conditions for the production of nuclear de-excitation radiation. The simulation was conducted assuming an average density of carbon atoms $n_C = 10\,cm^{-3}$. Several studies of the Cas A remnant structure have indicated, that dense ejecta clouds are present in the remnant (Sutherland & Dopita 1995; Docenko & Sunyaev 2010). The material in these clouds are mainly the products of nuclear burning in the interior of the preceding ccSN explosion. It is possible that elevated particle densities of specific nuclear species (such as carbon or oxygen) are present in the dense clouds of ejected material. However, the simulation for model 1 was conducted for a smooth particle distribution, that does not take into account dense knots of ejecta. Specifically in the case of model 1 a spherically symmet-

[1] http://lheawww.gsfc.nasa.gov/users/ramaty/code.htm

Table 6.2: Abundance mass ratios for most common elements in Cas A given as $\log_{10} \frac{n_A}{n_B}$. Here, n_X is number of particles per unit volume of elements A and B. First column are the elements, second column are the solar abundance ratios with respect to hydrogen (Lodders 2003), third column are abundance ratios in Cas A relative so silicon and relative to solar values (Chevalier & Kirshner 1979; Willingale et al. 2002). The last column contains the required abundance ratios with respect to hydrogen in Cas A.

Element A	Solar Abundance Ratio relativ to H	Cas A Abundance Ratio relative to Si and Solar	Cas A Abundance Ratio relative to H
H	0	2.29×10^{-5}	0
He	-1.08	4.93×10^{-5}	-1.08
C	-3.53	1.76	-1.77
O	-3.29	1.69	-1.60
Ne	-3.85	0.24	-3.61
Mg	-4.44	0.16	-4.28
Si	-4.49	0	-3.39
S	-4.85	1.25	-3.60
Ar	-5.50	1.38	-4.12
Ca	-5.68	1.46	-4.22
Fe	-4.52	0.4	-4.12

ric ejecta structure was assumed. As the composition of the ejecta is fully governed by the predetermined chemical abundance ratios, a carbon atom density of $n_C = 10\,cm^{-3}$ translates into a hydrogen particle density of $n_H \approx 600\,cm^{-3}$ in the remnant. The high hydrogen particle density is not supported by observations. Literature values for the smooth ejecta density are in the range of $n_H \approx 10\,cm^{-3}$ (Laming & Hwang 2003; Micelotta et al. 2016; Ahnen et al. 2017). This overestimate of the particle densities reflects in an overestimate of the expected line fluxes, as the strengths of the lines are dependent on the number of available target particles in the interaction region.

To determine the detectability of CR-induced de-excitation lines in Cas A, the simulation of the spectrum is repeated for smooth post shock ejecta conditions. The simulation (model 2) is conducted assuming a smooth particle density of $n_H \approx 10\,cm^{-3}$. The particle densities for the remaining elements are calculated assuming the abundance ratios given in table 6.2. For comparability with model 1 the same spectral shape as in Summa et al. (2011) is assumed for the accelerated particles. The spectrum follows a power law with index -2.3 (Abdo et al. 2010) and the energy contained in LECRs with $E_{kin,LECR} \leq 30\,MeV$ is $2 \times 10^{50}\,erg$, which constitutes $\approx 10\%$ of the SN's kinetic energy of $2 \times 10^{51}\,erg$ (Laming & Hwang 2003).
The resulting spectrum is shown in Figure 6.10. The kinematics of the inelastic scattering processes lead to a significant broadening of the de-excitation lines, especially in the energy range above $\approx 2\,MeV$ with line widths of up to 100 keV FWHM. Additionally, the unresolved emission due to the superposition of a multitude of significantly broadened de-excitation lines of heavy elements ($Z \geq 10$) is included in the spectrum, leading to an underlying continuum-like flux component. Furthermore, the emission from long term radioactive isotopes is included, such that some lines contain several components. Emission at 847 keV originates from the de-excitation of ^{56}Fe (cf. Table A.2). This excited state can be produced either by direct excitation of stable ^{56}Fe, present in the remnant, or by decay of CR

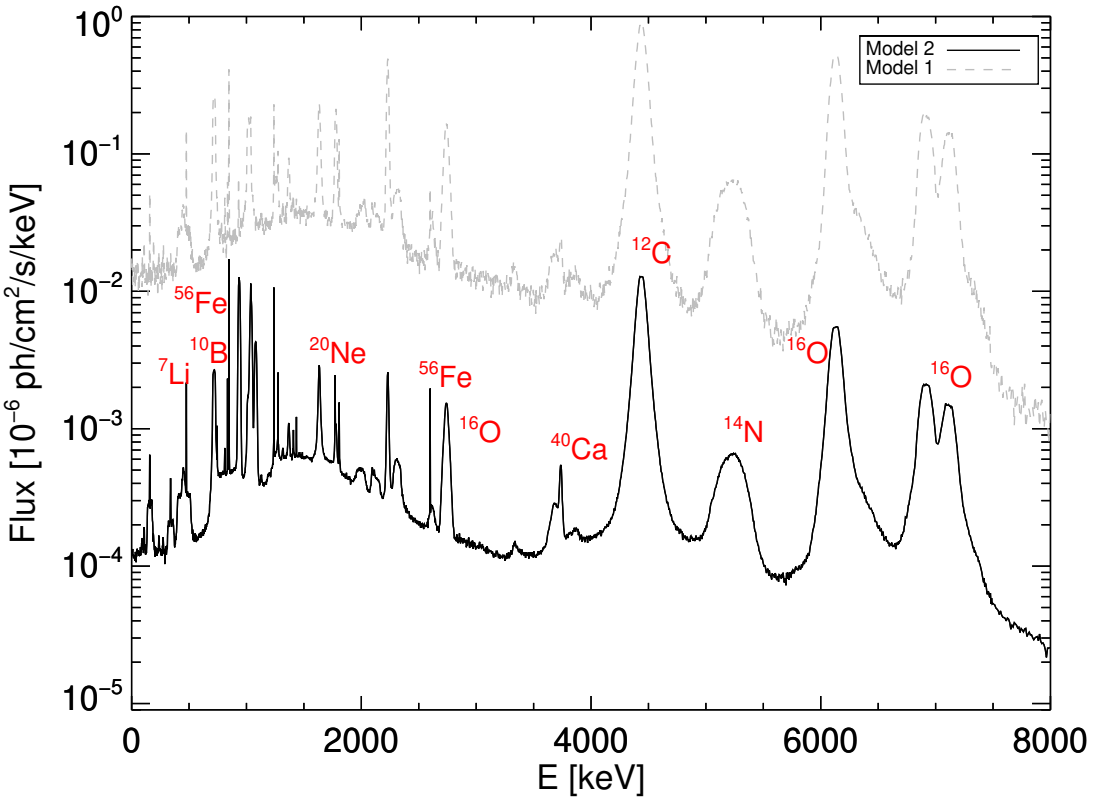

Figure 6.10: Simulated CR de-excitation spectrum of Cas A for an accelerated proton spectrum following a power law with index -2.3. A total of 10^7 photons are binned in energy intervals between 2 and 5 keV (Ramaty et al. 1979), similar to SPI's energy resolution at the respective energies (cf. Table 4.2). Model 1 is included for comparison as gray dashed line to indicate the large difference in the predicted line intensities.

interaction produced ^{56}Co with a half live of 77.2 d. The first mechanism produces the narrow component, the latter leads to the very narrow component. The line complex around $\approx$ 478 keV is introduced from the interactions

$$\alpha + \alpha \rightarrow {}^{7}\mathrm{Be} + \mathrm{n} \tag{6.10}$$

$$\alpha + \alpha \rightarrow {}^{7}\mathrm{Li} + \mathrm{p}. \tag{6.11}$$

Both nuclei are produced in an excited state, that promptly decay under emission of a 429 keV and a 478 keV photon, respectively, leading to two narrow components. ^{7}Be subsequently decays to ^{7}Li with a half-life of 53.2 d (NNDC 2020). The isotope has sufficient time to slow down and emit decay radiation at rest with respect to the surrounding medium (very narrow component). Line broadening and peak shift induced by the kinematics of the SN ejecta is not considered in the simulation. Note here, that contributions from NTB and synchrotron continua (cf. section 6.1) are not included in the spectrum.

The expected fluxes in the various strong de-excitation lines for model 2 are given in table 6.3. The fluxes in the lines are consistently lower by a factor of $\approx$ 60 with respect to the expected line fluxes in table 6.1. This is consistent with the adoption of a hydrogen density in the re-iterated spectrum, that is roughly a factor of 60 lower than in the initial, optimistic

simulation of model 1. The integrated fluxes in all lines are several orders of magnitude lower than SPI's sensitivity in the respective energy regions.

Neither of the two models can fully explain the high energy spectrum detected in SPI data. In model 1, the emission was assumed to originate from a high density matter, whose composition follows the ambient composition of ejecta in the shock region. While this model accounts to some extent for the broken power law continuum found in SPI data mainly between 1 and 3 MeV, it simultaneously would predict a high de-excitation flux in lines from ^{12}C and ^{16}O, incompatible with the observations. At the other extreme, the interaction of CRs in a fully diluted medium with a low ambient particle density (model 2) would explain the non-detection of nuclear de-excitation lines. However, the model cannot account for the continuum in SPI data.

Table 6.3: Same as 6.1. However, the expected fluxes are taken from the spectrum simulated with a smooth hydrogen particle density of $n_H \approx 10\,cm^{-3}$. The expected lines fluxes are significantly below the detection limit.

Isotope	Line Energy [keV]	Line FWHM [keV]	Flux Limit [10^{-5}ph cm^{-2} s^{-1}]	Expected Flux [10^{-7}ph cm^{-2} s^{-1}]
^{10}B	718	28	9.5	0.7
^{56}Fe	847	4	4.6	0.1
^{10}B	1022	26	8.8	0.2
^{20}Ne	1634	25	5.8	0.5
^{14}N	1635	Blend		
^{28}Si	1779	18	6.7	0.1
^{30}Si	2235	20	5.5	0.4
^{24}Mg	2742	52	7.1	0.7
^{16}O	2754	Blend		
^{12}C	4434	91	4.9	15.0
^{15}N	5269; 5298	232	7.7	1.4
^{16}O	6129	130	5.2	6.8
^{16}O	6917	135	6.3	2.9
^{16}O	7115	135	7.1	2.1

Within the framework of the simulations, a rather specific solution can be found, that would simultaneously account for the non-detection of lines, while on the other hand explaining the existent continuum. As indicated above, the reverse shock region is assumed as the location of particle acceleration and interaction. The reverse shock has progressed deep enough into the interior of the remnant, that dense clumps of ejecta, composed of nucleosynthesis material and unburnt heavier elements with $Z \geq 6$ are consumed by the shock. The density in these clumps can be $\approx 100 - 300$ particles cm^{-3} (Micelotta et al. 2016, ; and references therein), roughly one order of magnitude higher than in the diluted, smooth ejecta, and the abundance ratios can be significantly shifted towards heavier elements. For the specific solution (model 3), solely the intersections between the dense clumps and the reverse shock are assigned as the region of acceleration of CRs and the interaction of CRs with ambient, highly dense material. The simulated spectrum is then only a snapshot of currently occur-

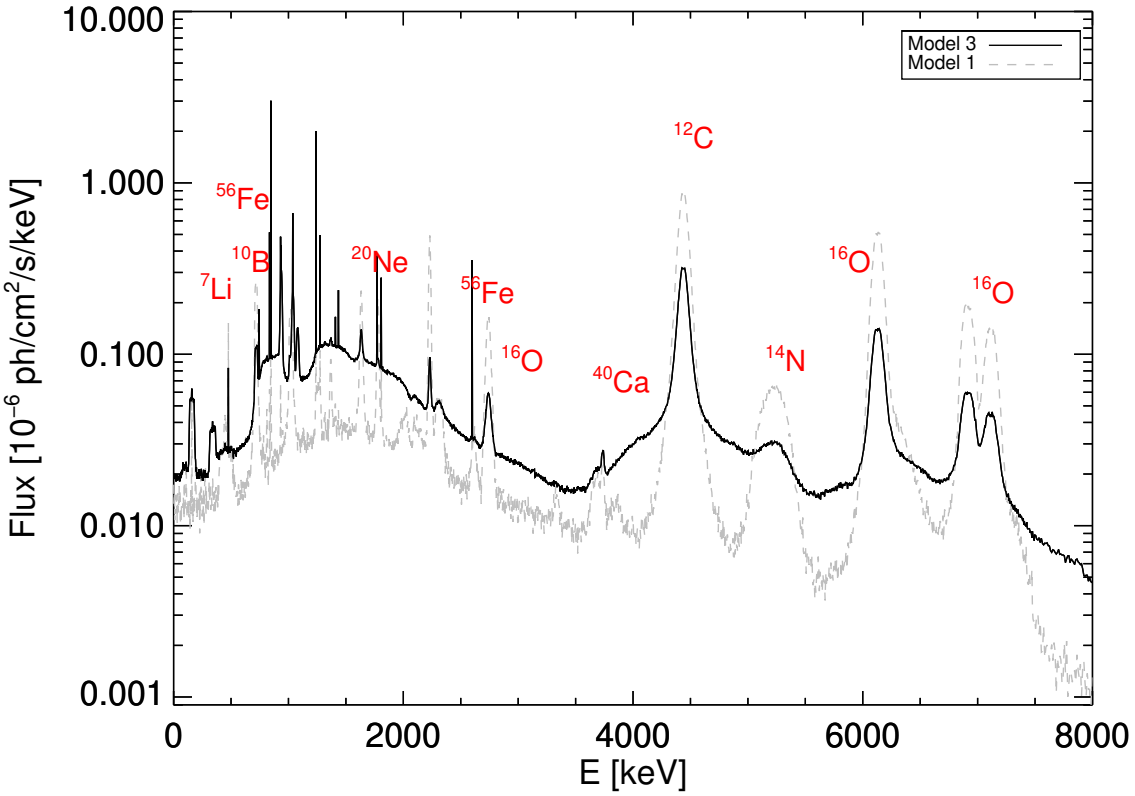

Figure 6.11: Simulated CR de-excitation spectrum of Cas A assuming an acceleration and excitation of lines in dense ejecta knots with enhanced heavy element abundances (see text). The majority of lines consist of a narrow and enhanced broad component, due to inverse scatterings of accelerated heavy nuclei on ambient hydrogen. The superposition of broad and unresolved lines leads to a continuum like emission, similar to the detected continuum in SPI data.

ring acceleration and interaction, as the composition of elements and ambient density is time-variable. This assumption allows, that the chemical composition and the density are not dependent on the determined abundance ratio in table 6.2. For model 3, the parameters are altered. For hydrogen, a particle density of $n_H = 100\,cm^{-3}$ is adopted, assuming that ambient hydrogen is piled up by the dense ejecta clumps. The ambient oxygen particle density is set to $n_O = 10\,cm^{-3}$, which is an increase by a factor of ≈ 40 with respect to the oxygen density in the smooth, homogeneous post shock medium. All other heavy element densities are scaled accordingly. As the acceleration region is now set solely to this specific region, it is assumed that the accelerated particles also contain an increased fraction of heavy elements. The abundances of the CRs are scaled accordingly.

The simulated spectrum is shown in Figure 6.11. The shape of the spectrum with respect to models 1 and 2 is considerably different now. All lines, that are not from radioactive decay, consist of two distinct components, a narrow one and a broad one. This is exemplified for the excitation of the ^{12}C level at 4.4 MeV by protons. The narrow component is introduced by the scattering of a CR proton on ^{12}C (^{12}C(p, p′)^{12}C*) that are approximately at rest with respect to the observer. The transfer of momentum from the proton to the interaction partner is small, so that the scattered, excited ^{12}C moves with a low velocity with respect to the

observer. This leads to a *small* kinematic broadening of the line of approximately 100 keV FWHM, i.e. a narrow component. This is the component of the 4.4 MeV line identified in model 1 and 2 (cf. tables 6.1 and 6.3). The broad component is introduced by the reverse interaction, where an accelerated ^{12}C is excited by scattering of an ambient proton ($p(^{12}C,^{12}C^{*})p'$). The CR particle retains most of its momentum and is at a high velocity with respect to the observer, resulting in a broadened line ($\approx$ 400 keV FWHM). This component of the lines is existent in models 1 and 2 as well, however, it is significantly enhanced in model 3 as the abundance of heavy CR particles is increased. The strong enhancement of the continuum component around 2 MeV is the result of superimposed, enhanced, broad lines, including the lines visible in the spectrum and additional transitions in heavy nuclei.
The model additionally contains several very narrow lines from the decay of produced radioactive isotopes, that apparently are above the detection limit in the respective energy regime. Note here, that these are modeled as Delta functions in the simulation, as the long lived isotopes are assumed to be at rest in the medium at the time of decay. In SPI data, these lines would appear broadened by the expansion velocity of the ejecta, similar to the ^{44}Ti decay lines. The broadened lines are below the detection limit.
The integrated fluxes in all individual emission lines above 3 MeV is below the 3σ upper limit in the respective energy range. The individual lines with the highest integrated flux are the two 4.4 MeV lines. The narrow component contains an integrated flux of 1.5×10^{-5} ph cm^{-2} s^{-1}, the broad components contains 1.8×10^{-5} ph cm^{-2} s^{-1}.

In addition to the lines, the continuum emission is described with the broken power-law model (cf. equation 6.1). The smoothness parameter for the break is modeled with 0.1. The power law indices before and after the break are $\lambda_{1,\mathrm{model3}} = -0.9$ and $\lambda_{2,\mathrm{model3}} = 2.3$. The normalization at 1 MeV is $N_{0,\mathrm{model3}} = 6.0 \times 10^{-8}$ ph cm^{-2} s^{-1} keV^{-1}. The break in the spectrum is at 1600 keV. These values are in agreement with the values of the best fit broken power law, fitted to the SPI data. Model 3 reproduces the main features of the SPI spectrum well. The normalization and therefore the energy contained in the spectrum below 3 MeV is lower than in the SPI spectrum. A further increase in the abundance of heavy elements in the composition of the CRs would further increase the total energy of the continuum emission, while the narrow line components are not significantly increased.

An identification of the SPI continuum with the superposition of unresolved nuclear de-excitation lines self-consistently explains the large difference between the flux in the 10^5-10^7 eV range and the low flux at $\approx 10^8$ eV (cf. Figure 6.3). In the energy region above 10 MeV no more strong transition lines are present. The continuum rapidly decreases approximately following a power law with an index of -8 (cf. Figure 6.12). A minor plateau is present around 15 MeV, caused by the broad component of a high level transition in ^{12}C at 15.1 MeV. The average flux level in this plateau is of the order of 10^{-10} ph cm^{-2} s^{-1} keV^{-1}, which is three orders of magnitude lower than the flux in SPI's energy range below 8 MeV. Above approximately 20 MeV the de-excitation flux shows a further steep decline. At and above 100 MeV, the de-excitation flux does not contribute significantly to the SED of Cas A and is subdominant to the NTB, IC and pion decay flux. The extended de-excitation continuum is compatible with the observed highest γ-ray emission above 100 MeV.

Model 3 is based on speculative assumptions, that describe the presence of a continuum in the SPI spectrum and the simultaneous absence of strong emission lines. So far, the location

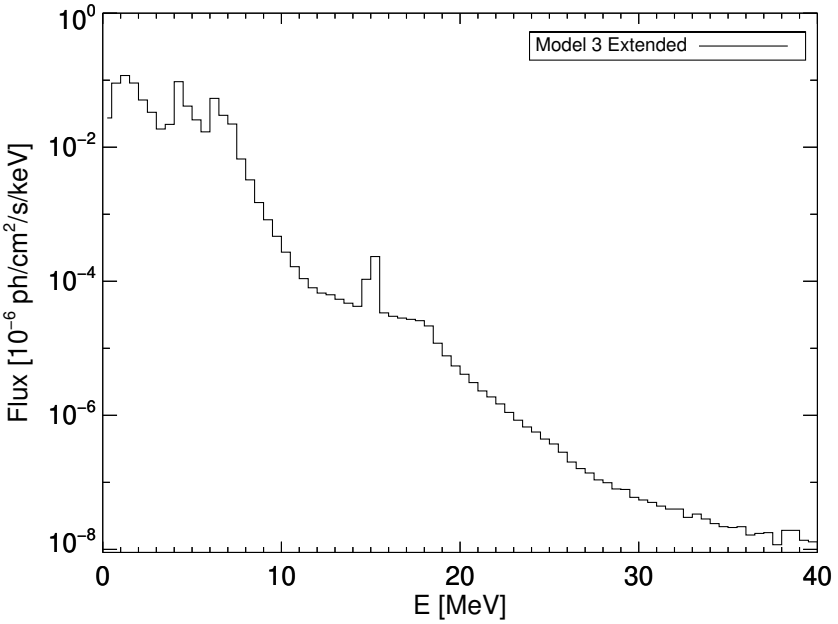

Figure 6.12: Extended nuclear de-excitation spectrum up to 40 MeV. The spectrum is binned into 500 keV bins. The input parameters of the model are identical to model 3. The steep decline of the continuum flux above 8 MeV is caused by the lack of strong, high-level de-excitation lines. The plateau around 15 MeV is due to a transition line in ^{12}C.

of proton and ion acceleration in the Cas A remnant could not be identified. Neither of the very high energy γ-ray telescopes, detecting the radiation of neutral pion decay, has the necessary angular resolution to pin point the location (Albert et al. 2007; Atwood et al. 2009; Kumar & VERITAS Collaboration 2015). Emission of a thin X-ray emitting shell, however, suggests that at least electrons are accelerated at the location of the reverse shock (Rho et al. 2003; Helder & Vink 2008; Uchiyama & Aharonian 2008). The presence of a continuum at MeV energies in SPI data can be interpreted as substantiation of simultaneous acceleration of hadrons at the same location. An overabundance of accelerated ions in the CR composition (with respect to the standard CR composition (Engelmann et al. 1990)) would produce a continuum like emission at low MeV energies from the overlap of several broadened and unresolved lines emitted specifically by these ions. The assumption of overabundant ions is based on the interaction of dense ejecta clumps with the reverse shock at the present stage of the SNR's evolution. With the present limited sensitivity of SPI the composition of the interaction region and the accelerated CRs cannot be further constrained. This would additionally require the direct detection of several de-excitation lines from various isotopes. The absolute line ratios could then be utilized to constrain the abundances of isotopes. The ratio between the broad and the narrow component in the lines could further be utilized to constrain the isotope ratios in the CRs. It is pointed out, that in the highly unfavorable case of particle interaction in a fully diluted, smooth ejecta composition, the detection of lines would require an increase in sensitivity of almost two orders of magnitude. For the scenario assumed in model 3, the required increase in sensitivity for the detection of several strong lines is in the range of approximately one order of magnitude. This underlines the importance of proposed future γ-ray missions with enhanced sensitivity, such as e-ASTROGAM (de Angelis et al. 2018), COSI (Tomsick et al. 2019) or AMEGO (McEnery et al. 2019).

6.5 Contribution of Cosmic Ray Induced Radiation to Nucleosynthesis Tracing Radioactivities

6.5.1 Extended ^{26}Al Emission

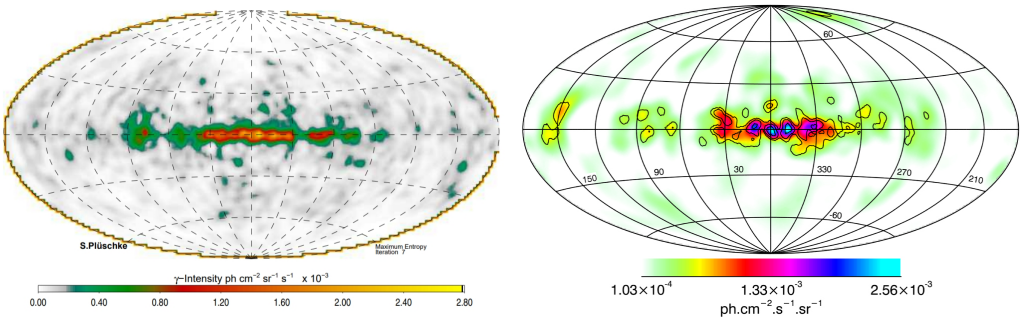

Figure 6.13: ^{26}Al all sky maps deconvolved from COMPTEL data (left: Plüschke et al. 2001) and INTEGRAL/SPI data (right: Bouchet et al. 2015) using a maximum entropy method.

The isotope ^{26}Al traces the ongoing nucleosynthesis in the Galaxy over timescales of several millions years due to its half-life of 717 kyr (NNDC 2020). The production of ^{26}Al is linked to all H burning sites, such as nuclear burning in massive stars, novae and SNe. The production cycle recycles ^{25}Mg, produced in previous stellar populations via ^{25}Mg(p,γ)^{26}Al. The most prominent production site of ^{26}Al are massive stars ($10\,M_\odot \leq M_{ZAMS} \leq 100\,M_\odot$) and their ccSNe (Diehl et al. 2006b). To a lesser extent, novae also contribute to the total production. The steady production of ^{26}Al in a multiplicity of sources leads to a stable ^{26}Al content in the Galaxy, traceable through its decay signature at 1.809 MeV (e.g. Diehl et al. 2006a; Siegert 2017; Pleintinger et al. 2019).
Due to the long half-life time of ^{26}Al, the majority of ^{26}Al from a single production site decays after it has been mixed with the ejecta from other individual sources. As a consequence, the Galaxy wide decay signal at 1.809 MeV cannot be linked to a single production site but traces the history of massive star formation, SN occurrence, and OB associations throughout the Milky Way (e.g. Diehl et al. 2006a). The first full sky map of the ^{26}Al emission was obtained from COMPTEL data, accumulating 9 yr of observation time (see Figure 6.13, Oberlack et al. (1996); Plüschke et al. (2001)). It shows a clumpy distribution of 1.8 MeV emission along the Galactic plane. An updated map of the Galactic ^{26}Al in the Galaxy was constructed from SPI data, showing a similar distribution of ^{26}Al in the Galactic plane (Bouchet et al. 2015). The integrated flux as observed with SPI in the 1.8 MeV line is $(17.1 \pm 0.6) \times 10^{-4}$ ph cm^{-2} s^{-1}, and the line has a FWHM of (3.2 ± 0.1) keV (Pleintinger 2020). Assuming a 3D density distribution for the Galactic ^{26}Al distribution, the flux can be converted into a total mass of radioactive ^{26}Al and a Galactic ccSN rate (e.g. Diehl et al. 2006a).
These quantities are deduced under the assumptions, that the entire emission in the 1.8 MeV line is solely due to the decay of ^{26}Al, produced in massive stars. This estimate neglects the potential influence of CR excited ^{26}Mg and the production of radioactive ^{26}Al through CR spallation at SN shocks and in the interstellar medium.

To determine the SNR contribution to the Galaxy wide 1.8 MeV line from CR-induced reactions, I estimate the flux under the assumptions:
1.) All ccSN remnants have the same CR spectrum, regardless of their age.
2.) The masses and chemical compositions of the CR interaction regions in the SNe's shocks are uniform, neglecting influences of the initial stellar mass on the SNR.
The flux contribution of one SNR is calculated from a single model, here using the example of Cas A. The flux in the vicinity of the 1.8 MeV line is evaluated from the simulated nuclear de-excitation spectrum of model 3. The de-excitation flux in this region around the 1.8 MeV line contains an unresolved component, a broadened component from $^{26}Mg^{*}$ de-excitation and a narrow component from ^{26}Al decay. The $^{26}Mg^{*}$ de-excitation flux is calculated by integrating the simulated spectrum over the energy range 1806–1812 keV, in agreement with the 2σ width of SPI's Galaxy wide 1.8 MeV line of 3 keV, containing 95% of the lines flux. The integrated flux of these components is $F_{1.8\,MeV} = 1.1 \times 10^{-6}\,ph\,cm^{-2}\,s^{-1}$.
The Galaxy wide flux is estimated from the flux of this single SNR multiplied with the total number of Galactic SNRs. As the correct number of SNRs in the Milky Way is not known, the total number of SNRs is estimated to be in the range between $N_{SNR} = 250 - 1500$. According to the Green catalog (Green 2019), a total number of 294 SNRs are identified in the Milky Way. On average, 85% of all SNe are ccSNe, which suggests an approximate number of 250 known ccSN remnants in the Milky Way. As the catalog is most likely incomplete due to a bias in radio observations, this number is treated as the minimum number of ccSN remnants in the Galaxy. For a ccSN rate of 2–3 explosions per century in the Milky Way (cf. section 5.3.6), an approximate number of 1000-1500 ccSN remnants should be present in the Galaxy with an age of less than 50000 yr. The average flux per SNR at Earth is lower than $F_{1.8\,MeV}$, as the average distance to a SNR is 10 kpc (cf. section 5.3.5.1) instead of 3.3 kpc (Cas A). Taking into account assumptions 1) and 2), and correcting the flux for the average distance, the total contribution of CR-induced nuclear de-excitation to the Galaxy wide 1.8 MeV flux is

$$F_{1.8\,MeV,CR} = N_{SNR} \times F_{1.8,cor} = (0.3 - 1.8) \times 10^{-4}\,ph\,cm^{-2}\,s^{-1}. \quad (6.12)$$

This constitutes between 1.4 and 8.6% of the Galactic observed 1.8 MeV flux. One should note here, that the nuclear de-excitation contribution is estimated from the emission of a single SNR at the upper limit. In model 3, the radioactive ^{26}Al decay flux is enhanced, as it is a byproduct of spallation reactions on - probably overabundant - isotopes with similar mass number. However, the production of excited ^{26}Mg is not limited to the shock fronts of SNRs, but can also occur in the interstellar medium (cf. Benhabiles-Mezhoud et al. 2013). It is possible that up to 10% of the 1.8 MeV line are contributed by CR excitation, and consequently, the steady state mass of ^{26}Al, originating in massive star nucleosynthesis, is reduced, as indicated by population synthesis simulations of massive star groups (Pleintinger 2020).

6.5.2 ^{44}Ca Excitation in Supernovae

In section 5.1.4 a potential enhancement of the flux in the ^{44}Sc decay line at 1157 keV from the excitation of $^{44}Ca^{*}$ was suggested. With the insight gained in the previous sections, the CR-induced flux in the $^{44}Ca^{*}$ de-excitation is evaluated. The flux in this line is estimated utilizing equation 6.5. The relevant reactions for production of a 1157 keV photon are $^{44}Ca(p,p\gamma)^{44}Ca^{*}$, relevant at proton energies up to $\approx$ 5 MeV, and $^{44}Ca(p,n)^{44}Sc$ with a

cross section of $\approx$ 600 mb in the energy range 5–10 MeV (Mitchell et al. 1982; Levkovski 1991).

At an age of 340 yr, 98% of the synthesized ^{44}Ti in Cas A has already decayed to stable ^{44}Ca. In the estimate, direct production of stable ^{44}Ca in the ccSN explosion is neglected, and the mass of currently present ^{44}Ca in the remnant is assumed to be identical to the ejected radioactive ^{44}Ti mass, corrected for the remaining 2%. For the particle density of ^{44}Ca, I assume that the entire amount of ^{44}Ca is evenly distributed in the interaction region with an ambient density of 5×10^{-5} ^{44}Ca atoms cm^{-3}. The flux in the 1157 keV line would then be increased with respect to the 78 keV decay-only-line by

$$F_{1157\,\mathrm{keV,CR}} = 1.7 \times 10^{-8}\,\mathrm{ph\,cm^{-2}\,s^{-1}}, \tag{6.13}$$

which is several orders of magnitude lower than the measured flux discrepancy of 8.4×10^{-5} ph cm^{-2} s^{-1} (c.f. Table 5.5). To account for the missing flux, it can be speculated that the ^{44}Ca density in the remnant is considerably higher, which could be explained when the outward moving blast wave has accumulated sufficient ^{44}Ca from the circumstellar medium. However, the required mass would then be in the order of 10^{-1} M$_\odot$ ^{44}Ca, which would significantly increase the abundance ratio of Ca in the remnant or the total mass in the interaction region. Neither of these assumptions appear very plausible. The first can be disproved by the observation of the abundance ratio in X-rays (c.f. Table 6.2). The second would lead to a detectable signal in other CR-induced nuclear de-excitation lines, such as the de-excitation lines at 4.4, 6.1, 6.9, and 7.1 MeV from ^{16}O, as the mass of ^{16}O in the interaction region would be significantly higher when the abundance ratios are preserved. Therefore, the presence of an increased ^{44}Ca mass is unlikely and cannot explain the flux offset in the 1157 keV line. As a final remark it should be noted here that the morphology of the CR interaction region might be significantly different than assumed in the simple treatment here, and a more localized acceleration and excitation in smaller and denser ejecta clumps could be responsible for the increased flux.

Chapter 7

Summary and Conclusion

This thesis was dedicated to analyzing SNRs in the young remnant phase in order to gain new insights into the driving mechanism of these explosions and their long term influence on the Galactic CR population. For that purpose, γ-ray measurements with the SPectrometer on INTEGRAL were utilized to assess the emission of radioactively decaying isotopes, synthesized in SN explosions. As the number of radioactive decay bright SNRs seems limited, a survey of the Galactic plane for previously unknown SNRs, that shine bright in ^{44}Ti decay radiation was conducted. The results of this survey were utilized to estimate a Galactic ccSN rate. To assess the robustness of the ccSN explosions mechanism, the results from the survey were compared to theoretical predictions from the populations synthesis code PSYCO. The study was utilized to constrain the recurrence rates of SN explosions of both core collapse and thermonuclear nature. The contribution of SNe to the Galactic CR content was analyzed from their excitation of nuclear transition lines in the ambient medium of the SNR. A Monte Carlo simulation technique was utilized to produce synthetic γ-ray spectra of CR-induced nuclear lines.

The explosion mechanism of SNe was investigated for the six youngest, close by SNRs in the vicinity of Earth by analyzing their decay signature of synthesized radioactive material. A significant detection of ^{44}Ti decay emission was found only in the remnant of Cas A. An analysis of the combined decay emission in all three strong decay lines of the ^{44}Ti decay chain revealed an integrated flux of $(4.2 \pm 1.0) \times 10^{-5}\,\mathrm{ph\,cm^{-2}\,s^{-1}}$, which translates into an ejected ^{44}Ti mass of $(2.6 \pm 0.6)\,\mathrm{M_\odot}$. The detected line is broadened with respect to the instrumental resolution at the respective energies, which is attributed to a Doppler broadening of the line due to the expansion of the ejecta containing ^{44}Ti. The width of the line translates into an expansion velocity of these ejecta of $(6400 \pm 1900)\,\mathrm{km\,s^{-1}}$. A measured Doppler shift of the line peak positions to energies lower than the determined laboratory energies suggests a bulk motion of the ejecta away from the observer. Both the high mass of the synthesized ^{44}Ti and the kinematic properties of the ejected material are incompatible with spherically symmetric ccSN explosions. Quite contrary to this, the result corroborates the induction of violent motion in the neutrino heating zone, leading to large scale asymmetric in and outflows of material close to the proto-NS in ccSNe. In the remaining ccSN remnants, no emission in the ^{44}Ti decay chain could be detected. The determined upper flux limits and inferred ejecta masses are compatible with canonical ccSNe ^{44}Ti ejecta masses, considering the remnants ages and distances. Likewise, upper flux limits were determined for three type Ia SNe in the Milky Way. The inferred limits on the ^{44}Ti ejecta masses indicate, that all three

explosions belong to the group of Chandrasekhar mass explosions, as other models would suggest ^{44}Ti nucleosynthesis yields, that are significantly higher.

Due to the low number of known, young SNRs in the Milky Way, an inherent bias was introduced when searching for ^{44}Ti only in these remnants. While the results presented in this thesis suggest specific scenarios for Cas A and the three type Ia explosions, due to the low number of analyzed remnants, it cannot be excluded that these three objects belong to an exceptional branch of their respective type, while the remaining population is characterized by an entirely different behavior. To circumvent this bias, the robustness of the mechanism is tested in the Milky Way, as especially a stable production of ^{44}Ti in ccSNe is expected to produce several detectable remnants. A survey for such previously unknown ^{44}Ti bright remnants in the Galaxy was conducted. The survey was concentrated on the Galactic plane region with latitudes $|b| \leq 18°$, where it reaches an unprecedented sensitivity of $5 \times 10^{-6}\,\mathrm{ph\,cm^{-2}\,s^{-1}}$ in the Galactic Center. Nine locations, that show an excess flux in the vicinity of the three decay lines with a significance of more than 3σ were identified in the survey. One position is identical with the location of Cas A. As the survey is governed by count statistics, and limited by the angular resolution of SPI, a total number of 8.1 statistical fluctuation, that mimic ^{44}Ti decay with a significance above 3σ were expected. The detection of eight *new* sources is largely compatible with statistical fluctuations, and the decay mimicking signal showed an inconsistent behavior in the three separate lines for the majority of the new sources. Further SPI exposure on the locations is required to confirm a potential new source.

To investigate the compatibility of our theoretical understanding of nucleosynthesis processes and their feedback on the Galaxy with findings of the survey, a bottom-up approach of modeling the ^{44}Ti emission in the Galaxy was investigated. The PSYCO code, utilized in this thesis, simulates a distribution of ^{44}Ti bright SNRs in the Galaxy by following the evolution of individual massive stars throughout their life span up to their explosion as ccSNe. Modeling results consistently suggest, that only moderate star formation rates of $2 - 4\,\mathrm{M_\odot\,yr^{-1}}$ are allowed to explain the observed distribution of ^{44}Ti bright SNRs.

A unified picture of fingerprints from SNe in the Galaxy can be gathered from combining the analysis of individual SNRs and the Galaxy wide scarcity of ^{44}Ti emission. Two independent, but consistent measures in this thesis constrain the ccSN recurrence rate to ≤ 3.2 explosions per century from the detection of only one remnant in a limited volume, and to the range of $\approx 1 - 2$ explosions per century from a compatibility argument of observation and simulated distribution. While the understanding gathered in this thesis favors asymmetric models for the explosions of ccSNe, that self-consistently reproduce the solar abundance ratios of ^{44}Ca to ^{56}Fe, it has also become evident, that ccSNe alone cannot be the sole producers of ^{44}Ca in the Milky Way. The convolution of the ejecta mass with the apparent ccSN recurrence rate leads to a ^{44}Ca production rate, that falls short by one order of magnitude. This gap can be filled by a rarely occurring subtype of thermonuclear SNe, that synthesize an exceptionally high amount of ^{44}Ti. However, the probability of their occurrence with respect to all type Ia explosions can be constrained to be less than 28%, to mediate their overproduction of ^{44}Ti with respect to ^{56}Ni. Thus, more than one scenario is required to explain the observed diversity of type Ia explosions.

The link between the acceleration of electrons in SNR shocks and their electromagnetic signature has long been established. In this thesis, the scenario for proton and ion acceleration in the identical sites was investigated by searching for an electromagnetic signature induced in hadronic CR collisions with the ambient medium. For that purpose, a self-consistent background model was developed for the high energy range of SPI, including single and double detector events. The background model was successfully calibrated on the Crab nebula.

The Cas A remnant was analyzed for CR-induced nuclear de-excitation signatures in the broad energy range covered by SPI between 100 keV and 8 MeV. A significant excess flux in the energy range above 1 MeV can only be explained by the presence of unresolved nuclear de-excitation lines, whose superposition produces a continuum-like emission. The unresolved continuum requires, however, that CR acceleration in Cas A occurs under highly specific conditions, not necessarily representative for the standard CR acceleration scenario. The presence of the unresolved component in Cas A involves implications for other radioactive tracers of nucleosynthesis feedback into the Galaxy. Flux excess in lines, that was previously assumed to solely originate from radioactive decay of isotopes synthesized in nuclear burning, may need to be corrected for the contribution of CR-induced excitation.

Unraveling the appearance of guest stars has provided mankind with a long standing mystery. From challenging the idea of an unchanging night sky, to understanding their influence on the evolution of the Universe, the understanding of SNe has progressed a long way over the recent history of humankind. In this thesis, pieces of the puzzle that are SNe were added by observing their inherent emission in hard X-ray and soft γ-ray bands from the emission of nuclear transition lines. Even though valuable information was gained on the explosion mechanism, SNe's chemical imprints on the Galaxy, and the origin of CRs, the task of fully understanding the nature of SNe can never be completed by one astrophysicist alone. While each piece gained will add to complete the puzzle, it will surely take a few, or maybe even a few hundred years more to fully solve the mystery. And even then, the author dares to proclaim one persistent truth: Supernovae; what a magnificent sight they are to behold!

Appendix A

Additional Figures and Tables

Stellar Nuclear Burning in Hydrostatic Equilibrium

A detailed list of nuclear fusion processes occurring during the evolution of a massive star ($M_* \geq 8\,M_\odot$) is given in Table A.1.
Once the star reaches the later burning stages towards heavier nuclei, the central region cannot be efficiently cooled anymore by the emission of photons. The evolution of the star further speeds up, as the central fusion processes are highly dependent on the central temperature and the amount of nuclear fuel decreases. Furthermore, the energy released in the fusion processes continuously decreases with higher atomic mass number, which makes burning of fuel less efficient. In addition, the production of neutrinos from thermal processes in the star's core increases. In contrast to photons, neutrinos can readily escape from the star, carrying away energy that needs to be compensated by an increased energy production rate. While the hydrogen burning phase of a star can last for several billion years, the timescale for the later fusion processes decreases, lasting only for several hundred days or less (Woosley et al. 2002). Due to this rapid evolution the central region decouples from the evolution of the stars surface.

Table A.1: List of the main nuclear burning reactions and cycle in stars. For the majority of a stars lifetime, the proton proton chains (pp-chains) are the dominant energy sources. The energy production by pp fusion characterizes the main sequence of all stars, as this fusion process is also available for low mass stars, that cannot reach sufficient central temperatures to start ensuing fusion processes. In addition, the minimum required mass and the temperature region for which the respective processes are dominant is included. Dominant reactions from Woosley et al. (2002); Unsöld & Baschek (2002); Lugaro & Chieffi (2011); Thielemann et al. (2011)

ppI-chain; $M \geq 0.08\,M_\odot$; $10\,MK \leq T \leq 14\,MK$ Energy Production : 26.7 MeV	ppII-chain; $M \geq 0.08\,M_\odot$; $14\,MK \leq T \leq 23\,MK$ Energy Production: 25.7 MeV	ppIII-chain; $M \geq 0.08\,M_\odot$; $23\,MK \leq T$ Energy Production: 19.3 MeV
$p + p \rightarrow d + e^+$ $p + d \rightarrow {}^3He$	${}^3He + \alpha \rightarrow {}^7Be$ ${}^3He + {}^3He \rightarrow \alpha + 2p$ ${}^7Be + e^- \rightarrow {}^7Li + \nu_e$ ${}^7Li + p \rightarrow 2\alpha$	${}^3He + \alpha \rightarrow {}^7Be$ ${}^7Be + p \rightarrow {}^8B$ ${}^8B \rightarrow {}^8Be + e^+ + \nu_e \rightarrow 2\alpha$
CNO Main Cycle; $M \geq 1.3\,M_\odot$; $T \geq 20\,MK$ Energy Production : 25.0 MeV	Triple-α process; $M \geq 0.5\,M_\odot$; $T \gtrsim 100\,MK$ Energy Production 7.3 MeV	Carbon Fusion; $M \gtrsim 7\,M_\odot$; $T \gtrsim 500\,MK$ Energy Production: in brackets
${}^{12}C + p \rightarrow {}^{13}N$ ${}^{13}N \rightarrow {}^{13}C + e^+ + \nu_e$ ${}^{13}C + p \rightarrow {}^{14}N$ ${}^{14}N + p \rightarrow {}^{15}O$ ${}^{15}O \rightarrow {}^{15}N + e^+ + \nu_e$ ${}^{15}N\ p \rightarrow {}^{12}C + \alpha$	$\alpha + \alpha \rightarrow {}^8Be$ (unstable) ${}^8Be + \alpha \rightarrow {}^{12}C$	${}^{12}C + \alpha \rightarrow {}^{16}O$ ${}^{12}C + {}^{12}C \rightarrow {}^{23}Na + p$ ${}^{12}C + {}^{12}C \rightarrow {}^{20}Ne + \alpha$ ${}^{23}Na + p \rightarrow {}^{20}Ne + \alpha$ ${}^{23}Na + p \rightarrow {}^{24}Mg$
Neon Fusion; $M \gtrsim 9\,M_\odot$; $T \gtrsim 120\,MK$	Oxygen Fusion; $M \gtrsim 9\,M_\odot$; $T \gtrsim 200\,MK$	Silicon Fusion; $M \gtrsim 9\,M_\odot$; $T \gtrsim 2700\,MK$
${}^{20}Ne + \gamma \rightarrow {}^{16}O + \alpha$ ${}^{20}Ne + \alpha \rightarrow {}^{24}Mg$ ${}^{24}Mg + \alpha \rightarrow {}^{28}Si$	${}^{16}O + {}^{16}O \rightarrow {}^{28}Si + \alpha$ ${}^{16}O + {}^{16}O \rightarrow {}^{31}S + n$ ${}^{16}O + {}^{16}O \rightarrow {}^{31}P + p$ ${}^{31}S \rightarrow {}^{31}P + e^+ + \nu_e$	${}^{28}Si + {}^{28}Si \rightarrow {}^{56}Ni$ ${}^{28}Si + (1\text{–}7)\ \alpha \rightarrow {}^{32}S - {}^{56}Ni$

Cosmic Ray Induced De-Excitation Lines

Table A.2: Cosmic ray induced de-excitation lines from the most abundant isotopes in SNRs. First column contains the line energy in MeV, second column is the level transition in the isotope, including the level energy in MeV, third column contains the level producing nuclear reaction. The last column contains the mean life time of the nuclear levels. While the majority of lines are prompt emission, some lines are produced from radioactive decay with long half-life times. Values adopted from Kozlovsky et al. (2002).

Energy [MeV]	Level Transition	Nuclear Reaction	Level Lifetime [s]
0.092	^{55}Fe*1.408→ ^{55}Fe*1.317	^{56}Fe(p, x)^{55}Fe*	5.5×10^{-11}
0.110	^{19}F*0.110→ g.s.	^{20}Ne(p, x)^{19}F*	8.5×10^{-10}
0.158	^{56}Co*0.158→ g.s.	^{56}Fe(p, n)^{56}Co*	1.4×10^{-10}
0.197	^{19}F*0.197→ g.s.	^{20}Ne(p, x)^{19}F*	1.3×10^{-7}
0.238	^{19}Ne*0.238→ g.s.	^{20}Ne(p, x)^{19}Ne*	2.6×10^{-8}
0.275	^{19}Ne*0.275→ g.s.	^{20}Ne(p, x)^{19}Ne*	6.1×10^{-11}
0.339	^{59}Ni*0.339→ g.s.	^{56}Fe(α , n)^{59}Ni*	9.8×10^{-11}
0.411	^{55}Fe*0.411→ g.s.	^{56}Fe(p, x)^{55}Fe*	8.7×10^{-12}
0.429	^{7}Be*0.429→ g.s.	^{4}He(α , n)^{7}Be*	1.9×10^{-13}
0.440	^{23}Na*0.440→ g.s.	^{20}Ne(α , p)^{23}Na* ^{24}Mg(p, x)^{23}Na*	1.6×10^{-12} 1.6×10^{-12}
0.451	^{23}Mg*0.451→ g.s.	^{24}Mg(p, x)^{23}Mg*	1.8×10^{-12}
0.477	^{55}Fe*1.408→ ^{55}Fe*0.931	^{56}Fe(p, x)^{55}Fe* ^{56}Fe(p, x)^{55}Co(e^{+}, ϵ)^{55}Fe*	5.5×10^{-11} 9.1×10^{4}
0.478	^{7}Li*0.478→ g.s.	^{4}He(α , p)^{7}Li* ^{4}He(α , n)^{7}Be(ϵ)	1.1×10^{-13} 6.64×10^{6}
0.718	^{10}B$^{*0.718}$→ g.s.	^{12}C(p, x)^{10}B* ^{12}C(p, x)^{10}C(ϵ)^{10}B* ^{16}O(p, x)^{10}B*	1.0×10^{-9} 27.8 1.0×10^{-9}
0.744	^{52}Cr*3.114→ ^{52}Cr*2.370	^{56}Fe(p, x)^{52}Cr* ^{56}Fe(p, x)^{52}Mn(e^{+}, ϵ)^{52}Cr*	6.0×10^{-11} 7.0×10^{5}
0.781	^{27}Si*0.781→ g.s.	^{28}Si(p, x)^{27}Si*	5.0×10^{-11}
0.812	^{56}Co*0.970→ ^{56}Co*0.158	^{56}Fe(p, n)^{56}Co*	1.7×10^{-13}
0.835	^{54}Cr*0.835→ g.s.	^{56}Fe(p, x)^{54}Mn(e^{+}, ϵ)^{54}Cr*	3.9×10^{7}
0.844	^{27}Al*0.844→ g.s.	^{28}Si(p, x)^{27}Al*	5.0×10^{-11}
0.847	^{56}Fe*0.847→ g.s.	^{56}Fe(p, p$'$)^{56}Fe* ^{56}Fe(α , α $'$)^{56}Fe* ^{56}Fe(p, n)^{56}Co(e^{+}, ϵ)^{56}Fe*	8.9×10^{-12} 8.9×10^{-12} 9.6×10^{6}
0.891	^{22}Na*0.891→ g.s.	^{24}Mg(p, x)^{22}Na*	1.4×10^{-11}
0.931	^{55}Fe*0.931→ g.s.	^{56}Fe(p, x)^{55}Fe* ^{56}Fe(p, x)^{55}Co(e^{+}, ϵ)^{55}Fe*	1.2×10^{-11} 9.1×10^{4}
0.936	^{52}Cr*2.370→ ^{52}Cr*1.434	^{56}Fe(p, x)^{52}Mn(e^{+}, ϵ)^{52}Cr*	7.0×10^{5}
0.937	^{18}F*0.937→ g.s.	^{16}O(^{3}He, p)^{18}F*	6.8×10^{-11}
0.957	^{27}Si*0.957→ g.s.	^{28}Si(p, x)^{27}Si*	1.7×10^{-12}
0.984	^{48}Ti*0.984→ g.s.	^{56}Fe(p, x)^{48}Ti*	6.2×10^{-12}

0.999	^{59}Ni*1.338→ ^{59}Ni*0.339	^{56}Fe(α , n)^{59}Ni*	1.4×10^{-12}
1.005	^{58}Ni*2.459 → ^{58}Ni*1.454	^{56}Fe(α , x)^{58}Ni*	$\geq 1.4 \times 10^{-12}$
1.014	^{27}Al*1.014 → g.s.	^{27}Al(p, p′)^{27}Al*	2.1×10^{-12}
		^{28}Si(p, x)^{27}Al*	2.1×10^{-12}
1.022	^{10}B*1.740 → ^{10}B*0.718	^{12}C(p, x)^{10}B*	7.5×10^{-15}
		^{16}O(p, x)^{10}B*	7.5×10^{-15}
1.038	^{56}Fe*3.123 → ^{56}Fe*2.085	^{56}Fe(p, n)^{56}Co(e$^+$, ϵ)^{56}Fe*	9.6×10^{6}
1.042	^{18}F*1.042 → g.s.	^{16}O(^{3}He, p)^{18}F*	2.6×10^{-15}
1.049	^{58}Co*1.049 → g.s.	^{56}Fe(α , x)^{58}Co*	2.2×10^{-13}
1.081	^{18}F*1.081 → g.s.	^{16}O(^{3}He, p)^{18}F*	2.8×10^{-14}
1.130	^{54}Fe*2.538 → ^{54}Fe*1.408	^{56}Fe(p, x)^{54}Fe*	5.8×10^{-12}
1.189	^{59}Ni*1.189 → g.s.	^{56}Fe(α , n)^{59}Ni*	3.3×10^{-13}
1.190	^{59}Co*1.190 → g.s.	^{56}Fe(α , p)^{59}Co*	7.5×10^{-14}
1.223	^{55}Fe*2.539 → ^{55}Fe*1.317	^{56}Fe(p, x)^{55}Fe*	1.3×10^{-11}
1.238	^{56}Fe*2.085 → ^{56}Fe*0.847	^{56}Fe(p, p′)^{56}Fe*	9.2×10^{-13}
		^{56}Fe(α , α ′)^{56}Fe*	9.2×10^{-13}
		^{56}Fe(p, n)^{56}Co(e$^+$, ϵ)^{56}Fe*	9.6×10^{6}
1.249	^{31}S*1.249 → g.s.	^{32}S(p, x)^{31}S*	3.5×10^{-13}
1.266	^{31}P*1.266 → g.s.	^{32}S(p, x)^{31}P*	7.5×10^{-13}
		^{28}Si(α , p)^{31}P*	7.5×10^{-13}
1.275	^{22}Ne*1.275 → g.s.	^{22}Ne(p, p′)^{22}Ne*	5.2×10^{-12}
		^{22}Ne(α , α ′)^{22}Ne*	5.2×10^{-12}
1.312	^{48}Ti*2.296 → ^{48}Ti*0.984	^{56}Fe(p, x)^{48}Ti*	1.8×10^{-12}
1.317	^{55}Fe*1.317 → g.s.	^{56}Fe(p, x)^{55}Fe*	3.0×10^{-12}
1.334	^{52}Cr*2.768 → ^{52}Cr*1.434	^{56}Fe(p, x)^{52}Cr*	3.6×10^{-12}
1.367	^{59}Ni*2.705 → ^{59}Ni*1.338	^{56}Fe(α , n)^{59}Ni*	5.0×10^{-13}
1.369	^{24}Mg*1.369 → g.s.	^{24}Mg(p, p′)^{24}Mg*	2.0×10^{-12}
		^{25}Mg(p, pn)^{24}Mg*	2.0×10^{-12}
		^{26}Mg(p, p2n)^{24}Mg*	2.0×10^{-12}
		^{24}Mg(α , α ′)^{24}Mg*	2.0×10^{-12}
		^{28}Si(p, x)^{24}Mg*	2.0×10^{-12}
1.370	^{55}Fe*2.301 → ^{55}Fe*0.931	^{56}Fe(p, x)^{55}Fe*	8.7×10^{-13}
1.408	^{55}Fe*1.408 → g.s.	^{56}Fe(p, x)^{55}Fe*	5.5×10^{-11}
	^{54}Fe*1.408 → g.s.	^{56}Fe(p, x)^{54}Fe*	1.2×10^{-12}
		^{56}Fe(p, x)^{55}Co(e$^+$, ϵ)^{55}Fe*	9.1×10^{4}
1.428	^{59}Ni*1.767 → ^{59}Ni*0.339	^{56}Fe(α , n)^{59}Ni*	8.7×10^{-13}
1.434	^{52}Cr*1.434 → g.s.	^{56}Fe(p, x)^{52}Cr*	9.8×10^{-13}
		^{56}Fe(p, x)^{52}Mn(e$^+$, ϵ)^{52}Cr*	7.0×10^{5}
1.441	^{53}Mn*1.441 → g.s.	^{56}Fe(p, x)^{53}Mn*	8.7×10^{-13}
1.454	^{58}Ni*1.454→ g.s.	^{56}Fe(α , x)^{58}Ni*	9.3×10^{-13}
1.460	^{59}Co*1.460→ g.s.	^{56}Fe(α , p)^{59}Co*	1.5×10^{-12}
1.600	^{23}Mg*2.051→ ^{23}Mg*0.451	^{24}Mg(p, x)^{23}Mg*	2.9×10^{-14}
1.634	^{20}Ne*1.634→ g.s.	^{20}Ne(p, p′)^{20}Ne*	1.1×10^{-12}
		^{20}Ne(α , α ′)^{20}Ne*	1.1×10^{-12}
		^{24}Mg(p, x)^{20}Ne*	1.1×10^{-12}

		^{24}Mg(α , x)^{20}Ne*	1.1×10^{-12}
		^{28}Si(p, x)^{20}Ne*	1.1×10^{-12}
1.635	^{14}N*3.948→ ^{14}N*2.313	^{14}N(p, p$'$)^{14}N*	6.9×10^{-15}
		^{14}N(α , α $'$)^{14}N*	6.9×10^{-15}
		^{16}O(p, x)^{14}N*	6.9×10^{-15}
1.636	^{23}Na*2.076→ ^{23}Na*0.440	^{24}Mg(p, x)^{23}Na*	3.8×10^{-14}
		^{24}Mg(α , x)^{23}Na*	3.8×10^{-14}
1.771	^{56}Fe*3.856→ ^{56}Fe*2.085	^{56}Fe(p, p$'$)^{56}Fe*	3.6×10^{-14}
		^{56}Fe(p, n)^{56}Co(e$^+$, ϵ)^{56}Fe*	9.6×10^{6}
1.779	^{28}Si*1.779→ g.s.	^{28}Si(p, p$'$)^{28}Si*	6.9×10^{-13}
		^{28}Si(α , α $'$)^{28}Si*	6.9×10^{-13}
		^{32}S(p, x)^{28}Si*	6.9×10^{-13}
1.809	^{26}Mg*1.809→ g.s.	^{26}Mg(p, p$'$)^{26}Mg*	6.9×10^{-13}
		^{26}Mg(α , α $'$)^{26}Mg*	6.9×10^{-13}
		^{27}Al(p, x)^{26}Mg*	6.9×10^{-13}
1.811	^{56}Fe*2.658→ ^{56}Fe*0.847	^{56}Fe(p, p$'$)^{56}Fe*	3.0×10^{-14}
2.000	^{11}C*2.000→ g.s.	^{12}C(p, x)^{11}C*	1.0×10^{-14}
2.029	^{31}P*3.295→ ^{31}P*1.266	^{32}S(p, x)^{31}P*	5.5×10^{-14}
2.034	^{31}S*3.283→ ^{31}S*1.249	^{32}S(p, x)^{31}S*	...
2.094	^{56}Fe*.2.942→ ^{56}Fe*0.847	^{56}Fe(p, p$'$)^{56}Fe*	6.5×10^{-13}
2.113	^{56}Fe*2.960→ ^{56}Fe*0.847	^{56}Fe(p, p$'$)^{56}Fe*	4.0×10^{-14}
2.124	^{11}B*2.125→ g.s.	^{12}C(p, x)^{11}B*	5.5×10^{-15}
2.164	^{27}Si$^{2.164}$→ g.s.	^{28}Si(p, x)^{27}Si*	6.3×10^{-14}
2.211	^{27}Al*2.211→ g.s.	^{27}Al(α , α $'$)^{27}Al*	3.8×10^{-14}
		^{24}Mg(α , x)^{27}Al*	3.8×10^{-14}
		^{28}Si(p, x)^{27}Al*	3.8×10^{-14}
2.230	^{32}S*2.230→ g.s.	^{32}S(p, p$'$)^{32}S*	1.2×10^{-13}
		^{32}S(α , α $'$)^{32}S*	1.2×10^{-13}
2.232	^{31}S*2.232→ g.s.	^{32}S(p, x)^{31}S*	1.4×10^{-13}
2.234	^{31}P*2.234→ g.s.	^{32}S(p, x)^{31}P*	3.6×10^{-13}
		^{28}Si(α , p)^{31}P*	3.6×10^{-13}
2.235	^{30}Si*2.235→ g.s.	^{27}Al(α , x)^{30}Si*	3.6×10^{-13}
2.263	^{23}Na*2.704→ ^{23}Na*0.440	^{20}Ne(α , x)^{23}Na*	1.1×10^{-13}
2.313	^{14}N*2.313→ g.s.	^{14}N(p, p$'$)^{14}N*	9.8×10^{-14}
		^{14}N(α , α $'$)^{14}N*	9.8×10^{-14}
		^{14}N(p, n)^{14}O(e$^+$, ϵ)^{14}N*2.313	102
		^{16}O(p, x)^{14}N*	9.8×10^{-14}
2.598	^{56}Fe*3.449→ ^{56}Fe*0.847	^{56}Fe(p, n)^{56}Co(e$^+$, ϵ)^{56}Fe*	9.6×10^{6}
2.614	^{20}Ne*4.248→ ^{20}Ne*1.634	^{20}Ne(p, p$'$)^{20}Ne*	9.2×10^{-14}
		^{20}Ne(α , α $'$)^{20}Ne*	9.2×10^{-14}
		^{24}Mg(p, x)^{20}Ne*	9.2×10^{-14}
		^{28}Si(p, x)^{20}Ne*	9.2×10^{-14}
2.640	^{23}Na*2.640→ g.s.	^{24}Mg(p, x)^{23}Na*	9.7×10^{-14}
2.742	^{16}O*8.872→ ^{16}O*6.130	^{16}O(p, p$'$)^{16}O*	1.8×10^{-13}
		^{16}O(α , α $'$)^{16}O*	1.8×10^{-13}
2.754	^{24}Mg*4.123→ ^{24}Mg*1.369	^{24}Mg(p, p$'$)^{24}Mg*	3.5×10^{-14}

		^{25}Mg(p, pn)^{24}Mg*	3.5×10^{-14}
		^{26}Mg(p, p2n)^{24}Mg*	3.5×10^{-14}
		^{24}Mg(α , α')^{24}Mg*	3.5×10^{-14}
3.333	^{20}Ne*4.967→ ^{20}Ne*1.634	^{20}Ne(p, p$'$)^{20}Ne*	4.8×10^{-12}
		^{20}Ne(α , α')^{20}Ne*	4.8×10^{-12}
3.562	^{6}Li*3.563→ g.s.	^{4}He(α , pn)^{6}Li*	1.2×10^{-16}
		^{4}He(^{3}He, p)^{6}Li*	1.2×10^{-16}
3.684	^{13}C*3.685→ g.s.	^{13}C(p, p$'$)^{13}C*	1.6×10^{-15}
		^{13}C(α , α')^{13}C*	1.6×10^{-15}
		^{16}O(p, x)^{13}C*	1.6×10^{-15}
3.736	^{40}Ca*3.736→ g.s.	^{40}Ca(p, p$'$)^{40}Ca*	2.9×10^{-11}
		^{40}Ca(α , α')^{40}Ca*	2.9×10^{-11}
3.853	^{13}C*3.854→ g.s.	^{13}C(p, p$'$)^{13}C*	1.2×10^{-11}
		^{13}C(α , α')^{13}C*	1.2×10^{-11}
		^{16}O(p, x)^{13}C*	1.2×10^{-11}
4.438	^{12}C*4.439→ g.s.	^{12}C(p, p$'$)^{12}C*	6.1×10^{-14}
		^{12}C(α , α')^{12}C*	6.1×10^{-14}
		^{14}N(p, x)^{12}C*	6.1×10^{-14}
		^{14}N(α , x)^{12}C*	6.1×10^{-14}
		^{16}O(p, x)^{12}C*	6.1×10^{-14}
		^{16}O(α , x)^{12}C*	6.1×10^{-14}
4.444	^{11}B*4.445→ g.s.	^{12}C(p, 2p)^{11}B*	5.6×10^{-19}
		^{12}C(α , x)^{11}B*	5.6×10^{-19}
		^{14}N(p, x)^{11}B*	5.6×10^{-19}
		^{14}N(α , x)^{11}B*	5.6×10^{-19}
5.099	^{28}Si*6.879→ ^{28}Si*1.779	^{28}Si(p, p$'$)^{28}Si	1.2×10^{-12}
		^{28}Si(α , α')^{28}Si	1.2×10^{-12}
5.105	^{14}N*5.106→ g.s.	^{14}N(p, p$'$)^{14}N*	6.3×10^{-12}
		^{14}N(α , α')^{14}N*	6.3×10^{-12}
		^{16}O(p, x)^{14}N*	6.3×10^{-12}
		^{16}O(α , x)^{14}N*	6.3×10^{-12}
5.180	^{15}O$^{5.181}$→ g.s.	^{16}O(p, x)^{15}O*	$<4.9 \times 10^{-14}$
		^{16}O(α , x)^{15}O*	$<4.9 \times 10^{-14}$
5.240	^{15}O*5.241→ g.s.	^{12}C(α , x)^{15}O*	3.25×10^{-12}
		^{16}O(p, x)^{15}O*	3.25×10^{-12}
		^{16}O(α , x)^{15}O*	3.25×10^{-12}
5.269	^{15}N*5.270→ g.s.	^{12}C(α , x)^{15}N*	2.58×10^{-12}
		^{16}O(p, x)^{15}N*	2.58×10^{-12}
		^{16}O(α , x)^{15}N*	2.58×10^{-12}
5.298	^{15}N*5.299→ g.s.	^{16}O(p, x)^{15}N*	1.2×10^{-14}
		^{16}O(α , x)^{15}N*	1.2×10^{-14}
6.129	^{16}O*6.130→ g.s.	^{16}O(p, p$'$)^{16}O*	2.7×10^{-11}
		^{16}O(α , α')^{16}O*	2.7×10^{-11}
		^{20}Ne(p, x)^{16}O*	2.7×10^{-11}
6.175	^{15}O*6.176→ g.s.	^{16}O(p, x)^{15}O*	$<2.3 \times 10^{-14}$
6.322	^{15}N*6.324→ g.s.	^{16}O(p, x)^{15}N*	1.0×10^{-15}

6.337	^{11}C*6.339→ g.s.	^{12}C(p, x)^{11}C* ^{12}C(α , x)^{11}C*	$<1.1 \times 10^{-13}$ $<1.1 \times 10^{-13}$
6.476	^{11}C*6.478→ g.s.	^{12}C(p, x)^{11}C* ^{12}C(α , x)^{11}C*	$<8.7 \times 10^{-15}$ $<8.7 \times 10^{-15}$
6.741	^{11}B*6.743→ g.s.	^{12}C(p, x)^{11}B* ^{12}C(α , x)^{11}B*	4.3×10^{-20} 4.3×10^{-20}
6.790	^{11}B*6.792→ g.s.	^{12}C(p, x)^{11}B* ^{12}C(α , x)^{11}B*	5.6×10^{-19} 5.6×10^{-19}
6.879	^{28}Si*6.879→ g.s.	^{28}Si(p, p$'$)^{28}Si* ^{28}Si(α , α $'$)^{28}Si*	1.2×10^{-12} 1.2×10^{-12}
6.916	^{16}O*6.917→ g.s.	^{16}O(p, p$'$)^{16}O* ^{16}O(α , α $'$)^{16}O*	6.8×10^{-15} 6.8×10^{-15}
7.115	^{16}O*7.117→ g.s.	^{16}O(p, p$'$)^{16}O* ^{16}O(α , α $'$)^{16}O*	1.2×10^{-14} 1.2×10^{-14}
7.299	^{15}N*7.301→ g.s.	^{16}O(p, x)^{15}N* ^{16}O(α , x)^{15}N*	1.4×10^{-16} 1.4×10^{-16}
15.10	^{12}C*15.11→ g.s.	^{12}C(p, p$'$)^{12}C*	1.5×10^{-17}

Energy Redistribution

The energy redistribution applied in section 6.3 is exemplified for an artificial line at 4.4 MeV. The initial line (cf. Figure A.1, black line) is modeled with an amplitude of 1 ph cm^{-2} s^{-1} keV^{-1} at the centroid energy of 4434 keV. The 1σ width of the line is set to 50 keV, representative for kinematic broadening of the line. Initially, the integral flux of the line $F_i = 1.25 \times 10^2$ ph cm^{-2} s^{-1} is redistributed according to the redistribution matrix for the 4.4 MeV line shown in Figure 6.8 for 5 keV wide output bins. The full energy peak efficiency is not scaled to unity here. This produces sharply defined structures such as the full energy peak at 4434 keV, the 511 and 1022 keV annihilation lines and the first and second escape peak at 3923 and 3412 keV ontop of the general Compton continuum (cf. Figure A.1, red line). To account for the initial broadening of the line, the integral flux F_o in the output 5 keV bins is further redistributed. The integral flux F_o is distributed in a Gaussian with the width 50 keV of the initial 4.4 MeV line. This leads to a blurring of the sharply defined structures into extended lines (cf. Figure A.1, blue line). The second escape peak is blurred into the Compton continuum. The first escape peak can be identified as hump ontop of the Compton continuum centered at 3923 keV. It is pointed out, that the 511 and 1022 keV lines are only broadened with the instrumental resolution, as these lines are considered to be produced by positrons that annihilate at rest with respect to the instrument.

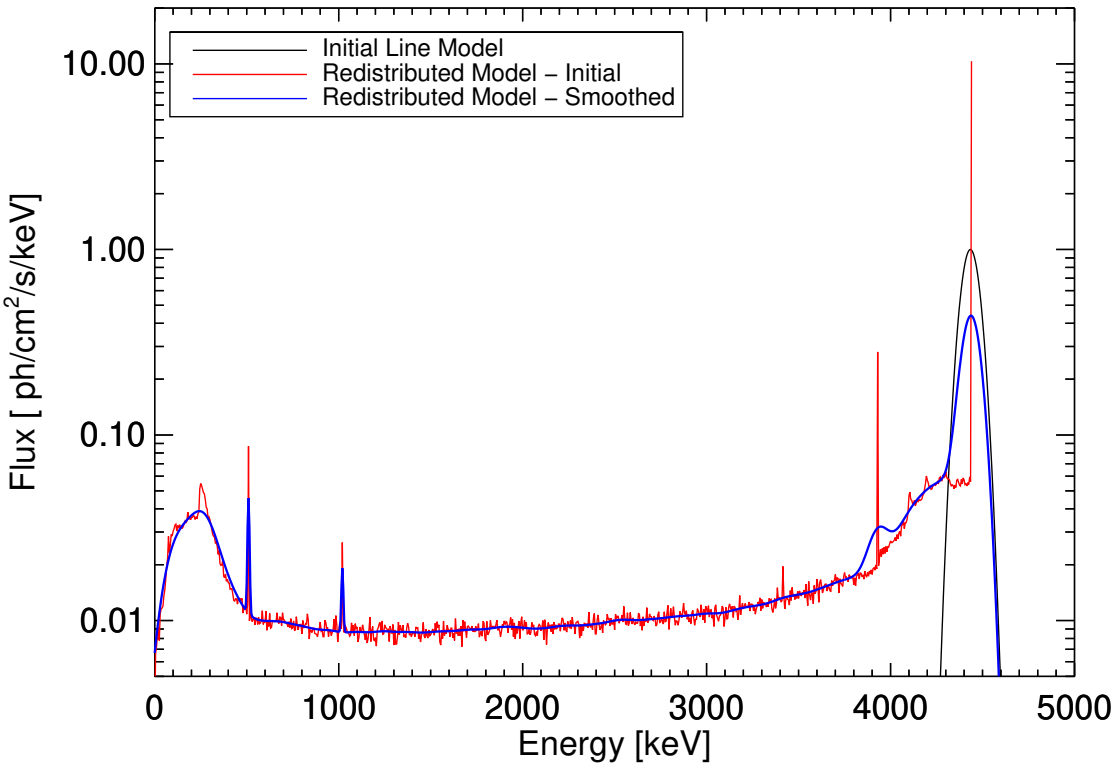

Figure A.1: Exemplified energy redistribution of the 4.4 MeV Line. The concept of redistribution is detailed in the text.

Appendix B

Bibliography

Abdo, A. A., Ackermann, M., Ajello, M., et al. 2010, The Astrophysical Journal, 710, L92
Abdo, A. A., Ackermann, M., Ajello, M., et al. 2011, The Astrophysical Journal, 734, 28
Acero, F., Ackermann, M., Ajello, M., et al. 2016, The Astrophysical Journal Supplement Series, 224, 8
Ackermann, M., Ajello, M., Allafort, A., et al. 2013, Science, 339, 807
Adams, S. M., Kochanek, C. S., Beacom, J. F., Vagins, M. R., & Stanek, K. Z. 2013, The Astrophysical Journal, 778, 164
Aharonian, F., Akhperjanian, A. G., Bazer-Bachi, A. R., et al. 2007, The Astrophysical Journal, 661, 236
Ahnen, M. L., Ansoldi, S., Antonelli, L. A., et al. 2017, Monthly Notices of the Royal Astronomical Society, 472, 2956
Alarie, A., Bilodeau, A., & Drissen, L. 2014, Monthly Notices of the Royal Astronomical Society, 441, 2996
Albert, J., Aliu, E., Anderhub, H., et al. 2007, Astronomy and Astrophysics, 474, 937
Albinson, J. S., Tuffs, R. J., Swinbank, E., & Gull, S. F. 1986, Monthly Notices of the Royal Astronomical Society, 219, 427
Allen, G. E., Chow, K., DeLaney, T., et al. 2014, The Astrophysical Journal, 798, 82
Allen, R. J. & Barrett, A. H. 1967, The Astrophysical Journal, 149, 1
Anders, E. & Grevesse, N. 1989, Geochimica et Cosmochimica Acta, 53, 197
Anderson, M., Rudnick, L., Leppik, P., Perley, R., & Braun, R. 1991, The Astrophysical Journal, 373, 146
Andrae, R., Schulze-Hartung, T., & Melchior, P. 2010, arXiv e-prints, arXiv:1012.3754
Angulo, C., Arnould, M., Rayet, M., et al. 1999, Nuclear Physics A, 656, 3
Araya, M. & Cui, W. 2010, The Astrophysical Journal, 720, 20
Arcones, A. & Thielemann, F. K. 2013, Journal of Physics G Nuclear Physics, 40, 013201
Arnett, W. D., Truran, J. W., & Woosley, S. E. 1971, The Astrophysical Journal, 165, 87
Asaoka, I., Egger, R., & Aschenbach, B. 1996, in Roentgenstrahlung from the Universe, ed. H. U. Zimmermann, J. Trümper, & H. Yorke, 233–234
Aschenbach, B. 1996, in Roentgenstrahlung from the Universe, ed. H. U. Zimmermann, J. Trümper, & H. Yorke, 213–220
Aschenbach, B. 1998, Nature, 396, 141
Aschenbach, B., Iyudin, A. F., & Schönfelder, V. 1999, Astronomy and Astrophysics, 350, 997
Attié, D., Cordier, B., Gros, M., et al. 2003, Astronomy & Astrophysics, 411, L71

Atwood, W. B., Abdo, A. A., Ackermann, M., et al. 2009, The Astrophysical Journal, 697, 1071
Audi, G., Kondev, F. G., Wang, M., Huang, W., & Naimi, S. 2017, Chinese Physics C, 41, 030001
Baade, W. & Zwicky, F. 1934a, Proceedings of the National Academy of Sciences, 20, 259
Baade, W. & Zwicky, F. 1934b, Physical Review, 46, 76
Badenes, C., Borkowski, K. J., Hughes, J. P., Hwang, U., & Bravo, E. 2006, The Astrophysical Journal, 645, 1373
Ballesteros-Paredes, J., Klessen, R. S., Mac Low, M. M., & Vazquez-Semadeni, E. 2007, in Protostars and Planets V, ed. B. Reipurth, D. Jewitt, & K. Keil, 63
Ballet, J. 2006, Advances in Space Research, 37, 1902
Bate, M. R. 2009, Monthly Notices of the RAS, 392, 590
Becker, W., Hurley-Walker, N., Weinberger, C., et al. 2021, Astronomy and Astrophysics, 648, A30
Bell, A. 2013, Astroparticle Physics, 43, 56
Bell, A. R. 1978, Monthly Notices of the Royal Astronomical Society, 182, 147
Bell, A. R., GULL, S. F., & KENDERDINE, S. 1975, Nature, 257, 463
Benhabiles-Mezhoud, H., Kiener, J., Tatischeff, V., & Strong, A. W. 2013, The Astrophysical Journal, 763, 98
Benjamin, R. A., Churchwell, E., Babler, B. L., et al. 2005, The Astrophysical Journal Letters, 630, L149
Berg, U., Wolf, H., Schäfer, B., & Wienhard, K. 1975, Nuclear Instruments and Methods, 129, 155
Bethe, H. A. & Wilson, J. R. 1985, The Astrophysical Journal, 295, 14
Bildsten, L., Shen, K. J., Weinberg, N. N., & Nelemans, G. 2007, The Astrophysical Journal, 662, L95
Bird, A. J., Bazzano, A., Malizia, A., et al. 2016, VizieR Online Data Catalog, J/ApJS/223/15
Blandford, R. D. & Ostriker, J. P. 1978, The Astrophysical Journal Letters, 221, L29
Blondin, J. M., Mezzacappa, A., & DeMarino, C. 2003, The Astrophysical Journal, 584, 971
Boggs, S. E., Harrison, F. A., Miyasaka, H., et al. 2015, Science, 348, 670
Bohlin, R. C., Savage, B. D., & Drake, J. F. 1978, The Astrophysical Journal, 224, 132
Boissier, S. & Prantzos, N. 2009, Astronomy and Astrophysics, 503, 137
Bombaci, I. 1996, Astronomy and Astrophysics, 305, 871
Bonnell, I. A., Larson, R. B., & Zinnecker, H. 2007, in Protostars and Planets V, ed. B. Reipurth, D. Jewitt, & K. Keil, 149
Borkowski, K. J., Reynolds, S. P., Green, D. A., et al. 2010, The Astrophysical Journal Letters, 724, L161
Borkowski, K. J., Reynolds, S. P., Hwang, U., et al. 2013, The Astrophysical Journal Letters, 771, L9
Bouchet, L., Jourdain, E., & Roques, J.-P. 2015, The Astrophysical Journal, 801, 142
Branch, D., Fisher, A., & Nugent, P. 1993, The Astronomical Journal, 106, 2383
Branch, D. & Tammann, G. A. 1992, Annual Review of Astronomy and Astrophysics, 30, 359
Bruenn, S. W., Mezzacappa, A., Hix, W. R., et al. 2013, The Astrophysical Journal, 767, L6
Burrows, A. 2013, Reviews of Modern Physics, 85, 245

Burrows, A., Hubbard, W. B., Lunine, J. I., & Liebert, J. 2001, Reviews of Modern Physics, 73, 719
Burrows, A. & Lattimer, J. M. 1985, The Astrophysical Journal, 299, L19
Burrows, A. & Lattimer, J. M. 1987, The Astrophysical Journal, 318, L63
Burrows, A., Radice, D., & Vartanyan, D. 2019, Monthly Notices of the Royal Astronomical Society, 485, 3153
Cappellaro, E., Evans, R., & Turatto, M. 1999, Astronomy & Astrophysics, 351, 459
Cappellaro, E., Turatto, M., Benetti, S., et al. 1993, Astronomy and Astrophysics, 273, 383
Caprioli, D., Blasi, P., & Amato, E. 2011, Astroparticle Physics, 34, 447
Caroli, E., Stephen, J. B., Cocco, G. D., Natalucci, L., & Spizzichino, A. 1987, Space Science Reviews, 45, 349
Cash, W. 1979, The Astrophysical Journal, 228, 939
Castellina, A. & Donato, F. 2013, Astrophysics of Galactic Charged Cosmic Rays, ed. T. D. Oswalt & G. Gilmore, Vol. 5, 725
Caughlan, G. R. & Fowler, W. A. 1988, Atomic Data and Nuclear Data Tables, 40, 283
Chabrier, G. 2003, Publications of the Astronomical Society of the Pacific, 115, 763
Chabrier, G. 2005, in The Initial Mass Function 50 Years Later (Springer Netherlands), 41–50
Chandrasekhar, S. 1935, Monthly Notices of the Royal Astronomical Society, 95, 207
Chevalier, R. A. 1977, Annual Review of Astronomy and Astrophysics, 15, 175
Chevalier, R. A. & Kirshner, R. P. 1979, The Astrophysical Journal, 233, 154
Chomiuk, L. & Povich, M. S. 2011, The Astronomical Journal, 142, 197
Churazov, E., Sunyaev, R., Isern, J., et al. 2015, The Astrophysical Journal, 812, 62
Clark, P. C., Bonnell, I. A., Zinnecker, H., & Bate, M. R. 2005, Monthly Notices of the RAS, 359, 809
Clifford, F. E. & Tayler, R. J. 1965, Memoirs of the Royal Astronomical Society, 69, 21
Compton, A. H. 1923, Physical Review, 21, 483
Crocker, R. M., Ruiter, A. J., Seitenzahl, I. R., et al. 2017, Nature Astronomy, 1
Cromartie, H. T., Fonseca, E., Ransom, S. M., et al. 2019, Nature Astronomy, 4, 72
Daly, E. 1994, Radiation Physics and Chemistry, 43, 1
Dame, T. M., Hartmann, D., & Thaddeus, P. 2001, The Astrophysical Journal, 547, 792
Dawson, P. C. & Johnson, R. G. 1994, Journal of the RAS of Canada, 88, 369
de Angelis, A., Tatischeff, V., Grenier, I. A., et al. 2018, Journal of High Energy Astrophysics, 19, 1
Dhawan, S., Leibundgut, B., Spyromilio, J., & Blondin, S. 2016, Astronomy & Astrophysics, 588, A84
Dib, S. 2014, Monthly Notices of the RAS, 444, 1957
Dicke, R. H. & Marshall, J. 1943, Physical Review, 63, 86
Diehl, R., Dupraz, C., Bennett, K., et al. 1995, Astronomy and Astrophysics, 298, 445
Diehl, R., Halloin, H., Kretschmer, K., et al. 2006a, Nature, 439, 45
Diehl, R., Prantzos, N., & von Ballmoos, P. 2006b, Nuclear Physics A, 777, 70
Diehl, R., Siegert, T., Greiner, J., et al. 2018, Astronomy & Astrophysics, 611, A12
Diehl, R., Siegert, T., Hillebrandt, W., et al. 2014, Science, 345, 1162
Diehl, R., Siegert, T., Hillebrandt, W., et al. 2015, Astronomy & Astrophysics, 574, A72
Dobbs, C. L., Krumholz, M. R., Ballesteros-Paredes, J., et al. 2014, in Protostars and Planets VI, ed. H. Beuther, R. S. Klessen, C. P. Dullemond, & T. Henning, 3
Docenko, D. & Sunyaev, R. A. 2010, Astronomy and Astrophysics, 509, A59

Drury, L. O. 1983, Reports on Progress in Physics, 46, 973
Dufour, F. & Kaspi, V. M. 2013, The Astrophysical Journal, 775, 52
Dupraz, C., Bloemen, H., Bennett, K., et al. 1997, Astronomy and Astrophysics, 324, 683
Dyk, S. D. V. 2017, Philosophical Transactions of the Royal Society A: Mathematical, Physical and Engineering Sciences, 375, 20160277
Einstein, A. 1905, Annalen der Physik, 322, 132
Ellinger, C. I., Young, P. A., Fryer, C. L., & Rockefeller, G. 2012, The Astrophysical Journal, 755, 160
Ellison, D. C., Berezhko, E. G., & Baring, M. G. 2000, The Astrophysical Journal, 540, 292
Ellison, D. C., Decourchelle, A., & Ballet, J. 2005, Astronomy & Astrophysics, 429, 569
Engelmann, J. J., Ferrando, P., Soutoul, A., et al. 1990, Astronomy & Astrophysics, 233, 96
Eriksen, K. A., Arnett, D., McCarthy, D. W., & Young, P. 2009, The Astrophysical Journal, 697, 29
Faucher-Giguere, C.-A. & Kaspi, V. M. 2006, The Astrophysical Journal, 643, 332
Fernández, R. 2010, The Astrophysical Journal, 725, 1563
Fesen, R. A., Hammell, M. C., Morse, J., et al. 2006, The Astrophysical Journal, 645, 283
Figer, D. F. 2005, Nature, 434, 192
Filippenko, A. V. 1997, Annual Review of Astronomy and Astrophysics, 35, 309
Filippenko, A. V., Chornock, R., Swift, B., et al. 2003, IAU Cirulars, 8159, 2
Filippenko, A. V., Richmond, M. W., Branch, D., et al. 1992a, The Astronomical Journal, 104, 1543
Filippenko, A. V., Richmond, M. W., Matheson, T., et al. 1992b, The Astrophysical Journal, 384, L15
Fink, M., Hillebrandt, W., & Röpke, F. K. 2007, Astronomy & Astrophysics, 476, 1133
Fink, M., Kromer, M., Seitenzahl, I. R., et al. 2014, MNRAS, 438, 1762
Fink, M., Röpke, F. K., Hillebrandt, W., et al. 2010, Astronomy and Astrophysics, 514, A53
Firestone, R. B. & Shirley, V. S. 1998, Table of Isotopes, 2 Volume Set
Flörs, A. 2020, PhD thesis, Technische Universität München, Garching bei München, Online available at: http://mediatum.ub.tum.de/?id=1553751
Frail, D. A., Goss, W. M., & Whiteoak, J. B. Z. 1994, The Astrophysical Journal, 437, 781
Fröhlich, C., Martínez-Pinedo, G., Liebendörfer, M., et al. 2006, Physical Review Letters, 96
Fryer, C. L., Young, P., Bennett, M., et al. 2008, arXiv e-prints, arXiv:0811.4648
Gaia Collaboration, Brown, A. G. A., Vallenari, A., et al. 2018, Astronomy and Astrophysics, 616, A1
Gall, E. E. E., Polshaw, J., Kotak, R., et al. 2015, Astronomy and Astrophysics, 582, A3
Grebenev, S. A., Lutovinov, A. A., Tsygankov, S. S., & Winkler, C. 2012, Nature, 490, 373
Green, D. A. 2002, Highlights of Astronomy, 12, 350
Green, D. A. 2014, Bulletin of the Astronomical Society of India, 42, 47
Green, D. A. 2019, Journal of Astrophysics and Astronomy, 40
Grefenstette, B. W., Fryer, C. L., Harrison, F. A., et al. 2017, The Astrophysical Journal, 834, 19
Grefenstette, B. W., Harrison, F. A., Boggs, S. E., et al. 2014, Nature, 506, 339
Grefenstette, B. W., Reynolds, S. P., Harrison, F. A., et al. 2015, The Astrophysical Journal, 802, 15
Grinberg, V., Hell, N., Pottschmidt, K., et al. 2013, Astronomy & Astrophysics, 554, A88
Güsten, R. & Mezger, P. 1982, Vistas in Astronomy, 26, 159

Guillochon, J., Dan, M., Ramirez-Ruiz, E., & Rosswog, S. 2010, The Astrophysical Journal, 709, L64
Hales, S. E. G., Waldram, E. M., Rees, N., & Warner, P. J. 1995, Monthly Notices of the Royal Astronomical Society, 274, 447
Harris, J. A., Hix, W. R., Chertkow, M. A., et al. 2017, The Astrophysical Journal, 843, 2
Harrison, F. A., Craig, W. W., Christensen, F. E., et al. 2013, The Astrophysical Journal, 770, 103
Hartmann, D., Woosley, S. E., & Eid, M. F. E. 1985, The Astrophysical Journal, 297, 837
Hatano, K., Fisher, A., & Branch, D. 1997, Monthly Notices of the Royal Astronomical Society, 290, 360
Hayato, A., Yamaguchi, H., Tamagawa, T., et al. 2010, The Astrophysical Journal, 725, 894
Heger, A. & Woosley, S. E. 2002, The Astrophysical Journal, 567, 532
Heitsch, F., Burkert, A., Hartmann, L. W., Slyz, A. D., & Devriendt, J. E. G. 2005, The Astrophysical Journal Letters, 633, L113
Helder, E. A. & Vink, J. 2008, The Astrophysical Journal, 686, 1094
Helder, E. A., Vink, J., Bykov, A. M., et al. 2012, Space Science Reviews, 173, 369
Hempel, M., Fischer, T., Schaffner-Bielich, J., & Liebendörfer, M. 2012, The Astrophysical Journal, 748, 70
Hermansen, K., Couch, S. M., Roberts, L. F., Schatz, H., & Warren, M. L. 2020, The Astrophysical Journal, 901, 77
Hess, V. F. 1912, Phys. Z., 13, 1084
Hillas, A. M. 2006, arXiv e-prints, astro
Hillebrandt, W., Kromer, M., Röpke, F. K., & Ruiter, A. J. 2013, Frontiers of Physics, 8, 116
Hiraga, J. S., Kobayashi, Y., Tamagawa, T., et al. 2009, Publications of the Astronomical Society of Japan, 61, 275
Hirata, K., Kajita, T., Koshiba, M., et al. 1987, Physical Review Letters, 58, 1490
Hix, W. R., Lentz, E. J., Endeve, E., et al. 2014, AIP Advances, 4, 041013
Hoeflich, P. & Khokhlov, A. 1996, The Astrophysical Journal, 457, 500
Hoffman, R. D., Woosley, S. E., Weaver, T. A., et al. 1995, in Gamma Ray Sky with Compton GRO and SIGMA, 267–278
Howell, D. A. 2001, The Astrophysical Journal Letters, 554, L193
Howell, D. A., Sullivan, M., Brown, E. F., et al. 2009, The Astrophysical Journal, 691, 661
Hoyle, F. & Fowler, W. A. 1960, The Astrophysical Journal, 132, 565
Iben, I. & Renzini, A. 1983, Annual Review of Astronomy and Astrophysics, 21, 271
Icko Iben, J., Ritossa, C., & Garcia-Berro, E. 1997, The Astrophysical Journal, 489, 772
Iliadis, C. 2015, Nuclear Physics of Stars (Weinheim: Viley-VCH), second Edition
Iyudin, A. 1999, Nuclear Physics A, 654, 900c
Iyudin, A. F., Aschenbach, B., Becker, W., Dennerl, K., & Haberl, F. 2004, Astronomy & Astrophysics, 429, 225
Iyudin, A. F., Diehl, R., Bloemen, H., et al. 1994, Astronomy and Astrophysics, 284, L1
Iyudin, A. F., Müller, E., & Obergaulinger, M. 2019, Monthly Notices of the Royal Astronomical Society, 485, 3288
Iyudin, A. F., Schönfelder, V., Bennett, K., et al. 1998, Nature, 396, 142
Janka, H., LANGANKE, K., MAREK, A., MARTINEZPINEDO, G., & MULLER, B. 2007, Physics Reports, 442, 38
Janka, H.-T. 2012, Annual Review of Nuclear and Particle Science, 62, 407

Janka, H.-T. 2017, in Handbook of Supernovae (Springer International Publishing), 1095–1150
Janka, H. T., Buras, R., Kitaura Joyanes, F. S., et al. 2005, Nuclear Physics A, 758, 19
Janka, H.-T., Hanke, F., Hüdepohl, L., et al. 2012, Progress of Theoretical and Experimental Physics, 2012
Jauch, J. M. & Rohrlich, F. 1976, The theory of photons and electrons. The relativistic quantum field theory of charged particles with spin one-half
Jean, P., von Ballmoos, P., Vedrenne, G., Teegarden, B. J., & Naya, J. E. 1996, in Gamma-Ray and Cosmic-Ray Detectors, Techniques, and Missions, ed. B. D. Ramsey & T. A. Parnell (SPIE)
Jeans, J. H. 1902, Philosophical Transactions of the Royal Society of London Series A, 199, 1
Jerkstrand, A., Fransson, C., & Kozma, C. 2011, Astronomy & Astrophysics, 530, A45
Jones, T. W., Rudnick, L., Jun, B.-I., et al. 1998, Publications of the Astronomical Society of the Pacific, 110, 125
Jourdain, E. & Roques, J. P. 2009, The Astrophysical Journal, 704, 17
Jourdain, E., Roques, J. P., & Malzac, J. 2011, The Astrophysical Journal, 744, 64
Kasen, D. & Woosley, S. E. 2009, The Astrophysical Journal, 703, 2205
Kasen, D., Woosley, S. E., & Heger, A. 2011, The Astrophysical Journal, 734, 102
Kasliwal, M. M., Kulkarni, S. R., Gal-Yam, A., et al. 2012, The Astrophysical Journal, 755, 161
Kato, M., Saio, H., Hachisu, I., & Nomoto, K. 2014, The Astrophysical Journal, 793, 136
Keane, E. F. & Kramer, M. 2008, Monthly Notices of the Royal Astronomical Society, 391, 2009
Kennicutt, Robert C., J. 1998, Annual Review of Astronomy and Astrophysics, 36, 189
Kennicutt, R. C. & Evans, N. J. 2012, Annual Review of Astronomy and Astrophysics, 50, 531
Kepler, S. O., Kleinman, S. J., Nitta, A., et al. 2007, Monthly Notices of the RAS, 375, 1315
Kerr, F. J. & Lynden-Bell, D. 1986, Monthly Notices of the Royal Astronomical Society, 221, 1023
Khokhlov, A. M. 1991, Astronomy and Astrophysics, 245, 114
Kiener, J., Berheide, M., Achouri, N. L., et al. 1998, Physical Review C, 58, 2174
Kippenhahn, R., Weigert, A., & Weiss, A. 2012, Stellar Structure and Evolution (Springer Berlin Heidelberg)
Kirsch, M. G., Briel, U. G., Burrows, D., et al. 2005, in UV, X-Ray, and Gamma-Ray Space Instrumentation for Astronomy XIV, ed. O. H. W. Siegmund (SPIE)
Kitaura, F. S., Janka, H.-T., & Hillebrandt, W. 2006, Astronomy and Astrophysics, 450, 345
Klein, O. & Nishina, T. 1929, Zeitschrift fur Physik, 52, 853
Klessen, R. S. & Glover, S. C. O. 2016, Saas-Fee Advanced Course, 43, 85
Knoll, G. F. 2010, Radiation Detection and Measurement (John Wiley & Sons, Inc.)
Kozlovsky, B., Murphy, R. J., & Ramaty, R. 2002, The Astrophysical Journal Supplement Series, 141, 523
Krause, O. 2005, Science, 308, 1604
Krause, O., Birkmann, S. M., Usuda, T., et al. 2008a, Science, 320, 1195
Krause, O., Tanaka, M., Usuda, T., et al. 2008b, Nature, 456, 617
Kretschmer, K. 2011, PhD thesis, Technische Universität München, Garching bei München, Online available at: https://https://mediatum.ub.tum.de/1074263

Kromer, M., Sim, S. A., Fink, M., et al. 2010, The Astrophysical Journal, 719, 1067
Kroupa, P. 2001, Monthly Notices of the Royal Astronomical Society, 322, 231
Kroupa, P., Weidner, C., Pflamm-Altenburg, J., et al. 2013, in Planets, Stars and Stellar Systems (Springer Netherlands), 115–242
Krumholz, M. R. 2014, Physics Reports, 539, 49
Krumholz, M. R., Matzner, C. D., & McKee, C. F. 2006, The Astrophysical Journal, 653, 361
Krumholz, M. R., McKee, C. F., & Bland-Hawthorn, J. 2019, Annual Review of Astronomy and Astrophysics, 57, 227
Kuiper, L., Hermsen, W., Cusumano, G., et al. 2001, Astronomy & Astrophysics, 378, 918
Kumar, S. & VERITAS Collaboration. 2015, in International Cosmic Ray Conference, Vol. 34, 34th International Cosmic Ray Conference (ICRC2015), 760
Labanti, C., Cocco, G. D., Ferro, G., et al. 2003, Astronomy & Astrophysics, 411, L149
Lada, C. J. & Lada, E. A. 2003, Annual Review of Astronomy and Astrophysics, 41, 57
Laming, J. M. & Hwang, U. 2003, The Astrophysical Journal, 597, 347
Larsson, J., Fransson, C., Spyromilio, J., et al. 2016, The Astrophysical Journal, 833, 147
Lattimer, J. M. & Swesty, D. F. 1991, Nuclear Physics A, 535, 331
Lebrun, F., Leray, J. P., Lavocat, P., et al. 2003, Astronomy & Astrophysics, 411, L141
Lee, Y.-H., Koo, B.-C., Moon, D.-S., & Lee, J.-J. 2015, The Astrophysical Journal, 808, 98
Leibundgut, B., Kirshner, R. P., Phillips, M. M., et al. 1993, The Astronomical Journal, 105, 301
Leising, M. D. & Share, G. H. 1994, The Astrophysical Journal, 424, 200
Leonard, D. C. 2007, The Astrophysical Journal, 670, 1275
Leung, S.-C. & Nomoto, K. 2020, The Astrophysical Journal, 888, 80
Levkovski, V. 1991, Activation cross section nuclides of averagemasses (A= 40–100) by protons and alpha particles with at medium (E= 10–50 MeV) energies (experiment and systematics) (Inter Vesi, Moscow)
Li, W., Chornock, R., Leaman, J., et al. 2011, Monthly Notices of the RAS, 412, 1473
Li, W., Leaman, J., Chornock, R., et al. 2011, Monthly Notices of the Royal Astronomical Society, 412, 1441
Lichti, G. & Georgii, R. 2001, Instruments, ed. V. Schönfelder, 27–76
Limongi, M. & Chieffi, A. 2003, The Astrophysical Journal, 592, 404
Limongi, M. & Chieffi, A. 2018, The Astrophysical Journal Supplement Series, 237, 13
Ling, J. C. & Wheaton, W. A. 2003, The Astrophysical Journal, 598, 334
Lingenfelter, R. E. 2019, The Astrophysical Journal Supplement Series, 245, 30
Lodders, K. 2003, The Astrophysical Journal, 591, 1220
Lopez, L. A., Grefenstette, B. W., Reynolds, S. P., et al. 2015, The Astrophysical Journal, 814, 132
Lugaro, M. & Chieffi, A. 2011, Radioactivites in Low- and Intermediate-Mass Stars, ed. R. Diehl, D. H. Hartmann, & N. Prantzos, Vol. 812, 83–152
Luhman, K. L. & Potter, D. 2006, The Astrophysical Journal, 638, 887
Lund, N., Budtz-Jørgensen, C., Westergaard, N. J., et al. 2003, Astronomy & Astrophysics, 411, L231
Lunnan, R., Kasliwal, M. M., Cao, Y., et al. 2017, The Astrophysical Journal, 836, 60
Ma, H., Woosley, S. E., Malone, C. M., Almgren, A., & Bell, J. 2013, The Astrophysical Journal, 771, 58
Madsen, K. K., Forster, K., Grefenstette, B. W., Harrison, F. A., & Stern, D. 2017, The

Astrophysical Journal, 841, 56
Maeda, K. & Nomoto, K. 2003, The Astrophysical Journal, 598, 1163
Maeda, K., Röpke, F. K., Fink, M., et al. 2010, The Astrophysical Journal, 712, 624
Maeda, Y., Uchiyama, Y., Bamba, A., et al. 2009, Publications of the Astronomical Society of Japan, 61, 1217
Magkotsios, G., Timmes, F. X., Hungerford, A. L., et al. 2010, The Astrophysical Journal Supplement Series, 191, 66
Manchester, R. N., Hobbs, G. B., Teoh, A., & Hobbs, M. 2005, VizieR Online Data Catalog, VII/245
Mannucci, F. 2005, in Astronomical Society of the Pacific Conference Series, Vol. 342, 1604-2004: Supernovae as Cosmological Lighthouses, ed. M. Turatto, S. Benetti, L. Zampieri, & W. Shea, 140
Mas-Hesse, J. M., Giménez, A., Culhane, J. L., et al. 2003, Astronomy & Astrophysics, 411, L261
Massey, P. 2003, Annual Review of Astronomy and Astrophysics, 41, 15
Matz, S., Share, G., Leising, M., et al. 1988, Nature, 331, 416
Mazurek, T. J. 1982, The Astrophysical Journal, 259, L13
Mazzali, P. A., Chugai, N., Turatto, M., et al. 1997, Monthly Notices of the Royal Astronomical Society, 284, 151
Mazzali, P. A. & Hachinger, S. 2012, Monthly Notices of the Royal Astronomical Society, 424, 2926
Mazzali, P. A., Kawabata, K. S., Maeda, K., et al. 2007, The Astrophysical Journal, 670, 592
McCray, R. 2017, The Physics of Supernova 1987A, ed. A. W. Alsabti & P. Murdin, 2181
McEnery, J., van der Horst, A., Dominguez, A., et al. 2019, in Bulletin of the American Astronomical Society, Vol. 51, 245
McKee, C. F. 1999, in NATO Advanced Study Institute (ASI) Series C, Vol. 540, The Origin of Stars and Planetary Systems, ed. C. J. Lada & N. D. Kylafis, 29
McKee, C. F. & Ostriker, E. C. 2007, Annual Review of Astronomy and Astrophysics, 45, 565
McKee, C. F. & Williams, J. P. 1997, The Astrophysical Journal, 476, 144
McKinnon, R., Torrey, P., & Vogelsberger, M. 2016, Monthly Notices of the Royal Astronomical Society, 457, 3775
Medd, W. J. & Ramana, K. V. V. 1965, The Astrophysical Journal, 142, 383
Melson, T., Janka, H.-T., Bollig, R., et al. 2015, The Astrophysical Journal Letters, 808, L42
Melson, T., Janka, H.-T., & Marek, A. 2015, The Astrophysical Journal, 801, L24
Meneguzzi, M. & Reeves, H. 1975, Astronomy and Astrophysics, 40, 91
Messer, B., Bruenn, S., Blondin, J., et al. 2010, in Nuclei in the Cosmos, 27
Meyer, B. S. 1994, Annual Review of Astronomy and Astrophysics, 32, 153
Miceli, M., Sciortino, S., Troja, E., & Orlando, S. 2015, The Astrophysical Journal, 805, 120
Micelotta, E. R., Dwek, E., & Slavin, J. D. 2016, Astronomy & Astrophysics, 590, A65
Mighell, K. J. 1999, The Astrophysical Journal, 518, 380
Mitchell, L., Anderson, M., Kennett, S., & Sargood, D. 1982, Nuclear Physics A, 380, 318
Miyaji, S. & Nomoto, K. 1987, The Astrophysical Journal, 318, 307
Moll, R. & Woosley, S. E. 2013, The Astrophysical Journal, 774, 137
Morlino, G. & Caprioli, D. 2012, Astronomy & Astrophysics, 538, A81

Mulchaey, J. S., Kasliwal, M. M., & Kollmeier, J. A. 2013, The Astrophysical Journal, 780, L34
Murphy, R. J., Share, G. H., Grove, J. E., et al. 1996, in AIP Conference Proceedings (AIP)
Nagano, M. & Watson, A. A. 2000, Reviews of Modern Physics, 72, 689
Nagataki, S., Shimizu, T. M., & Sato, K. 1998, The Astrophysical Journal, 495, 413
Neyman, J. & Pearson, E. S. 1933, Philosophical Transactions of the Royal Society of London Series A, 231, 289
NNDC. 2020, - Table of Nuclides, Website, information extracted from the NuDat 2, https://www.nndc.bnl.gov/nudat2/, accessed: 2020-07-21
Nomoto, K. 1982, The Astrophysical Journal, 253, 798
Nomoto, K., Kobayashi, C., & Tominaga, N. 2013, Annual Review of Astronomy and Astrophysics, 51, 457
Nomoto, K. & Kondo, Y. 1991, The Astrophysical Journal, 367, L19
Nomoto, K. & Leung, S.-C. 2017, in Handbook of Supernovae (Springer International Publishing), 1275–1313
Nomoto, K., Thielemann, F. K., & Yokoi, K. 1984, The Astrophysical Journal, 286, 644
Norbury, J. W. 2009, Nuclear Instruments and Methods in Physics Research Section B: Beam Interactions with Materials and Atoms, 267, 1209
Nugent, P., Baron, E., Branch, D., Fisher, A., & Hauschildt, P. H. 1997, The Astrophysical Journal, 485, 812
Oberlack, U., Bennett, K., Bloemen, H., et al. 1996, Astronomy and Astrophysics Supplement, 120, 311
Oey, M. S. & Clarke, C. J. 2005, The Astrophysical Journal Letters, 620, L43
Offner, S. S. R., Clark, P. C., Hennebelle, P., et al. 2014, in Protostars and Planets VI, ed. H. Beuther, R. S. Klessen, C. P. Dullemond, & T. Henning, 53
Ohnishi, N., Iwakami, W., Kotake, K., et al. 2008, Journal of Physics: Conference Series, 112, 042018
Opik, E. 1922, The Astrophysical Journal, 55, 406
Oppenheimer, J. R. & Plesset, M. S. 1933, Physical Review, 44, 53
Padoan, P., Federrath, C., Chabrier, G., et al. 2014, in Protostars and Planets VI, ed. H. Beuther, R. S. Klessen, C. P. Dullemond, & T. Henning, 77
Padoan, P., Nordlund, Å., Kritsuk, A. G., Norman, M. L., & Li, P. S. 2007, The Astrophysical Journal, 661, 972
Pakmor, R., Hachinger, S., Röpke, F. K., & Hillebrandt, W. 2011, Astronomy & Astrophysics, 528, A117
Pakmor, R., Kromer, M., Röpke, F. K., et al. 2010, Nature, 463, 61
Pakmor, R., Kromer, M., Taubenberger, S., et al. 2012, The Astrophysical Journal, 747, L10
Pakmor, R., Kromer, M., Taubenberger, S., & Springel, V. 2013, The Astrophysical Journal, 770, L8
Panov, I. V. & Janka, H.-T. 2008, Astronomy & Astrophysics, 494, 829
Parizot, E., Marcowith, A., van der Swaluw, E., Bykov, A. M., & Tatischeff, V. 2004, Astronomy and Astrophysics, 424, 747
Parker, E. A. & Shakeshaft, J. R. 1968, Monthly Notices of the Royal Astronomical Society, 138, 407
Patnaude, D. J., Badenes, C., Park, S., & Laming, J. M. 2012, The Astrophysical Journal, 756, 6
Patnaude, D. J. & Fesen, R. A. 2009, The Astrophysical Journal, 697, 535

Pavlov, G. G., Sanwal, D., Kızıltan, B., & Garmire, G. P. 2001, The Astrophysical Journal, 559, L131
Pavlović, M., Urošević, D., Vukotić, B., Arbutina, B., & Göker, . D. 2012, The Astrophysical Journal Supplement Series, 204, 4
Perets, H. B., Gal-Yam, A., Mazzali, P. A., et al. 2010, Nature, 465, 322
Perlmutter, S., Aldering, G., Valle, M. D., et al. 1998, Nature, 391, 51
Pfeffermann, E. & Aschenbach, B. 1996, in Roentgenstrahlung from the Universe, ed. H. U. Zimmermann, J. Trümper, & H. Yorke, 267–268
Pflamm-Altenburg, J., González-Lópezlira, R. A., & Kroupa, P. 2013, Monthly Notices of the Royal Astronomical Society, 435, 2604
Pflamm-Altenburg, J., Weidner, C., & Kroupa, P. 2007, The Astrophysical Journal, 671, 1550
Phillips, M. M. 1993, The Astrophysical Journal, 413, L105
Phillips, M. M., Lira, P., Suntzeff, N. B., et al. 1999, The Astronomical Journal, 118, 1766
Phillips, M. M., Wells, L. A., Suntzeff, N. B., et al. 1992, The Astronomical Journal, 103, 1632
Pietrzyński, G., Graczyk, D., Gallenne, A., et al. 2019, Nature, 567, 200
Planck Collaboration, Ade, P. A. R., Aghanim, N., et al. 2014, Astronomy and Astrophysics, 571, A13
Pleintinger, M. 2020, PhD thesis, Technische Universität München, Garching bei München, Online available at: http://mediatum.ub.tum.de/?id=1554296
Pleintinger, M. M. M., Siegert, T., Diehl, R., et al. 2019, Astronomy & Astrophysics, 632, A73
Plüschke, S., Diehl, R., Schönfelder, V., et al. 2001, in ESA Special Publication, Vol. 459, Exploring the Gamma-Ray Universe, ed. A. Gimenez, V. Reglero, & C. Winkler, 55–58
Pravdo, S. H., Angelini, L., & Harding, A. K. 1997, The Astrophysical Journal, 491, 808
Ramaty, R., Kozlovsky, B., & Lingenfelter, R. E. 1979, The Astrophysical Journal Supplement Series, 40, 487
Ramaty, R., Kozlovsky, B., & Lingenfelter, R. E. 1996, The Astrophysical Journal, 456, 525
Reed, B. C. 2005, The Astronomical Journal, 130, 1652
Reed, J. E., Hester, J. J., Fabian, A. C., & Winkler, P. F. 1995, The Astrophysical Journal, 440, 706
Reich, W., Fuerst, E., Reich, P., & Reif, K. 1990, Astronomy and Astrophysics, 85, 633
Reid, M. J., Dame, T. M., Menten, K. M., & Brunthaler, A. 2016, The Astrophysical Journal, 823, 77
Reid, M. J., Menten, K. M., Brunthaler, A., et al. 2019, The Astrophysical Journal, 885, 131
Renaud, M., Vink, J., Decourchelle, A., et al. 2006, New Astronomy Reviews, 50, 540
Rest, A., Foley, R. J., Sinnott, B., et al. 2011, The Astrophysical Journal, 732, 3
Reynolds, S. P. 2008, Annual Review of Astronomy and Astrophysics, 46, 89
Reynolds, S. P., Borkowski, K. J., Green, D. A., et al. 2008, The Astrophysical Journal Letters, 680, L41
Reynolds, S. P., Borkowski, K. J., Hwang, U., et al. 2007, The Astrophysical Journal Letters, 668, L135
Rho, J., Reynolds, S. P., Reach, W. T., et al. 2003, The Astrophysical Journal, 592, 299
Rickett, B. J. 1990, Annual Review of Astronomy and Astrophysics, 28, 561
Riess, A. G., Filippenko, A. V., Li, W., et al. 1999, The Astronomical Journal, 118, 2675
Ritossa, C., Garcia-Berro, E., & Icko Iben, J. 1999, The Astrophysical Journal, 515, 381

Roberts, L. F., Ott, C. D., Haas, R., et al. 2016, The Astrophysical Journal, 831, 98
Robitaille, T. P. & Whitney, B. A. 2010, The Astrophysical Journal Letters, 710, L11
Rodriguez, J., Grinberg, V., Laurent, P., et al. 2015, The Astrophysical Journal, 807, 17
Röpke, F. K. 2007, The Astrophysical Journal, 668, 1103
Roques, J. P., Schanne, S., von Kienlin, A., et al. 2003, Astronomy & Astrophysics, 411, L91
Roth, J., Primbsch, J. H., & Lin, R. P. 1984, IEEE Transactions on Nuclear Science, 31, 367
Ruiz-Lapuente, P., Cappellaro, E., Turatto, M., et al. 1992, The Astrophysical Journal, 387, L33
Ruiz-Lapuente, P., Comeron, F., Méndez, J., et al. 2004, Nature, 431, 1069
Ryle, M. & Smith, F. G. 1948, Nature, 162, 462
Saio, H. & Nomoto, K. 1998, The Astrophysical Journal, 500, 388
Salpeter, E. E. 1955, The Astrophysical Journal, 121, 161
Sankrit, R., Raymond, J. C., Blair, W. P., et al. 2016, The Astrophysical Journal, 817, 36
Sasaki, M., Breitschwerdt, D., & Supper, R. 2004, Astrophysics and Space Science, 289, 283
Sato, T. & Hughes, J. P. 2017, The Astrophysical Journal, 840, 112
Sato, Y., Nakasato, N., Tanikawa, A., et al. 2015, The Astrophysical Journal, 807, 105
Sato, Y., Nakasato, N., Tanikawa, A., et al. 2016, The Astrophysical Journal, 821, 67
Savchenko, V., Ferrigno, C., Kuulkers, E., et al. 2017, The Astrophysical Journal, 848, L15
Scalzo, R. A., Ruiter, A. J., & Sim, S. A. 2014, Monthly Notices of the Royal Astronomical Society, 445, 2535
Schanne, S. 2006, Journal of Physics: Conference Series, 41, 46
Schmidt, M. 1959, The Astrophysical Journal, 129, 243
Schoenfelder, V. 2000, in AIP Conference Proceedings (AIP)
Schulz, C., Pflamm-Altenburg, J., & Kroupa, P. 2015, Astronomy & Astrophysics, 582, A93
Schure, K. M., Bell, A. R., O'C Drury, L., & Bykov, A. M. 2012, Space Science Reviews, 173, 491
Sedov, L. I. 1959, Similarity and Dimensional Methods in Mechanics
Seitenzahl, I. R., Ciaraldi-Schoolmann, F., Röpke, F. K., et al. 2013, MNRAS, 429, 1156
Seitenzahl, I. R., Timmes, F. X., & Magkotsios, G. 2014, The Astrophysical Journal, 792, 10
Shen, H., Toki, H., Oyamatsu, K., & Sumiyoshi, K. 1998, Nuclear Physics A, 637, 435
Shibata, M., Zhou, E., Kiuchi, K., & Fujibayashi, S. 2019, Physical Review D, 100
Siegert, T. 2017, PhD thesis, Technische Universität München, Garching bei München, Online available at: https://mediatum.ub.tum.de/doc/1340342/document.pdf
Siegert, T., Diehl, R., Krause, M. G. H., & Greiner, J. 2015, Astronomy and Astrophysics, 579, A124
Siegert, T., Diehl, R., Weinberger, C., et al. 2019, Astronomy & Astrophysics, 626, A73
Sim, S. A., Fink, M., Kromer, M., et al. 2012, Monthly Notices of the Royal Astronomical Society, 420, 3003
Sim, S. A., Röpke, F. K., Hillebrandt, W., et al. 2010, The Astrophysical Journal, 714, L52
Sinitsyna, V. G., Sinitsyna, V. Y., & Stozhkov, Y. I. 2019, Advances in Space Research, 64, 2585
Skinner, G. K. 2008, Applied Optics, 47, 2739
Skinner, M. A., Burrows, A., & Dolence, J. C. 2016, The Astrophysical Journal, 831, 81
Slane, P., Hughes, J. P., Edgar, R. J., et al. 2001, The Astrophysical Journal, 548, 814

Slane, P., Lee, S.-H., Ellison, D. C., et al. 2014, The Astrophysical Journal, 783, 33
Smartt, S. J. 2009, Annual Review of Astronomy and Astrophysics, 47, 63
Smith, L. F., Biermann, P., & Mezger, P. G. 1978, Astronomy and Astrophysics, 66, 65
Spiegel, D. S., Burrows, A., & Milsom, J. A. 2011, The Astrophysical Journal, 727, 57
Spyromilio, J., Meikle, W. P. S., & Allen, D. A. 1990, Monthly Notices of the Royal Astronomical Society, 242, 669
Stephenson, F. R. & Green, D. A. 2002, Historical supernovae and their remnants, 5
Stockinger, G., Janka, H.-T., Kresse, D., et al. 2020, Monthly Notices of the Royal Astronomical Society, 496, 2039
Strickman, M. S., Johnson, W. N., & Kurfess, J. D. 1979, The Astrophysical Journal, 230, L15
Stritzinger, M., Mazzali, P. A., Sollerman, J., & Benetti, S. 2006, Astronomy & Astrophysics, 460, 793
Strong, A. W., Porter, T. A., Digel, S. W., et al. 2010, The Astrophysical Journal, 722, L58
Sullivan, M., Kasliwal, M. M., Nugent, P. E., et al. 2011, The Astrophysical Journal, 732, 118
Sullivan, M., Le Borgne, D., Pritchet, C. J., et al. 2006, The Astrophysical Journal, 648, 868
Summa, A., Elsässer, D., & Mannheim, K. 2011, Astronomy and Astrophysics, 533, A13
Summa, A., Hanke, F., Janka, H.-T., et al. 2016, The Astrophysical Journal, 825, 6
Sutherland, R. S. & Dopita, M. A. 1995, The Astrophysical Journal, 439, 381
Tammann, G. A., Loeffler, W., & Schroeder, A. 1994, Astrophysical Journal Supplement, 92, 487
Tatischeff, V. 2003, EAS Publications Series, 7, 79
Taubenberger, S. 2017, in Handbook of Supernovae (Springer International Publishing), 317–373
Taylor, J. H. & Cordes, J. M. 1993, The Astrophysical Journal, 411, 674
The, L.-S., Clayton, D. D., Diehl, R., et al. 2006, Astronomy & Astrophysics, 450, 1037
Thielemann, F. K., Hirschi, R., Liebendörfer, M., & Diehl, R. 2011, Massive Stars and Their Supernovae, ed. R. Diehl, D. H. Hartmann, & N. Prantzos, Vol. 812, 153–232
Thielemann, F.-K., Isern, J., Perego, A., & von Ballmoos, P. 2018, Space Science Reviews, 214, 62
Thielemann, F.-K., Nomoto, K., & Hashimoto, M.-A. 1996, The Astrophysical Journal, 460, 408
Timmes, F. X., Woosley, S. E., Hartmann, D. H., & Hoffman, R. D. 1996, The Astrophysical Journal, 464, 332
Tomsick, J., Zoglauer, A., Sleator, C., et al. 2019, in Bulletin of the American Astronomical Society, Vol. 51, 98
Troja, E., Segreto, A., La Parola, V., et al. 2014, The Astrophysical Journal Letters, 797, L6
Tsunemi, H., Miyata, E., Aschenbach, B., Hiraga, J., & Akutsu, D. 2000, Publications of the Astronomical Society of Japan, 52, 887
Tsygankov, S. S., Krivonos, R. A., Lutovinov, A. A., et al. 2016, Monthly Notices of the RAS, 458, 3411
Tueller, J., Barthelmy, S., Gehrels, N., et al. 1990, The Astrophysical Journal Letters, 351, L41
Tur, C., Heger, A., & Austin, S. M. 2010, The Astrophysical Journal, 718, 357
Turatto, M., Benetti, S., Cappellaro, E., et al. 1996, Monthly Notices of the Royal Astronomical Society, 283, 1

Ubertini, P., Lebrun, F., Cocco, G. D., et al. 2003, Astronomy & Astrophysics, 411, L131
Uchiyama, Y. & Aharonian, F. A. 2008, The Astrophysical Journal Letters, 677, L105
Unsöld, A. & Baschek, B. 2002, Der neue Kosmos. Einführung in die Astronomie und Astrophysik
Urquhart, J. S., Figura, C. C., Moore, T. J. T., et al. 2013, Monthly Notices of the Royal Astronomical Society, 437, 1791
Valenti, S., Yuan, F., Taubenberger, S., et al. 2013, Monthly Notices of the Royal Astronomical Society, 437, 1519
van den Bergh, S. & Tammann, G. A. 1991, Annual Review of Astronomy and Astrophysics, 29, 363
van Riper, K. A. 1978, The Astrophysical Journal, 221, 304
Vedrenne, G., Roques, J.-P., Schönfelder, V., et al. 2003, A&A, 411, L63
Vestrand, W. T., Share, G. H., Murphy, R. J., et al. 1999, The Astrophysical Journal Supplement Series, 120, 409
Vink, J. 2011, The Astronomy and Astrophysics Review, 20
Vink, J., Bleeker, J., van der Heyden, K., et al. 2006, The Astrophysical Journal, 648, L33
Vink, J., Laming, J. M., Kaastra, J. S., et al. 2001, The Astrophysical Journal, 560, L79
Vink, J. S., Heger, A., Krumholz, M. R., et al. 2015, Highlights of Astronomy, 16, 51
Völk, H. J., Berezhko, E. G., & Ksenofontov, L. T. 2008, Astronomy & Astrophysics, 483, 529
von Kienlin, A., Beckmann, V., Rau, A., et al. 2003, Astronomy & Astrophysics, 411, L299
Waldman, R., Sauer, D., Livne, E., et al. 2011, The Astrophysical Journal, 738, 21
Wanajo, S., Janka, H.-T., & Müller, B. 2010, The Astrophysical Journal, 726, L15
Wanajo, S., Müller, B., Janka, H.-T., & Heger, A. 2018, The Astrophysical Journal, 852, 40
Wang, B., Meng, X.-C., Wang, X.-F., & Han, Z.-W. 2008, Chinese Journal of Astronomy and Astrophysics, 8, 71
Wang, W. & Li, Z. 2014, The Astrophysical Journal, 789, 123
Weaver, T. A. & Woosley, S. E. 1980, in Ninth Texas Symposium on Relativistic Astrophysics, Vol. 336, 335–357
Wegg, C., Gerhard, O., & Portail, M. 2015, Monthly Notices of the RAS, 450, 4050
Weidenspointner, G., Kiener, J., Gros, M., et al. 2003, Astronomy & Astrophysics, 411, L113
Weidner, C. & Kroupa, P. 2004, Monthly Notices of the Royal Astronomical Society, 348, 187
Weidner, C. & Kroupa, P. 2005, The Astrophysical Journal, 625, 754
Weidner, C., Kroupa, P., & Bonnell, I. A. D. 2010, Monthly Notices of the RAS, 401, 275
Weinberger, C., Diehl, R., Pleintinger, M., Siegert, T., & Greiner, J. 2020, Astronomy and Astrophysics, —,
Whelan, J. & Icko, J. I. 1973, The Astrophysical Journal, 186, 1007
Wilk, K. D., Hillier, D. J., & Dessart, L. 2017, Monthly Notices of the Royal Astronomical Society, 474, 3187
Wilks, S. S. 1938, The Annals of Mathematical Statistics, 9, 60
Willingale, R., Bleeker, J. A. M., van der Heyden, K. J., Kaastra, J. S., & Vink, J. 2002, Astronomy & Astrophysics, 381, 1039
Wilson-Hodge, C. A., Cherry, M. L., Case, G. L., et al. 2011, The Astrophysical Journal, 727, L40
Winkler, C., Courvoisier, T. J.-L., Cocco, G. D., et al. 2003, Astronomy & Astrophysics,

411, L1
Wolter, H. 1952, Annalen der Physik, 445, 94
Wongwathanarat, A., Janka, H. T., & Müller, E. 2013, Astronomy and Astrophysics, 552, A126
Wongwathanarat, A., Janka, H.-T., Müller, E., Pllumbi, E., & Wanajo, S. 2017, The Astrophysical Journal, 842, 13
Woosley, S. E., Arnett, W. D., & Clayton, D. D. 1973, The Astrophysical Journal Supplement Series, 26, 231
Woosley, S. E., Heger, A., & Weaver, T. A. 2002, Reviews of Modern Physics, 74, 1015
Woosley, S. E. & Kasen, D. 2011, The Astrophysical Journal, 734, 38
Woosley, S. E., Pinto, P. A., Martin, P. G., & Weaver, T. A. 1987, The Astrophysical Journal, 318, 664
Woosley, S. E., Taam, R. E., & Weaver, T. A. 1986, The Astrophysical Journal, 301, 601
Woosley, S. E. & Weaver, T. A. 1994, The Astrophysical Journal, 423, 371
Woosley, S. E. & Weaver, T. A. 1995, The Astrophysical Journal Supplement Series, 101, 181
Yanasak, N. E., Wiedenbeck, M. E., Binns, W. R., et al. 2001, Advances in Space Research, 27, 727
Young, P. A. & Fryer, C. L. 2007, The Astrophysical Journal, 664, 1033
Young, P. A., Fryer, C. L., Hungerford, A., et al. 2006, The Astrophysical Journal, 640, 891
Yuan, Y., Funk, S., Jóhannesson, G., et al. 2013, The Astrophysical Journal, 779, 117
Zeković, V., ARBUTINA, B., DOBARDŽIĆ, A., & PAVLOVIĆ, M. Z. 2013, International Journal of Modern Physics A, 28, 1350141
Zhou, P., Vink, J., Li, G., & Domček, V. 2018, The Astrophysical Journal, 865, L6
Zinnecker, H. 1982, Annals of the New York Academy of Sciences, 395, 226
Zinnecker, H. & Yorke, H. W. 2007, Annual Review of Astronomy and Astrophysics, 45, 481
Zirakashvili, V. N., Aharonian, F. A., Yang, R., Oña-Wilhelmi, E., & Tuffs, R. J. 2014, The Astrophysical Journal, 785, 130
Zoglauer, A., Reynolds, S. P., An, H., et al. 2015, The Astrophysical Journal, 798, 98